Design Studies for the Pixelized Readout of a TPC for the ILD

Dissertation
zur
Erlangung des Doktorgrades (Dr. rer. nat.)
der
Mathematisch-Naturwissenschaftlichen Fakultät
der
Rheinischen Friedrich-Wilhelms-Universität Bonn

vorgelegt von
THORSTEN KRAUTSCHEID
aus
Siegburg

Bonn 2015

Angefertigt mit Genehmigung der Mathematisch-Naturwissenschaftlichen Fakultät der Rheinischen Friedrich-Wilhelms-Universität Bonn

Referent:	Prof. Dr. Klaus Desch
Koreferent:	Prof. Dr. Ian Brock
Tag der Promotion:	11. September, 2015
Erscheinungsjahr:	2016

Abstract

A large Time Projection Chamber (TPC) is foreseen as central tracking device of the International Large Detector (ILD), as it provides a large number of measured track points simultaneously with a minimum of material budget. Many modern TPCs rely on micro-pattern gaseous detectors (MPGDs) as amplification stage and a readout based on pads or strips. The performance can be further improved with a pixelized readout structure, as the size of the amplification stage is matched by the granularity of the readout.

A pixelized readout can be realized with pixel chips with an integrated Micromegas structure which is added to the chips by techniques of industrial post-processing. The holes of the grid are perfectly aligned to the pixels, i.e. there is only one hole above each pixel. Due to the alignment, the gas amplification takes place directly above a single pixel and the created charge is mostly collected by this pixel. This way, even single electrons of the primary ionization can be separated.

To apply this kind of readout in large experiments, such as the TPC of the ILD, the technology has to be available in large quantities, as several square meters of readout area have to be covered. To this end, the original production process is transferred to the production on $8\,''$-wafers. Post-processed chips from this new production process are tested in terms of energy resolution, occupancy, detection efficiency and discharge stability. The results are compared with those obtained with devices of the original method of fabrication.

For the application in a TPC for the ILD it has to be ensured that pixelized readouts are capable of dealing with backgrounds present in the detector. Hence, the two main backgrounds, $\gamma\gamma \rightarrow$ hadrons and e^+e^--pairs are simulated with the required precision and the performance of an integrated pixel readout is examined, especially with the respect to the momentum resolution required at the ILD.

Contents

Chapter 1

Introduction

It is the endeavor of particle physics to fathom the natural order of things by describing the elementary constituents of matter and their fundamental interactions. To this end, the Standard Model (SM) has been established. Since its development, it provides the most accurate description of elementary particles and their complex dynamics. It includes three of the four fundamental forces and explains their interactions with the known particles by the mediation of gauge particles.[1] The SM has been very successful in explaining many phenomena and predicting new particles, an effort which has been crowned by the recent discovery of the Higgs boson. Still, it has some shortcomings and fails to explain some experimental observations. Consequently, further development of the current model is required.

The search for new physics beyond the SM is one of the main motivations for the design of new particle accelerators with ever higher collision energies. The past has proven that the interplay of lepton and hadron colliders combines great discovery power with high precision measurements. The Large Hadron Collider and its planned leptonic successor, the International Linear Collider (ILC) are thereby the latest iteration of this strategy.

To fully exploit the potential offered by a new collider, detectors are tailored for the operation in its particular environment. This requires the development of new technologies and the continuous improvement of existing ones, to keep up with ever more demanding experimental requirements. An example for this is the time projection chamber (TPC), which is foreseen as main tracking device by one detector concept for the ILC. Since their invention in the 1970's they have improved a lot. Especially, amplification stage and readout have evolved from multi-wire setups to modern techniques relying on micro-pattern gaseous detectors and a segmented readout plane.

This thesis is part of the effort to develop a TPC which satisfies the requirement of an ILC tracking detector. To this end, a novel technology is investigated which combines multi-pattern gaseous detectors with the high granularity of pixels chips. The thesis investigates two facets of the topic. First, a technological aspect is addressed, dealing with the production and characterization of these readout devices. Second, the performance of this approach, applied to a TPC at the ILC, is investigated in the presence of detector backgrounds typical to the ILC environment.

1.1 Outline of the thesis

The International Linear Collider is discussed in Chapter 2 of this thesis. A brief motivation for its construction leads to the reasons for the requirement of a detector with unprecedented resolution and

[1] Gravity is at currently accessible energies too weak to play a role in the interactions of elementary particles.

precision. Such a detector, the International Large Detector (ILD) is described in the second part of the chapter. To reach the required level of accuracy, it is very important to have a thorough understanding of the backgrounds present in the detector. Hence, the origin of detector backgrounds, as well as their influence on the detector performance are addressed.

Chapter 3 deals with gaseous detectors in general and time projection chambers (TPCs) in particular. A detailed discussion of the fundamental processes in gaseous detectors, like ionization, drift and gas amplificaton provides the basis for the description of a time projection chamber. Since the performance of a TPC as main tracker of the ILD is a central topic of this thesis, its operation is described in depth. This includes readout schemes like integrated pixel readouts and the application of an ion gate.

In Chapter 4 the production and performance of pixel readouts with integrated amplification stage is discussed. This includes the original method which yields up to nine devices as well as the novel wafer-scale production process by which a whole wafer of pixel chips is processed. Devices fabricated by the wafer-scale process are tested in terms of energy resolution, gas amplification and discharge stability and the results of these tests are presented.

Chapter 5 provides on overview of the tools and methods required for a detailed simulation of a TPC at the ILD relying on pixel chips with integrated amplification stage for its readout. A full detector simulation is required to take background processes into account. The data obtained from these simulations can be used for the calculation of field distortions in the TPC volume. The calculation methods are briefly summarized before a detailed TPC simulation is introduced, focusing in particular on the parts required for the simulation of a pixelized readout.

The application of the simulation methods to a pixelized ILD TPC in the presence of detector backgrounds is presented in Chapter 6. Charge depositons in the TPC volume are discussed as well as their impact on the occupancy of the readout. Backgrounds are not only the main contributors to the occupancy but also the source for distortions of the electric drift field which is consequently addressed as well as the deviation of the electron drift paths caused by them. The deviation of the electrons from their regular paths impacts the track reconstruction and as a result the obtainable momentum resolution. This phenomen, as well as its dependence on the gas amplification, ion gate and particle momentum are finally discussed in the last part of the chapter.

Chapter 2

ILD - A detector for the Inernational Linear Collider

Particle accelerators have played a key role throughout the history of high energy physics. Especially the interplay of lepton and hadron colliders has been beneficial for continuous progress. For the discovery of new physics at the high energy frontier higher and higher energies are required, as demanded by Einstein's mass energy relation $E = mc^2$. For this reason, the development of increasingly powerful colliders, leptonic as well as hadronic ones, is a main priority of particle physics.

Most modern particle accelerators are storage rings, i.e. circular accelerators. The advantage of this concept is that particles can traverse the acceleration range many times until they reach their designed collision energy. Another advantage is the possibility to create interaction points at several positions in the storage ring. Thus, it is possible to operate several experiments in parallel. The circular shape of storage rings has disadvantages too. Charged particles moving on curved tracks emit synchrotron radiation resulting in an energy loss, which has to be compensated for by the accelerator. The energy loss of the particle is proportional to the fourth power of its energy divided by its mass and inversely proportional to the curvature radius of the particle track. Thus, the emitted energy depends strongly on the mass of the particle, so that the energy loss becomes a problem for lepton colliders at much lower energies than for their hadronic counterparts. While larger curvature radii of the accelerating structures can reduce the occurrence of synchrotron radiation, this approach is limited by the practicability of building ever larger acceleration structures.

As favorable hadron colliders behave in terms of synchrotron radiation, they also suffer from the fact that hadrons are no elementary particles. Hadrons consist of quarks and qluons, each carrying part of the total momentum. This circumstance complicates the determination of center-of-mass energy and momentum of the colliding particles. The large amount of involved constituent particles is a constant source of background, from which the events under study have to be distinguished. Lepton colliders are not affected by these problems. As leptons are elementary particles, their initial states are well defined and the produced background is near to negligible.

As already mentioned above, the complementary use of lepton and hadron colliders has been a recipe for success in the history of particle physics. Hadron colliders can reach highest center-of-mass energies, providing a great discovery potential. Lepton colliders are well suited for high precision measurements of newly discovered particles. The collider with the currently highest center-of-mass energy is the Large Hadron Collider (LHC) [1–3] near Geneva, Switzerland. It is designed to operate at center-of-mass energies of up to 14 TeV. The operation of the LHC has been very successful so far and was

crowned with the discovery of a new particle [4, 5], which is widely believed to be the long searched for HIGGS boson [6–8]. Especially in the light of this new discovery, the design of a complementary leptonic machine is an enterprise of highest importance.

This chapter presents the design of the International Linear Collider. After a short motivation, the general layout of the collider is described in Section 2.1. A strong focus is put on the structure of the beam and its implications for machine induced backgrounds. The International Large Detector, a detector designed to be operated at the ILC, is presented in Section 2.2. After a general description of the detector and its components, machine induced backgrounds are discussed before the whole chapter is concluded.

2.1 The International Linear Collider

The ILC is planned to be the next major project of particle physics. Nearly twenty years of research and development lead to its current design. Thus, the ILC has evolved to be the most advanced concept for high energy electron positron collisions which is currently available. Other concepts, like e.g. CLIC[9], have been proposed and their prospects are promising in many regards, but none of them reach the maturity of ILC. Therefore, the ILC is an obvious choice to complement the LHC at CERN[1] with high precision measurements of e^+e^--collisions.

2.1.1 Motivation

The ILC is designed to be a precision tool, capable to measure not only newly discovered particles with unprecedented accuracy. Most considerations of a physics program for the ILC have assumed the discovery of new physics at the terascale by the LHC, but even without such discoveries the ILC remains the obvious continuation of research in high energy physics.

The Standard Model (SM) of particle physics has been thoroughly tested at leptonic colliders like SLC [10] and LEP [11] as well as hadronic ones like the Tevatron [12] and most recently the LHC [1–3]. Although, these measurements have confirmed, that strong and electroweak interactions are correctly described by the SM many important aspects need further investigation.

Measuring the interactions among gauge bosons with a much higher precision than it was possible at LEP, the Tevatron and at the LHC is a very important task, for which the ILC is well suited. The ILC will be capable to access masses, widths and couplings of the W and Z bosons at a new level of precision. To this end, the pair production of electroweak gauge bosons, $e^+e^- \to W^+W^-$ and $e^+e^- \to ZZ$, are important processes to be studied. The mass of the W-boson, for instance, can be measured at a very high precision by performing a threshold scan at the production threshold of W-pairs [13]. As the beams of the ILC can be polarized (cf. Section 2.1.2), the production of the W-pairs can be enhanced or suppressed, because of the $V-A$ nature of the interactions. This can be exploited to estimate backgrounds by switching polarization states and contributes to the accuracy of the measurement.

Since the discovery of the top quark [14, 15], the ILC will be the first e^+e^--collider capable of providing a center-of-mass energy above the production threshold for direct $t\bar{t}$-production at about 350 GeV. As the SM's heaviest particle, the top quark is more strongly coupled to the electroweak symmetry breaking sector than any other fermion. Hence, it is expected to play an important role in its dynamics. The couplings of the top quark to the gauge bosons can be measured in a model independent way. This is particularly interesting, because many models expect these couplings to be very sensitive to non-SM physics. At the ILC, many properties of the top quark can be determined at an unprecedented level of

[1] CERN - European organization for nuclear research.

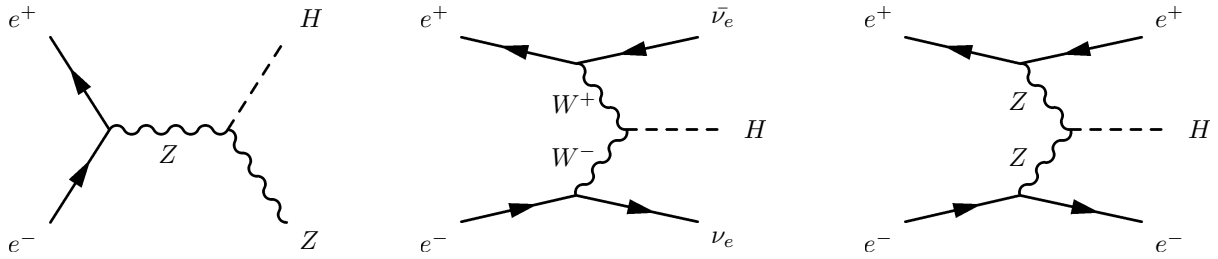

(a) Higgs-strahlung (b) WW-fusion (c) ZZ-fusion

Figure 2.1: Feynman graphs of the three main production processes of the Higgs-boson at the ILC, which are Higgs-strahlung (a), WW-fusion (b) and ZZ-fusion (c).

accuracy. It is expected that the mass of the top can be measured by threshold scans with an uncertainty of $\Delta m_t = 34\,\text{MeV}$ and its total decay width, with an accuracy of about 2.4 % [16].

Higgs physics at the ILC

A major motivation for the construction of the ILC is the Higgs boson. As the Higgs field couples to every kind of massive particle it is likely to play a key role in answering the open questions of particle physics. Owing to its very recent discovery [4, 5], many of its properties are sill unknown and measuring them is of utmost importance. The ILC is perfectly suited for this task, as it provides a well-controlled environment to precisely measure mass, quantum numbers, and couplings of this new particle. Only if all these properties are known the question of whether the new particle is indeed the SM Higgs boson can be answered.

The main production mechanisms for a SM Higgs boson at e^+e^--colliders are Higgs-strahlung, WW-fusion and ZZ-fusion processes, whose Feynman-diagrams are depicted in Figure 2.1. The Higgs-strahlung process is the dominant production process for center-of-mass energies of up to $\sqrt{s} \approx 450\,\text{GeV}$[2] where the WW-fusion process becomes dominant. The production cross section of ZZ-fusion is one magnitude smaller than the cross section for WW-fusion, as the neutral couplings to the Higgs are much smaller than the charged current couplings.

In its initial phase, the ILC will focus on a center-of-mass energy of 250 GeV, to obtain the highest cross section for the Higgs-strahlung process. At this center-of-mass energy, only an integrated luminosity of $250\,\text{fb}^{-1}$ is required to collect approximately 8.0×10^4 events containing a Higgs, thereby it is assumed that the polarization has been chosen to enhance the production rate.

A precision measurement of its mass is a good starting point for a detailed investigation of the Higgs boson. The mass can be cleanly determined with the help of the Higgs-strahlung process and its further decay products,

$$e^+e^- \to Zh \qquad \text{and} \qquad Z \to \begin{cases} \mu^+\mu^-, \\ e^+e^-. \end{cases}$$

For this processes the Higgs-mass, m_h, can be determined in a model independent way from the reconstructed recoil mass. The measurement can be performed with a precision of 40 MeV and 80 MeV for the decay in $\mu^+\mu^-$-pairs and e^+e^--pairs, respectively [17, 18], yielding an uncertainty of 32 MeV for both channels combined [18]. A huge advantage of this kind of measurement is that it relies only on

[2] $\sqrt{s} = \sqrt{(p_1 + p_2)^2}$ is a common abbreviation for the center-of-mass energy of two particles with four momenta p_1 and p_2.

Parameter	Accuracy $\Delta X/X$	$\sqrt{s}$	Remarks
m_H	0.03%	250 GeV	Δm_H =35 MeV
Γ_H	1.60%	250 GeV and 500 GeV	
$g(hWW)$	0.25%		
$g(hZZ)$	0.25%		
$g(hb\bar{b}ar)$	0.25%		
$g(hc\bar{c})$	0.25%		
$g(hgg)$	0.25%		
$g(h\tau^+\tau^-)$	0.25%		
$BR(h \rightarrow$ invisible)	$< 0.30\%$		at 95 % confidence level
$g(ht\bar{t})$	3.70%	1 TeV	
$g(hhh)$	26.00%		
$g(h\mu^+\mu^-)$	16.00%		

Table 2.1: Overview of possible measurements of the Higgs boson at the ILC [16].

the leptonic decay products of the Z and therefore is completely independent of the decay mode of the Higgs. Hence, the measurement can also be performed if the Higgs decays invisibly and is therefore completely independent of any model assumption.

While the mass measurement of the Higgs is best performed at a center-of-mass energy of $\sqrt{s}$ = 250 GeV, other studies can profit from higher energies. One would be a measurement of the top Yukawa coupling at tree level via the process $e^+e^- \rightarrow t\bar{t}h$ [19, 20], which becomes accessible at a center-of-mass energy of $\sqrt{s}$ = 500 GeV [21]. As the top quark is the heaviest particle of the SM, such a measurement would contribute greatly to the understanding of the mechanism for the mass generation of fermions.

One of the most important measurements concerning the Higgs at the ILC is its self-coupling, which is a cornerstone of the Higgs potential. As this, its measurement is of utmost importance for a deeper understanding of the electroweak symmetry breaking. The self-coupling can be probed by measuring the process $e^+e^- \rightarrow Zhh$, to which the triple Higgs couplings contribute at tree level. A simulation study, using $h \rightarrow b\bar{b}$ as secondary decay has shown that a cross section measurement of $\Delta\sigma/\sigma = 0.27$ is possible [13]. The self coupling, λ, can only be determined with an error of $\Delta\lambda/\lambda = 0.44$ because of contributions from background diagrams. This result can be improved by the development of more sophisticated jet clustering algorithms.

The sketched measurements of the Higgs boson and its properties are just a small example of what is possible at the ILC. See [13] for more details on the processes described above and further possible measurements. An overview of some of these measurements together with their expected accuracies are listed in Table 2.1.

2.1.2 Accelerator design

According to its baseline design, the ILC covers the energy range from 200 GeV up to 500 GeV continuously and may deliver an integrated luminosity of 500 fb^{-1} within the first four years of operation. The ILC is about 31 km long and can be upgraded to a center-of-mass energy of 1 TeV by increasing the range. Further upgrade options include the possibility of e^-e^-, γe^- or $\gamma\gamma$ collisions if required by new physics.

To allow for two detectors, a so-called push-pull system is foreseen so that the detectors can be placed at the interaction point alternately. A schematic layout of the whole accelerator is depicted in Figure 2.2.

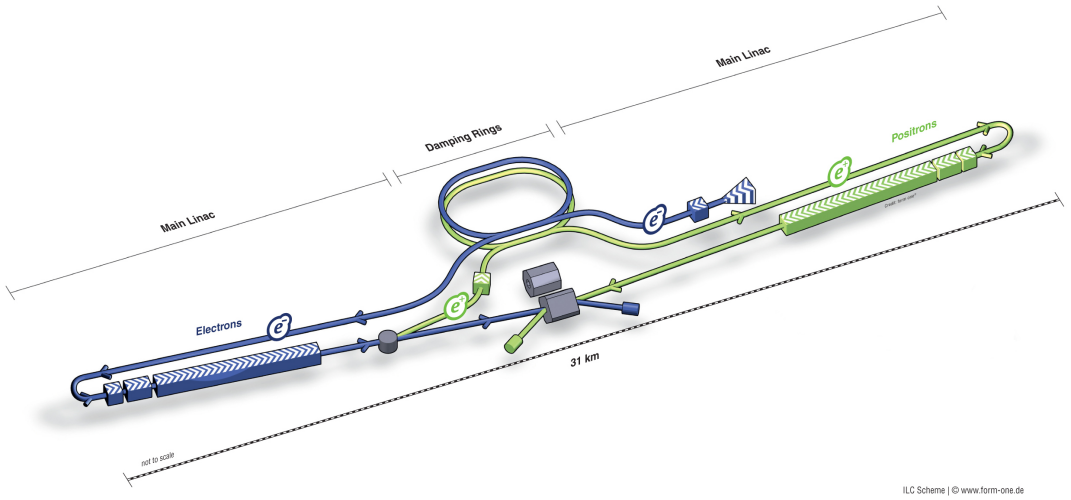

Figure 2.2: A schematic layout of the ILC [16].

At the ILC, an electron and a positron beam are brought to collision. Both beams are polarized. The electron beam is generated from a polarized source and reaches a polarization of at least 80%. It is generated in a DC gun by laser illumination of a photocathode. The beam is bunched and pre-accelerated to 76 MeV before it enters the superconducting booster linac which accelerates it to 5 GeV for the injection into the damping ring. Polarization, charge and lifetime requirements are well known demands which have already been met by the polarized electron source of the SLC [22], leaving the length of the bunch trains as the main challenge. The lenght of nearly 1 ms demands conducting structures which can deal with high power levels in the radio frequency regime. Furthermore, a laser system is required, which is more powerful than those at any previous accelerators.

The creation of the positron beam is more complicated. After the electron beam has been accelerated to 150 GeV in the main linac, part of it is diverted into an undulator of 150 m length and then returned into the main linac. The electrons, traversing the periodic magnetic field of the helical undulator, emit photons of about 10 MeV. These photons are directed at a rotating target made of a titanium alloy, creating an electron-positron beam with some remaining photons. The beam is captured by an optical matching device and then focused by a cavity operating in the L-band. Electrons and photons are filtered out before the beam is injected into the damping ring in the same way as for the electron beam.

After leaving the booster linacs, the beams are injected into two damping rings of 6.7 km length. Despite their name, the damping structures are not circular but divided into six arcs and as many straight sections. Operating at an energy of 5 GeV, they perform the critical task of transforming the incoming beams into highly stable beams of low emittance, as they are required for high luminosity production. A constraint of their configuration is the timing scheme of the main linacs. Therefore, the rings have to store a full bunch train. This way it is ensured that feed-forward systems can compensate for pulse-to-pulse variations like the differences in the bunch charge. Furthermore, the damping rings reduce the emittance of the incoming beams to the required level in a time span smaller than the interval between two bunch trains, which is about 200 ms. Further mandatory requirements are the injection and extraction of individual bunches, because of the bunch separation, which is much smaller within the damping rings than within the main linacs. These injections and extractions have to occur without altering the emittance or stability of the remaining bunches. This can only be done if the kicker fields are negligible for the bunches next to the injected/extracted bunch.

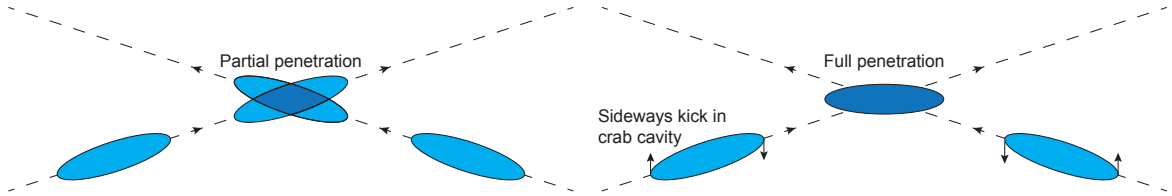

(a) Without crab crossing.

(b) With crab crossing.

Figure 2.3: Sketch of the crab crossing scheme. The oblong shape of the bunches is understated, while the crossing angle is exaggerated.

From the damping rings the beams are transported to the main linacs where they are accelerated to their designated center-of-mass energy. The acceleration capabilities are based on superconducting cavities, which operate at a radio-frequency of 1.3 GHz. A single cavity has a length of about 1 m and has to be operated at a temperature of 2 K, which is achieved by liquid argon cooling. Nine or ten cavities are usually assembled together and placed into a common cryostat. To reach a center-of-mass energy of 500 GeV, a field gradient of 31.5 MV/m is required throughout the main linacs. Although gradients of over 50 MV/m have been achieved in single-cell cavities [23], the required value is still a challenge for the mass production, as about 17 000 nine-cell cavities are required for the whole acceleration range. The efforts are currently focusing on the optimization of the production yield, so that even gradients of 36 MV/m can be achieved, as they are required for the 1 TeV upgrade.

After their final acceleration the beams reach the beam delivery system, which is responsible for the final focusing, the collision at the interaction point and the disposal of the spent beams. The beam delivery system foresees a single interaction point where the beams are brought to collision under a crossing angle of 14 mrad, even though head-on collisions would be the best choice concerning physics. This choice has been made, because it is difficult to separate the incoming from the outgoing beam in case of head-on collisions. The presence of a crossing angle can result in a decrease of luminosity if the bunches possess a non-circular shape. In case of the ILC, the bunches have a very elongated shape, which results in a very poor mutual penetration of the colliding bunches and an effective reduction of the luminosity by more than a factor of three [24]. The reasons for the highly non-uniform bunch shape is that such shapes are well suited to suppress the occurrence of beamstrahlung, a topic which is addressed below. It is possible to compensate this effect by rotating the bunches in the horizontal plane just before the collision. This way, the spatial overlap can be restored and the luminosity can be almost fully retained. A sketch of the partial penetration in case of elongated bunches is shown in Figure 2.3, as well as the effect of a rotation of the bunches. The technique of rotating the bunches is commonly referred to as *crab crossing*, as the rotated bunches seem to move sideways, similar to a crab.

2.1.3 Beam parameters

The most important figures of merit of any collider are its center-of-mass energy, $\sqrt{s}$, and the instantaneous luminosity $\mathcal{L}$ which it can deliver. While the center-of-mass energy defines the amount of energy available for the production of new particles, the luminosity is an important measure for the rate, R, at which these particles are created. For particles with production cross section, σ, the production rate, R, is given by

$$R = \mathcal{L} \cdot \sigma. \tag{2.1}$$

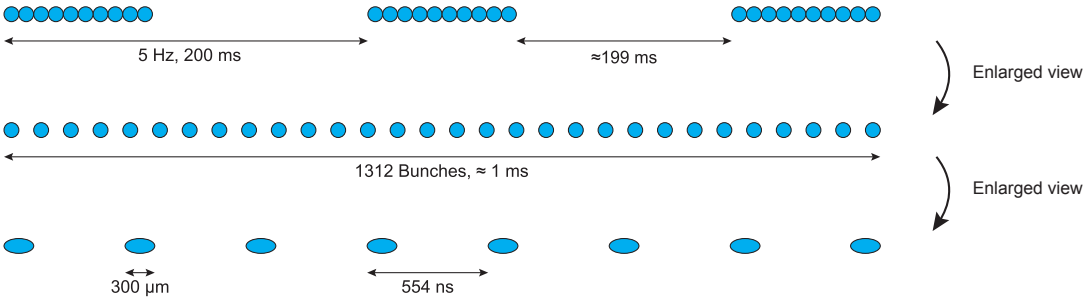

Figure 2.4: Beam structure of the ILC for the nominal 500 GeV beam.

As new accelerators like the ILC are intended to study rare phenomena, it is desirable to create as high as possible event rates, thus, the luminosity should be maximal. For head-on collisions it is given by

$$\mathcal{L} = \frac{N_- N_+}{4\pi\sigma_x\sigma_y} f_{rep} n_b H_D, \tag{2.2}$$

with electron and positron bunch population N_- and N_+, horizontal and vertical beam sizes σ_x and σ_y, collision rate f_{rep}, number of bunches n_b and beam enhancement factor H_D. Practical values of these parameters are given along other beam defining parameters in Table 2.2. Listed are three sets of parameters for different center-of-mass energies, as they are planned for the ILC [16]. From Equation (2.2) it is evident that in order to maximize the luminosity the beam should be focused as much as possible, i.e. σ_x and σ_y should be as small as possible. While the size of the beam should be chosen as small as possible, the number of particles in each bunch should be large, creating very high charge densities within the bunches.

The beams of the ILC are not continuous. This means that the bunches are organized in so called bunch trains. For a center-of-mass energy of $\sqrt{s}$ =500 GeV such a train contains 1312 bunches. After all the bunches in the train have been brought to collision with their counterparts in the bunch train of the oncoming beam, there is a break of about 199 ms before the next train arrives. Given the bunch spacing of 554 ns, this results in a frequency of five bunch trains per second. Figure 2.4 depicts a schematic overview on the beam structure at a nominal center-of-mass energy of $\sqrt{s}$ = 500 GeV.

The structure of the beam has a major impact on the design of the detectors. For example the long break between two bunch trains allows for a pulsed readout of some subdetectors in between two trains. This results in a reduced power consumption. More details on so-called power-pulsed readout schemes are given in Section 2.2.

Beamstrahlung

Beamstrahlung [26] is a type of bremsstrahlung that is caused by the electric field of the beams. In order to reach the high luminosities planned at the ILC, the bunches of the beams have to be tightly focused, resulting in a very high charge density. The electrical field caused by this charge density is high enough to be seen by the oncoming bunch, focusing that bunch even more with the beneficial side effect of an increase in luminosity, known as pinch effect. This enhancement of the luminosity is described by the parameter H_D in Equation (2.2).

Besides the increase in luminosity, the deflection of particles in bunches is accompanied by the emission of photons by the accelerated charged particle. The deflected particles lose some of their initial

Parameter	Symbol	250 GeV	500 GeV	1 TeV ($B1b_{ws}$)	Unit
Beam energy	E_{beam}	125	250	500	GeV
Collision rate	f_{rep}	5	5	4	Hz
Number of bunches	n_b	1312	1312	2450	#
Bunch separation	Δt_b	554	554	366	ns
Electron bunch population	N_-	2.0	2.0	1.74	$\times 10^{10}$
Positron bunch population	N_+	2.0	2.0	1.74	$\times 10^{10}$
Horizontal emittance	$\gamma\epsilon_x$	10	10	10	µm
Vertical emittance	$\gamma\epsilon_y$	35	35	30	µm
IP horizontal beta function	β_x	13.9	11.0	11.0	mm
IP vertical beta function	β_y	0.41	0.48	0.23	mm
IP RMS horizontal beam size	σ_x	729	474	335	nm
IP RMS vertical beam size	σ_y	7.7	5.9	2.7	nm
RMS bunch length	σ_z	0.3	0.3	0.225	mm
Beam enhancement factor	H_D	1.8	2.0	1.6	
Luminosity	$\mathcal{L}$	0.75	1.8	4.9	$\times 10^{34}$ cm^{-2}s^{-1}

Table 2.2: Beam parameters at the ILC for several center-of-mass energies [25].

energy which is not available for hard collisions anymore, consequently resulting in a spread of the beam's energy spectrum. The average energy loss, δ, of an individual particle is described by [27]

$$\delta \propto \frac{\gamma}{E_{beam}\sigma_z}\left(\frac{N_\pm}{\sigma_x+\sigma_y}\right)^2, \tag{2.3}$$

with Lorentz-factor γ, beam energy E_{beam}, number of particles per bunch $N_\pm$ and the beam size at the interaction point σ_x,σ_y and σ_z in the respective directions. The losses of individual particles in a bunch accumulate quite an amount of energy with an average of about 10^8 TeV being carried away in a single bunch crossing. As illustrated by Equation (2.3), the energy strongly depends on the size of the beam and can be reduced by increasing the beam size. In transverse direction, this is always a trade off between energy loss and luminosity, as the transverse beam size is directly correlated to the luminosity as shown in Equation (2.2). A good compromise is to choose a rather large beam size in one transverse direction and a shorter one in the other direction. This works because the luminosity depends on the product of both sizes and the energy loss on the sum. Another possibility is to increase the beam size in longitudinal direction, but this is limited due to the hourglass effect [28].

In addition to these undesirable influences on the beam properties, the emitted beamstrahlung photons may interact and become a source of background. Beamstrahlung is expected to be the main source of detector backgrounds at the ILC. More details on beam induced backgrounds are given in Section 2.2.2.

2.2 ILD - The International Large Detector

As outlined in the previous section, the ILC is designed to offer a clean experimental environment for high precision measurements at an energy scale which up to now has been only accessible at hadron colliders. The construction of a detector that fully exploits this setup is an obvious requirement.

The International Large Detector (ILD) originates from two different detector concepts, which have evolved independently. The Large Detector Concept (LDC) was mainly a European design effort, while

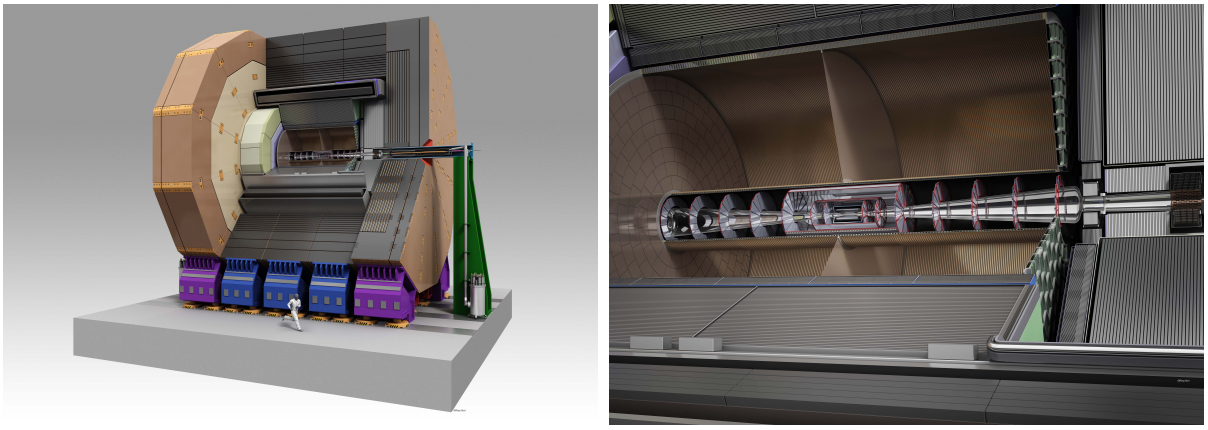

(a) Full detector view.

(b) Enlarged view of the tracking systems.

Figure 2.5: An artistic view of the ILD [29]. The whole detector (a) and an enlarged view of the inner detector components with focus on vertex detector, beam calorimeters and central tracker (b).

the Global Large Detector (GLD) was a concept originating from Asia. Both concepts were very similar in their general layout and choice of technology, but differed in the dimensions of individual components. Consequently, they have been merged into a joined and global design effort.

The ILD is a detector designed to meet all requirements for an experiment at the ILC, which tries to measure particle collisions with unprecedented precision and accuracy. The conceptual approach is the particle flow paradigm which aims at the individual reconstruction of all particles and a strict separation of charged and neutral particles, even within jets. To achieve this, all detector systems have to be designed with a strong emphasis on spatial resolution. In addition, an extremely high momentum resolution for charged particles as well as a very good secondary vertex reconstruction are important requirements. These necessities are reflected in the design of the individual subdetectors.

Although the ILD has been designed with an application at the ILC in mind, it could also be used at other accelerators. Subsystems developed for the ILD are under investigation as future upgrades of already operating detectors like T2K, ATLAS, Belle II and others. Moreover, the whole detector layout might be used at different colliders. The detector concept has already been adopted by the Compact Linear Collider (CLIC) community, which is investigating its applicability at center-of-energies up to 3 TeV.

2.2.1 Detector layout

In its general design, the ILD is typical multi-purpose detector as employed in many collider experiments of high energy physics. A high precision vertex detector at its center is surrounded by a hybrid tracking system, featuring a combination of silicon tracking devices and a time projection chamber, followed by highly segmented calorimeter systems. Tracking and calorimeter systems are located within a solonoid providing an axial magnetic field of 3.5 T, whose iron return yoke is instrumented with a muon detector.

No final decision has been made on the choice of technology for the individual subsystems. Thus, several options are discussed and investigated for each detector component, in order to stay as flexible as possible. Therefore, the following subsections describe the general layout of the individual subdetectors and the different technologies which are considered, whereby one should be aware of the fact that even these technologies may be exchanged in the future.

Vertex detector

The vertex detector is the innermost part of the tracking system and by this the central part of the whole detector. In its baseline design, it consists of three nearly cylindrical layers, which are equipped on both sides with pixel sensors [30]. The innermost layer is positioned at a radius of 15 mm from the beam line and the outermost at 60 mm. To reduce the occupancy resulting from background hits, the innermost layer is only half as long as the outer two. By this design the detector provides six precision measurements for charged particles traversing the detector, which should be sufficient to reach the performance goal of a track impact parameter resolution better than $\sigma_b < 5 \oplus 10/p \sin(\theta)^{\frac{3}{2}}$ μm. This goal is quite ambitious and can only be met if the six track points are measured with a spatial resolution of less than 3 μm. Other important requirements are the very low material budget of less than 0.15 X_0 per layer and the capability to withstand the radiation arising from the particle interactions.

Three sensor technologies have come close to the detector requirements and are developed in parallel until a final decision has been made. Each of them offers different advantages and opportunities. Therefore, it may well be that a technology different from the three baseline options described below is chosen for the final application.

The first option is a detector based on CMOS[3] pixel sensors (CPS) [31]. For this sensor concept a thin (10 μm to 20 μm) epitaxial layer of high resistivity is placed on the low resistive substrate of an industrial CMOS chip. The layer incorporates a high density lattice of sensing nodes, which offer a high spatial resolution. An advantage of this technology is to integrate the signal processing circuitry completely into the same substrate as the sensitive volume. This makes such detectors very flexible concerning their readout, for which a power-pulsed scheme is under investigation. The technology is very mature and it has already been shown that single, full scale devices, which meet all of the above requirements, can be fabricated industrially. In these devices the two sensors of the innermost layer have been equipped with two different type of sensors. The sensor on the inner side of the first layer features pixels with a pitch of ≈17 μm and reaches a spatial resolution of less than 3 μm. The frame readout time of 50 μs can lead to a high occupancy if the estimation of the beam related backgrounds are too low. On the other side of the layer is another type of CPS sensor, optimized for a high time resolution. Because of its rectangular pixels with a size of $17 \times 85\,\mu m^2$ there are five times less pixels in a column which results in a five times faster readout time of 10 μs but a worse spatial resolution of about 6 μm. The sensors of the outer layer cover a much larger area but have to deal with considerably less occupancy. The pixels have a pitch of 34 μm, which translates into a spatial resolution of about 4 μm at a readout time of 100 μs.

Another technology option is the DEPFET[4] [32] active pixel detector concept, which relies on field effect transistors in each pixel of the sensor. To detect charged particles a voltage is applied, depleting the sensor of free charge carriers. This ensures a fast collection of the charges, which modulate the source-drain current and results in a first amplification signal, already in the pixel. By this process the excellent signal-to-noise ratio of the detector is achieved. As in the case of CPSs, a power-pulsed readout scheme is studied for DEPFET based detectors. But unlike for CPS sensors, the signal processing units are not incorporated into the sensor itself, so that dedicated ASICs[5] have to be used for this [33]. They perform the readout in a rolling shutter mode, so that there is at any given time only one active row of pixels. This readout scheme ensures, that the power consumption remains within the ILD budget. Readout times of 80 ns have been reached for single rows which translates into readout times of 100 μs for the inner and 200 μs for the outer layers. Current R&D goals foresee half of these values. Further improvements are possible by reading out more than two rows in parallel and/or increasing the length

[3] Complementary metal–oxide–semiconductor (CMOS) is a technology for the production of integrated circuits.
[4] DEPFET - Depleted p-channel field-effect transistor.
[5] ASIC - Application-specific integrated circuit.

of the pixels for the sensors of the outer layers.

Sensors based on fine pixel CCDs (FPCCD) [34] are a third technology option under investigation. They allow for an extremely high granularity with a pixel pitch of about 5 μm. This can be exploited to obtain a spatial resolution below one micron and an excellent two-track separation. To limit the occupancy, the sensitive volume, an epitaxial layer of 15 μm thickness, is fully depleted, limiting the charge spread. A low occupancy is of particular importance, as the large number of pixels demands for a slow readout scheme, i.e. the detector is read out in between two bunch trains at a very low frequency to reduce the power consumption. Similar to the CPS and DEPFET sensors a FPCCD based detector would employ smaller pixel sizes on the innermost layer than on the outer layers to limit the occupancy because of beam induced backgrounds. The pixel pitch would be 5 μm for the inner two sensors and 10 μm for the outer four sensors. This setup leads to a significant improvement on the impact parameter resolution compared to the baseline design if a spatial resolution of pixel size divided by $\sqrt{12}$ is assumed for the individual layers.

Tracking system

The ILD features a hybrid tracking system that consists of silicon detectors in combination with a large time projection chamber as central tracking device. As this thesis focuses on developments in the context of a TPC for the ILD its discussion is postponed to Chapter 3 where the detection processes as well as the ILD specific demands are addressed in detail. An artistic view of the tracking system is depicted in Figure 2.5b.

The silicon tracking system of the ILD consists of four subdetectors, which form the so-called silicon envelope. The silicon inner tracker (SIT) and silicon external tracker (SET) are located at the inner and outer field cage of the TPC respectively. Together with the end-cap tracking detector (ETD), which is installed in the gaps between the end-caps of the TPC, they enclose the TPC completely. The last component of the silicon tracking system is the forward tracking detector (FTD), which enables high precision measurements of tracks which are emitted under angles too small to be measured with the TPC.

The main purpose of the silicon envelope is to link the vertex detector, the TPC and the calorimeter system together to provide high precision measurements of single track points. Together with the high time resolution of the system these precision measurements can time stamp tracks and associate them to individual bunches. The silicon detectors can be very helpful for the alignment of the TPC, as SIT and SET provide an independent set of measurements.

All components of the silicon envelope are based on the same technology, i.e. the same type of sensors, whereby the overall complexity of the system is greatly reduced. The detectors are composed of single layers, each featuring two single-sided strips. The strips are tilted by a small angle with respect to each other to allow for two-dimensional measurements, a technique also known as “false” double-sided layers. Two of such “false” double-sided layers are included into the SIT and another one in the SET, complementing the tracking information from TPC and vertex detector by three high precision measurements. The EDT also incorporates one such layer, guaranteeing three high precision measurements, even for tracks which pass through the end-cap.

The microstrips used as sensor feature an active area of $10 \times 10\,\mathrm{cm}^2$ with a pitch of 50 μm. The sensor material has a thickness of 200 μm and is implemented with only a few 10 μm of non-active material at the edges. These kind of sensors permit the design of detectors without any overlapping sensors which leads to a reduction of the used material.

The forward silicon tracking detector consists of seven disks located between the inner field cage of the TPC and the beam pipe. The forward tracking systems face a very particular set of challenges. The

first problem is that particles emitted under a low angle to the beam line are not bend much, so that a precise measurement of their momentum is difficult. Another problem is the high occupancy in this region. The occupancy results from forward jets, which are not opened up as much as in the barrel region and from backgrounds originating from the interaction region nearby. Because of this, it is foreseen to realize the first two disks as pixel detectors, while for the remaining five disks strip detectors should be sufficient.

The same technologies under investigation for the vertex detector are considered for the pixel disks. The concepts have been adapted to the special needs of the FTD. In case of CPSs the pixel size, i.e. the length of the pixel would increase with the radius, resulting, in a spatial resolution of 6 μm to 9 μm. The concept relying on DEPFET sensors has chosen a similar approach, also with radially increasing pixel lengths. The sensors have been optimized to yield a very high spatial resolution in the $r\varphi$-plane which is in the range of 3 μm to 5 μm. The FPCCD approach again relies on a very high granularity to cope with the occupancy, which is realized with a pixel pitch of 10 μm. This pixel size results in an expected spatial resolution of 3 μm. Similar to their counterparts for the vertex detector CPS and DEPFET make use of a power pulsing scheme to limit the power consumption, while the FPCCD has to be read out between the bunch trains.

Because of the low occupancy compared to the first two disks, the remaining five disks can be realized as strip detectors. The strips are installed on both sides of the disk with a stereo angle between them to allow for two dimensional measurements of the impact parameter.

Calorimetry

The calorimeter system of the ILD is designed for particle flow and, therefore, faces a unique set of challenges. The particle flow paradigm demands the individual reconstruction of each particle in the detector. For this to work, the calorimeter systems are required to possess an unprecedented granularity, emphasizing imaging capabilities over intrinsic energy resolution. At the same time full hermeticity has to be ensured to limit energy leakage.

Calorimeter systems are usually divided into an electromagnetic (ECAL) and a hadronic component (HCAL). It consists of a huge barrel which is terminated on each end by large end-caps. The whole system is completed by three specialized calorimeters in the very forward region which are dedicated to luminosity (LumiCal) and beamstrahlung (BeamCal) monitoring as well as low angle coverage for neutral hadrons (LHCAL).

The main challenge in the design of the hadronic and electromagnetic calorimeters is their granularity. It has been shown by detailed simulation that the granularity has to be of the same size as a radiation length, in all spatial directions. This can be achieved by choosing a sampling calorimeter for both systems. The high granularity also implies a vast number of readout channels on the order of $O(10^8)$ for the whole system. Dealing with that many channels is very complicated, especially if hermeticity and a compact design have to be preserved. Therefore, the sensitive layers have to incorporate as much of the readout systems as possible without compromising the power pulsing scheme of the detector.

For the realization of the particle flow paradigm, the ECAL has to be able to effectively separate overlapping showers from each other and photons from nearby particles. A further requirement is the identification of hadronic showers starting in the electromagnetic part of the calorimeter. The baseline design of the ECAL relies on silicon pin diodes with a pixel size of $5 \times 5\,\mathrm{mm}^2$ in combination with tungsten as radiating material. Tungsten is a good choice for the radiator, as it is a dense material providing a high ratio of interaction length to radiation length. The current design foresees 30 readout layers which correspond to a thickness of 24 X_0. This is a good compromise between cost and performance, given the fact that the whole calorimeter system has to be placed within the solonoid.

The role of the HCAL is to distinguish charged and neutral hadrons and measure the energy of the latter as precisely as possible. A difficult task given the much higher abundance of charged hadrons. For the fulfillment of this task the HCAL has been designed as sampling calorimeter with steel as absorbing material. Because of the high rigidity of steel, it is possible to realize a self-supporting structure, that minimizes dead regions since no auxiliary supports are required. Another benefit of the material choice is the moderate ratio of the hadronic interaction length to the electromagnetic radiation length. It permits a fine sampling in longitudinal direction even with comparatively few layers.

Two options are considered for the active medium, the analog option based on scintillating tiles and a semi-digital one using gaseous devices. The scintillating tiles are based on silicon photo-multipliers. This is a rather novel but very promising technology. The tiles can be realized with a thickness of 3 mm and allow, therefore, for a very compact design with a transverse cell size of $3 \times 3\,\mathrm{cm}^2$. The technology has been successfully realized within the AHCAL prototype of the CALICE collaboration [35], which has already encouraged other experiments to use this technology in future upgrades.

The second candidate for the active medium are gaseous detectors, which are known to offer a very high efficiency. The baseline technology for this approach are glass resistive plate chambers (GRPC). They are proposed to cover an area of 1 cm × 1 cm in transverse direction at a thickness of 3 mm. Indeed, this technology allows for the realization of an even higher granularity, which is basically limited only by the size of the readout electronics.

With LumiCal and BeamCal the ILD possesses two small, but specialized calorimeter systems in the very forward region. The LumiCal is intended to monitor the luminosity delivered by the accelerator with a precision better than 10^{-3} at a center-of-mass energy of 500 GeV. It has already been stated in Section 2.1.3 that the luminosity is a defining property of each accelerator, which makes the LumiCal a very important system. It is located within the ECAL end-cap next to the beam pipe. It consists of a sandwich structure of finely segmented silicon comprising an absorber disk made of tungsten [36]. The actual measurement is done by detecting and counting the outgoing particles of Bhabha scattering processes. This process has been chosen as precise calculations of its cross section are available [37]. The luminosity, $\mathcal{L}$, is then given by $\mathcal{L} = N_B/\sigma_B$, with N_B being the counted occurrence of the process and σ_B the differential cross section integrated over the angular coverage of the LumiCal.

The main purpose of the BeamCal is to monitor the amount of beamstrahlung, which has already been treated in Section 2.1.3 and is the main source of background at the ILC. This stresses the importance of the BeamCal as key component for background estimates. It is similar to that of the LumiCal but makes use of gallium arsenide (GaAs) instead of silicon.

Solonoid and muon systems

The tracking systems of the ILD are designed to operate at a magnetic field of 3.5 T, which is provided by a solenoid. An anti detector integrated dipole (anti-DID) is required to suppress the background from incoherent e^+e^--pairs (see Section 2.2.2). Both fields have to be mapped with a very high precision to ensure the tracking performance of the TPC [38]. The layout of the magnet has been adapted from the CMS detector [39], with altered geometrical dimension and the addition of the anti-DID. It consists of three parts, which are the solenoid coil, the already mentioned anti-DID and the return yoke [40].

The solenoid is built from three modules, each 2.45 m long, resulting an overall length of 7.35 m. It is positioned at a radius of 3.615 m, enclosing the calorimeter systems. The modules have four layers, each layer incorporates 105 turns of superconducting cable. By employing the inner winding technique the coil is wound inside of the mandrel. The mandrel is made of an aluminum alloy and has a cylindrical form with a radius of about 25 mm. This mandrel is an essential part in the design of the coil. It acts as mechanical mandrel, takes part in the cooling of the coil and is used as a quench back tube.

The anti-DID is located at the outer radius of the main solenoid at a radial distance of 4.19 m to the beam axis. It provides the magnetic field of a dipole with inverted polarity, thus the term anti-DID. Its purpose is to suppress backgrounds in the detector by steering background particles towards the outgoing beam pipes. Up to now there is no final decision on the form the field should take or on its technological realization. It is commonly accepted, that the magnetic field of the anti-DID should have a maximum field value of $B_x = 0.035\,\mathrm{T}$ at a distance of $z = 3\,\mathrm{m}$ to the interaction point. The form of the field around the interaction point is still under discussion and further iterations, magnet design simulations, and physics/background studies are required to find a technically feasible solution with acceptable background rates. In any case, the field has to be precisely mapped to maintain a high performance of the tracking detectors.

The iron yoke is another detector component with several functions. Apart from returning the magnetic flux of the solenoidal field it also acts as the main mechanical structure of the ILD. Additionally, it is instrumented with detectors, which are not only responsible for the efficient detection of muons, but also for measuring energy leaking out of the calorimeters. To cope with both requirements the sensitive layers of the system are not evenly spaced. The ten inner layers of the system, which complement the calorimeter system, are closely spaced. The minimal distance between these layers is constrained by mechanical robustness of the yoke to 10 cm. Two outer layers in the endcap region and three in the barrel region of the detector act solely as muon detectors, allowing for a larger distance of 60 cm between them.

2.2.2 Detector backgrounds

A main advantage of lepton colliders is their clean experimental environment. Even though the background is very low compared to hadron colliders, there is still a considerable contribution of backgrounds to any signal measured.

In the case of the ILC, the event rate is very low. Less than one electroweak interaction per second is expected at a center-of-mass energy of $\sqrt{s} = 500\,\mathrm{GeV}$ and a nominal luminosity of $\mathcal{L} = 1.8 \times 10^{34}\,\mathrm{cm}^{-2}\,\mathrm{s}^{-1}$. This leaves machine induced backgrounds as the main source of undesirable interactions within the detector. The term machine induced background most commonly refers to interactions that occur because of the operation of the collider and its dedicated detectors.

Background at the ILC is mainly caused by beamstrahlung, which has been described in Section 2.1.3. Beamstrahlung photons are focused in the very forward direction and most of them leave the detector through the beampipe. Those photons which do not leave the active volume may either interact with detector material or with other photons, provoking particle interactions capable of interfering with actual measurements.

Electron-positron pairs

The dominant background source at the ILC are electron-positron pairs which result from scattering processes of beamstrahlung photons. If these particles carry a sufficiently large transverse momentum they do not exit the beam pipe through the exhaust port and enter the detector. There are two modes of production, coherent (CPC) and incoherent (IPC) pair creation.

In the coherent process a beamstrahlung photon is turned into an electron-positron pair by the interaction with the collective field of the oncoming beam, similar to pair conversion in the electric fields of atomic nuclei. The structure of the beam at the ILC is chosen to suppress coherent pair creation completely, even at center-of-mass energies of 1 TeV.

The incoherent production takes place by the interaction of two photons, whereby it should be noted

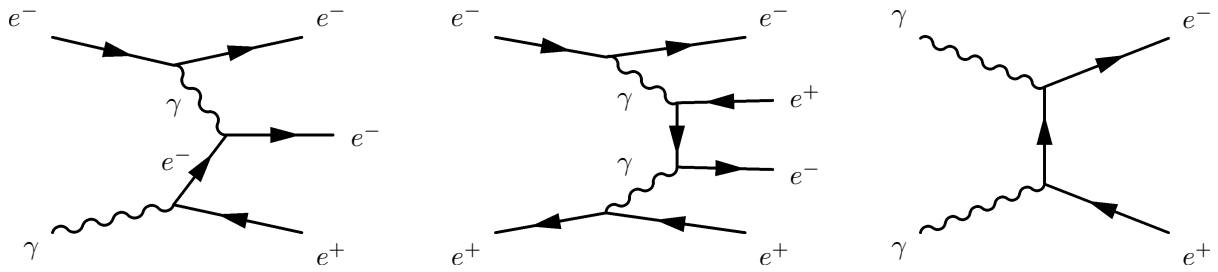

(a) BETHE-HEITLER (b) LANDAU-LIFSHITZ (c) BREIT-WHEELER

Figure 2.6: FEYNMAN graphs of the three processes responsible for incoherent pair creation at the ILC.

that these photons may be real or virtual. Three combinations of virtual and real photons are possible. Their FEYNMAN graphs are depicted in Figure 2.6. The interaction of a real and a virtual photon is denoted as the BETHE-HEITLER process. The LANDAU-LIFSHITZ process describes the interaction of two virtual photons. They dominate by an approximate ratio of 2 : 1 compared to the BREIT-WHEELER process of two real photons [27].

If the polar angle, under which the e^+e^--pairs are emitted is large enough, they have a sufficiently high transverse momentum to traverse several layers of the vertex detectors, leaving a charge signal in the process. Although the fraction of particles which reach the vertex detectors is very small, these background particles are the dominant contribution to the occupancy of the vertex detector. The BeamCal is hit by a much larger fraction of e^+e^--pairs, because of its polar angle coverage from 5 mrad to 50 mrad. This puts constraints on the design of the BeamCal, which has to be very radiation hard in order to withstand the constant flux of particles. The e^+e^--pairs hitting the BeamCal can induce electromagnetic showers. This is a further source of background, as secondary electrons, positrons and photons are back-scattered into the inner parts of the detector. Most of the charged particles resulting from these interactions are confined to the inner regions of the detector due to the presence of the magnetic field. Therefore, they are unable to reach the central tracker or main calorimeters, but can reach the vertex detector and contribute to its occupancy. In contrast, photons are not affected by the magnetic field and are capable to reach the central tracker where they produce hits by the photoelectric effect or COMPTON scattering. Furthermore, electromagnetic showers can produce neutrons by photonuclear interactions. Neutrons can traverse the detector almost unhindered, being only reflected on some surfaces.

Hadronic background

Electron-positron pairs from beamstrahlung interactions are not the only source of detector backgrounds. Interactions of photons can also result in the production of hadronic jets. These photons may either result from the already discussed beamstrahlung or from processes treated by the WEIZSÄCKER-WILLIAMS approximation [41, 42], which describes the main features of radiation by relativistic electrons. The occurrence of such hadronic background events is less frequent than for e^+e^--pair background. Similar to e^+e^--pairs the hadrons are tightly focused in the very forward direction. Their transverse momentum distribution has a tail towards high values, allowing these hadrons to directly produce hits in the central detector. Another effect is the production of neutral particles, like π^0 or K^0 which are not collimated into the forward direction by the magnetic field and therefore might enter the detector at rather low transverse momenta.

2.3 Summary

The measurements of currently running hadron colliders like LHC and Tevatron have to complemented by a lepton collider. The ILC is well suited for this task. It provides a clean experimental environment with well defined initial states allowing for high precision measurements, especially with regard to the discovery of the HIGGS boson at the LHC.

To exploit the full potential of a precision machine like the ILC, a high-performance detector is required. The ILD is designed to perform measurements of the highest precision, surpassing all its predecessors at former collider experiments. Several options are developed for the different subdetectors, each of them capable of providing the required performance. Although the ILC can be considered a clean experimental environment, backgrounds from beamstrahlung processes can not be avoided. This fact is reflected in the design of the detector and has to be taken into account in analyses of physics events.

Chapter 3

Photon detection and particle tracking with gaseous detectors

Particles are always measured by their interaction with the material of the detector. Gaseous detectors have a long tradition in both, the detection of photons and the measurement of the trajectories of charged particles. In any case, the detection principle of gaseous detectors relies on the ionization of the gas of the detector by the measured particle. The products of these ionization processes are drifted to an electrode. The electrons are amplified and eventually transformed into an electric signal which is read out. A detailed knowledge of all these processes is crucial for the development of high-performance detectors.

This chapter discusses the individual processes taking place in gaseous detectors. These are ionization in Section 3.1, drift and diffusion of electrons and ions in Sections 3.2 and 3.3, and eventually signal creation by gas amplification in Section 3.4. The readout of gaseous detectors is addressed in Section 3.5, including the conventional readout via pads as well as the novel technique of integrated pixel readouts. With the knowledge of these processes at hand a special kind of gaseous tracking detector, the time projection chamber, is introduced in Section 3.6 and discussed in detail, also with respect to its application in the context of the ILD.

3.1 Ionization and energy loss

The detection principle of any gaseous detector relies on the fact that charged particles traversing the detector leave and ionization trace and that photons are absorbed in the gas. Any interaction of the measured particle and gas results in an energy transfer towards the shell electrons of the gas atoms/molecules. Depending on the amount of transferred energy this leads to excitation or ionization of the gas particles. The details of these interactions differ for charged particles and photons. Photons are either absorbed by the medium, i.e. they transfer all their energy to the gas, or escape detection. Charged particles can also loose all their kinetic energy and are stopped by the gas, it is much more likely that they transfer only part of it, leaving a trail of ionization in the gas.

3.1.1 Energy loss of charged particles

Charged particles traversing matter interact with the atomic shells of the medium via their electric charge. These interactions result in a loss of kinetic energy, which is dominated by ionization and

excitation. Other processes like Cherenkov radiation, transition radiation or bremsstrahlung become non negligible at very high energies. Usually the energy loss is small and occurs in single collisions, with energy transfers of less than 100 eV. The occurrence of these collisions is randomly distributed and is expressed by the mean free path, λ, between two collisions, which is determined by the electron density of the medium, n_e, and σ_I, its ionization cross section

$$\lambda = \frac{1}{\sigma_I n_e}. \tag{3.1}$$

From (3.1) it is evident, that the number of collisions along a track of length L has to follow a Poissonian distribution around a mean value, L/λ. However, σ_I and thereby λ depend on the charge, mass and kinetic energy of the incident particle.

In collisions of the fast charged particle (e.g. pions $\pi^{\pm}$), with a gas particle, A, several processes can lead to ionization. If enough energy is transferred, the gas particle can be ionized directly, freeing one or more electrons

$$\pi^{\pm}A \rightarrow \pi^{\pm}A^{+}e^{-}, \pi^{\pm}A^{++}e^{-}e^{-}, \pi^{\pm}A^{+++}e^{-}e^{-}e^{-}... \tag{3.2}$$

This processes are usually referred to as primary ionization, as the ionization is caused directly by the collision of the incident particle with the atoms or molecules of the medium. Because of their small momentum compared to the incident particle, primary electrons are usually emitted perpendicular to the track, losing their kinetic energy in collisions with particles of the gas. If their initial energy is high enough they are able to cause ionization themselves, a process which is known as secondary ionization:

$$e^{-}A \rightarrow e^{-}A^{+}e^{-}, e^{-}A^{++}e^{-}e^{-}, ... \tag{3.3}$$

Indeed, most ions along the paths of charged particles result from secondary ionization. Besides the primary and secondary ionization processes, there is also an indirect way for gas particles to be ionized. This process is only possible in mixtures of several gas components. In this case, a gas particle of species A is not ionized by primary or secondary processes but is excited into a higher energy level

$$\pi^{\pm}A \rightarrow \pi^{\pm}A^{*}. \tag{3.4}$$

If the gas mixture contains a second species of particles B, with an ionization threshold below the excitation energy of species A, B can be ionized by collisions with A^{*}

$$A^{*}B \rightarrow AB^{+}e^{-}, \tag{3.5}$$

a process known as Penning effect. This effect results in a decrease of the mean energy required to cause ionization in a gas mixture.

In some cases, primary electrons, so called δ-electrons, possess enough energy to form small, but observable tracks. The maximum amount of kinetic energy, T_{max}, which can be transferred from the incident particle to a gas atom in one collision can be calculated from its mass m_0 and momentum $p = mv = \gamma m_0 \beta c$ [43]

$$T_{max} = \frac{2m_e c^2 \beta^2 \gamma^2}{1 + \frac{2\gamma m_e}{m_0} + \left(\frac{m_e}{m_0}\right)^2}, \tag{3.6}$$

where, m_e is the electron mass, γ the Lorentz factor and $\beta = v/c$ the velocity in units of the speed of

light, c.

For the discussion of the mean energy loss of the incident particle, it is convenient to distinguish between electrons and heavier particles ($m_0 > m_e$). For heavier particles equation (3.6) can be written as

$$T_{max} = \frac{E^2}{E + \frac{m_0^2 c^2}{2m_e}}, \tag{3.7}$$

wherein $E = \gamma m_0 c^2$ denotes the total kinetic energy of the charged particle. The mean energy loss of fast charged particles traversing matter, not only gas, can be expressed with the help of the Bethe-Bloch formula [44]

$$-\left\langle \frac{\mathrm{d}E}{\mathrm{d}x} \right\rangle = 4\pi N_A r_e^2 m_e c^2 \frac{Z^2}{A} \frac{1}{\beta^2} z^2 \left(\frac{1}{2} \ln \left(\frac{2m_e c^2 \beta^2 \gamma^2 T_{max}}{I^2} \right) - \beta^2 - \frac{\delta(\beta\gamma)}{2} \right), \tag{3.8}$$

with

N_A	Avogadro's number N_A =6.022 × 10^{-23} mol^{-1},
r_e	classical electron radius $r_e = e^2/4\pi\epsilon_0 m_e c^2$ =2.82 fm,
Z, A	atomic number and atomic mass of the absorbing material,
z	charge of the incident particle in units of e,
I	mean excitation energy, approximately $I \approx 16 \cdot Z^{0.9}$eV for $Z > 1$ [43] and
$\delta(\beta\gamma)$	relativistic density correction factor.

The Bethe-Bloch formula as given in (3.8), validly describes the mean rate of energy loss in the range of materials with intermediate Z values and particles with $\beta\gamma$ values in the range $0.1 \lesssim \beta\gamma \lesssim 1000$. Slow particles, i.e. particles which have a velocities comparable to those of atomic electrons, are not described by (3.8) as they can also lose energy by being deflected by the electric fields of the nuclei. Starting at its lower limit of $\beta\gamma \approx 0.1$ the energy loss declines as a function of $1/\beta^2$ until reaching a broad minimum at approximately $\beta\gamma \approx 4$ which corresponds to an energy loss of

$$-\left\langle \frac{\mathrm{d}E}{\mathrm{d}x} \right\rangle \Bigg|_{\beta\gamma \approx 4} \approx 1.5\,\mathrm{MeV}/(\mathrm{g/cm}^2). \tag{3.9}$$

Particles residing in this energy regime are called minimum ionizing particles (MIPS). For values of $\beta\gamma \gtrsim 4$ large energy transfers towards few, even single electrons become more likely which can result in the creation of the already mentioned δ-electrons. The energy loss in this regime shows a logarithmic increase. The logarithmic rise is reduced by density corrections, represented by the term $\delta(\beta\gamma)$. These correction are especially important for highly relativistic particles, as in this case the atoms surrounding the projectile particle are polarized, screening the charge of the particle. The strength of this effect depends strongly on the density of the medium, hence its name. It is mostly important for very dense materials and can be neglected in most gases. At particle energies corresponding to values of $\beta\gamma \gtrsim 1000$ equation (3.8) stops to be valid description, as these particles are highly relativistic and radiative losses become dominant over interactions with the medium. The "Bethe-Bloch" region of Figure 3.1a shows the course of function (3.8) for positive muons in copper, as well as the influence of radiative losses at higher values of $\beta\gamma$.

The mean energy loss is a value difficult to access. It is described by so called straggling functions, which depend on the energy of the incident particle and properties of the absorbing material, especially

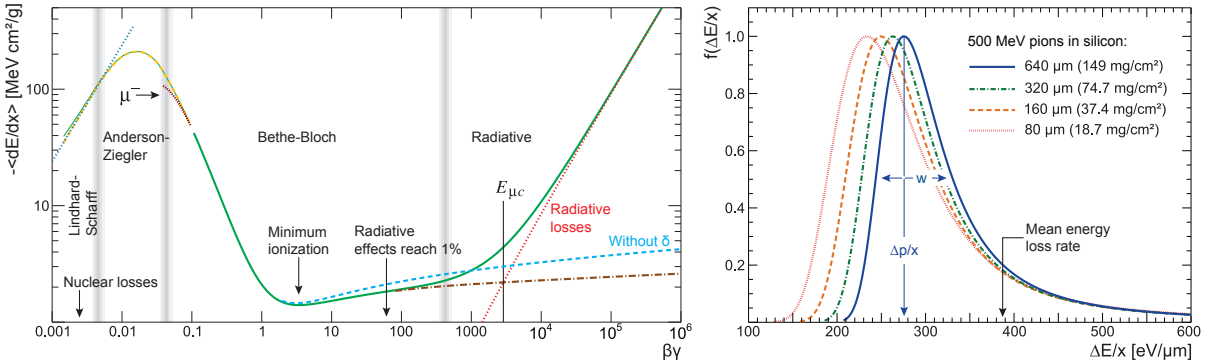

(a) Stopping power of copper

(b) Energy loss distributions of silicon

Figure 3.1: Stopping power (i.e. $-<\mathrm{d}E/\mathrm{d}x>$) of copper for positive muons as function of $\beta\gamma$ (a) and normalized straggling functions for 500 MeV pions in silicon (b). Both figures are adapted from [44].

its thickness. These straggling functions describe the probability of a certain amount of energy deposition to occur. The mean of the energy deposition is weighted by rare events depositing large amounts of energy in a detector. This is in particular true for detectors of moderate or very low thickness, where all gaseous detectors can be considered to fall into this category. At moderate detector thicknesses the probability distribution of energy loss is best described by a Landau distribution [45]. In this case the most probable value Δp can be calculated from [46]

$$\Delta p = \xi\left(\ln\left(\frac{2m_0c^2\beta^2\gamma^2}{I}\right) + \ln\left(\frac{\xi}{I}\right) + j - \beta^2 - \delta(\beta\gamma)\right) \qquad \text{with} \qquad \xi = \frac{4\pi N_A r_e^2 m_e^2 c^2}{2}\left\langle\frac{Z}{A}\right\rangle\frac{x}{\beta^2}, \tag{3.10}$$

detector thickness, x, in $\mathrm{g\,cm^{-2}}$ and the free parameter $j = 0.2$ [46]. For very thick absorbers the distribution evolves accordingly to the central limit theorem into a distribution resembling a Gaussian distribution. Here, mean and most probable value are equal, even though the distribution remains a little bit skewed. Although often used to describe the energy loss in gaseous detectors, the Landau distribution is not suitable for the application in very thin detectors such as silicon detectors [46] and gaseous cells of time projection chambers [47]. For very thin absorbers the mean energy loss is still described by equation (3.10), but the straggling function has a much larger width than a Landau distribution, where the width is given by $w = 4\xi$. Figure 3.1b depicts four straggling functions describing the energy deposition of 500 MeV pions in silicon of variable width. It is apparent, that for thinner absorbers the distributions widen up and possess a more distinct falling edge towards higher energies than for thick absorbers.

The description of energy loss as presented above is valid for heavy charged particles. Electrons as incident particles have to be treated differently. One reason for this is the occurrence of bremsstrahlung processes, which can not be neglected even at low energies. Another, even more important, reason is that the masses of incident particle and target electrons are the same. Therefore, it is impossible to distinguish between them after a collision and the energy loss probability has to be interpreted in a different way. In principle it is possible for the incident electron to transfer all of its kinetic energy to its collision partner, i.e.

$$T_{max} = E - m_e c^2. \tag{3.11}$$

From an outside point of view this looks like no collision has occurred at all, as the scattered and incident particle just swap their roles. Therefore, it is sufficient to consider only energy transfers up to half of the maximal possible value to cover all cases. This can be used to derive a formula [48] for projectile electrons analog to (3.8)

$$-\left\langle \frac{\mathrm{d}E}{\mathrm{d}x} \right\rangle = 4\pi N_A r_e^2 m_e c^2 \frac{Z}{A}\frac{1}{\beta^2}\left(\ln\left(\frac{\gamma m_e c^2 \beta\sqrt{\gamma-1}}{\sqrt{2}\,I}\right) + \frac{1-\beta^2}{2} - \frac{2\gamma-1}{2\gamma^2}\ln(2) + \frac{1}{16}\left(\frac{\gamma-1}{\gamma}\right)^2\right), \quad (3.12)$$

which includes screening effects and the kinematics of electron-electron collisions.

3.1.2 Ionization by photons

While traversing matter, be it all-solid, liquid or gaseous, a photon can participate in three different types of interactions. Depending on its energy the photon may be completely absorbed or scatter under a large angle. The three effects are:

- The photoelectric effect ($E_\gamma < 200\,\mathrm{keV}$),
- Compton scattering and ($200\,\mathrm{keV} < E_\gamma < 5\,\mathrm{MeV}$)
- Pair production ($E_\gamma > 5\,\mathrm{MeV}$).

Each effect dominates in a regime depending mainly on the energy of the photon, E_γ, but also on the atomic number, Z, of the absorbing material.

Photoelectric effect

A photon can be absorbed completely by an electron of the atomic shell in the medium. The whole energy of the photon is absorbed, which is not possible for free electrons because of energy and momentum conservation. The process requires a third collision partner, in this case the atomic nucleus, which absorbs the recoil of the scattered electron.

$$\gamma + A \rightarrow e^- + A^+ \quad (3.13)$$

The atom is ionized in the process and the ejected electron carries away a fraction of the photon's energy as kinetic energy. The amount of energy transferred depends on the ionization energy of the medium. Electrons emitted in such a way are usually referred to as photoelectrons.

The cross section for absorption of a photon of energy E_γ is largest for electrons in the innermost shell, the K-shell, accounting for about 80 % of the total cross section. For K-shell absorption the total cross section σ^K_{Photon} described by the non-relativistic Born approximation

$$\sigma^K_{Photo} = \sqrt{32}\left(\frac{m_e c^2}{E_\gamma}\right)^{3.5} \alpha^4\, Z^5\, \sigma_{Thomson}, \quad (3.14)$$

containing the finestructure constant, α, and Thomson cross section, $\sigma_{Thomson}$, for elastic scattering of photons off electrons. From equation (3.14), it is obvious, that the process is dominant only for low photon energies ($E_\gamma \leq 5\,\mathrm{MeV}$) and high atomic numbers, Z.

Besides the emission of electrons of significant energy, the photoeffect may be accompanied by secondary effects. If an electron of an inner shell, e.g. the K-shell is freed by the photoelectric effect, the free state left behind may be filled with an electron from the outer shells. The difference in energy

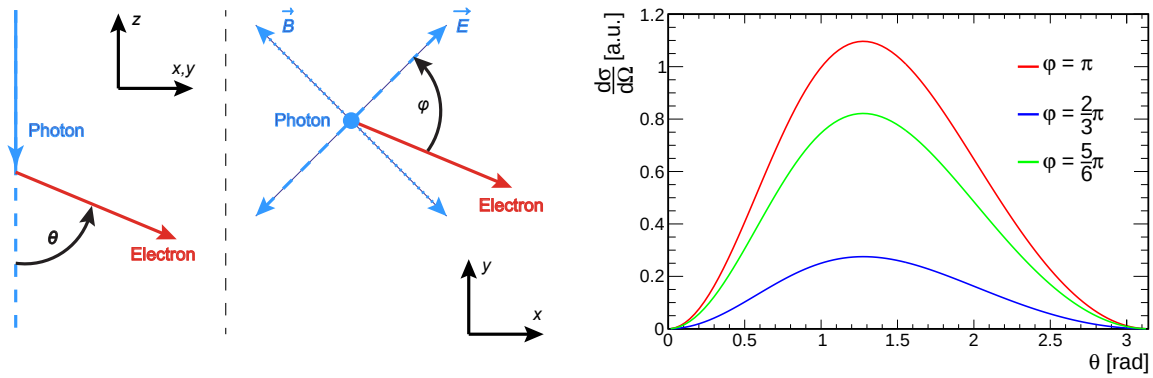

(a) (b)

Figure 3.2: Photoelectric effect. (a) Definition of the scattering angles θ and φ. (b) The differential cross section as a function of the scattering angle θ, for three values of φ. The kinetic energy of the electron is set to $E_e \approx 5.89\,\text{keV}$, corresponding to a value of $\beta = 0.152$.

between the two shells is then emitted in the form of a X-ray photon which is according to Moseley's law

$$E = Ry\ (Z-1)^2 \left(\frac{1}{n^2} - \frac{1}{m^2}\right), \tag{3.15}$$

where Ry (= 13.6 eV) is Rydbergs constant, and n and m are the principal quantum numbers of the participating atomic shells. Instead of being emitted as X-ray photon, the energy can also be transferred to another electron in one of the outer shells. In case of an energy difference surpassing the binding energy of that shell, a further electron is freed. Such electrons are known as Auger electrons and have usually a very low kinetic energy.

The direction of the emitted photoelectrons strongly depends on the direction of the initial photon. The differential cross section is given by [49]

$$\frac{\mathrm{d}\sigma^K_{Photo}}{\mathrm{d}\Omega} \propto \frac{\sin^2(\theta)\cos^2(\varphi)}{(1-\beta\cos(\theta))^4}, \tag{3.16}$$

with θ being the angle between the initial photon and the photoelectron, φ representing the angle between the photoelectron and the polarization vector of the initial photon, and β being the photoelectron's speed in units of the speed of light. An illustration of the angles is shown in Figure 3.2a. As indicated by the differential cross section, emission of the photoelectron in directions perpendicular to the initial photon direction are preferred, as depicted in Figure 3.2b.

Compton scattering

The inelastic scattering of a photon by free, or quasi-free electrons is called Compton scattering, in which the binding energy of the electron, if any, is neglected. The photon is deflected in the process and transfers part of it's energy to the electron

$$\gamma + e^- \rightarrow \gamma + e^-. \tag{3.17}$$

The atomic number, Z, of the material has only to be taken into account when determining the atomic cross section, $\sigma^{A}_{Compton}$, which is Z times larger than the single electron cross section, $\sigma^{e}_{Compton}$. The reason for this is, that there are exactly Z electrons available in the atomic shell to act as scattering partners. The total ross section for a single electron is given by [50]

$$\sigma^{e}_{Compton} = 2\pi r_e^2 \left(\left(\frac{1+\epsilon}{\epsilon^2} \right) \left(\frac{2\,(1+\epsilon)}{1+2\epsilon} - \frac{1}{\epsilon} \ln\left(1+2\epsilon\right) \right) + \frac{1}{2\epsilon} \ln\left(1+2\epsilon\right) - \frac{1+3\epsilon}{(1+2\epsilon)^2} \right), \tag{3.18}$$

with $\epsilon = \frac{E_\gamma}{m_e c^2}$. The energy dependence of Compton scattering for high energetic photons is described by

$$\sigma^{e}_{Compton} \propto \frac{\ln\left(\epsilon\right)}{\epsilon}. \tag{3.19}$$

From (3.19) it is apparent, that the total cross section decreases for further increasing energies of the incident photon. The energy of the photon after the scattering process E_γ depends on the initial energy of the photon and the scattering angle θ. It is calculation is straight forward from four momentum conservation and yields

$$\frac{E'_\gamma}{E_\gamma} = \frac{1}{1+\epsilon\left(1-\cos(\theta_\gamma)\right)}. \tag{3.20}$$

From equation (3.20) it becomes apparent, that the energy transfer to the electron becomes largest in case of backscattering, i.e. $\theta_\gamma = \pi$. The scattering angle θ_e of the electron can be calculated from

$$\cot\left(\theta_e\right) = (1+\epsilon)\tan\left(\frac{\theta_\gamma}{2}\right). \tag{3.21}$$

It can not exceed a value of $\pi/2$ for reasons of momentum conservation.

Pair production

In this process the incident photon is transformed into an electron-positron pair in the presence of an atomic nucleus N.

$$\gamma + N \rightarrow e^+ + e^- + N \tag{3.22}$$

The energy of the photon has to exceed the invariant masses, m_e, of the two particles plus the energy absorbed by the recoil of the atomic nucleus. Thereby, the threshold energy, E_γ, can calculated via

$$E_\gamma \geq 2m_e c^2 + 2\frac{m_e^2}{m_{Nucleus}} c^2. \tag{3.23}$$

As the mass of the nucleus, $m_{Nucleus}$, is usually much larger than the electron/positron mass i.e. $m_{Nucleus} >> m_e$, the second term in (3.23) can be neglected and the threshold energy only has to surpass twice the invariant mass of an electron,

$$E_\gamma \geq 2m_e c^2 \approx 1\,\mathrm{MeV}/c^2. \tag{3.24}$$

This is only true for the conversion of a photon in the Coulomb field of an atomic nucleus. This is the usual case, as the conversion process in the field of an electron is strongly suppressed.

Furthermore, the cross section of the production depends on the photon energy and whether the nucleus is screened by its atomic shell. If the photon comes very close to the nucleus, i.e. sees its unscreened field the cross section for pair production is described by

$$\sigma_{Pair} = 4\alpha r_e^2 Z^2 \left(\frac{7}{9}\ln\left(\frac{E_\gamma}{2m_e c^2}\right) - \frac{109}{54}\right). \tag{3.25}$$

In this case pair production can happen even for low energetic photons. In contrast, if the nucleus is screened by its atomic shell, the cross section changes to

$$\sigma_{Pair} = 4\alpha r_e^2 Z^2 \left(\frac{7}{9}\ln\left(\frac{183}{Z^{1/3}}\right) - \frac{1}{54}\right). \tag{3.26}$$

Although, not dependent on the photon energy, it is only valid for high energetic photons. The largest cross sections for pair production are obtained in the case of high energy photons traversing through a medium with a high atomic number.

Energy spectrum of ^{55}Fe in argon-based gas mixtures

Its common practice to use radioactive isotopes for the creation of photons with fixed energies. This is especially useful for the testing and calibration of detectors. Radioactive iron, namely the isotope ^{55}Fe is such a source. It decays with a half-life of 2.737 y [51] via electron capture in the K-shell into an excited state of ^{55}Mn. The deexcitation of the manganese is accompanied by the emission of photons in the keV range

$$^{55}\text{Fe} \rightarrow ^{55}\text{Mn}^* \rightarrow ^{55}\text{Mn} + \gamma. \tag{3.27}$$

Measuring these photons yields the characteristic spectrum of ^{55}Fe. The spectrum is dominated by the K_α and K_β emission lines with energies of 5.899 keV and 6.490 keV respectively [52].

The detection of these photons exploits their conversion in the detector medium. With energies of roughly 6 keV, pair production is excluded. Due to the low energy of the photons the photo effect is much more likely to occur than Compton scattering.

For detectors not capable of separating these two lines it is helpful to suppress the K_β line by shielding the source with a thin foil of chromium, which has a Compton edge at 5.989 keV. As a consequence, when using a foil of 10 µm thickness the K_β line is suppressed to 15 % of its original occurrence, while the transmission of K_α line remains at 80 % [53]. This results in a more precise measurement of the energy resolution for the K_α line which is not additionally broadened by the K_β line in this case.

3.2 Drift

Ions and electrons originating from the ionization processes move for two different reasons. First, they move according to their charge in opposite directions as a result of the presence of electric and magnetic fields. Second, they already have a velocity because of their thermal energy. This velocity is subject to random changes due to collisions with the gas atoms, or molecules, respectively. Electrons and ions show greatly differing behaviors in this process, which is not surprising given the mass differences of $O(10^3)$.

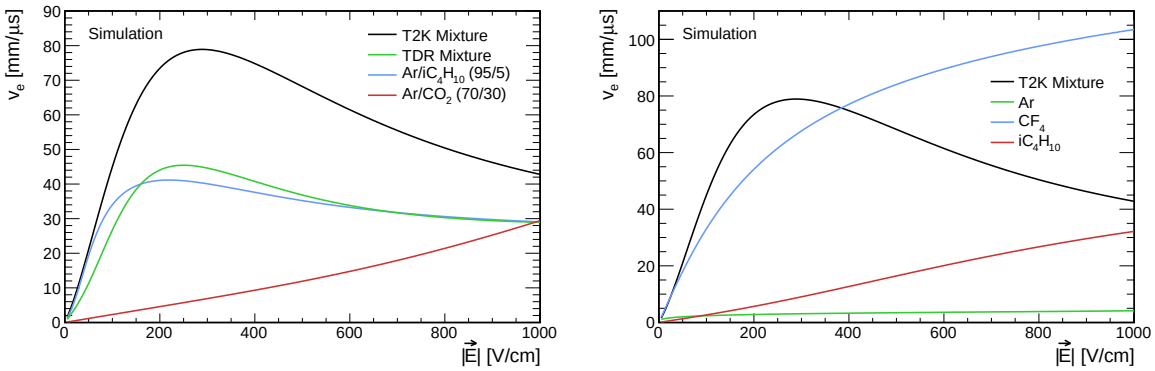

(a) (b)

Figure 3.3: The electron drift velocities for several gas mixtures are shown in (a), while (b) depicts a comparison of drift velocities in the T2K gas mixture and its component gases, as simulated with `Magboltz` [54]. The compositions of the T2K mixture and TDR mixture are given in the text.

3.2.1 Drift of electrons

Electrons are accelerated in an external electric field $\vec{E}$ until they collide with a particle of the gas. These collisions are isotropic as the electron mass, m_e, is very low compared to the masses of the gas particles. Therefore, electrons lose any preference in direction. After such a collision electrons are accelerated again in the direction of the field lines of the electric field until their next collision. The mean velocity, $\vec{v}_e$, picked up by the electrons is then given by the acceleration, due to the electric field, multiplied with the mean time, τ, between two collisions

$$\vec{v}_e = \frac{e}{m_e}\tau\vec{E} = \mu_e\vec{E}. \tag{3.28}$$

The electron mobility, μ_e, is given by the specific mass of the electron, $\frac{e}{m_e}$, times the characteristic time, τ. Equation (3.28) provides a good description of the electron drift velocity as measured macroscopically, i.e. on time scales large compared to the characteristic time, i.e. for times with $t >> \tau$ and in the absence of a magnetic field $\vec{B}$. It is a mean value and much lower than the actual electron velocity, v_i, between two collisions.

The characteristic time, τ, can be calculated from the particle density $n = \frac{N}{V}$, i.e. the number of particles per volume, the instantaneous electron velocity, $\langle v_i \rangle$, and the scattering cross section σ via

$$\tau = (n \cdot \sigma \cdot \langle v_e \rangle)^{-1}. \tag{3.29}$$

The characteristic time is inverse proportional to the collision cross section of electrons. For de-Broglie wavelengths of the electrons of the same size as the radii of the gas particles, the cross section reaches a minimum. This behavior, known as the Ramsauer effect [55], causes the electron drift velocity to become maximal. Figure 3.3 shows the drift velocity for various gas mixtures, as well as for the single components of the T2K mixture [56]. Large differences are observed between the different mixtures, which is because of the different collision cross sections. The T2K mixture consists of 95% argon, 3% tetrafluoromethane and 2% isobutane and is a rather fast gas, allowing for electron drift velocities of nearly 80 mm/µs. The TDR mixture, as proposed in the context of the Tesla project [57], is composed of 93% argon, 5% methane and 2% carbon dioxide. For this mixture, the maximum velocity is only

about 45 mm/µs, which is rather slow compared to the T2K mixture.

The characteristic time, described by equation (3.29), can be related to temperature, T, and pressure, P, with the help of the equation of state for the ideal gas

$$P \cdot V = N \cdot k_B \cdot T \qquad \text{or} \qquad n = \frac{N}{V} = \frac{P}{k_B T}, \tag{3.30}$$

respectively, with Boltzmann constant k_B. Inserting (3.30) into (3.29) yields a temperature and pressure dependent expression for the macroscopic drift velocity

$$v_e = \frac{e}{m_e} \frac{k_B T}{\sigma v_i P} \vec{E}. \tag{3.31}$$

From equation (3.31), it is immediately evident, that the drift velocity of electrons increases proportionally to the temperature and decreases anti proportionally to the pressure of the gas.

3.2.2 Drift of ions

The drift ions is much different from the drift of electrons, due to their much higher masses. The energy ions obtain between two collisions is mostly lost in their next collision, as their mass is comparable to the mass of their collision partner. For this reason, their direction of motion is not randomized as much as in the case of electrons. The kinetic energy ions obtain from the electric field is in the same range as their thermal energy. As a consequence, their mobility, μ_I, is independent of the electric field and their drift velocity is proportional to the electric field, $\vec{E}$,

$$\vec{v}_I = \mu_I \vec{E}. \tag{3.32}$$

The ion drift velocity is lower by several orders of magnitude, $O(10^{-3} - 10^{-4})$, than the velocity of drifting electrons in the same field and gas.

Upon collision with a gas particle with ionization threshold below the kinetic energy of the incoming ion, a charge exchange may occur. In this process the ion becomes electrically neutral and its collision partner is ionized. In gas mixtures ions with very different mobilities can be created in this manner.

3.2.3 Drift in electric and magnetic fields

Often, a magnetic field, $\vec{B}$, is applied in addition to an electric field $\vec{E}$. Charged particles moving within electric and magnetic fields are subject to Lorentz forces, which have a huge impact on the drift of charged particles. This can be described by the Langevin equation

$$m \frac{\mathrm{d}\vec{v}}{\mathrm{d}t} = q\vec{E}(\vec{x}) + q\left[\vec{v} \times \vec{B}(\vec{x})\right] - K\vec{v}, \tag{3.33}$$

an equation of motion for particles of charge, q, in the presence of electromagnetic fields, extended by a friction term. The friction constant is given by

$$K = \frac{m}{\tau}$$

and depends only on the mean time between collisions, τ, and the mass of the particle, m. For times, t, much larger than the characteristic time, i.e. $t >> \tau$, the solution for the steady state ($\frac{\mathrm{d}|\vec{v}|}{\mathrm{d}t} = 0$) is given

by the expression

$$\vec{v} = \frac{q}{m}|\vec{E}|\frac{\tau}{1+\omega^2\tau^2}\left(\hat{E} + \omega\tau\left[\hat{E}\times\hat{B}\right] + \omega^2\tau^2\left(\hat{E}\cdot\hat{B}\right)\hat{B}\right). \tag{3.34}$$

This relies on the unit vectors along the electric $\hat{E}$ and magnetic $\hat{B}$ field and the electron cyclotron frequency ω, defined by $\omega^2 = \omega_x^2 + \omega_y^2 + \omega_z^2 = (\frac{e}{m})^2 B^2$. The direction of the drift is mainly determined by the dimensionless term $\omega\tau$. For small values of $\omega\tau$ the drift occurs predominantly along the lines of the electric field while particles with a large $\omega\tau$ drift mainly in the direction of the magnetic field.

The last term in (3.34) vanishes for electric and magnetic fields perpendicular to each other. Thus, the drift direction is mainly determined by the $\hat{E}\times\hat{B}$ term, at least for large magnetic fields. In some drift chambers, like e.g. the time projection chambers, both fields are aligned in parallel, so that the $\hat{E}\times\hat{B}$ becomes zero and the drift occurs along the field lines.

In the absence of a magnetic field, the cyclotron frequency ω vanishes and the drift can again be described by (3.28) and (3.32) for electrons and ions respectively.

The presence of a magnetic field affects not only the direction of the drift but also the magnitude of the drift velocity. With the help of the Langevin equation (3.34) an expression for the ratio of the drift velocity with and without magnetic field can be derived to be

$$\frac{|\vec{v}(\omega)|^2}{|\vec{v}(0)|^2} = \frac{1+\omega^2\tau^2\cos(\phi)}{1+\omega^2\tau^2}, \tag{3.35}$$

wherein ϕ denotes the angle between electric and magnetic fields, $\phi = \angle\left(\vec{E},\vec{B}\right)$. While the magnitude of the drift velocity does not change if both fields are parallel to each other, the presence of a magnetic field has a large effect if this is not case. The result is an increase of the angle ϕ. Thus, in the worst case scenario of perpendicular fields $\vec{E}\perp\vec{B}$ the drift velocity can be described by

$$|\vec{v}(\omega)| = \frac{\mu|\vec{E}|}{\sqrt{(1+\omega^2\tau^2}} = \frac{\mu|\vec{E}|}{\sqrt{1+\tan^2(\psi)}}, \tag{3.36}$$

with the Lorentz angle ψ.

3.3 Diffusion

A cloud of free charge carriers in a gas expands by the process of thermalization. Either the charge carriers recombine with particles of opposite charge, or they diffuse within the gas, colliding with other particles. In case of diffusing electrons, it can be assumed that these collisions are isotropic as the gas particles are much heavier and their time dependent density distribution can be expressed by a three dimensional Gaussian distribution

$$\rho_e = \left(\frac{1}{\sqrt{4\pi D' t}}\right)^3 \exp\left(\frac{-r^2}{4D't}\right). \tag{3.37}$$

Thereby, $r^2 = x^2 + y^2 + (z - v_{Drift}t)^2$ is the distance to the center of the charge cloud and D' the diffusion constant. Here, the origin of the coordinate system lies in the center of the original cloud. Hence, the

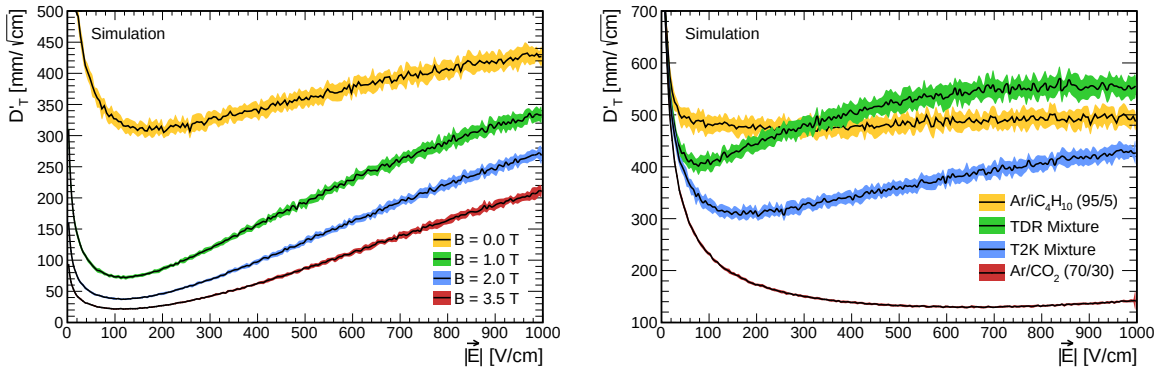

(a) (b)

Figure 3.4: Influence of magnetic fields in the transverse diffusion of the T2K gas mixture (a) and the comparison of diffusion values of several gas mixtures (b), as simulated with `Magboltz`[54].

width of the distribution in each direction is given by

$$\sigma = \sqrt{2D't} = \sqrt{\frac{2D'L}{\mu|\vec{E}|}}. \tag{3.38}$$

Here, the second equality relies on the drift distance, L, which in many cases is more convenient than the dependence on the drift time, t, into which it can be transformed using the relation $t = L/(\mu|\vec{E}|)$. The drift velocity $v_{Drift} = \mu|\vec{E}|$ in (3.38) becomes zero in the absence of an electric field. The diffusion constant, which is mainly responsible for the width of the distribution, is related to the particles' mobility, μ, and their mean energy, ϵ, via

$$D' = \frac{2}{3}\frac{\epsilon\mu}{e}. \tag{3.39}$$

This equation transforms to the Nernst-Townsend or Einstein formula [58]

$$\frac{D'}{\mu} = \frac{kT}{e}, \tag{3.40}$$

for particles with purely thermal energies $\epsilon = \frac{3}{2}kt$. It defines the diffusion constant's lower limit. The collision cross section of electrons depends strongly on the electron energy and thereby on the direction of the electric field, as already mentioned in Section 3.2.1. This is of consequence for the diffusion. Hence, the diffusion is usually accounted for in transverse, D'_T, and longitudinal, D'_L, direction, i.e. in the directions perpendicular and parallel to the electric field. Values for transverse and longitudinal diffusion are different [59], which is a consequence of the energy dependence of the cross section for elastic scattering. The result is an energy dependence of the electron mobility and, hence, a dependence of the electron mobilities on their position in a drifting electron cloud. This leads to

$$\rho_e = \frac{1}{\sqrt{4\pi D'_L t}}\left(\frac{1}{\sqrt{4\pi D'_T t}}\right)^2 \exp\left(-\frac{x^2+y^2}{4D'_T t} - \frac{\left(z - v_{Drift}t\right)^2}{4D'_L t}\right) \tag{3.41}$$

as an expression for the diffusion, in which D_T and D_L have different values, but are of the same order of magnitude. Equation (3.41) depends on the diffusion coefficients $D'_{T,L}$ which is difficult to access experimentally. For this reason, the diffusion constant $D_{T,L}$ is used commonly. Both values are related to each other by

$$D'_{T,L} = \frac{v_{Drift}}{2} D^2_{T,L} \quad \text{and} \quad D_{T,L} = \sqrt{\frac{2D'_{T,L}}{v_{Drift}}} \,. \tag{3.42}$$

The diffusion is influenced by the presence of a magnetic field. In this case, the diffusion movement of the particle curls up in the plane perpendicular to the field. If magnetic and electric field are parallel to each other, the trajectory of the particle becomes a helix, effectively decreasing the movement in the transverse direction. The diffusion, in dependence of the magnetic field strength can be calculated from the diffusion without field, $D_T(0)$, the cyclotron frequency, ω, and the mean free time between two collisions, τ, by

$$D_T(\omega) = \frac{1}{1 + \omega^2\tau^2} D_T(0) \,. \tag{3.43}$$

The longitudinal diffusion remains unaffected by a magnetic field. The effect of diminished diffusion values is illustrated in Figure 3.4a, showing the diffusion of the T2K gas mixture at several values of the magnetic field.

Tracking applications usually profit from small diffusion values, as this improves the spatial resolution. This is a beneficial circumstance, given the fact that most tracking detectors use a magnetic field to bend the trajectories of charged particles and allow for momentum measurements. As advantageous small diffusion values may be in tracking application, other applications, like X-ray detectors can profit from large diffusion values. In this case, the diffusion causes the primary charge cloud to drift apart, so that all its primary electrons can be detected separately, allowing for precise energy measurements. Therefore, gases have to be chosen according to the requirements of the application in question. Diffusion values for several gas mixtures are plotted in Figure 3.4b, including the already mentioned T2K and TDR gas mixtures.

3.4 Gas amplification

The amount of charge created in the primary ionization processes is too small to create electronically detectable signals. Consequently, the charges have to be multiplied, which is done by the process of gas amplification.

The multiplication of electrons happens in strong electric fields. If the field strength is high enough, electrons can pick up enough energy between two collisions to ionize a gas particle by inelastic scattering. In sufficiently high electric fields, a new electron-ion pair is produced in each inelastic collision. This leads to an electron avalanche, as the electrons freed in a collision immediately pick up enough energy to ionize the gas, too. This process takes place only for electrons. For ions it is inhibited by their much larger mass. Gains reached in this fashion typically range from 10^3 to 10^5. The size of the electric field and, therefore, the gain is limited by the occurrence of discharges, which prevent a stable operation of the amplification stage. Which gain can be achieved by gas amplification strongly depends on the amplification structure, the carrier gas and the rate at which the amplification is triggered.

The multiplication of the electrons is described by the Townsend coefficient, $\alpha(\epsilon)$, which depends on

the energy of the electrons, ϵ, and can be expressed by

$$\alpha(\epsilon) = n\sigma_I(\epsilon), \tag{3.44}$$

with the number density of the gas particles n and the ionization cross section, $\sigma_I(\epsilon)$. The Townsend coefficient is also influenced by many other factors, like pressure, temperature, recombination and the Penning transfers [60]. For practical applications it is more feasible to use an expression for α depending on the strength of the electric field $\vec{E}$ instead of the electron energy ϵ. Even though both values are strongly correlated it is not trivial to transform one into the other. In particular, $\alpha(|\vec{E}|)$ cannot be calculated analytically for field strengths usually employed in the amplification stage. Therefore, one has to rely on measurements and simulations to obtain values for $\alpha(|\vec{E}|)$.

Given values for $\alpha(|\vec{E}|)$ it is possible to derive the number of electron-ion pairs, $N(x)$, which are created on a path of length x, by

$$\mathrm{d}N(x) = N(x)\,\alpha\left(|\vec{E}(x)|\right)\mathrm{d}x. \tag{3.45}$$

Integrating (3.45), over the length of the amplification region, i.e. from the starting point, x_1, to the endpoint, x_2, yields the total number of electrons created in the avalanche. Thereby, it is possible to calculate the gain G, defined as the number of electrons after the amplification divided by the initial number N_0, by

$$G = \frac{N(x)}{N_0} = \exp\left(\int_{x_1}^{x_2} \alpha(x)\,\mathrm{d}x\right). \tag{3.46}$$

The amplification process, or more specifically the development of the avalanche, is a statistical process which fluctuates. Therefore, the gas gain, as calculated in equation (3.46), is merely an expected mean value. A distribution function is required that fully describes the multiplication of electrons in the amplification stage. A commonly employed distribution for this purpose is the Polya distribution. A suitable parametrization, as found in [60], is denoted by

$$P(N) = \frac{1}{\bar{N}}\frac{(\theta+1)^{\theta+1}}{\Gamma(\theta+1)}\left(\frac{N}{\bar{N}}\right)^{\theta}\exp\left(-(\theta+1)\frac{N}{\bar{N}}\right), \tag{3.47}$$

with mean value $\bar{N}$ and the parameter θ, which is connected to the width, σ, of the distribution by

$$\sigma^2 = \frac{\bar{N}^2}{\theta+1}. \tag{3.48}$$

Although, the Polya distribution is only motivated for the description of avalanche fluctuations in inhomogeneous fields, it is also frequently used in case of homogeneous field configurations. While this approach has been debated [61, 62], recent results, like those presented in [53, 63] show that Polya distributions may indeed be a valid description.

In addition to electrons colliding with the gas particles, photons in the UV regime may contribute to the amplification process. The photons originate from excitation processes of the gas molecules, which can be either caused by the recombination of ion and electron pairs, or by their collisions. When these photons are absorbed they can ionize the gas. If the absorption occurs in the amplification region, it may create a secondary avalanche which can be displaced from the primary one. If the photons are not absorbed they can reach some of the surrounding material, like metal surfaces of the electrodes, and free electrons by the photoelectric effect. Both origins of the secondary avalanches, ionization or

photoelectric effect, can create signals, which are difficult to be distinguished from signals of primary electrons. For this reason, UV photons have to be prevented from creating fake signals and small fractions of quencher gases are added to the carrier gas. The role of these quencher gases is to absorb photons without being ionized. Gases chosen as quenchers are usually molecular gases, like CO_2, CF_4 iC_4H_{10}, which have many absorption lines in the UV regime. With their high absorption cross sections they have a high probability of stopping the photons before they can ionize the carrier gas. The deexcitation happens through multiple vibration states accompanied by the emittance of photons of the infrared regime.

In addition to statistical fluctuations the gas gain is also dependent on environmental variables like temperature and pressure. The influence of pressure variations, $\mathrm{d}p$, follows a proportional law [60]

$$\frac{\mathrm{d}G}{G} \propto \frac{\mathrm{d}p}{p}. \tag{3.49}$$

In practice gain fluctuations resulting from pressure variations can be corrected for as the gas pressure can be usually monitored very precisely.

3.4.1 Micropattern-gaseous detectors

Many gaseous detectors have relied on proportional wires for gas amplification. Here, the high field strengths required for gas amplification are created by the application of a high voltage to the wires. The wires have a very small radius, usually in the range of 25 µm to 100 µm. Because of the small radii, the field lines become very dense in the vicinity of the wires and its amplitude is anti-proportional to the distance, r, to the wire. Electrons in the drift field approach the wires on these field lines undergo gas amplification as they approach them. By connecting suitable readout electronics to the wires, they can be used for the readout of the drifting electrons as well.

In particular in tracking applications, the use of wires is subject to certain limitations. To cover large areas, many wires have to be mounted in parallel at distances of a few mm to each other. Besides the difficulties of clamping the wires with enough tension to keep them at their nominal position the achievable spatial resolution is strongly limited by the minimal distance between the wires, which is about 1 mm. Additionally, $\vec{E} \times \vec{B}$ effects can further reduce the spatial resolution. This happens as the electric field lines are radially bent towards the wires and hence, not parallel to the lines of the drift field anymore. Given the presence of a magnetic field parallel to the drift field, e.g. to reduce transverse diffusion and allow for momentum measurements, a Lorentz angle appears which further decreases the resolution of the readout. These are some of the reasons which led to the development of new concepts.

The invention of micropattern gaseous detectors (MPGD) was the result of research aimed at overcoming the limitations of proportional wires. MPGDs have very granular amplification structures and are therefore well suited for setups requiring a very high spatial resolution. Several different concepts have emerged in the last decades, of which gas electron multipliers and micro-mesh gaseous detectors are the most popular ones. Today MPGDs play an important role and are employed in all kinds of gaseous detectors.

GEMs

Gas electron multipliers (GEMs) [66] are thin foils used for gas amplification. They consist of a thin insulating foil, coated on both sides with a metal layer. The insulating material is usually made of

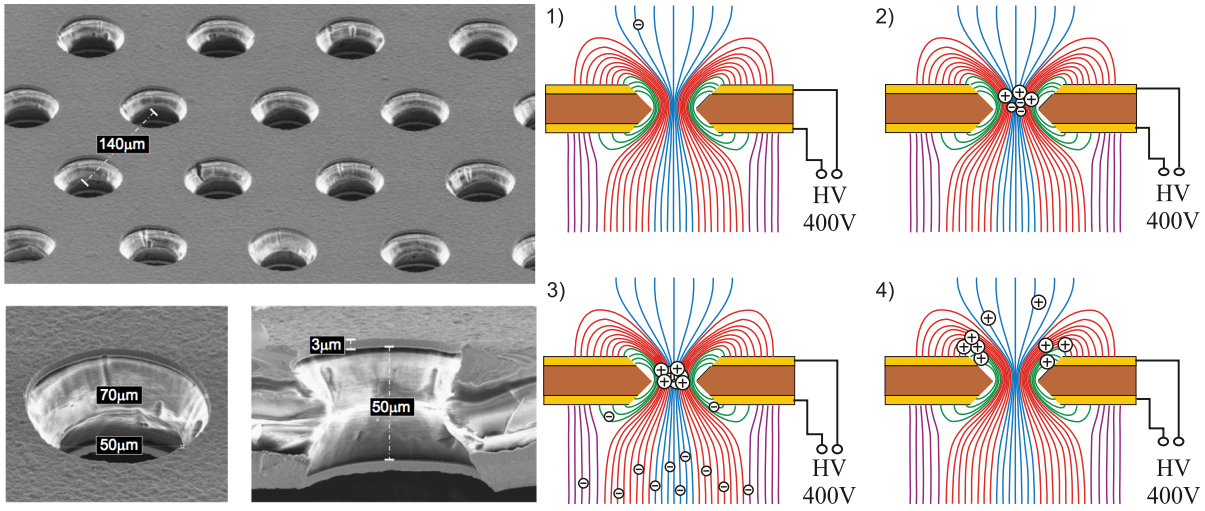

Figure 3.5: Electron microscope pictures of a GEM [64], showing the dimensions of the holes (a). Working principle of a GEM [65] in four stages (b).

Kapton®[1] and the metal layers are in most cases made of copper. Small holes are etched into the sandwich structure, forming a regular hexagonal pattern. Figure 3.5a shows an electron microscope picture of a GEM with annotations denoting the dimensions of the layers and holes of typical GEMs as they are produced at CERN.

To perform gas amplification with a GEM, voltages are applied to both metal layers, creating a strong electric field within the holes of the GEM. This field is strong enough for gas amplification. The field configuration of a GEM and the individual steps of the amplification process are illustrated in Figure 3.5b. The amplification process starts with an electron in the drift region being collected in a GEM hole. The field lines in this region are focused into the GEM holes, thus providing a high electron transparency. In the high field within the hole, the electron obtains enough energy to initiate an electron avalanche with possible gains of up to $O(10^3)$ for a single foil. The freed electrons leave the GEM, drifting either to another amplification stage or to the readout area. The signal formed by GEMs is formed directly by the electrons and is thereby much faster than slow ion signals [67]. Furthermore, GEMs are operated independently of the readout scheme below them, hence, offer a high flexibility in the design of detectors.

To obtain a higher operational stability, it has proven useful to cascade multiple GEMs. In this manner, the amplification is distributed upon several stages, thus, reducing the required field strength per GEM. Moreover, the charge from the amplification processes is spread over a large readout area, because of the high fields usually applied in and between the GEMs . This allows for very precise position measurements, as described in Section 3.5. Apart from the increase in high voltage stability and precision measurements, such setups can be exploited to limit the amount of ions entering the active region of the detector [68].

The concept of GEMs is very successful. Popular examples for detectors relying on GEMs can be found at the COMPASS[69], LHCb[70] and TOTEM[71] experiments at CERN and several more planned experiments are considering their usage. The general layout of GEMs leaves room for cus-

[1] Kapton is a polyimide material known for its very high insulating capabilities. It is a registered trademark of the DuPont company.

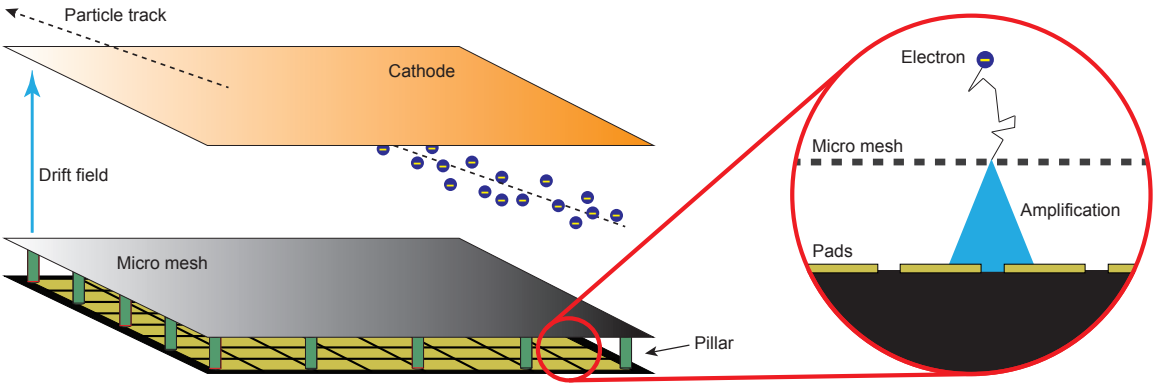

Figure 3.6: Schematic view of the functional principle of a Micromegas detector (not to scale).

tomization, as size, pitch and shape of the holes, as well as thickness of the insulator and used materials can be adapted to meet the requirements of an experiment, which makes GEMs a very versatilely applicable technology.

Micromegas

Micro-mesh gaseous detectors (Micromegas) [72] are another widely used detector concept. They consist of a very fine mesh, which separates the gas volume into a drift and an amplification region. The mesh is supported by small insulating pillars and resides at a small distance in the range of 50 µm to 100 µm above the drift anode of the detector which also acts as readout. By applying a high voltage of about 400 V with respect to the anode to the mesh, a field strong enough for gas amplification is created in this region. By this design the amplification structure remains independent of the underlying readout scheme and can be used with unsegmented anodes, pads strips or even pixels. A sketch of the functional principle of a Micromegas detector with pad readout is shown in Figure 3.6. Micromegas detectors possess many advantageous properties. The development of the signal is very fast and happens in about 1 ns, hence, allowing these detectors to be used in environments requiring a very high readout rate. They have proven to be radiation hard, i.e. resistant to even large doses of radiation, and can be easily built to cover large areas. Additionally, Micromegas can be tuned to minimize the amount of back drifting ions [73]. Micromegas detectors possess an excellent energy [74] and spatial resolution [75].

Several techniques of production and variations of the original concept have been developed. Bulk Micromegas [76] are one such variation. In this case, the micro-mesh is not electroformed[2], like for standard Micromegas, but made of a woven wire mesh. It is laminated upon a photoresistive film which is placed on the readout plane. The pillars are then washed out from the photoresistive film by a photolithographic method. By this process it is possible to construct a Micromeags detector covering the whole readout area in one process. This technique has proven to be very reliable and allows even to equip curved readout areas (e.g. [77]). Another variation are Microbulk Micromegas [78], which take the concept of Bulk Micromegas even further. In this concept, the Micromegas are not only built as one object but also by a single production process. This is realized by constructing the readout area as well as the amplification structure from Kapton® foils, which are coated on both sides with copper. The readout, except for the electronics, is patterned into the copper in the same way as the holes into the mesh by photolithographic processing. This results in very flexible structures which can easily be

[2] Electroforming is a process to fabricate thin metal parts by depositing thin layers of metal onto a base part which is removed after the process.

adapted to different environments.

Since the introduction of the concept in 1996, Micromegas detectors have been successfully employed in a huge variety of experiments. The time projection chamber of the T2K experiment [79], is just one example for the operation of Bulk Micromegas as large area readout, while CAST [80] and n-TOF [81] are prominent examples for the application of Microbulk Micromegas. Given their success, it is not surprising that this technology is also under investigation for the readout of the time projection chamber at the ILC [30].

3.5 Readout

Modern gaseous detectors usually rely on a segmented readout area for the detection of charge signals from the amplification processes. The charge is transformed into an electrical signal by induction. Any charge q close to an electrode induces a mirror charge $-q$ in that electrode, which is according to Gauss' law independent of its distance to the electrode. In case of a segmented electrode the charge, q_n, induced on segment, n, depends on the position, $\vec{x}(t)$, of the charge, q, relative to the segment, while the sum of all induced charges $Q^{Ind.}_{Total}$ remains unchanged and matches the original charge

$$Q^{Ind.}_{Total} = \sum_n q_n = -q. \tag{3.50}$$

As the charge q moves the induced charges, q_n, changes as well, resulting in a currents $I^{Ind.}_n(t)$ in the segments. Obviously, the intensity of the induced currents depends on the velocity $v = \frac{\mathrm{d}\vec{x}(t)}{\mathrm{d}t}$ of the moving charge

$$I^{Ind.}_n(t) = -\frac{\mathrm{d}q_n(\vec{x}(t))}{\mathrm{d}t} = -\vec{\nabla} q_n(\vec{x}(t)) \cdot \frac{\mathrm{d}\vec{x}(t)}{\mathrm{d}t}. \tag{3.51}$$

This means that the total amount of charge $Q^{Ind.}_n$ induced on a segment of the electrode at time T can be calculated by integrating the current on the segment

$$Q^{Ind.}_n(T) = \int_0^T I_n(t)\mathrm{d}t. \tag{3.52}$$

From Equation (3.52), it is apparent, that the amount of induced charge is subject to change until the movement of the original charge has stopped. Moreover, the movement of the charge will only stop when the charge is absorbed on the electrode. At that time, the amount of charge on the collecting segment has to be as high as the original charge, while the integral over the induced charges on all other segments vanishes.

Although the description above is accurate, it is usually very difficult to calculate the signal caused by moving charges for realistic, i.e. more complex geometries. A simpler method to obtain these signals is given by the Shockley-Ramo theorem [82, 83], which can be expressed by

$$Q^{Ind.}_{Total} = -q\Phi_w(\vec{x}(t)) \qquad \text{and} \qquad I^{Ind.} = -\frac{\mathrm{d}Q}{\mathrm{d}t} = -q\vec{E}_w(\vec{x}(t)) \cdot \frac{\mathrm{d}\vec{x}(t)}{\mathrm{d}t}, \tag{3.53}$$

with weighting potential $\Phi_w(\vec{x}(t))$ and weighting field $\vec{E}_w(\vec{x}(t))$. Equation (3.53), allows the calculation of the induced charge for an arbitrary configuration of electrode segments. This is done by setting the potential of the segment of interest to unity, while the potential of all the other segments is set to

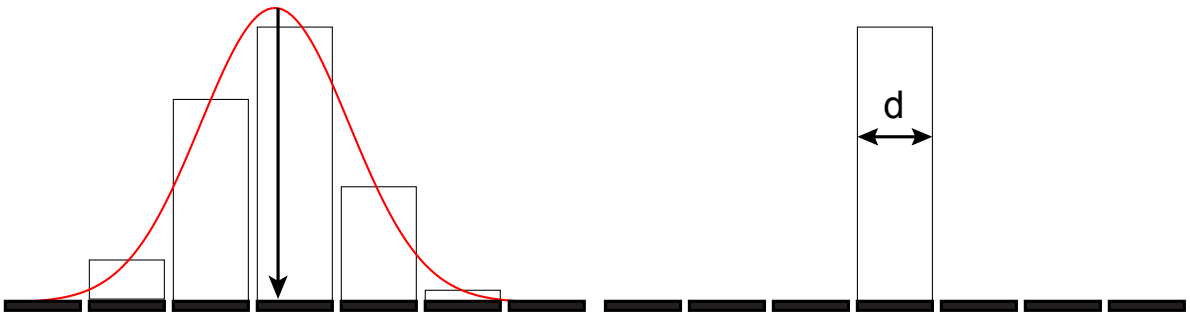

Figure 3.7: Benefits of charge sharing. Position measurements by the means of the center of gravity method (a) and by detection on a single segment (b).

zero. Solving the LAPLACE equation for the resulting configuration, yields the weighting potential, from which the weighting field can be obtained via $\vec{E}_{w,n}(\vec{x}(t)) = -\vec{\nabla}\Phi_{w,n}(\vec{x}(t))$ as usual. A formal proof of the theorem can be found in [84]. From (3.53) it is apparent that the induced charge depends only on the endpoints of the moving charge's trajectory because of the conservative nature of the weighting potential $\Phi_w(\vec{x}(t))$. As a consequence, the total amount of charge induced on an electrode segment is equal to the charge collected by it.

The resolution at which the position of a detected charge deposition can be measured strongly depends on the granularity of the readout area. Finer segmentation usually leads to a better resolution. This is obviously true as long as all the charge from a single amplification process is collected on only one segment of the readout. If the readout segments are smaller, charge may be spread out over several segments. This is beneficial as the amount of charge measured on the individual segments can be used to determine the center of gravity of the charge distribution, as depicted in Figure 3.7. This method yields more precise results than charge measurements on single segments, which is constrained to the hodoscope limit. This is taken advantage of by many detector setups. In detectors based on GEMs and pads the charge from the amplification process is usually distributed over several pads, allowing for a very precise determination of the original charge position. Micromegas detectors usually have a too low diffusion to spread the amplified charge over multiple pads or strips. In this case a thin resistive layer placed upon the readout electrode can be used to expand the charge spread and exploit the center of gravity effect.

Most modern gaseous detectors possess a readout based on pads or strips. For pad readouts the anode is segmented in two dimensions and the signal development occurs just as described above. Typical sizes of readout pads are several square mm. Strip detectors are not fundamentally different, but the readout is just segmented in one dimension and, therefore, provides just a position measurement in this direction. By using multiple layers of strips oriented in different directions precise position measurements in two dimensions are possible. Strips with a width as small as some ten µm are known.

3.5.1 Integrated pixel readout

As pointed out in the previous sections of this chapter MPGDs provide amplification stages of very high granularity, providing gas amplification with a resolution in the µm regime. Conventional readouts like pads ore strips fail to take full advantage of this, as they have typical sizes of $O(\text{mm}^2)$. An improvement

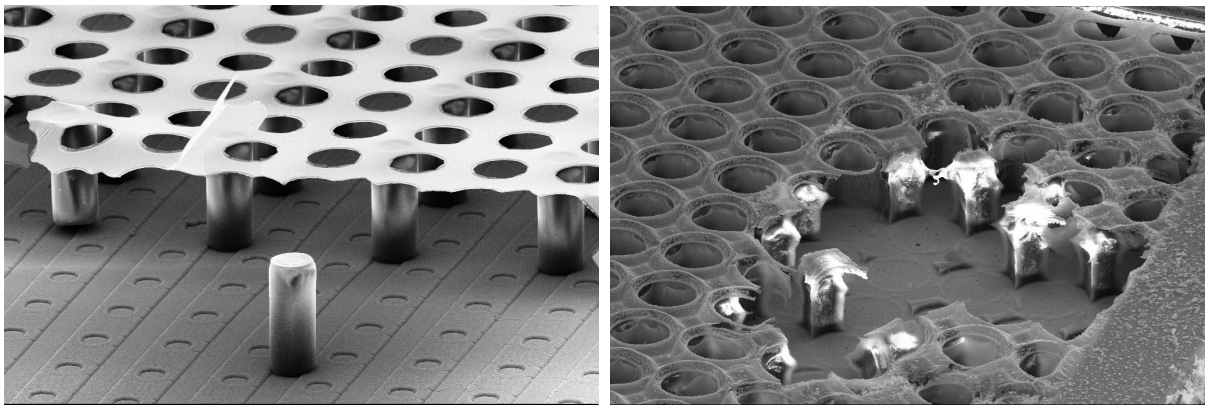

(a) InGrid (b) GEMGrid

Figure 3.8: Scanning electron microscope pictures of integrated pixel readouts. (a) An InGrid on a pixel chip. Some of the grid has been peeled off. (b) A GEMGrid on bare substrate. Some of the structure has been damaged to expose walls supporting the grid.

in the obtained resolution may therefore be obtained by matching the size of the readout with the size of the amplification stage. This approach is taken by pixelized readouts. Here, the bump-bond pads of a pixel chip are used for the charge collection in the same way as pads in the case of a conventional readout. As the pixel pitch of these chips is usually of $O(10\,\mu\text{m}$ to $100\,\mu\text{m})$, they provide a very high segmentation, matching those of MPGDs. The feasibility of this approach has been demonstrated for GEMs [85] and Micromegas [86] as amplification structures.

Integrated pixel readouts are a novel technique for the readout of gaseous detectors which take this approach a step further. Similar to the already described Microbulk Micromegas detectors, they combine the gas amplification stage and readout in a single device. The amplification structure is placed directly on top of the pixel chip by means of industrial post processing. Consequently, the electron multiplication takes place above individual pixels allowing to separate even primary electrons. Obviously, the higher granularity of this approach also results in a lower fraction of readout channels being occupied. Furthermore, all the electronics, like preamplifier, discriminator and digitization, are already included in the chip, eliminating the need to connect and operate dedicated electronic devices.

The original approach to create chips with an integrated amplification stage was to modify pixel chips with the standard Micromegas production process [86, 87]. Although that approach was in general successful and yielded functional devices, some drawbacks became apparent during the first tests. Even if the holes in the mesh are nearly of the same size as the pitch of the pixels beneath, a misalignment of both structures is almost unavoidable. This results in the appearance of a Moiré pattern, i.e. an interference pattern of the micromesh and the underlying pixels. Another problems is the appearance of dead areas on the pixel chip, due to the pillars supporting the mesh. Each pillar covers some pixels, preventing any charge carries from being collected by them. An obvious improvement of this situation is the usage of smaller pillars, which are placed between the pixels, an approach which requires a very precise alignment of both structures.

To achieve the precise alignment of the amplification structure and the pixel chip, the production process was transferred to photolithographic post processing [88, 89]. This kind of production results in an integrated device, housing both, readout and amplification stage. The mesh of such devices usually consists of aluminum with holes etched into it and is therefore usually referred to as “grid“. The production process is precise enough to align each hole in the grid to a single pixel of the underlying chip. A

detailed discussion of the production process is postponed to Chapter 4, where the efforts of fabricating such structures in large quantities and the characteristics of the resulting devices are discussed.

So far, two types of integrated pixel readouts have been developed. The first one is the integrated grid readout (InGrid) [89], which is the precisely aligned micromegas-like structure described above. A second version are the GEMGrids [90], which got there name from there resemblance to GEMs glued on top of a pixel chip. GEMGrids rely on the same principle for gas amplification as InGrids, but the grid is supported by a solid layer of insulating material instead of pillars. The solid layer contains cylindrical holes above pixels, where gas amplification can take place. With this design, it is impossible for charges to be spread over several pixels. Additionally, the structure has a higher mechanical stability due to the increase of the supporting surface.

3.6 Time projection chambers

The concept of the time projection chamber has first been introduced in Reference [91] and has since been employed in a variety of experiments. TPCs are drift chambers with an uniform electric field between drift cathode and the readout plane, which acts as an anode. Charged particles traversing the drift volume ionize the gas along the trajectory as described in the previous sections. Electrons and ions are separated by the electric field and drift in different directions. As the readout plane is segmented, their detection provides a projection of the incident particles trajectory. The third coordinate is obtained by measuring the drift time, t, of the arriving electrons, i.e. the time between the moment the incident particle traverses the detector, t_0, and the detection of the electrons, t_1. If the electron drift velocity, v_e, in the gas is known, the z coordinate can be calculated from

$$z = (t_1 - t_0)\, v_e. \tag{3.54}$$

For this to work, the crossing of the incident particle at t_0 has to be measured by an external trigger system. In this manner, a TPC is capable of measuring the tracks of charged particles in all three directions in space. At collider experiments, the TPC is usually built around the beam pipe, with a common central cathode at the position of the interaction point and two dedicated readout areas. The functional principle of such a TPC is sketched in Figure 3.9.

One of the main advantages of TPCs is the large number of track points they provide. Basically, each primary ionization process creates a measurable signal, provided that amplification stage and readout are sensitive to single electrons. Even TPCs with conventional pad readouts and low single electron efficiency can easily provide $O(10^2)$ track points (e.g. about 150 track points for particles completely traversing the TPC at the ALICE experiment [92]). At this point it should be noted, that in the context of drift chambers usually a somewhat different naming convention is used than for ionization in general. In the jargon of drift chambers each ionization process in the sensitive volume of the detector is considered as “primary ionization”, while the ionization processes in the amplification region are referred to as “secondary ionization”. This definition is contrary to the wording used in the previous sections for the discussion of ionization by charged particles. In the following, the drift chamber definition is used, with “primary ionization” referring to all ionization processes in the sensitive volume of the detector.

The drift field of TPCs is usually chosen to obtain the maximum drift velocity. This reduces the impact of field strength fluctuations, which have close to the field strength of maximum drift velocity only a minor impact on the drift velocity (compare Figure 3.3). In addition, this minimizes the readout time of the detector, which is given by the time required by electrons to reach the anode. This is particularly important, as typical readout times of some 10 µs for large drift distances make the TPC a comparatively slow detector. In any case, the direction of the drift field should be as homogeneous as possible, which

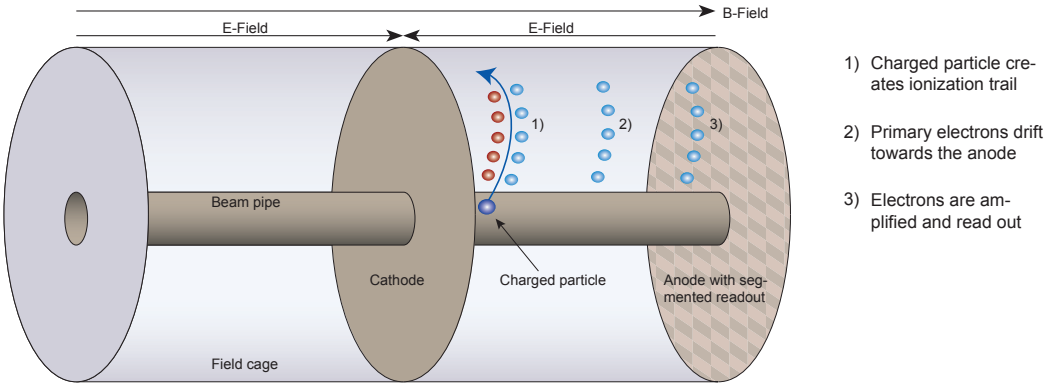

Figure 3.9: Schematic view of the functional principle of a TPC for collider experiments (adapted from [93]).

is usually ensured by the presence of a field cage, which consists of conducting strips placed along the boundary of the gas volume between anode and cathode. These strips are set to a potential according to the nominal potential in the detector volume. This ensures a homogeneous drift field even close to the boundaries of the gas volume.

Electrons reaching the anode have to be amplified in order to create a detectable signal. Several mechanisms of amplification have already been described in Section 3.4. In the past most experiments relied on proportional wires for amplification and they are still applied in modern detectors. A TPC can greatly profit from the higher granularity offered by MPGDs.

Especially for tracking applications at collider experiments, TPCs are usually operated in a magnetic field parallel to the drift field. The magnetic field, $\vec{B}$, exerts a LORENTZ force on charged particles bending their trajectories in a direction perpendicular to both fields. By accurately measuring the curvature of the trajectory, ω, the transverse momentum, p_T, of a particle with charge q can be calculated via

$$p_\mathrm{T} = \frac{q \cdot |\vec{B}|}{\omega}. \tag{3.55}$$

This is not the only effect of the magnetic field. As becomes apparent from Equation (3.43)), the transverse diffusion is reduced by the magnetic field, thus, the spatial resolution is greatly increased.

A further measurement TPCs are capable of, is the determination of $\mathrm{d}E/\mathrm{d}x$. The amount of charge detected on the readout is a direct measure for the energy deposited in the detector, provided, that the amplification stage has been properly calibrated. Recent studies (e.g. [94, 95]) conclude that the resolution of $\mathrm{d}E/\mathrm{d}x$ can even be improved by not measuring the amplified charge on the readout, but by counting the number of primary ionization clusters. This approach can particularly benefit from the use of integrated pixel readouts, as these have a very high single electron efficiency. Under perfect conditions, i.e. for 100 % detection efficiency, this could push the $\mathrm{d}E/\mathrm{d}x$ resolution to below 2 % and improve the particle separation power [94].

Since their invention TPCs have been used in a large variety of experiments. Prominent examples for their successful application in experiments of modern particle physics are the ALICE [92] and T2K [56] experiments.

3.6.1 Ion back drift

It has already been pointed out that a homogenoues drift field is essential for precise measurements with TPCs. Distortions of the electric field can alter the path of drifting electrons which results in a decreased

performance of the detector.

A frequent problem in terms of field homogeneity is the occurrence of space charges within the active volume of the TPC. Space charges create an electric field which distorts the actual drift field by superposition. They either originate from the primary ionization during the crossing of charged particles or from gas amplification. Primary ions are unavoidable, as the detection principle of the detector relies on their creation. They are few in numbers compared to the ions created in the amplification stage and usually of no concern for the homogeneity of the drift field. In contrast, secondary ions, i.e. ions originating from gas amplification are created in the same amount as electrons for signal creation. Since ions have opposite charge than electrons, they slowly drift (compare Section 3.2.2) towards the cathode. Hence, secondary ions have to traverse the whole drift volume, before they are absorbed at the cathode. This effect is known as ion back drift.

Ion back drift, I_B, is defined as the ratio of the number of ions being absorbed on the cathode to the amount of detected electrons on the anode

$$I_B = \frac{\text{\# of ions on cathode}}{\text{\# of electrons on anode}}. \tag{3.56}$$

The number of ions reaching the cathode is experimentally difficult to access. The same is true for electrons arriving at the anode, even though they are amplified for signal creation. Easier to access are the currents induced by the arriving charges. A measurement of the currents yields the same ratio as a measurement of the charge carriers, so that equation (3.56) is still applicable.

Some amplification structures intrinsically suppress the occurrence of back drifting ions. In Micromegas detectors most field lines of the amplification region end on the micro-mesh, so that most secondary ions are neutralized on the mesh. For higher field strengths more field lines end up on the mesh, effectively reducing the fraction of ions capable of entering the sensitive volume. Especially if the ratio of drift field to amplification field is properly tuned, ion back drift values in the range of 2 to 3 ‰ are possible [73].

The intrinsic ion back drift suppression of GEMs is also very good. Studies on the minimization of back drifting ions in TPCs relying on a triple GEM stack for gas amplification [68] have shown that it is possible to greatly reduce the amount of back drifting ions by applying a certain potential configuration in the GEM stack. Such configurations allow to reduce the ion back drift to become smaller than 2 ‰ [68].

In general, it is assumed that influence of back-drifting ions is of no concern if the amount of back-drifting ions is in the same order of magnitude as the amount of ions created by primary ionization. However, this should always be checked, as even comparable small space charges can considerably distort the drift field if they are confined to a very small volume. Therefore, a precise mapping of back-drifting ions and the resulting field distortions is of importance, as this allows to correct for them. Methods for the calculation of field distortions due to space charge effects in a collider TPC and their application to the situation at the ILD are discussed in Chapters 5 and 6.

Ion gating

Ion gates are one possibility to limit the influence of back-drifting ions. In the past such gates have been realized by implementing an additional layer of wires. The wires are located close to the amplification stage in the gas volume. If the gate is open, all the wires are set to the potential corresponding to their position in the drift field. This way the wires scarcely interfere with the electric field and electrons from the primary ionization processes in the sensitive volume can pass the gate and reach the amplification stage. If the gate is closed the wires are set alternately to a slightly higher respectively lower potential

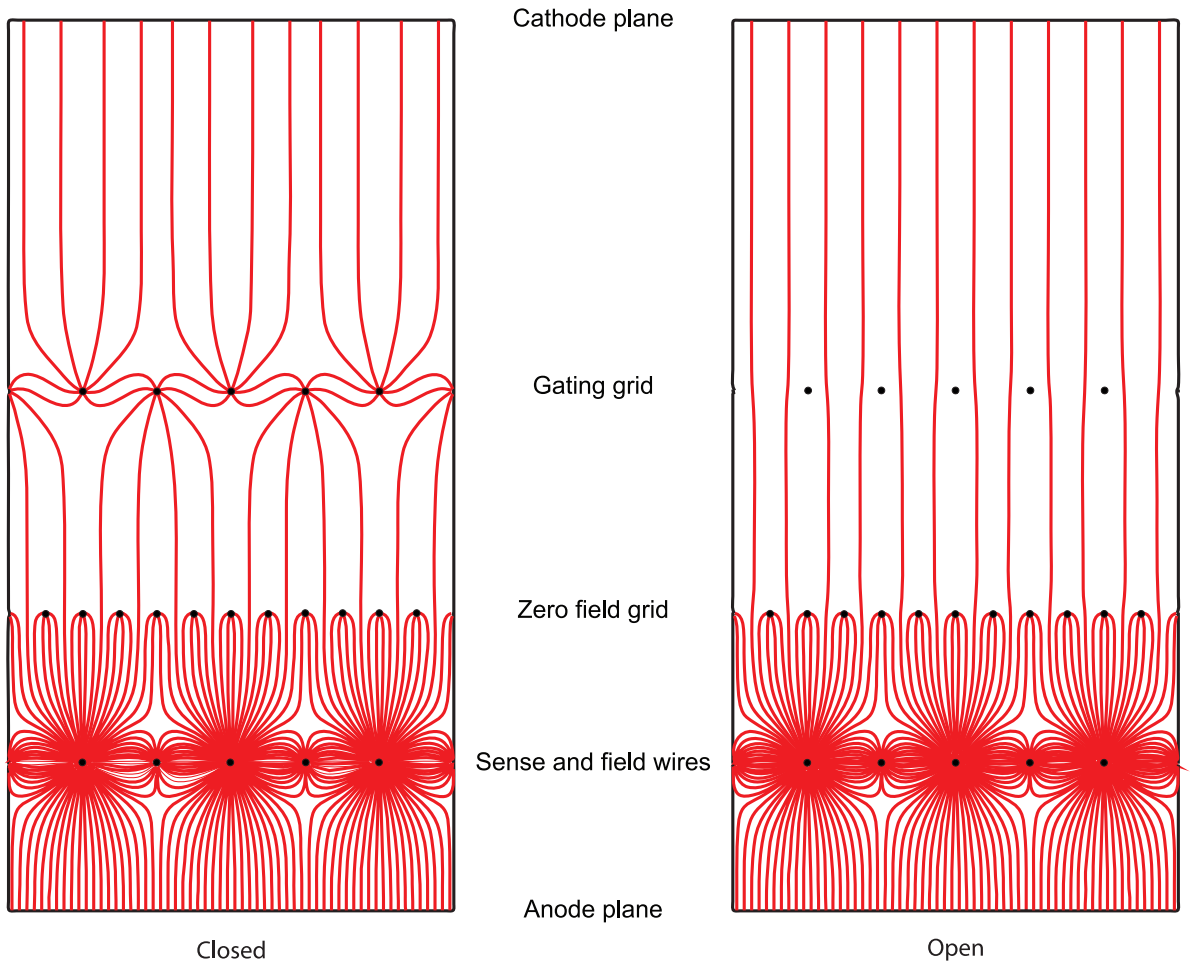

Figure 3.10: Operation of a gating grid [96], in closed (left) and open (right) state. This configuration contains also a zero field grid, responsible for straightening the field lines of the drift field when the gate is open.

than in the opened state. In this way a field is created between the wires, altering the field in the drift region as well as the field in the amplification region. The field lines of the drift field are bend towards the wires set to the higher potential, while the field lines of from the amplification region now end on the wires set to a lower potential. The resulting field configuration prevents ions and electrons alike from passing the gate. The principle of a wire based ion gate in a TPC relying on wires for gas amplification is demonstrated in Figure 3.10, including the field configuration in closed (left) and open (right) state. Opening and closing of the ion gate has to happen according to the beam structure of the collider. To prevent the loss of sensitive volume due to operation of the ion gate, it is opened just before a bunch crossing and in the absence of a trigger signal closed again. If a trigger signal arrives the gate stays open for the maximum possible drift time of an electron. This mode of operation prevents events which create no trigger, e.g. cosmic muons, from creating any back-drifting ions, as the primary electrons end up on the gate wires instead of entering the amplification stage. The time required by ions to reach the gate is much larger than the maximum drift time of electrons and in many cases even larger than the time between two bunch crossings, so that ions may stay for several bunch crossings between gate and amplification structure before they are neutralized at the gate.

Parameter	Value	Remarks
Material budget	$\approx 0.05 X_0$	in r direction, including the outer field cage
	$< 0.25 X_0$	in z direction, including the readout
Point resolution (transverse $\sigma_{r\varphi}$)	60 µm	for zero drift
	< 100 µm	overall
Point resolution (longitudinal σ_{rz})	0.4 mm	for zero drift
	< 1.4 mm	for full drift
Double hit resolution	≈ 2 mm	in transverse direction
	≈ 6 mm	in longitudinal direction
Energy resolution (dE/dx)	≈ 5 %	
Momentum resolution $\sigma(1/p_\mathrm{T})$	$\approx 10^{-4} \frac{c}{\mathrm{GeV}}$	at $\vec{B}$ =3.5 T, TPC only

Table 3.1: Performance requirements for a TPC at the ILD [30].

3.6.2 A TPC for the ILD

In Chapter 2 it has already been pointed out that the ILD foresees a large TPC as central tracking detector. The decision has been made in favor of a silicon tracker because of the large number of track points providing continuous tracking with a minimum amount of material [30]. Thereby, the large number of three-dimensional space points compensates for the moderate point resolution and double hit resolution compared to silicon trackers. The low material budget is in many regards beneficial. It limits the influence of beamstrahlung photons traversing the barrel region [97] and helps to achieve the highest calorimeter performance. The main design goals for the TPC are summarized in Table 3.1.

The TPC is designed as a large cylindrical volume surrounding the beam pipe. It contains a central cathode at the position of the interaction point, dividing the sensitive volume into two halves each with a length of 2225 mm. Inner and outer radius of the active region is 384 mm respectively 1718 mm.

The inner and outer field cages are made of lightweight composite materials [98]. They consist of a sandwich structure of honeycomb, covered on both sides with reinforced epoxy. The field shaping electrodes are mounted on the inner and outer cylinder, facing the gas volume. They are made of metallized Kapton® foils, so that a good insulation of the cylinder walls is guaranteed. A resistive divider inside of the gas volume defines the potential of the field forming strips. An additional layer of field strips on the backside of the Kapton® foils shields the outside of the TPC from the drift field. The conceptual design has been tested with a prototype TPC [98], proving the feasibility of this approach. Based on the results from the large prototype, material budgets as low as 1 % X_0 and 3 % X_0 for inner respectively outer field cage seem to be within reach.

The drift volume is on both ends terminated by an endplate, wich contains the readout of the TPC. The readout is realized by 240 independent modules which are placed concentrically on each endplate. The endplate has to be as lightweight as possible to ensure a high particle flow performance [99]. A material budget of no more than 25 % X_0, including the readout modules, is foreseen for the whole endplate. This should be sufficient to satisfy the demands of particle flow while retaining the mechanical stability required to house the modules [100].

No final decision on the gas to be used has been made yet. The gas employed in the TPC of the T2K experiment [101] is a promising candidate. It is a mixture of 95 % argon, 3 % tetrafluoromethane and 2 % isobutane. This mixture allows for a fast electron drift and small diffusion at the same time.

The readout of the TPC is foreseen to be modular and consists of self-contained modules. Each module incorporates its own gas amplification stage, readout electronics, supply voltages and cooling

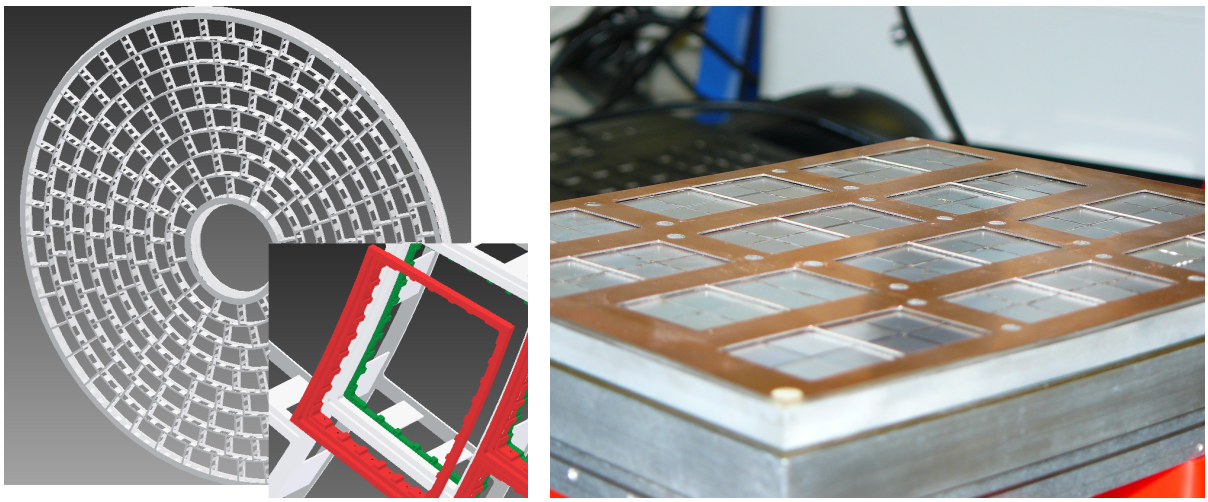

(a) TPC endplate [30].

(b) Large scale InGrid module [105]

Figure 3.11: Schematic view of the endplate of the TPC (a) and a large scale InGrid (prototype) module with 96 InGrid detectors (b).

mechanism [100]. A schematic layout of the supporting structure with on closeup of a single module housing is depicted in Figure 3.11a.

No final decision has been made yet on the technology to be used for gas amplification and readout. While the use of proportional wires has been ruled out [102], GEMs or Micromegas in combination with a conventional pad based readout system are currently the most mature options [99]. Yet, pixelized readouts are a promising alternative regarding energy resolution, background identification and spatial resolution. Prove of concept has already been delivered by the successful operation of modules with multiple chips. Modules with eight InGrid detectors [103], as well as a module with pixel chips and a triple GEM stack for amplification [104] have been successfully operated in testbeam campaigns. The applicability on even larger areas has just been demonstrated by the successful operation of a module equipped with $O(100)$ InGrid detectors (see Figure 3.11b) and a new large scale readout system [105].

The overall design of the TPC has to be studied in detail, to ensure the performance goals as listed in Table 3.1 are met. The main distortions of electron drift paths are assumed to be caused by the magnetic field. The reason for this is the presence of the anti-DID, which is required to suppress beamstrahlung background to acceptable levels (see. Chapter 2.2.2). The field of the anti-DID overlays with the magnetic field of the coil resulting in the total magnetic field not being parallel to the electric drift field anymore. The field of the anti-DID is constant in time, so that a precise mapping will allow to correct for its influence [38].

Besides the nonuniform magnetic fields, space charges accumulating in the gas volume are another source of deviations. The requirement of continuous readout and the small distance of 554 ns between two bunch crossings make an active gating during the course of a bunch train impossible. The particular structure of the ILC beam has also an impact on the structure of the back-drifting ions. Ions which are produced during a bunch train accumulate in a thin disc before the amplification stage. This is because of the small length of bunch train of just 727 µs. In this small period of time, ions drift only for a very short distance of $O(\text{mm})$. Hence, they stay close to the readout and form a thin disc. After the bunch train, it takes about 199 ms until the next bunch train arrives. During this interval no further secondary ions are created, as no beam interactions take place. The ion disc slowly drifts towards the cathode. It

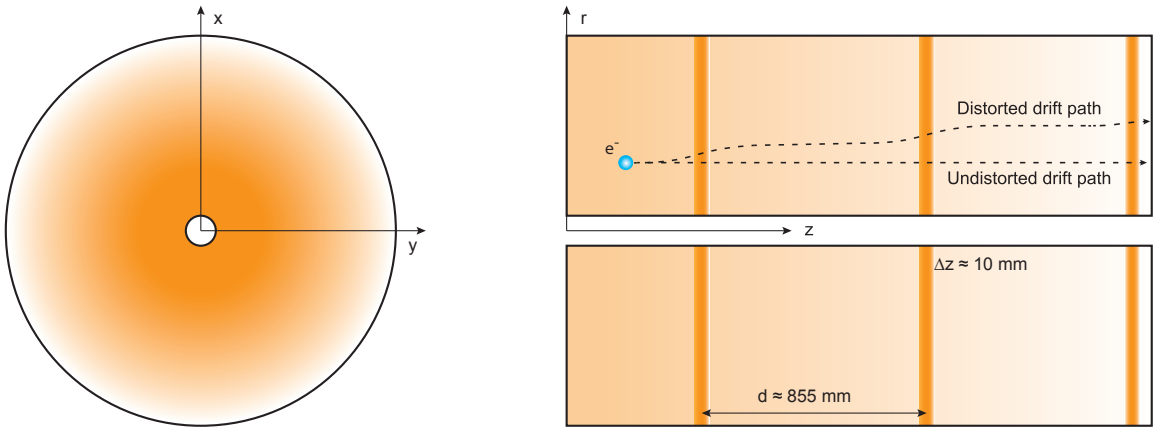

Figure 3.12: Schematic view of the effect of ion discs on the drift of electrons (not to scale). The distances given are for the T2K gas mixture (see text).

takes the discs several bunch trains to finally reach the cathode. This way it is possible for several discs to be in the volume, each separated by the distance an ion disc drifts between two bunch trains. The number of discs in the sensitive volume is determined by the ion drift velocity in the chamber gas. For gases currently considered for the ILD TPC up to three discs are possible. A schematic view of ion discs and their impact on the drifting electrons is sketched in Figure 3.12. The main contribution to the ion discs results not from physics events, but from beam induced backgrounds as described in Section 2.2.2.

While active gating during a bunch train is not possible, the drifting discs can well be gated. For this the ion gate is opened shortly before the arrival of a bunch train and closed after it. With such a gating scheme the build up of a ion disc can not be avoided, but the disc is prevented from drifting into the sensitive area. Two options for an ion gate are under consideration [106]. In any case an ion gate will be realized on a per module base and not for the whole detector. The first option follows the conventional approach by employing wire gates. Although this technology is well known because of its successful application in the past, it has to be reviewed with focus on the high magnetic field and extreme spatial resolution requirements. The second option is the use of GEMs as gating device, which is the purpose for which they have originally been proposed [107]. This approach seems to be well suited for the modular readout structure but it is difficult to operate the GEM in a way retaining a high electron transmission.

3.7 Summary

The time projection chamber is a powerful detector concept for the tracking of charged particles, as well as for the measurement of photon energies. To exploit its full potential a detailed knowledge of the single processes in a TPC is required, which are primary ionization, drift of electron and ions and gas amplification. MPGDs are the only amplification stage capable of providing the high resolution required for the ILD. Thus, its TPC will feature either Micromegas or GEMs in combination with pads or pixels. The novel technology of integrated pixel readouts is thereby the most recent readout scheme. Even though it is currently not as mature as options relying on conventional pad readouts, it offers many advantages which make it a promising option for a TPC in the environment of a future linear collider.

Chapter 4

InGrid - Pixel readout with integrated amplification stage

As already explained in Chapters 2 and 3 traditional amplification and readout schemes, as for example wires, do not meet the requirements of a tracking TPC in the environment of the ILC [102]. To reach goals for spatial, and even more important momentum resolution new readout strategies are required. Only the resolution offered by the granularity of MPGDs seems to be high enough to be adequate in such a detector. If MPGDs are employed, conventional readouts like pads or strips do not match the high granularity of the gas amplification stage, and hence, may be seen as a waste of potential. Matching the size of the readout structures to the size of the amplification stage is an obvious approach to solve this problem. As this requires a readout with the granularity in the micrometer regime pads or strips with an increased segmentation are not an option anymore, as it is virtually impossible to provide a proper routing to the readout electronics for such small pads.

The above considerations lead to the idea of combining MPGDs with a pixelized readout. The idea behind this approach is to use a chip designed for the operation with semiconductor detectors for the readout of gaseous detectors. Instead of connecting a chip to the semiconductor it is placed directly behind the amplification stage, so that its bare bump-bond pads act as charge collecting pixels, thus, providing an extremely high segmentation. The gas amplification is either performed by a GEM-stack or an integrated amplification structure on top of the chip (cf. Section 3.5.1). Efforts to realize such readouts schemes have shown great potential for both approaches [86, 108]. Key features of this readout scheme are the ability of resolving individual primary electrons and a spatial resolution very close to the diffusion limit [109, 110], which could be observed for both amplification technologies. Although not as mature as conventional pad based readout schemes, the results of pixelized readouts are promising enough to be considered for the readout of the time projection chamber of the ILD (cf. Section 3.6.2). To be used in such large scale experiments a production process is required, which is capable of providing these devices in sufficient large numbers.

This chapter deals with pixel readouts with integrated gas amplification stage and in particular with the effort to develop a fabrication process capable of providing a large number of devices per production cycle. As a basis a short overview on the used pixel chip and its properties is given in Section 4.1. Section 4.2 addresses the development of integrated pixel readouts. Starting with a description of the original single device production through to a detailed description of the large scale production on wafers. In Section 4.3 devices produced by the new fabrication method are characterized and their properties presented before the chapter is finally concluded.

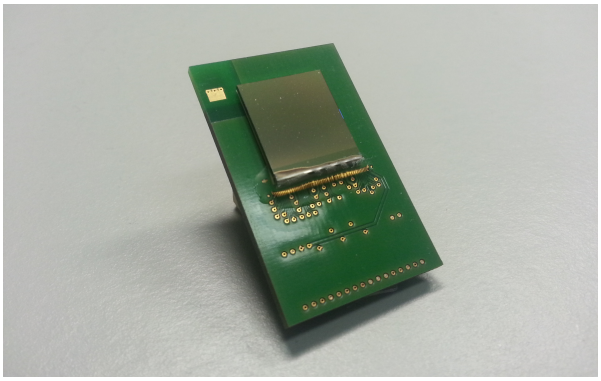

(a) Bonded Timepix chip.

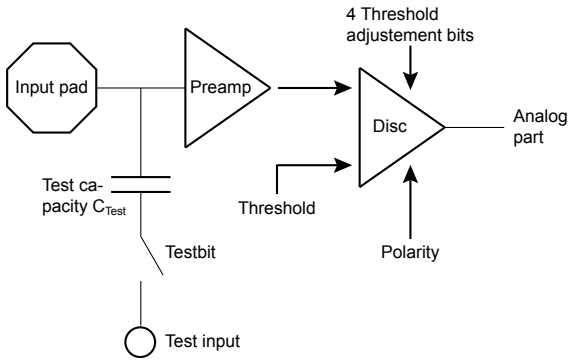

(b) Analog pixel circuitry.

Figure 4.1: The Timepix chip. Timepix mounted on a carrier board is shown in (a). The wirebonds are protected with a layer of glob-top to increase their mechanical stability and protect them from discharges. In (b) a schematic view of the analog pixel circuitry is depicted.

4.1 The Timepix chip

The chip used to provide proof of principle of the pixelized readout approach was the Medipix-2 [111]. It is not suited very well for the use in gaseous detectors, as it lacks the capability for charge as well as time measurements. To compensate for these shortcomings the Timepix chip [112], a direct descendant of the Medipix-2, has been developed. Like its predecessor, the Timepix is fabricated in 0.25 µm CMOS technology. It features an active area of $14 \times 14\,\mathrm{mm}^2$, divided in 256×256 pixels with a pitch of $55\,\mu\mathrm{m} \times 55\,\mu\mathrm{m}$ each. With dimensions of $16 \times 14\,\mathrm{mm}^2$ the chip is slightly larger than its active area alone, which is due to the space required for some peripheral electronics and to place bond pads for a connection of the chip to its carrier board. The chip can not be read out continuously, instead it is only active as long as a shutter signal is applied. The length of the shutter signal defines the time interval for which the pixels are active. It is synchronized to the clock in each pixel to avoid glitches and can be either set by the readout system, or injected by an external trigger system. The clock for the chip has to be supplied externally. Frequencies in the range of 10 MHz to 150 MHz are possible.

Figure 4.1a shows a photograph of the a Timepix chip mounted on a carrier board. The bond wires are protected with a layer of glob-top to protect them from discharges and provide additional mechanical stability. During operation the power consumption and dissipated heat of the chip is less than 1 W. The pixels are equipped with charge sensitive amplifier, discriminator and a 14-bit counting logic each and are capable of detecting either positive or negative charges. A sketch of the analog part incorporated in each pixel is depicted in Figure 4.1b and a detailed discussion of the pixel circuitry can be found in Reference [113]. The pixels can be set individually to one of four modes:

- **Time over threshold (ToT):** A pixel in this mode measures the amount of charge induced on it. When a charge signal above the threshold is detected the pixel starts counting. Its counter is incremented with each clock cycle. The counting stops as soon as the signal drops below the threshold. The number of counted clock cycles is related to the amount of charge gathered and can be translated into charge value if a calibration of the ToT-values has been performed, as described in Section 4.1.1. In case of several charge depositions being detected during a single shutter period the resulting charges are added up, as the chip can not distinguish between consecutive hits.

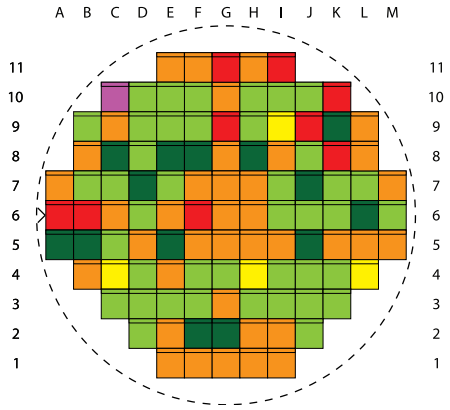

Class	Properties	Color
A	No dead columns	
B	One dead column	
C	Two dead columns	
D	More than two dead columns	
E	Broken DACs	
F	Bad digital test	
-	Not functional	

Figure 4.2 & Table 4.1: Probing results of a Timepix wafer. The chips are categorized according to their functionality as listed in the table.

- **Time of arrival (ToA):** As implied by its name this mode is intended for drift time measurements. Counting starts on the detection of an input signal. The counter is increased on each clock cycle until the shutter is closed. As clock frequency and shutter length are known the drift time of the detected charge can be calculated from the counted clock cycles by the relation

$$ToA = t_{\text{Shutter}} - \frac{n}{f_{\text{Clock}}}, \tag{4.1}$$

  with the length of the shutter signal, t_{Shutter}, the number of counted clock cycles, n, and the clock frequency, f_{Clock}.

- **Medipix:** In this mode the counter is incremented each time a charge surpassing the threshold is detected while the shutter is open. This mode is called Medipix mode, because this is the main mode of operation of the Medipix and Medipix-2 chips in photon counting applications. It is the only mode capable of detecting multiple hits during a single shutter period.

- **One hit:** This mode is mainly useful for testing applications. It measures whether a pixel has detected charge or not. While the chip is active the counter is set to one, once a charge signal above the threshold is detected. Further signals are ignored.

Obviously, the mode of a pixel has to be chosen according to the chip's application. Medipix-mode and one-hit-mode are usually of no interest for the application in drift detectors. For photon detection it is most advisable to put all pixels into the ToT-mode, while an alternating pattern of ToT and ToA has been proven to be a good setup if the chip is used as readout in a GEM TPC [110]. If InGrids are used for the readout all pixels should be set to ToA-mode in order to measure the arrival times of the detected electrons.

Timepix chips are produced on 8″-wafers, with each wafer yielding 107 chips. After the production they are probed and tested for some basic functionality, like their controlling DACs (Digital to Analog Converter) and the digital part of the pixels. Based on the results of the probing they are classified into categories ranging from A to F. Table 4.1 gives an overview on what is expected to work for chips from the different quality classes. Figure 4.2 depicts the probing results for a Timepix wafer. Each chip can be identified by its column letter and row number.

4.1.1 Calibration

For an optimal performance the Timepix chip has to be calibrated. To this end, three calibration methods are available, each of them optimizing different properties of the chip. The main calibration procedures are:

- Threshold equalization,
- Charge calibration, and
- Time walk compensation.

Although the threshold equalization is actually no calibration, but an adjustment procedure. For the testing of InGrids produced on wafer scale only threshold equalization and charge calibration are of relevance, as no time measurements are performed (see. Section 4.3). For this reason, only those two methods are summarized in this section. A detailed description of the time walk compensation is given in Reference [114].

Threshold equalization

The threshold which has to be exceeded for a pixel to be activated has to be set globally for the whole chip. Due to variations of the production process the individual pixels do not respond homogeneously throughout the chip. That means that the effective threshold differs from pixel to pixel for the same threshold value, a phenomenon known as threshold dispersion. This has been accommodated for in the design of the chip by implementing an adjustment mechanism.

A so called pixel configuration register (PCR), is included in the digital part of each pixel. Four bits of this register are reserved to store threshold equalization values. To determine these adjustment values a reference signal of constant height is required. In addition to the possibility to inject such a signal via the test pulse capacity with an external pulse generator, the noise threshold can be used. At first the adjustment bits of each pixel are set to zero and the threshold value is gradually lowered. The threshold value at which a pixel is activated is registered and the pixel is masked for the remaining steps. This is done until all pixels have been activated, whereby the number of pixels firing at a threshold value is filled into a histogram which yields a GAUSSIAN distribution. The whole process is repeated with the adjustment bits set to their maximum value of 15.

The width of the two distributions corresponds to the threshold dispersion on the chip without equalization. To improve on that the total threshold for the whole chip is chosen to be in the middle between the mean values of the two distributions. Each pixel is then adjusted to this value, by linearly interpolating between the minimum value and the maximum value obtained from the previous measurements, so that it is as close as possible to the total threshold.

The results of the equalization procedure can be seen in Figure 4.3a. The green distribution shows the threshold dispersion for all adjustment bits set to 0 and the red one for all bits set to 15. The dispersion after equalization, as shown by the red distribution, is much reduced.

Charge calibration

As explained above the ToT-mode is used for charge measurements. A calibration of the used chip is required to relate the measured ToT-values with a physical charge value. The charge calibration of a Timepix is described in References [115, 116].

To calibrate the ToT-response of a Timepix chip, negative charge is injected into the pixels. This can be done by a dedicated test capacity C_{Test} of 8 fF, incorporated in each pixel (cf. Figure 4.1b). By

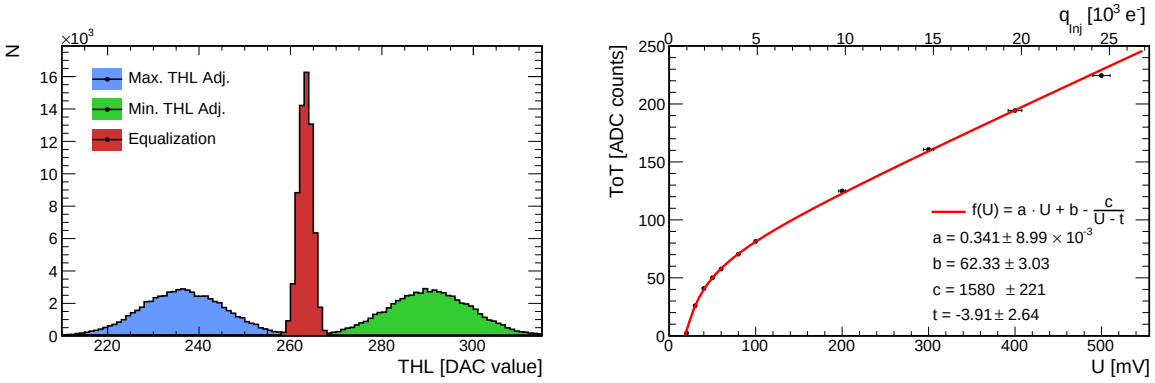

(a) Threshold equalization

(b) ToT-calibration

Figure 4.3: Calibration of the Timepix. Threshold equalization (a) and charge calibration (b) as they have been performed for the chip G02-W0056.

applying a voltage step, U, to the test capacity a well defined amount of charge, q_{Inj}, is injected into the pixel, which can be described by the equation

$$q_{\text{Inj}} = C_{\text{Test}} \cdot U. \tag{4.2}$$

A positive gradient of the voltage step results in the injection of a positive charge while a negative gradient injects a negative charge. To guarantee a maximum of accuracy rising edge and falling edge of the voltage step should be as short as possible, i.e. smaller than the 150 ns peaking time of the charge sensitive amplifier of the pixel.

For the calibration a test-pulse with a very slow rise of 1.5 µs and steep falling edge of 5 ns is applied in order to inject a negative amount of charge. By averaging over multiple charge injections the influence of electronic noise can be reduced significantly. Figure 4.3b depict this relation for several input voltages in the range from 20 mV to 500 mV. The dependency of the measured ToT-counts on the injected charge is not linear for small input values. The surrogate function

$$ToT\,(U) = a \cdot U + b - \frac{c}{U - t}, \tag{4.3}$$

in which a, b, c and t act as free parameters describes the relation between charge and ToT-counts well. An example of (4.3) is depicted in Figure 4.3b. Inserting (4.2) and solving for q_{Inj} yields

$$q_{\text{Inj}}\,(ToT) = C_{\text{Test}} \cdot \frac{(ToT + ta - b) \pm \sqrt{(ta + b - ToT)^2 + 4ac}}{2a}, \tag{4.4}$$

which is used for data calibration, whereby the second solution, $(-\sqrt{(\dots)})$, is discarded for not being physical.

The uncertainty on the determination of the free parameters in Equation (4.3) are rather large, so that the conversion of ToT-values into physical amounts of charges is not very precise and yields only the correct order of magnitude. This is in particular true for the determination of the detection threshold, which can be determined with a much higher precision by a so-called S-curve measurements as elaborated in Reference [117].

4.1.2 Outlook: Timepix-3

The Timepix chip has been designed to be applicable as readout for semiconductor detectors and gas-filled detectors. It cannot measure time and charge simultaneously in one pixel which is serious constraint, especially regarding the use in a tracking detector. But there is more room for improvement. The readout of an event requires the readout of the whole chip regardless of how many pixels have been activated. This introduces a considerable amount of dead time. To improve on this, a successor has been developed. The Timepix-3 overcomes these shortcomings and provides some additional functionality [118, 119].

Similar to its predecessor, the Timepix-3 features a 256×256 pixel matrix, with a pitch of 55 µm. The pixels can be arranged in so-called super pixels composed of 4×2 normal pixels. The pixels are designed to provide high resolution time measurements by a dedicated fast clock of 640 MHz per super pixel. Further features are the capability of a continuous and triggerless readout, the low threshold (about 500 electrons) and the possibility of measuring positive and negative charges. However, one of its most important improvement with respect to its predecessor is its ability to measure charge and time in each pixel at the same time.

The design phase of the Timepix-3 has just been finished and sample chips are currently tested and characterized, so that larger quantities will be available soon.

4.2 InGrid production on 8″-Timepix wafers

The concept of integrated pixel readouts has already been introduced in Section 3.5.1. A disadvantage of pixel chips is that a single chip covers only a small area. In case of the Timepix chip the active area is $1.4 \times 1.4\,\mathrm{cm}^2$. This means that for the application in large experiments many chips are required. The readout area of the ILD-TPC is of a size of nearly $9\,\mathrm{m}^2$ which would require about 45 000 chips for a total coverage with InGrid devices.

The original production procedure takes a lot of time and is therefore not applicable for the fabrication of large quantities as they are required for their application in large experiments. Although not suitable for mass production, the original single chip production process acts as starting point for the development of a large scale process. Therefore, the single device process is briefly summarized below, before the production process on 8″-wafers is introduced.

4.2.1 Single device production

Since their invention the production process for single devices has been optimized and applied to the simultaneous production of up to nine chips [63, 120–122]. This effort led to a process which continuously yielded functional devices of very high quality. The general production process can be divided into seven individual steps which are sketched in Figure 4.4.

1. The process begins with a bare Timepix chip. The chip is covered by a passivation layer in which the pixels appear as hexagonal openings. The first step is to clean the chip. This is done to remove any impurities resulting from packaging, storage or transportation of the wafer.

2. To shield the chip from discharges a protection layer of silicon nitride (Si_xN_y) is added on top of the chip. The thickness of this layer can vary, where values from 4 µm to 8 µm seem to be sufficient to quench most sparks [123]. The technology typically employed for the deposition of Si_xN_y is low pressure chemical vapor deposition (LPVD) which creates low stress layers with very good film qualities at temperatures in the range of 700 °C to 900 °C. For the post-processing of

Timepix chips this method is not an option, as the chips can not withstand such high temperatures. An alternative process relies on plasma enhanced chemical vapor deposition (PECVD) which allows the deposition at much lower temperatures and is therefore compatible with CMOS post-processing. With PECVD it is possible to create low stress layers at temperatures as low as 300 °C [124]. The deposition is done in multiple steps. This limits the time interval for which the chips are exposed to high temperatures and prevent them from overheating. One such run takes approximately 30 min during which 2 µm of material is deposited. Hence, the procedure has to be repeated 2 to 4 times to create protection layers with a total thickness of 4 µm to 8 µm.

3. In this step spin coating is used to apply a 50 µm thin layer of SU-8, a negative photoresist, onto the chip. This is the layer from which the grid supporting pillars will be formed. Spin coating is a standard technique for planar structuring. It is very precise and allows to deposit SU-8 at thicknesses in the range of 1 µm to 200 µm with a precision of up to 1 %. After the spin coating, the wafer is baked at a moderate temperature to evaporate excessive material.

   The deposition of a metal on top of unexposed SU-8 can cause the top layer of the resist to cross-link. Therefore, an additional 2 µm thick layer of a positive resist (OiR 907-17) is added. The purpose of this layer is to absorb most of the energy set free during the deposition of the aluminum and, thus, prevents the SU-8 from cross-linking. Even exposed OiR 907-17 can be easily removed by standard cleaners like acetone and isopropanol.

4. Now the pillars are structured. As the SU-8 is a negative photoresist, only the parts exposed to ultraviolet light become insoluble. This way, well defined pillars remain after the development and cleaning of the resist. These pillars typically have a diameter of 30 µm and are located between the pixels with a pitch of 110 µm, which is between every second pixel. Thus, no dead areas are created. In addition to the formation of the pillars this step is also used to form supporting dikes at the edges of the active area.

   Being a positive tone, the OiR 907-17 can be exposed together with the SU-8. Developing the positive resist afterwards leaves just the area above the unexposed SU-8 covered.

5. A layer of aluminum is sputtered onto the undeveloped SU-8. This layer is intended to form the amplification grid once it has been patterned. The deposition is performed in several runs to avoid an overheating of the underlying photoresists and prevent cross-linking. A layer 100 nm is added per run until the final thickness of 1 µm has been reached.

6. To be capable of acting as amplification grid the aluminum has to have holes through which the drifting electrons can enter the amplification region. These holes are patterned into the aluminum, by wet etching. For the etching a solution phosphoric acid is used. It has been found that diameters of 30 µm to 40 µm are a good choice for the size of the holes [63].

7. The last step is the development of the SU-8. For this purpose the device is bathed several times in a solution of acetone and water. The fraction of acetone is gradually increased for each bath. Afterwards the dissolved SU-8 is rinsed out of the grid holes with isopropanol and acetone.

The production process is very complex and the steps described above are only a summary of the most important processing steps of the fabrication. More details on the used photolithographic processes can be found in [125, 126]. This fabrication process works reliable for the production of single chips and has been successfully applied to the simultaneous production of up to nine chips. For several reasons the process does not scale very well and has to be modified to be applicable on wafers.

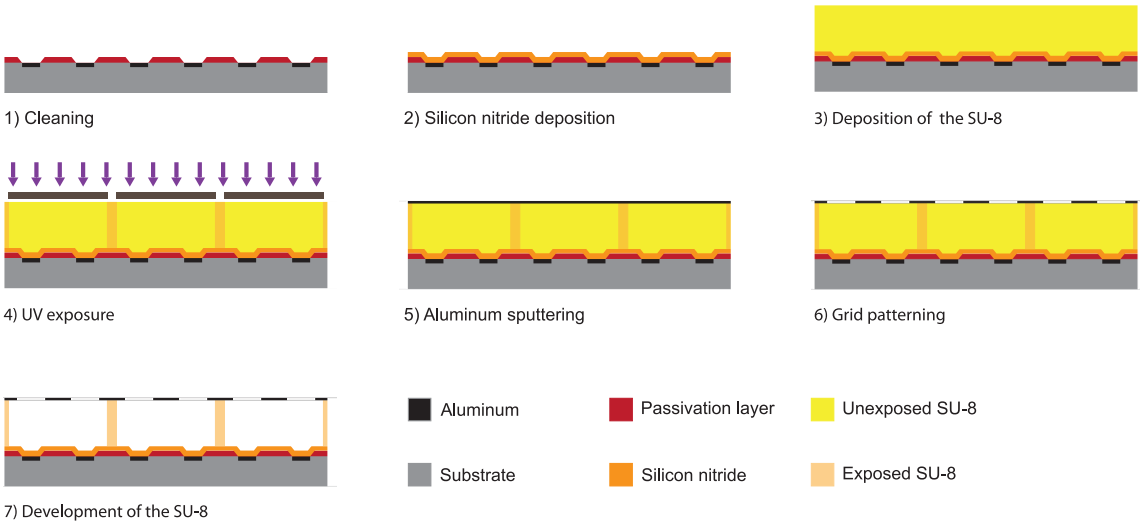

Figure 4.4: Scheme of the fabrication of InGrids on a Timepix chip by means of photolithographic wafer post-processing.

4.2.2 Wafer-scale production

To obtain a fabrication process which yields a large number of devices the single device process is transferred to the production on 8″-wafers. While similar to the production of single devices, the larger scale of the fabrication introduces new challenges which have to be dealt with.

Preparation of the wafer

The first step for the production of InGrids on wafers is the probing of the chips. This is done to assess the quality of the chips. This allows to determine whether the chips are damaged by the post-processing of the wafer, as probing results form before and after the post-processing can be compared with each other. In addition to the probing the wafer is visually inspected and a detailed map of all the surface defects is created. Afterwards, the wafer is cleaned by bathing it in acetone and isopropanol. If the level of impurities attached to the wafer is high, it is additionally cleaned with a high pressure water jet.

Silicon nitride deposition

The formation of a protection layer is a particular challenge when transferring the production from a single chips to a whole wafer. A major problem when adding the layer is to apply it to selected areas of the wafer surface only. Si_xN_y is no photolithographic material which makes it hard to apply it selectively. Especially the bond pads, by which a connection from the chip to its carrier board is made, have to stay free of silicon nitride. Otherwise wire bonding becomes impossible as the Si_xN_y is impenetrable for the wires and too hard and robust to scratch it off effectively. Thus, it is important to have a method to mask the bond pads, so that they remain free of material.

The process for single device production relies on metal masks to keep the bond pads free of Si_xN_y. Up to nine chips are fixed in a metal frame, covering their inactive area as depicted in Figure 4.5a. The same approach has been tried for the large scale production (cf. Figure 4.5b) but without success.

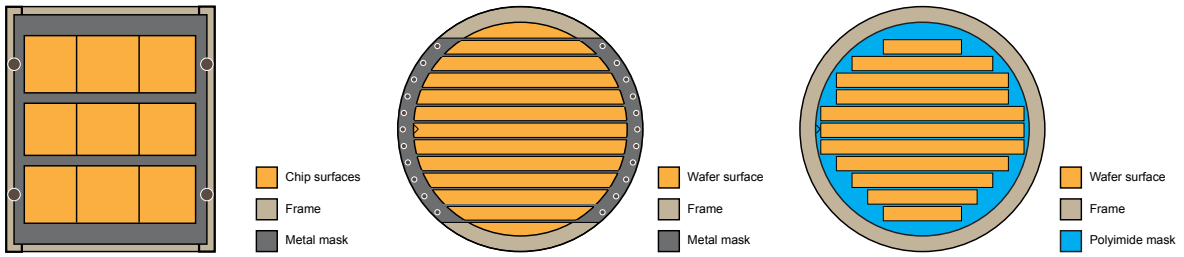

(a) 3 × 3 Metal mask (b) Metal mask (c) Polyimide mask

Figure 4.5: Different masks for the protection of the bond pads during the Si_xN_y-deposition. The 3 × 3 is used in the original production process to protect up to nine chips. The metal mask (b) and polyimide mask (c) have been tested for the application on a 8″-wafer. The sketches are not to scale.

The Si_xN_y deposition is done by PECVD, a technique which has to be performed at temperatures of about 300 °C. While this is of no concern on small scales, larger metal masks are more sensitive to high temperature. Metal has a larger coefficient of thermal expansion than silicon (16.5×10^{-6} K for copper in contrast to 2.6×10^{-6} K for silicon). Thus, the expansion of the metal mask and the expansion of the silicon wafer due to thermal induced stress are very different. Consequently, the stripes of the mask are bend more and part of the underlying bond pads are revealed and consequently coated by Si_xN_y. It is also next to impossible predict the thermal deformation as the head development due to the PECVD is not equally distributed across the wafer. Moreover, the situation is aggravated by alignment problems which always apply for rigid masks. For this reasons, metal masks are not an option.

A silicon mask made from a plane silicon wafer, was another option considered. The idea behind this approach was to use a mask made of the same material as the wafer. In this case, mask and wafer have the same coefficient of thermal expansion and should expand similarly when heated. Tests with a mask cut from a bare silicon wafer have shown that such masks are very brittle which makes their handling very difficult. The long strips, which cover the bond pads, are easily twisted during the cutting of the mask. This results in a poor coverage of the bond pads and may result in the overdeposition of the Si_xN_y.

The effects of overdeposition are illustrated in Figure 4.6a which depicts a microscope photograph of bond pads covered with Si_xN_y. The pads on the right hand side of the picture look golden, as the uncovered aluminum pads reflect the light of the microscope. This means that the masking has worked for them and they are free of Si_xN_y. In contrast, the pads on the bottom row of the chip are completely covered which is indicated by their brown color.

The tests with shadow masks made of aluminum or silicon finally led to the conclusion that the usage of a rigid mask should be abandoned in favor of a photolithographic approach. The final solution is the usage of a polyimide material (HD-4100 by HD MicroSystems™). The used polyimide is a photodefinable negative tone, which is applied in an approximately 25 µm thick layer by the means of spin coating. After a short period of soft baking in order to evaporate any residual solvent, the polyimide is briefly exposed to UV-light and baked. Time and temperature of the post-exposure baking are chosen in such a way that only a fraction of the exposed material polymerizes. Developing the unexposed polyimide afterwards yields a mask which only covers the insensitive areas of the chip, as sketched in Figure 4.5c. With the mask in place the Si_xN_y is deposited by PECVD, coating the whole surface of the wafer. Thereby, the temperature is controlled to not exceed 300 K to prevent further cross-linking of the polyimide mask. Thus, the deposition is performed in multiple steps similar to the single device

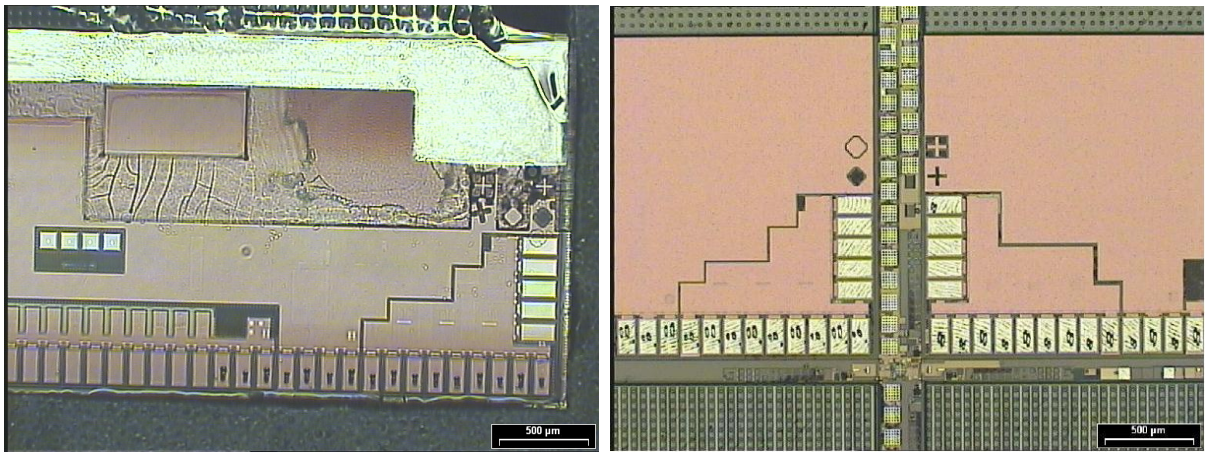

(a) Covered bond pads. (b) Clean bond pads.

Figure 4.6: Masking of the bond pads. The two microscope pictures show the bond pads of Timepix ship. In (a) most of the pads are covered by Si_xN_y, while the pads in (b) are free of any coating.

production. The next step is the removal of the polyimide mask. Uncovering the protected areas is difficult, as polymerized polyimide is not supposed to be removable. But if the polyimide is not fully cross-linked it can be activated and dissolved. For this reason it is so important to keep the temperature below 300 K during the post-exposure baking and the deposition of the Si_xN_y. For the activation fuming nitrogen acid is used, in which the wafer is bathed for about 10 h. After its activation the polyimide can be removed like the unexposed material. Figure 4.6b shows a photograph of bond pads which have been protected by a polyimide mask during the Si_xN_y deposition. It can be seen that the pads are completely free of any coating. The scratch marks on the pads are not caused by the removal of the polyimide but result from the probing before the post-processing of the wafer.

Deposition of the SU-8 and creation of the aluminum grid

With the protection layer in place the next step is the deposition of the SU-8, which will later form the grid supporting pillars. The deposition is done in the same way as in the production of single devices. By spin coating a layer with a thickness of 50 µm is deposited. After a short period of soft-baking, which removes any residual material, the SU-8 is exposed through a mask to ultraviolet light. Where exposed, the SU-8 cross-links, and thereby forms the pillars. An additional layer of OiR 907-17 is thereby added in the same way as in the original production process.

After the SU-8 layer has been deposited the grid is created. The aluminum layer is added by the means of sputtering. The process has to be repeated several times until the total thickness of about 800 nm is reached. In each run a layer of 40 nm thickness is deposited, before a cooling interval. The whole procedure takes about 1 h in modern machines. For older models the procedure is much more time consuming, as the wafer has to be manually removed after each run.

After the aluminum has been deposited, holes are added above the pixels by wet-etching, just as for the single device production.

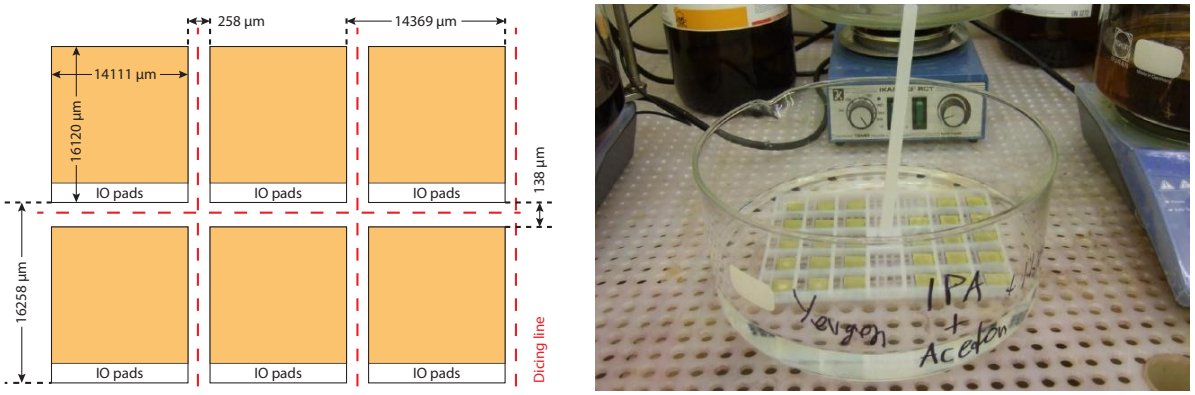

(a) Dicing lines on a Timepix wafer.

(b) Final development of multiple devices.

Figure 4.7: Dicing and final development. A sketch of the dicing lines on a Timepix wafer (a) and a photograph of the simultaneous development of 29 devices in a common bath (b).

Wafer dicing and final development

The dicing of the wafer is the next processing step to be performed. The wafer is divided into single chips by saw dicing. This method induces a considerable amount tensile force in the wafer. Furthermore, the dicing saw has to be cooled with a water jet. For this reasons, the dicing has to be performed before the final development of the SU-8. Otherwise, the dicing would easily destroy the fragile amplification structure as the dicing lines run closely along the edges of the chips (cf. Figure 4.7a). Before the development the grid still rests on a solid layer of SU-8 which provides sufficient mechanical stability to withstand the forces exerted by the dicing saw and the water jet.

The final development and rinsing of the SU-8 can be done for multiple devices in parallel as it is mainly done by bathing the devices in different solvents. For this it is not necessary to have the devices in any way aligned. A photograph of the cleaning of several Timepix InGrids is shown in Figure 4.7b. The devices are bathed in solvents made from acetone, isopropanol and water, whereby the admixture of water is gradually decreased. A remover, Microstrip 6001, is used afterwards to cleanse the device of any residuals of partially cross-linked SU-8. After last baths in pure isopropanol and acetone the InGrids are dried in the clean air of a clean room. Finally, oxygen plasma cleaning is applied to remove the last residuals and impurities on the grid. The final development may even be performed a long time after the dicing. This is of advantage, as it allows to store the devices in a mechanical robust state until they are put to use. The success of this process is crucial for the quality of the produced devices. Unexposed SU-8 which has not been removed from under grid can introduce dead or unresponsive areas on the chip. The remaining material can prevent electrons from reaching the pixels underneath. Therefore, this issue is addressed in Section 4.3.3 where occupancy and active area are examined.

4.3 Characteristics of InGrids produced on wafer scale

Transferring the fabrication of single devices to wafer scale production can only be regarded as success if devices created by the latter process are of the same quality as devices from the original one. Thus, the performance of devices from both processes have to be compared with each other. For the application in a time projection chamber at the ILC it would be best to do this by comparing track measurements. With testbeam measurements this takes a lot of time even for a single InGrid chip. Nevertheless a comparison

Chip	Class	Prod. cycle	Measurements					
			Geometry	Active area	Efficiency	Energy resolution	Gain	Resistivity
F11-W0011	A	1	x	-	-	-	-	-
K07-W0057	A	2	x	x	-	x	-	-
J07-W0057	A	2	x	-	-	-	-	-
G02-W0056	B	3	-	x	x	x	x	x
F02-W0056	B	3	x	x	x	x	x	x
H04-W0056	C	3	x	x	x	x	x	x
L04-W0056	C	3	-	x	-	-	-	x
G06-W0056	D	3	x	-	-	-	-	-

Table 4.2: Overview of the performed measurements.

of the devices can also be done by comparing the experimental data of X-ray measurements. A source indicating the performance of InGrids in this kind of measurements is Reference [127], which presents an application in the environment of the CAST[1] experiment. If the performance in X-ray measurements is the similar for InGrids from both production processes, there is no reason for their tracking capabilities to be different.

Several runs of production on full 8″-wafers have been performed. For this thesis Timepix-InGrids from the first three production cycles are examined. The performed tests include an optical inspection of the devices and measurements with a radioactive source. The optical inspection is discussed first. After this, the experimental setup used for the measurements is described, before energy resolution, detection efficiency, amplification properties, active region and discharge resistivity of the devices are discussed. An overview of the measurements conducted for the individual chips originating from the three production cycles is given in Table 4.2.

As indicated in the Table 4.2, the performed measurements differ for the three production cycles. Only geometric parameters are examined for the first run. This is for two reasons. First, most chips have at least part of their bond pads covered with Si_xN_y, as a shadow mask made of copper has been used to keep them free (cf. Section 4.2.2). This resulted in most of the chips being not bondable. Second, the solvent used to rinse the SU-8 reacted with the protection layer. This caused a irregular swelling of this layer, deforming the whole amplification structure. The deformations make a controlled, homogeneous gas amplification impossible. The second and third runs of fabrication yielded functional devices, whose geometry, active region, detection efficiency, energy resolution and amplification behavior, have been studied. Tests of spark resistivity have been added to the measurement program for the third production cycle, as devices from the second run have been found to be very vulnerable to discharges.

The experimental setup used for all X-ray measurements is described in Section 4.3.2. The measurements were performed with ^{55}Fe as radioactive source at various grid voltages. The voltage has been raised from 310 V to 390 V in steps of 10 V. 10 000 to 15 000 events have been measured for each grid voltage. An additional data set of roughly 1 500 000 events has been measured with G02-W0056 from the third production cycle at a grid voltage of $U_{Grid} = 345$ V to study the homogeneity of the gas gain and peak energy resolution.

[1] CAST - CERN Axion Solar Telescope. See [128] for further information.

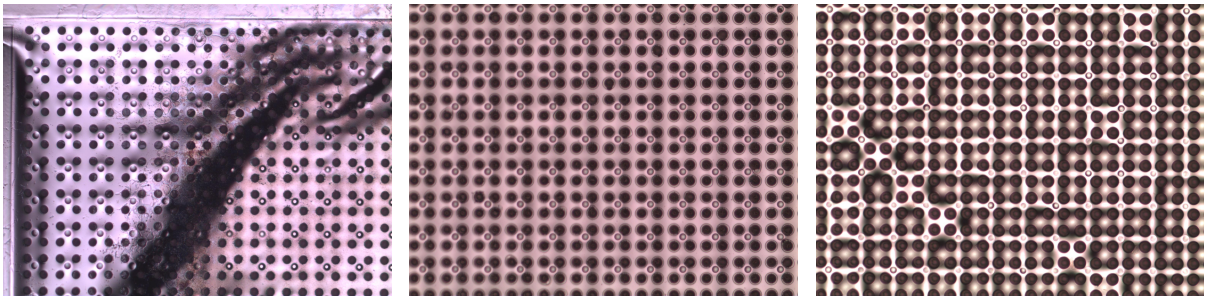

(a) First run. (b) Second run. (c) Third run.

Figure 4.8: A comparison of the grid qualities of InGrids made in the first (a), the second (b) and the third (c) production cycle.

4.3.1 Optical inspection

Uniform grids with a homogeneous surface and constant distance to the underlying pixels are required to realize a uniform gas gain throughout the active area of the chip. A first assessment of the homogeneity of the grid surface is done by optical inspection with a microscope. Figure 4.8 depicts exemplary microscope images of devices from the three production cycles. The images have been taken with the same amplification. Grid holes as well as position and diameter of the pillars are clearly visible, yet the grids look very different for each production cycle.

The grid of device F11-W0011, from the first production cycle is depicted in (a). As mentioned above, this cycle was a failure because of the swelling of the protection layer. The deformation causes the grid to bend. In the microscope image the bend regions appear as dark shadows as the light is reflected away from the lens of the microscope. The bending is particularly strong close to the corners of the device. In areas which do not suffer from the swelling of the SU-8, as seen in the lower right area of the image, the surface of the grid is flat and homogeneous. Still, the bend regions prevent a stable operation with a uniform amplification behavior.

The InGrid (K07-W0057) shown in (b) comes from the second production run. Grid holes and pillars form a regular pattern and no inhomogenieties are observed. In contrast to this, the grid of a device (F02-W0056) from the third run looks less uniform. Even though the holes and pillars are at their design position, the pattern of the surface is less regular than for the devices made in previous production cycles. At close inspection it can be seen that the pillars form a regular pattern and that the areas close to them are clearly visible. But the areas between the pillars, where the grid is not supported directly appears to be darker and out of focus. This hints at the grid in these areas being at a lower height than the grid in the vicinity of pillars. While the highly uniform grids from the second run demonstrate the ability to manufacture high quality grids also by the wafer-based production process, technical problems with the aluminum sputtering machine prevented this for devices from the third run [129]. Still, they can be operated reliably as will be shown in the following sections.

Size and geometry

The size and pitch of the holes in the amplification grid are further properties of InGrids which can be observed with an optical microscope. An image of the grid of an InGrid (F02-W0056) made in the third production cycle is shown in Figure 4.9a. The holes are well defined, appear to be perfectly circular and at a constant pixel pitch. The outline of pillars under the grid can be seen. This is because of the layer of OiR 907-17 which is added on top of the unexposed SU-8 to prevent it from cross-linking (cf.

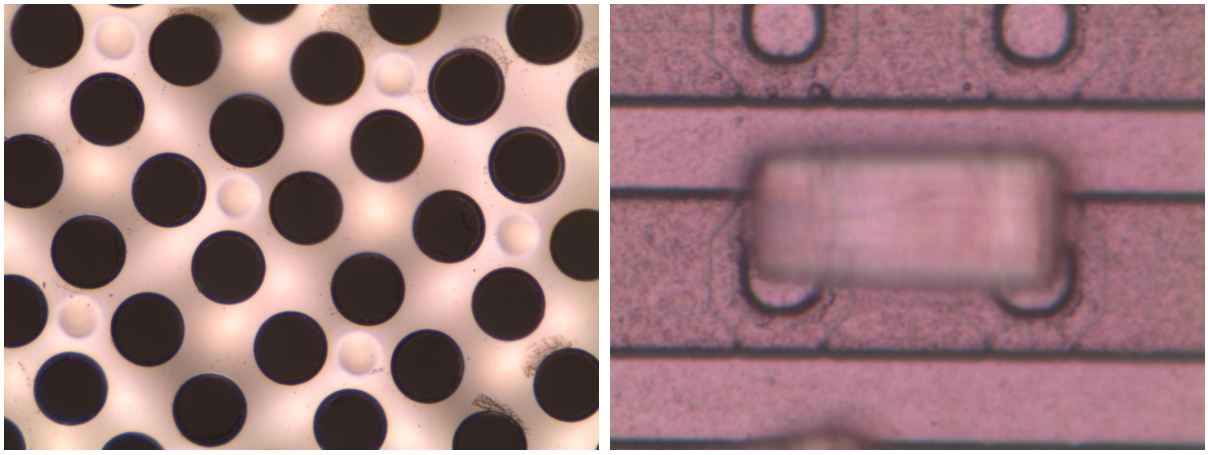

(a) Close-up of the grid surface. (b) Fallen SU-8 pillar.

Figure 4.9: Microscope images of an InGrid (F02-W0056) fabricated in the third wafer scale production run.

Section 4.2). This layer adds about 2 µm of additional height to the unexposed part of the SU-8. The difference in height is partly compensated for as exposed SU-8 expands, still the top of the pillars and the surface of the OiR 907-17 layer are not on the same level. Therefore, the pillars appear as circular dips on surface of the aluminum grid. In Figure 4.9b a close up of a lying SU-8-pillar is shown. For images like this the grid has to be damaged. This reveals the pillars beneath the grid and causes some of them to fall over. The image already hints at the height of the pillar, even without a direct measurement. The octagonal patterns in the image are outlines of the bumpbond pads of the Timepix chip. They have a pitch of exactly 55 µm (cf. Section 4.1), making it clearly visible that the height of the pillar is larger than its design value of 50 µm. Attempts to measure the height of the grid by nondestructive means, like focusing the microscope on the grid and afterwards on a pixel under a hole have a too large margin of error to be of any use [130].

The dimension of InGrids from all three wafer-based production cycles are measured with an optical microscope. The measurement system has a precision of 0.1 µm. The main difficulty is to measure along the correct axis. For the pillars this is along the cylinder axis. A small angle between both axis results in too large measurements. Another problem is apparent in Figure 4.9b. Due to its cylindrical shape, it is difficult to focus on the ends of the pillar. For the measurements of the hole and pillar diameters the situation is different. In this case, it is important to have the line of measurement aligned along a diameter of the hole/pillar, i.e. the line of measurement has run through the central point. Otherwise, the obtained values are too small. To avoid a bias by these kind of errors, the measurement are repeated several times. This means, that diameters are measured along horizontal and vertical axis independently. The measurements of the pillar height are performed from left to right (or bottom to top) and afterwards repeated from right to left (top to bottom). In each case, ten pillars/holes are measured. The final value is then given by mean value and its error by its standard deviation.

The results of these measurements are summarized in Table 4.3. Values for the pillar pitch and hole pitch are not listed as they are at their design values of 110 µm and 55 µm respectively within the limits of accuracy of the measurements. The large difference in the diameter of the holes results from a change of the design value. The intended value was 30 µm for the first two production cycle and was increased to 40 µm for the third production run. From the second run on, the measured diameters are in very good agreement with their design values. Like for the holes, the diameter of the SU-8-pillars is for all

Chip	Wafer ID	Prod. cycle	Hole diameter	Pillar height	Pillar diameter
F10-W0011	ATFWTLX	1	27.24 ± 1.47 µm	69.92 ± 2.12 µm	18.16 ± 1.14 µm
K07-W0057	EL5MX3X	2	30.37 ± 1.38 µm	69.95 ± 2.59 µm	19.58 ± 1.17 µm
F02-W0056	E85MXGX	3	40.85 ± 2.04 µm	70.07 ± 2.60 µm	20.28 ± 1.12 µm
H04-W0056	E85MXGX	3	39.86 ± 1.97 µm	70.69 ± 2.48 µm	20.31 ± 1.36 µm
G06-W0056	E85MXGX	3	39.44 ± 2.37 µm	70.74 ± 2.88 µm	20.10 ± 1.40 µm

Table 4.3: Dimensions of InGrids fabricated in different production cycles as measured with a high-resolution optical microscope. Values for pillar pitch and hole pitch are not listed, as they are in good agreement with their design values of 110 µm and 55 µm respectively.

production cycles very close to its design value of 20 µm. Given that these diameters are created using standard photolithographic techniques it is not surprising that they match their designated values. In contrast, the height of the pillars shows a larger deviation from its design value of 50 µm. This applies for all measured devices, i.e. all three production cycles. The size of the deviation is nearly the same for all devices resulting in a total pillar height of about 70 µm, which is by 40 % more than the target value. The reason for this is aged SU-8 [129]. If SU-8 is stored too long it becomes more viscous. This impacts the deposition process and results in a thicker layer if the remaining parameters are left unchanged during the spin coating.

4.3.2 Experimental setup

Starting with the second production cycle the fabrication on wafer scale yields functional InGrid devices. To test them they have been operated in a detector which is a further development of the prototype detectors described in Reference [127] and Reference [131], which have been designed for the use at the CAST experiment. It is a small drift chamber which is mostly made of acrylic glass.

On the cathode side the active volume is limited by the cathode plate which is made of copper. On the outside the copper is enclosed by a cover made of acrylic glass. The reason for this cover is to insulate the cathode to the outside, allowing for a safe handling of the detector. Furthermore, the cathode plate contains a small hole which acts as entry point for the decay products of radiative sources, which can be mounted on the outside. A collimator with a hole radius of 1 mm is used to focus the X-rays on the central region of the chip. To ensure gas tightness, the hole is covered with a thin Kapton-foil. Figure 4.10a depicts the cathode side of the detector with a source of ^{55}Fe mounted on it.

The active volume of the detector consists of a cylindrical volume with a diameter of 82 mm. The maximum drift length is defined by the height of the acrylic ring limiting the volume in the direction perpendicular to the drift field. Thus, the length of the drift field can be adjusted by exchanging the ring. The ring includes no field cage, so that the drift field is only homogeneous in central region between anode and cathode, while large field distortions are expected near to the ring. For all performed measurements presented in this thesis a ring with a height of 2 cm has been used.

The anode side of the detector is more complex than the cathode side. The gas volume of the detector is terminated by a printed circuit board. This board contains all the electronics and connectors for the connection of the chip to the readout and for the high voltage supplies of the grid and the drift field. The chip is mounted on a dedicated carrier board which is placed directly on top of the circuit board, supported by frame of acrylic glass and held in place by a plug connection (see Figure 4.10c). The top of the grid of the InGrid defines the anode plane. To increase the homogeneity of the drift field, a copper

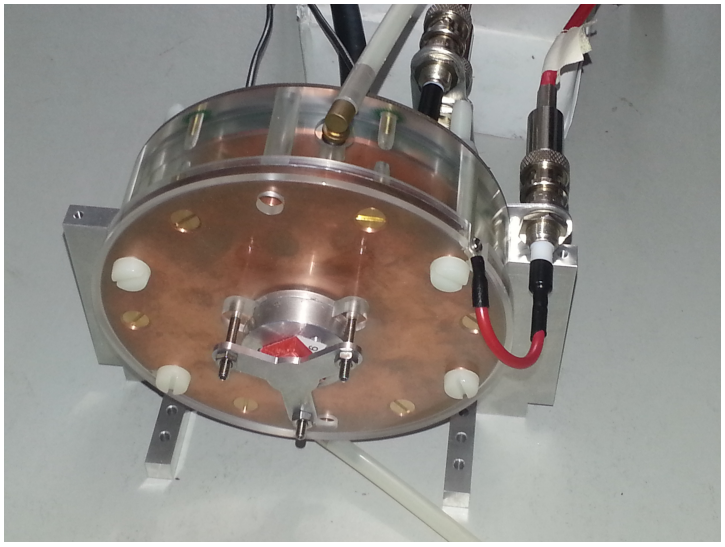

(a) Cathode side of the detector.

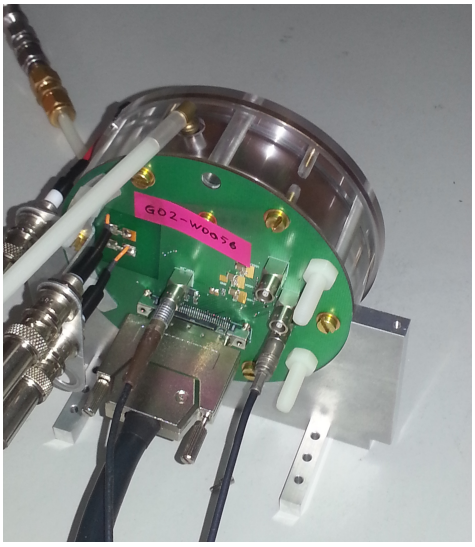

(b) Readout side of the detector.

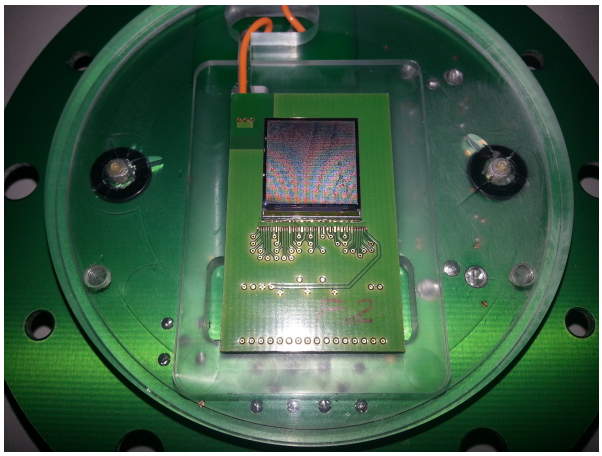

(c) Mounted Timepix chip without anode plate.

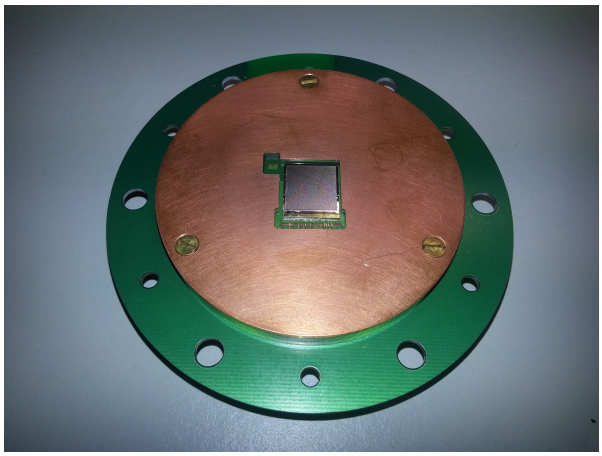

(d) Mounted Timepix chip with anode plate.

Figure 4.10: Experimental setup. Cathode side (a) and readout side (b) of the detector used for the testing of the Timepix-InGrids fabricated with the wafer scale production process. The mounted Timepix InGrid is shown without (c) and with (d) the surrounding anode plate in place.

coated PCB[2] is used as anode plate. This anode board contains a cutout for the InGrid, so that the top of the grid is on the same level as the surrounding copper surface, as depicted in Figure 4.10d. The rear side of the detector is shown on Figure 4.10b. The connectors on the left hand side are for high voltage supplies of the drift field and amplification grid while the broad connector is used for the readout of the Timepix chip.

The gas volume of the detector is constantly flushed with a gas mixture of 95 % argon and 5 % isobutane at flow rate of approximately 2 l/h. Drift velocity and transverse diffusion as a function of the electric field are shown in Figure 3.3a and Figure 3.4b respectively. The setup is not pressure stabilized which means that the pressure depends on the barometric pressure. The above flow rate ensures together

[2] PCB - Printed circuit board.

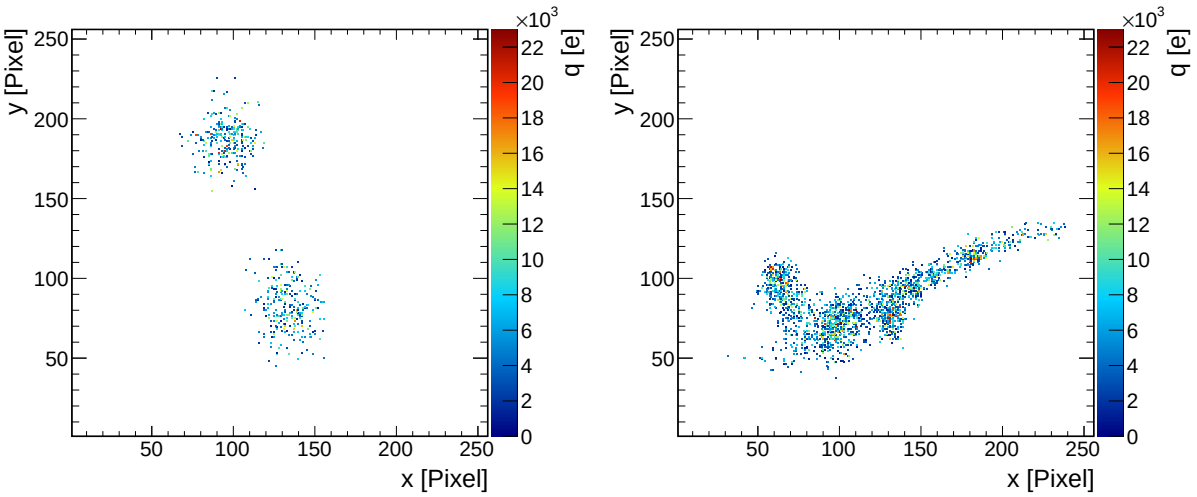

(a) Double photon event

(b) Background event

Figure 4.11: X-ray events detected with the experimental setup. A two photon event (a) and a background event (b). Each dot in the event displays represents one activated pixel.

with a 3 m exhaust pipe an overpressure of a few millibar. The temperature of the gas is determined by the environmental temperature. It is controlled for the whole laboratory and can therefore be considered to be constant in the range of ±1 K.

The drift field of the detector is set to $E_D = 225\,\mathrm{V/cm}$, which is approximately the maximum drift velocity of 41.15 mm/µs for the used gas mixture (cf. Figure 3.3a). The transverse and longitudinal diffusion at this field strength are $D_T = 475.05\,\mu\mathrm{m}/\sqrt{\mathrm{cm}}$ and $D_L = 281.92\,\mu\mathrm{m}/\sqrt{\mathrm{cm}}$ respectively.

Timepix readout

The readout of the Timepix chip is performed by the Medipix reusable readout system (MUROS) [132], version 2.1 which is connected to the chip by a low voltage differential signal (LVDS) line. The data transmission is controlled by a FPGA[3] on the board, which incorporates all the logic required to control the chip. Using the serial data interface of the chip this kind of connection requires 917 768 clock cycles for a complete readout of the pixel matrix and allows for a daisy-chained readout of up to eight chips. Communication with a PC[4] for data acquisition is achieved by a commercially available general-purpose interface card, allowing for full control of the chip by software.

The software for configuration and readout of the chip is `Pixelman` [133, 134]. The software is available in `Java` and `C++` and thereby usable on multiple operating systems. It incorporates all the functionality required for data taking and can be extended by user provided plugins. A plugin shipped with the software allows for an automatic threshold equalization in the same way as described above.

For the X-ray measurements presented below, a random shutter has been used. This means, a shutter window of fixed length is opened, as soon as the chip is ready. All the pixels are set to the ToT-mode and counting is possible for the whole shutter length. For this reason, the length of the shutter signal has to be chosen carefully, as a too long shutter window results in many events containing multiple X-ray hits, while a too short window creates a lot of dead time and a considerable amount of empty data.

[3] FPGA - Field programmable gate array, an integrated circuit which is configurable after its production.
[4] PC - Personal computer

In the presented setup a ^{55}Fe source has been used for whose activity a shutter length of 0.075 s has been found to be a good compromise between the number of empty frames and two-photon events. This resulted in a mean detection rate of one X-ray event per 15 frames. Example events measured with the presented setup are illustrated in Figure 4.11. An event with two X-ray photons (a) as well as a background event (b) are shown.

Event reconstruction

The reconstruction of the X-ray events is done with the help of the `MarlinTPC` package, which introduced in detail in Section 5. The heuristic is a modified version of the clustering technique used for cluster finding of tracks in a TPC with GEMs and a Timepix readout [110]. The new heuristic does not only look for adjacent pixels to assemble cluster, but in an adjustable square around each pixel. This way also electrons which have diffused apart by more than one pixel can be assigned to the same cluster. If the size of the square has been chosen carefully, this allows to reconstruct even multiple X-ray hits per event, provided the distance between the hits is large enough. A more detailed description of the reconstruction method can be found in Reference [127].

The characteristics of the reconstructed data samples can be improved by applying selected cuts to remove background events and reject events of poor quality [127, 135]. The only selection applied for the analyses in the following is a cut on the center of the reconstructed X-ray objects. If the central position of an reconstructed X-ray object is more than 2 mm away from the center of the pixel area it is rejected. This is done to ensure that all electrons resulting from a X-ray event are collected on the active area of the chip. Without the cut, electrons created by X-rays close to the chip edges might drift to the anode plate surrounding the chip or to insensitive areas of the dykes and thus, escape detection. Such events can bias the number of reconstructed pixels towards lower values and are therefore excluded from further analysis.

4.3.3 Active region and occupancy

An important characteristic of InGrid detectors is their active region. The more of the pixel area is sensitive to the detection of charge carriers the better. This active area of InGrids is already reduced as some pixels are covered by grid supporting dykes. The dykes are made of undeveloped SU-8 and positioned at the borders of the pixel area. They have a width of about 500 µm and provide additional support and thereby mechanical stability for the grid. The drawback is that a considerable amount of pixels is covered by solid SU-8 and therefore insensitive to arriving charge carriers. For future production cycles an improved layout is proposed which provides a considerable increase of the active area by moving the dykes partly out of the pixel area [129, 130].

Besides the insensitive areas introduced for technical reasons, it is of importance to avoid any additional dead spots. To examine to what extent the pixel area of the chip is sensitive to arriving charge carriers the occupancy of the devices is studied. To this end a two-dimensional histogram is created, resembling the pixel chip as each pixel of the chip is matched with a pixel in the histogram. Each pixel in the histogram are then filled with the number of times its equivalent on the chip has been activated.

The occupancy histograms obtained with a ^{55}Fe source at a grid voltage of 350 V are shown in Figure 4.12 for two devices from the second production cycle (a,b) and for four devices from the third run (c-f). Broken columns are masked and show therefore no entries.

The general structure of the observed occupancy is very similar for all tested devices. The position of the source above the InGrids is marked by the area of high occupancy near to the center of the chips. Towards the edges of the chip the number of hits decreases. Nearly no hits are observed close to the

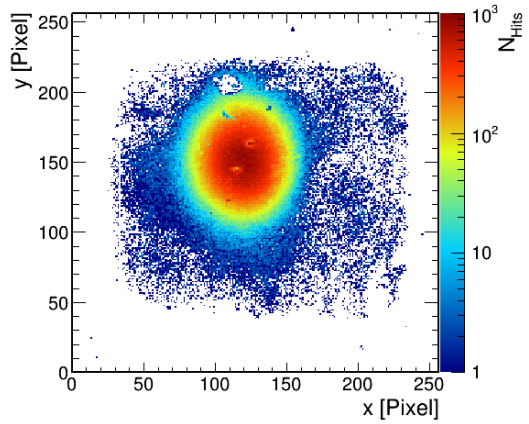

(a) K07-W0057

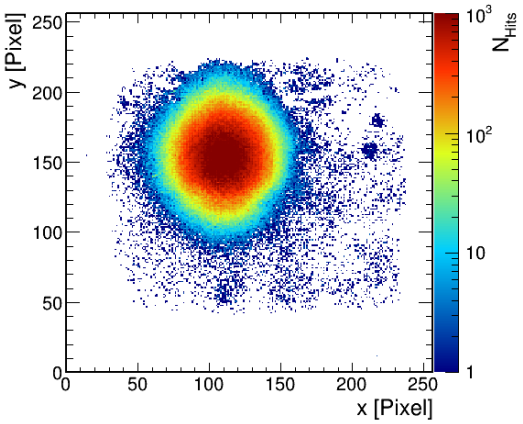

(b) J07-W0057

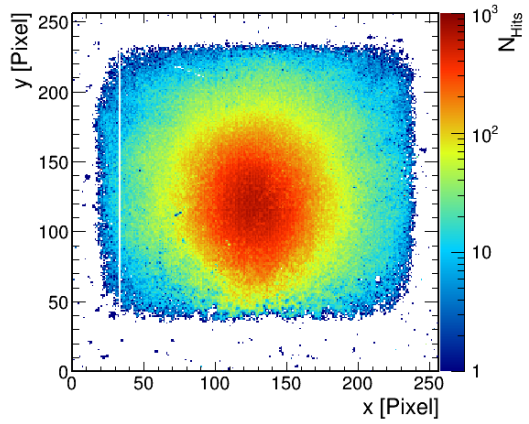

(c) G02-W0056

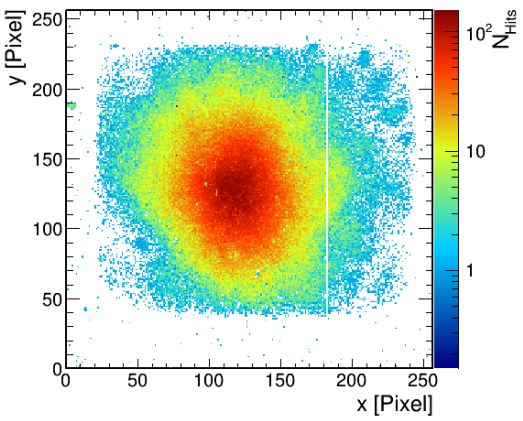

(d) F02-W0056

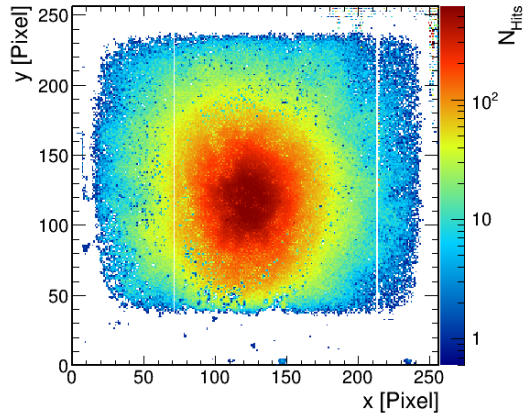

(e) H04-W0056

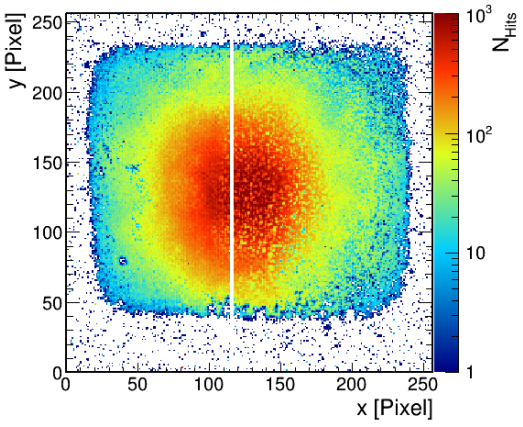

(f) L04-W0056

Figure 4.12: Occupancy plots from InGrids produced on 8″-wafers. The devices in (a) and (b) are from the second production run, while those in (c) to (f) were fabricated in the third run.

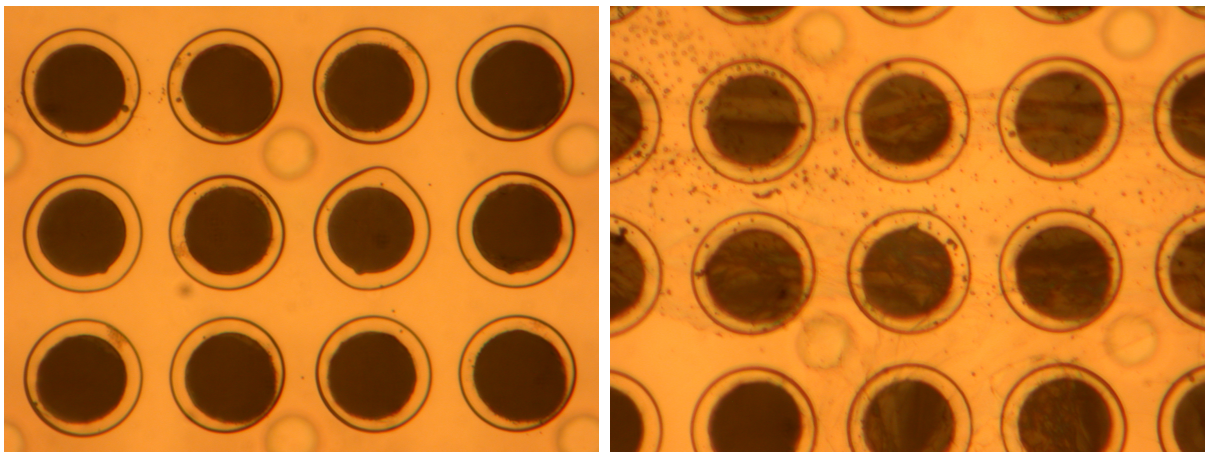

(a) Clean (b) Residuals

Figure 4.13: Microscope image of grid holes of the chip K07-W0057. In (a) an area with normal sensitivity is shown, while (b) depicts an area with reduced sensitivity.

dykes. This is caused by the detector setup. The InGrid is separated from the anode plate by a gap with the size of $\mathcal{O}$(mm) (see. Figure 4.10d). The gap is at a much lower potential than grid and anode plate, causing the field lines of the drift field to bend towards it. Electrons following these field lines end up in the gap instead of being detected close to the dykes in the outer regions of the pixel area.

Apart from this general agreement with the expectation, small areas with a reduced number of hits are observed. This is in particular conspicuous for device K07-W0057 from the second production cycle. Small spots with less occupancy than in their close proximity are present in the region of high occupancy. Additionally, a larger area where nearly no hits are detected is present in upper central region of the device. Although less distinct, the same observation can be made for all presented devices. The affected areas are much smaller for devices from the third production cycle with only single pixels being affected in some cases.

The reason for the less sensitive and unresponsive areas respectively are residuals from the final development and cleaning of the SU-8-layer (cf. Section 4.2.2). Leftovers from this last production steps can attach to the grid and influence the amplification in two different ways. The first one is apparent from Figure 5.7 which shows a cutout of the amplification grid free of any residuals (a) and one (b) with most holes completely covered by residuals. Closed grid holes can not collect electrons, which are accordingly not amplified and escape detection. This is the more severe impact leftovers can have. In the other case, pixels are not completely blocked but are less often activated than pixels in their neighborhood. This also caused by residuals attached to the amplification grid, but they do not cover or close any grid holes. Thus, it is still possible for electrons to enter the amplification region in that area. The effect of the residuals is a decreased electric field in the amplification stage. This is due to a higher relative permittivity, ϵ_r, of the leftover material compared to the gas of the detector (ϵ_r =3.2 to 4.1 for SU-8 compared to ϵ_r = 1.0 for argon). The reduced electric field results in a smaller detection efficiency due to a lower gas gain (cf. Equation 4.5 in Section 4.3.5). Hence, less hits are counted on these pixels. The effect can be verified by considering occupancy diagrams at increasing grid voltages as presented in Figure 4.14. Small spots of reduced efficiency are distributed all over the pixel area at a grid voltage of U_{Grid} = 310 V. The situation improves a lot for U_{Grid} = 340 V and even more at U_{Grid} = 370 V. Thus, it can be concluded that the unresponsive spots are indeed caused by local reductions of the electric

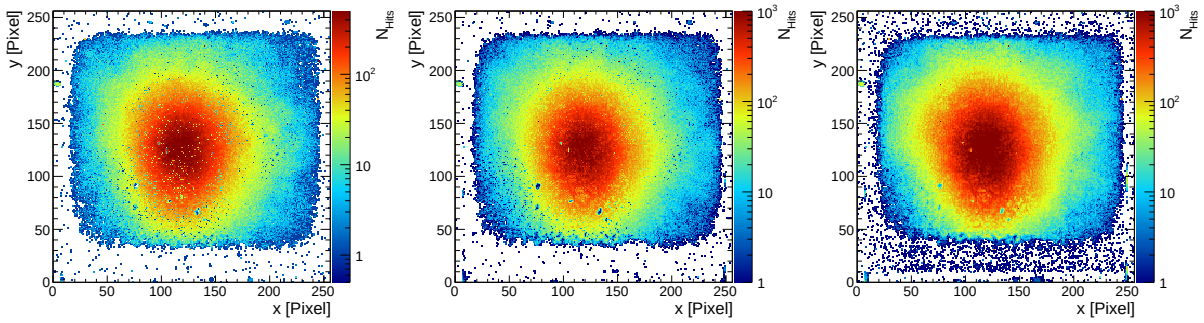

(a) U_{Grid} = 310 V (b) U_{Grid} = 340 V (c) U_{Grid} = 370 V

Figure 4.14: Occupancy of the chip F02-W0056 at three different grid voltages.

field in the amplification gap. To some extent the effect can be observed for all devices from the third production cycle. Graphs corresponding to Figure 4.14 can be found for G02-W0056 and H04-W0056 in Appendix A.2 (cf. Figure A.2 and Figure A.3 respectively).

As a consequence, the procedure for the final cleaning of InGrids fabricated on 8″-Timepix wafer has been extended by an additional cleaning procedure. The step of oxygen-plasma cleaning has been added and will be applied in future production runs (it is already included in the description of the cleaning procedure in Section 4.2.2).

4.3.4 Energy resolution

A key-figure in the context of X-ray measurements is the energy resolution. In case of an InGrid-based readout their are several possibilities of determining the energy resolution. One way is to use the number of pixels activated. This is possible as the number of electrons created by a X-ray photon is given by the energy deposited in the detector divided by the mean ionization energy in the gas. If the electrons diffuse apart and are detected on a single pixel each, counting their number is thereby equivalent to an energy measurement. Fitting a Gaussian, with width σ and central value μ, the energy resolution is given by the ratio, σ/μ. A second method uses the amount of charge detected on the pixel chip. In general this method works similar to the one relying on pixel counting, but the energy resolution is obtained from the charge spectrum. The obtainable resolution is thereby slightly worse than that of the pixel spectrum, as it is also affected by fluctuations of the amplification processes. Another method is to measure the charge signal at the amplification grid. When primary electrons are amplified in the amplification gap, the moving charge carriers induce a on the grid. This signal manifests in short pulse which can be decoupled from the otherwise constant potential of the grid with the help of a capacitor and a charge sensitive amplifier.

The first two methods are used to obtain the energy resolution for three Timepix InGrids from the third production cycle and for one from the second cycle. The resulting spectra are illustrated together in Figure 4.15a and Figure 4.15b for the pixel and charge method respectively. Device K07-W0057 from the second production run is not included in Figure 4.15b, as no ToT-calibration exists for it. The energy resolutions obtained with both methods are listed in Table 4.4 along with the charge thresholds[5] of the pixel chips.

[5] The threshold values have been calculated via Equation (4.4). The according calibration parameters can be found in Appendix A.1 (cf. Figure A.1).

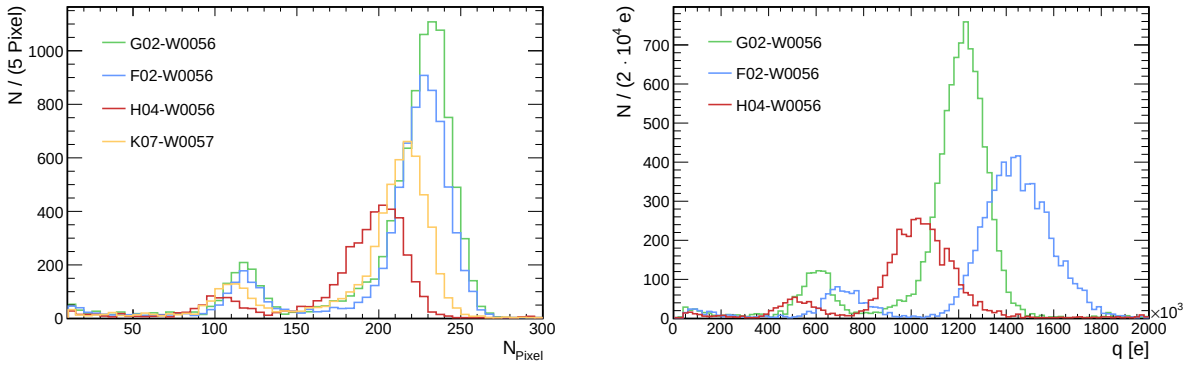

(a) Pixel spectra.

(b) Charge spectra.

Figure 4.15: Comparison of pixel spectra (a) and charge spectra (b) measured with different InGrids at a grid voltage of 350 V. Device K07-W0057 is missing in (b), as no charge calibration exists for it.

Chip	Wafer ID	Production cycle	Threshold	Energy resolution by pixels	Energy resolution by charge
K07-W0057	EL5MX3X	2	–	6.13 % ± 0.11 %	(6.87 % ± 0.10 %)
G02-W0056	E85MXGX	3	≈ 952.34 *e*	5.32 % ± 0.08 %	7.21 % ± 0.07 %
F02-W0056	E85MXGX	3	≈ 922.22 *e*	6.13 % ± 0.07 %	8.54 % ± 0.12 %
H04-W0056	E85MXGX	3	≈ 1455.22 *e*	6.67 % ± 0.15 %	10.9 % ± 0.21 %

Table 4.4: Energy resolution and charge threshold as obtained for several Timepix InGrids produced in the second and third production cycle. All measurements have been performed at a grid voltage of U_{Grid} = 350 V.

For the pixel spectra it can be observed that the position of the photopeak for the 5.7 keV line is located at about 230 pixels for devices G02-W0056 and F02-W0056 from the third production cycle. The peak measured with the devices K07-W0057 and H04-W0056 is located at smaller values of 216 and 202 respectively. For H04-W0056 this can be explained with a roughly 1.5 times higher threshold value which reduces the detection efficiency (see. Section 4.3.5 for more details on the detection efficiency of devices from the third production cycle). For K07-W0057 it is also assumed that the smaller value of the peak position is caused by a higher charge threshold without a charge calibration this can not be conclusively confirmed. The measured resolutions are very close to each other. The best and worst result are separated by 1.35 %. The worst energy resolution is obtained for H04-W0056. It is slightly higher than that of the other devices. This is according to expectation, given the high charge threshold. The high threshold results in systematically less pixels being activated and consequently in a smaller denominator when the resolution is calculated.

The charge spectra of three InGrids form the third production run are plotted in Figure 4.15b. The peaks are not centered around a common value, although the same grid voltage of U_{Grid} = 350 V has been applied in each case. For device H04-W0056 this is explained by the higher threshold. This can be confirmed by comparing the mean charge per pixel for both devices, i.e. the mean value of the charge peak (the photopeak in the charge spectrum) divided by the mean value of the pixel peak. This computes to 5148 and 5261 for H04-W0056 and G02-W0056 respectively (cf. Figure A.4 and Figure A.5). From the agreement between both values it can be concluded that the different position of the charge peaks are

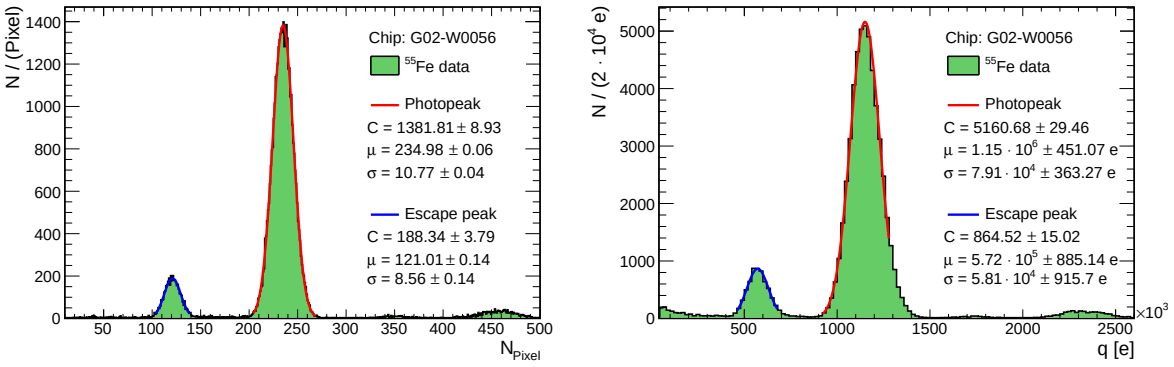

(a) Pixel spectrum

(b) Charge spectrum

Figure 4.16: Energy resolution of a chip (G02-W0056) fabricated by the wafer scale production process. Pixel spectrum (a) and charge spectrum (b), as measured with a ^{55}Fe source at a grid voltage of U_{Grid} = 345 V.

indeed caused by different threshold values. The same argument can not be used to explain the position of the charge peak for F02-W0056, as it has approximately the same charge threshold as G02-W0056. This hints at a higher gas amplification and is further addressed in Section 4.3.6.

A last observation is that the energy resolution obtained with G02-W0056 is for both methods significantly better than for F02-W0056 and H04-W0056 which also originate from the third production cycle. A possible explanation are the pixels/spots of reduced sensitivity discussed in Section 4.3.3. Pixels with a reduced detection efficiency will broaden the pixel spectrum and bias it towards lower values. As already discussed, the effect decreases for higher grid voltages. This means, that for a grid voltage of U_{Grid} = 350 V the effect is already small. Still, the gas amplification is reduced for these pixels which results in an additional broadening of the charge distributions. By comparing Figure 4.14 in Section 4.3.3 with Figures A.3 and A.2 in Appendix A.2 it becomes apparent that G02-W0056 is less affected than F02-W0056 and H04-W0056 which explains the higher energy resolution obtained with this device.

Peak performance

The values in Table 4.4 have been obtained from spectra of reconstructed X-ray events. As explained in Section 4.3.2 the only cut applied is on the position of the reconstructed photon on the pixel area. To determined the best obtainable energy resolution further event selection is required. To this end a cuts on root mean square deviation in transverse direction is applied in addition to the position cut. Only reconstructed photons with a transverse RMS between 0.5 mm and 0.8 mm are used. This ensures that only events are used for the spectra in which the electrons have diffused widely apart. This minimizes the probability of having two (or more electrons) ending up on the same pixel.

The resulting distributions measured with the Timepix InGrid G02-W0056 at a grid voltage of 345 V are depicted in Figure 4.16. Due to the much higher statistics compared to the measurements presented in Figure 4.15 the features of the distributions become much more apparent. Photopeak (PP) and escape peak (EP) are clearly distinguishable. Furthermore, a small accumulation of events at roughly twice the amount of pixels/charge in the photopeak is observed which result from double photon events. The energy resolution is determined for photopeak and escape peak which represent energies of 5.9 keV and

2.7 eV respectively. The values compute to

$$\left(\frac{\sigma}{\mu}\right)_{\mathrm{PP}} = 4.97\,\% \pm 0.3\,\% \qquad \text{and} \qquad \left(\frac{\sigma}{\mu}\right)_{\mathrm{EP}} = 8.03\,\% \pm 0.12\,\%$$

for the peaks in the pixel spectrum and to

$$\left(\frac{\sigma}{\mu}\right)_{\mathrm{PP}} = 6.88\,\% \pm 0.03\,\% \qquad \text{and} \qquad \left(\frac{\sigma}{\mu}\right)_{\mathrm{EP}} = 10.16\,\% \pm 0.16\,\%$$

for the charge spectrum. The obtained values are for both methods compatible for what has been measured with a device from the original production run (cf. Reference [136]). Hence, at least single devices made by the new production process are capable of achieving a performance similar to the one of devices created by the old method. Confirmation that the improvement is indeed the result of the cuts can be found in Appendix A.6, where the corresponding values are presented for the same conditions as used for the measurements summarized in Table 4.4.

4.3.5 Detection efficiency

The single electron detection efficiency, ϵ_D, is another important figure of merit for InGrid detectors. If an InGrid is fully efficient at detecting single electrons, each electron arriving at its amplification grid is collected in a grid hole where it is sufficiently multiplied to exceed the charge threshold of the underlying pixel. Thus, the detection efficiency strongly depends on the threshold of the pixels and the charge distribution of the amplification process. For a charge threshold t it can be calculated from the normalized gain distribution, $p(N)$, by

$$\epsilon_D = \int_t^\infty p\,(N)\,\mathrm{d}N. \tag{4.5}$$

This yields the fraction of charge distribution for which the number of electrons exceeds the threshold of the pixel. In case of InGrid detectors the charge distribution is given by Polya distribution (cf. Section 3.4), so that Equation (4.5) becomes

$$\epsilon_D = \int_t^\infty \frac{1}{\bar{N}} \frac{(\theta+1)^{\theta+1}}{\Gamma(\theta+1)} \left(\frac{N}{\bar{N}}\right)^\theta \exp\left(-(\theta+1)\frac{N}{\bar{N}}\right)\mathrm{d}N \tag{4.6}$$

where $\bar{N}$ is the mean gain, i.e. $\bar{N} = G$. Solving the integral yields

$$\epsilon_D = \frac{\Gamma\left(\theta+1, \frac{(\theta+1)t}{\bar{N}}\right)}{\Gamma\,(\theta+1)}, \tag{4.7}$$

where $\Gamma(a, z)$ denotes the incomplete gamma function[6]. Equation (4.7) depends only on the width parameter, the mean amplification and the threshold. The efficiency is plotted in Figure 4.17 as a function of the grid voltage for different values of θ (a) and for a different gas gains as a function of θ in (b). The efficiency increases for higer grid voltages, i.e. higher gains, and with higher values of the Polya width parameter θ.

The detection efficiency can be studied by comparing the number of activated pixels, N_{Pixel}, with the number of primary electrons, N_e. For measurements with a ^{55}Fe source, the latter can be calculated

[6] Incomplete gamma function: $\Gamma(a, z) = \int_z^\infty t^{a-1}\mathrm{e}^{-t}\mathrm{d}t$

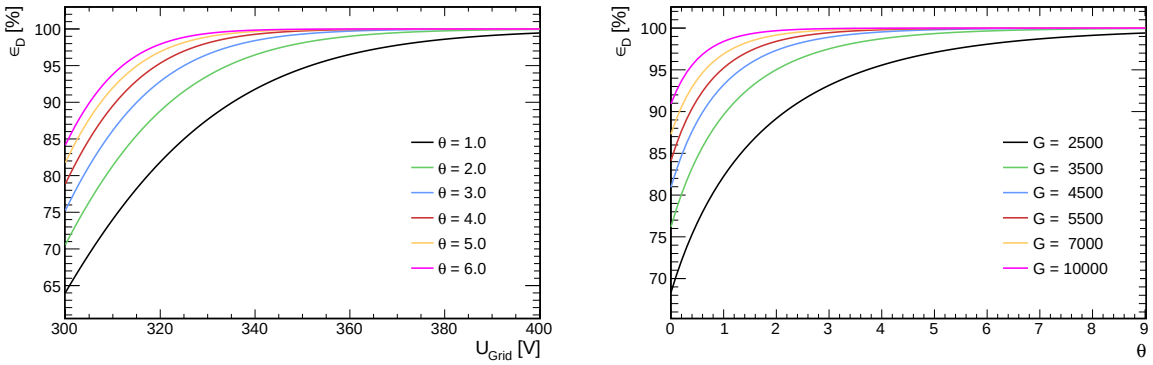

(a) (b)

Figure 4.17: Theoretical detection efficiency for a charge threshold of $t = 1000$ electrons as a function of the grid voltage (a) and as a function of θ (b).

from the energy of the photoelectron (5.9 keV) and the mean ionization energy of the gas mixture, $w_{95/5} = 26\,\text{eV}$ [44], via

$$N_\text{e} = \frac{5.9\,\text{keV}}{26\,\text{eV}} \approx 227. \tag{4.8}$$

The above number should be considered as a lower limit of the total number of electrons, as the used gas mixture of argon and isobutane (95/5) is a Penning gas for which the ionization yield is increased because of the Penning effect. The naive expectation is thereby given by the product of ϵ_D and N_e.

The number of pixels is obtained by fitting a Gaussian to the photopeak. It is plotted in Figures 4.18a to 4.18c as a function of the applied grid voltage for three Timepix InGrids of the third production cycle. The expected efficiency is added for better comparison (red broken line). It is calculated from the threshold values of the individual chips (cf. Figure A.1) and the gain curves obtained from charge-per-pixel spectra of isolated pixels only (cf. Section 4.3.6). As the width parameter of the used pixel spectra is given in ToT-counts (cf. Figure 4.20) it can not be expressed electrons and thus, not be used in the efficiency calculation. For this reason, a value of $\theta = 1$ is assumed, so that the calculated efficiency represents a lower limit of the expectation (cf. Figure 4.17a). The number of pixels, as indicated by the black squares, shows for all devices a very poor agreement with the expected behavior. N_Pixel rises continuously with increasing voltage. While it is too small for low grid voltages, it reaches the expectation value at approximately 350 V. From this point on it continues to rise in a roughly exponential manner, exceeding the expectation value by far. The reason for the large number of activated pixels at high voltages is that at high gas gains the charge from the amplification process of a single electron can be spread over multiple pixels due to the presence of the protection layer. If the amount of charge spread onto a neighboring pixel is large enough to exceed the charge threshold of that pixel, two pixels are activated instead of only one [123]. This phenomenon is more likely to occur at higher gas gains where more charge is created in the amplification processes. To correct for this, the charge asymmetry,

$$A = 1 - q_\text{Low}/q_\text{High}, \tag{4.9}$$

is calculated from the high, q_High, and low, q_Low charge values of each pair of adjacent pixels, as plotted

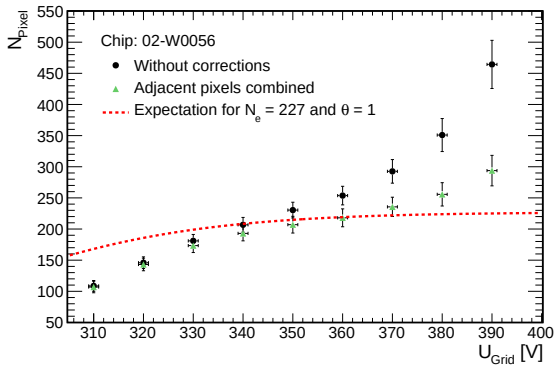

(a) N_{Pixel} against U_{Grid} for G02-W0056

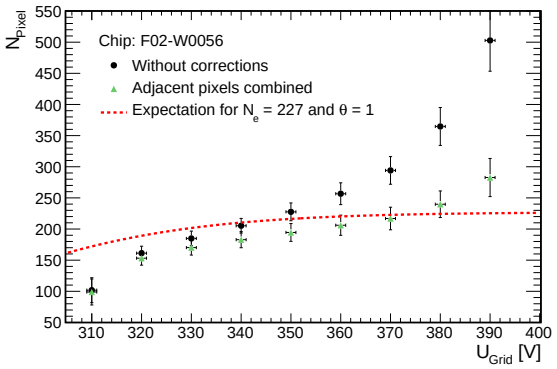

(b) N_{Pixel} against U_{Grid} for F02-W0056

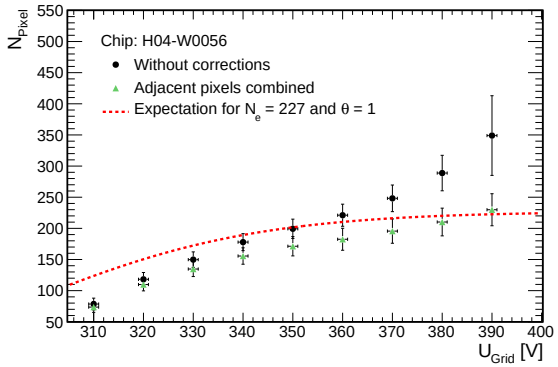

(c) N_{Pixel} against U_{Grid} for H04-W0056

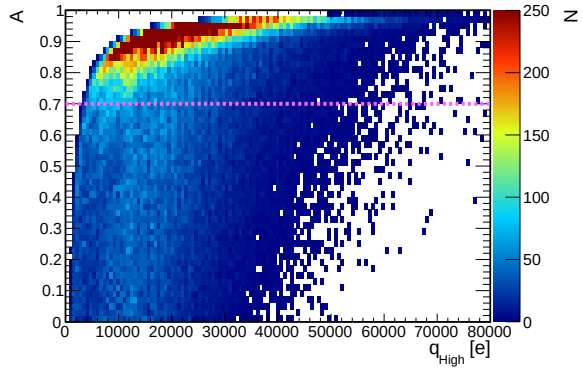

(d) Charge asymmetry $A = q_{\text{Low}}/q_{\text{High}}$ as function of q_{High} for the device G02-W0056 and a grid voltage of $U_{\text{Grid}} = 390\,\text{V}$

Figure 4.18: Number of pixels as a function of the grid voltage for three Timepix InGrids from the third production cycle (a) to (c). The charge asymmetry, A, as function of the higher charge value, q_{High}, (d).

in Figure 4.18d as a function of q_{High}. Pairs with an asymmetry of at least 0.7, i.e. above the magenta line, are combined to one charge deposition located at the position of q_{High}. The result of the procedure is depicted in Figures 4.18a to 4.18c by the green triangles. The rise for large voltages is decreased significantly, even though an excess can still be observed for very high voltages. This may result from an increasing number of isolated pixels with very low charge depositions, as observed in Reference [136].

Even more striking is the fact, that the number of pixels is much lower than the expected value for low grid voltages. Systematic effects, like attachment of primary electrons in the drift volume or a reduced collection efficiency cannot be the reason for this. Attachment would result in a constant offset independent of the grid voltage. The observed deviation is larger for $U_{\text{Grid}} = 310\,\text{V}$ than for $U_{\text{Grid}} = 350\,\text{V}$. A reduced collection efficiency, ϵ_C, can be ruled out with a similar argument. ϵ_C describes the probability of electron in the drift volume to reach a grid hole instead of ending up on the grid. It depends on the ratio of the amplification field and the drift field, FR. For the used grid geometry it reaches a maximum at $FR \approx 20$ and remains nearly constant for larger values [63]. For the conducted measurements, the field ratios vary from 198 to 248 and fall thereby into range of constant ϵ_C.

An explanation for the observed behavior are local variations of the gas gain. The detection efficiency is a function of the mean gas gain and its fluctuations. Thus, deviations from the gain distribution can have a severe impact it. Such deviations have been observed in the previous section as result of the

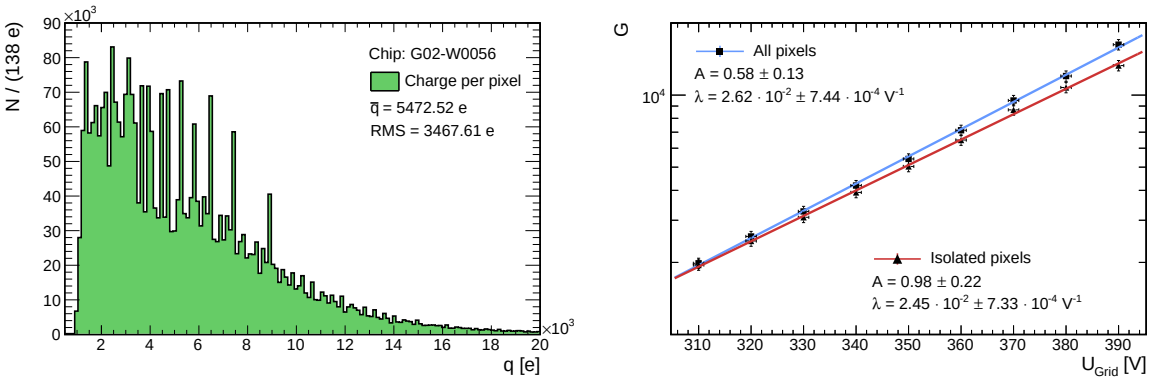

(a) Charge per pixel scaled in electrons at $U_{Grid} = 350\,V$.

(b) Comparison of curves obtained with charge-per-pixel spectra for all pixels (blue line) and isolated pixels (red line).

Figure 4.19: Gain determination with charge-per-pixel spectra for the Timepix InGrid G02-W0056.

production process. These deviations apply only locally to single/few pixels and are not represented in Equation 3.47. Hence, these deviations are not taken into account in the calculation of the expected efficiency by Equation 4.6, which results in too high values. Form Figure 4.14 (and Figures A.2 and A.3) it is apparent that this effect is less important at higher grid voltages. This agrees very well with the expectation, as depicted in Figure 4.17. For values of θ in the range of 2 to 3, full detection efficiency is expected at a grid voltage of approximately 350 V. For higher grid voltages moderate fluctuations are of no concern, as the detection efficiency has reached a saturation value. For low voltages a fluctuation of 5 % has an considerably impact. At $U_{Grid} = 320\,V$, for instance, a reduction of the electric field by 5 % already results in reduction of the efficiency by 10 %.

4.3.6 Gas amplification

The mean gas amplification of an InGrid detector can be determined in three different ways. Two of them are discussed below. The third method requires the decoupling of charge signals from the amplification grid. The general procedure for this is described in Section 4.3.7 where it is used to identify sparks. It has not been used for measurements of the gas gain and is therefore not considered in its discussion.

For both discussed methods the gas gain is measured for three devices from the third production cycle at several grid voltages. Starting at a grid voltage of 310 V it is increased in steps of 10 V up to a value of 390 V. From the 5000 to 10 000 events obtained at each voltage the gain is determined and plotted as function of the voltage. As elaborated in Section 3.4, the mean gas gain is expected to show an exponential dependence on the applied grid voltage. Thus, an exponential function of the form

$$A \cdot e^{\lambda \cdot U}, \tag{4.10}$$

where A and λ are free parameters, is fitted to the data points. The curves obtained in that way are used to compare the gain of the tested devices.

Gain by charge per pixel

A method of measuring the amplification relies on the charge-per-pixel spectrum. Assuming that each electron is detected on a single pixel, the charge measured on a pixel represents a direct measurement

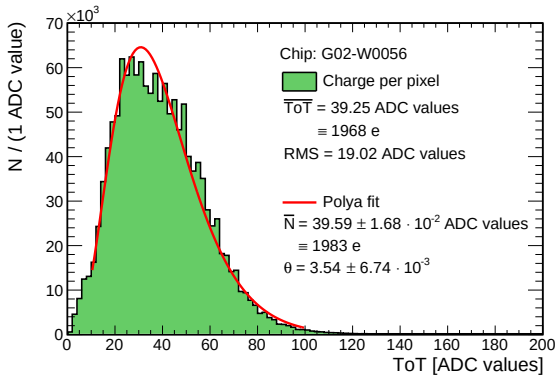

(a) Charge per pixel at $U_{Grid} = 310$ V.

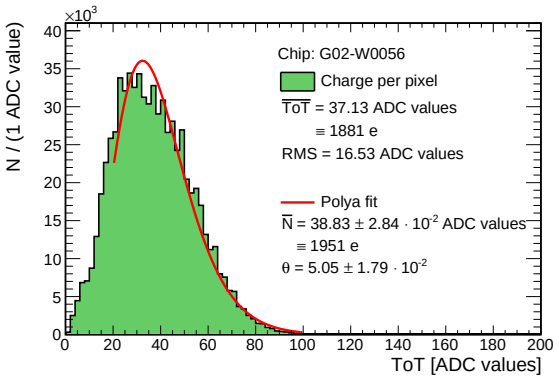

(b) Charge per isolated pixel at $U_{Grid} = 310$ V.

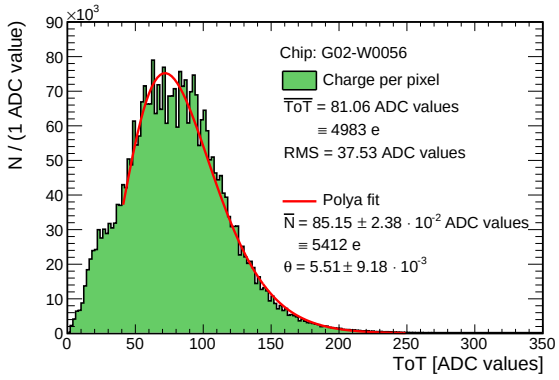

(c) Charge per pixel at $U_{Grid} = 350$ V.

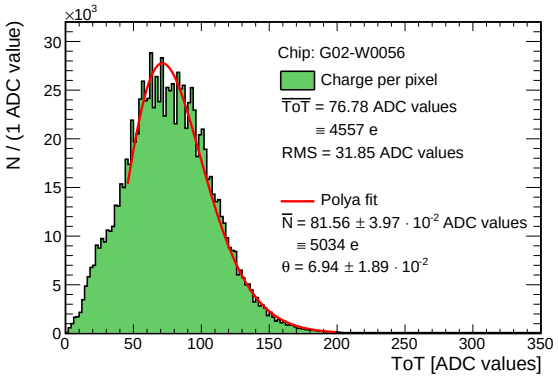

(d) Charge per isolated pixel at $U_{Grid} = 350$ V.

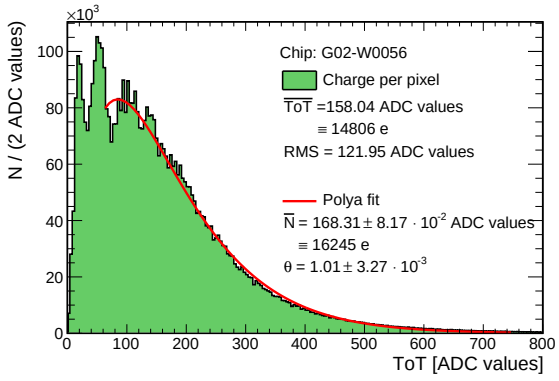

(e) Charge per pixel at $U_{Grid} = 390$ V.

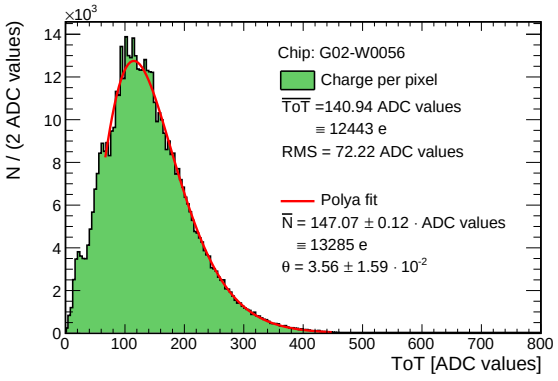

(f) Charge per isolated pixel at $U_{Grid} = 390$ V.

Figure 4.20: Charge per pixel spectra for a Timepix InGrid of the third production cycle. Compared are the spectra for all pixels (a,c,e) and isolated pixels only (b,d,f) at grid voltages of 310 V, 350 V and 390 V.

of the gas amplification. For InGrids, the gas gain can be described by a Polya distribution [63]. Thus, the mean of Function (3.47), fitted to the charge-per-pixel distribution yields the mean gas gain. It is difficult to determine the gain from distributions scaled in electrons. The reason for this can be seen Figure 4.19a which depicts the charge-per-pixel spectrum for the device G02-W0056 and a grid voltage of 350 V. The distribution is governed by extreme fluctuations which are strongest for small amplification values. These are caused by the non-linear relation of charge in electrons and ToT-counts (cf. Section 4.1.1) in contrast to the linear binning of the histogram. To avoid this problem, charge-per-pixel spectra scaled in ToT-values are used for the fitting of the Polya distribution. The mean value of the fit result is then converted into electrons via Equation 4.4 and considered as the mean gas gain for the following discussion.

The method is prone to being biased by charge depositions of two (or more) electrons entering the same grid hole. This is of particular importance given the small drift distance of the detector (d_{max} = 2 cm). Assuming that all the electrons from the photon conversion are created at the maximum possible drift length and at the same position, 95 % of the electrons end up in an area covered by approximately 1875 pixels (for a transverse diffusion of $D_T = 475.05\,\mu\text{m}/\sqrt{\text{cm}}$). From this naive estimation it can be concluded that the probability that at least one pixel detects two electrons is larger than 10 %. Hence, their influence is non negligible. As charge depositions resulting from two (or more) electrons are much larger than for single electrons, they are much more likely to activate a adjacent pixel by charge sharing. Consequently, taking only isolated pixels, i.e. pixels without activated neighboring pixels, into account reduces the effect. The gain plotted in Figure 4.19b as a function of the grid voltage for the two cases of "all pixels included" and "isolated pixels only". According to expectations it is in both cases well described by an exponential. Additionally, the slope is steeper if all pixels are considered which is attributed to exclusion of charge depositions from multiple electrons. Exemplary charge-per-pixel distributions used to determine the gas gains in Figure 4.19b are shown in Figure 4.20 for grid voltages of 310 V, 350 V and 390 V. At U_{Grid} = 310 V the distributions look very similar. This is due to the fact that for a low gas gains even charge depositions caused by two electrons may be not sufficient to exceed the charge threshold of two pixels. The distributions start to diverge at higher voltages until two distinctive peaks have appeared on the left edge of the distribution for all pixels at U_{Grid} = 390 V. The distributions obtained from isolated pixels alone shows for the same grid voltage a much better agreement with a Polya distribution. The peaks on the rising edge are still present, even though they are strongly suppressed. From this it can be concluded that they do not result from charge sharing alone.

It should be mentioned, that taking only isolated pixels pushes the gain towards lower values. Charge sharing is not only caused by multiple electrons entering the same grid hole. It can also occur at the amplification of single electrons, especially, if high grid voltages are applied. Thus, the slope of the actual gain curve should be between the slopes of the two methods presented above. Given the high probability of electrons ending up in the same grid hole the actual gain should be closer to the gain obtained from isolated pixels than to the gain obtained from all pixels. However, up to now there is no scheme to differentiate between charge sharing induced by amplification of multiple electrons and charge sharing due to high gain.

Gain by charge per event

The gain can also be determined from the amount of charge and number of pixels observed in the photopeak of the measured ^{55}Fe spectra. Their ratio is a measurement of the mean gas gain, i.e.

$$G = \frac{q\,[e]}{N_e}, \tag{4.11}$$

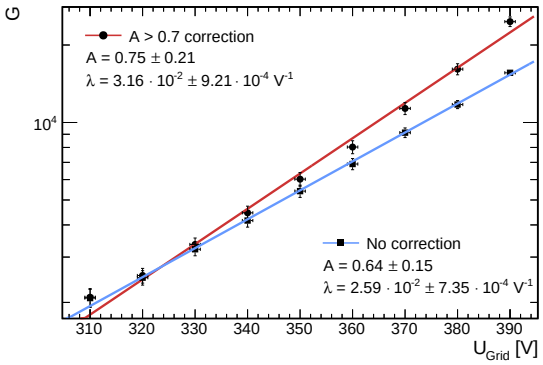

(a) Comparison of gain determined with corrected (red line) and uncorrected (blue line) number of pixels.

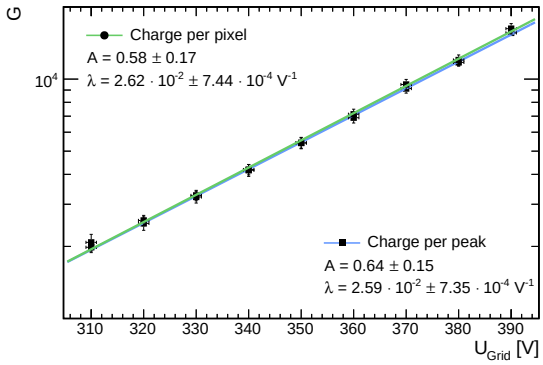

(b) Comparison of the uncorrected method (blue line) with the charge-per-pixel method (also uncorrected, green line).

Figure 4.21: Gain determination with the charge in the photopeak. Comparison for corrected and uncorrected number of pixels (a) and comparison with charge-per-pixel method (b).

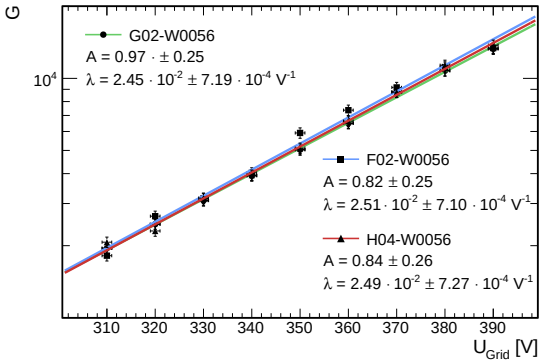

(a) Gain by charge-per-pixel method.

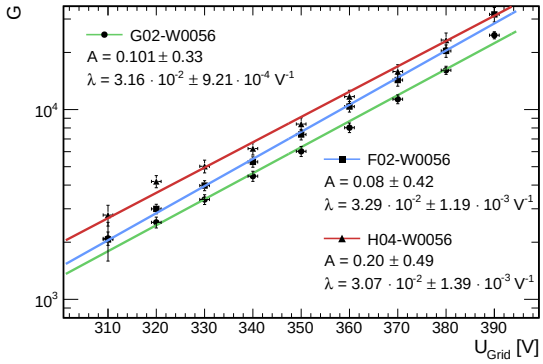

(b) Gain by charge-per-photopeak method.

Figure 4.22: Comparison of the gas gain for three different chips of the third production cycle for the charge-per-pixel method (a) and the charge-per-photopeak method (b).

where N_e is the number of detected electrons from the primary ionization processes. This method does not allow to measure fluctuations of gas gain, as it measures the mean of N_e processes. For an InGrid detector N_e is ideally identical to the number of activated N_{Pixel}. As already discussed, N_{Pixel} may be larger than N_e, thus, the same correction as presented Section 4.3.5 can be applied.

Gain as function of the grid voltage is depicted in Figure 4.21a for the corrected (red line) and uncorrected (blue line) case. In both cases, the gain shows an exponential behavior. The gain is steeper if a correction is applied, as N_{Pixel} is reduced while the amount of charge is left unchanged. By comparison with the gain obtained from the charge-per-pixel spectra it can be determined that the gain rises too fast in the corrected case. As can be seen in Figure 4.21b, the gain obtained with uncorrected values of N_{Pixel} (blue line) agrees very well with the gain obtained from charge-per-pixel spectra (green line), if all pixels are included in the analysis. In both cases, pixels with small charge depositions which result from charge sharing, are taken into account.

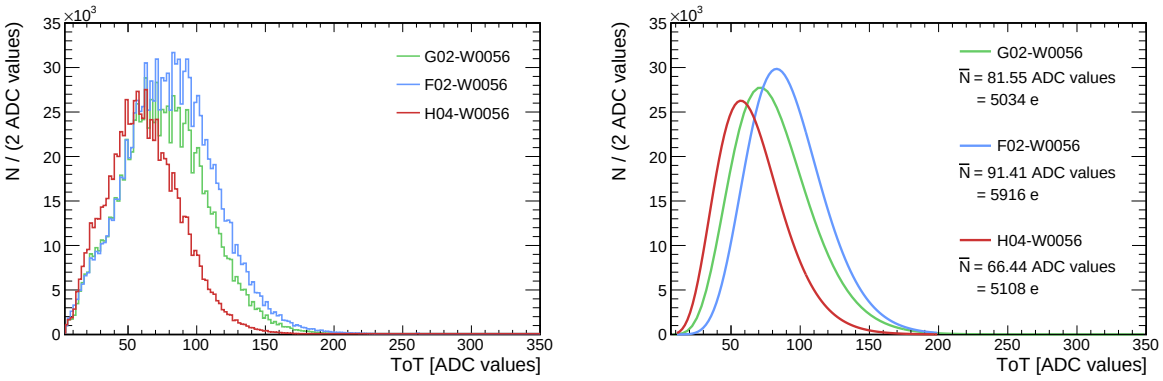

(a) Charge-per-pixel spectra.

(b) Fitted Polya functions.

Figure 4.23: Comparison of charge-per-pixel spectra for different devices from the third production cycle, measured at a grid voltage of 350 V.

Gain for different chips

The gain curves obtained for three chips from the third production cycle (G02-W0056, F02-W0056 and H04-W0056) is depicted in Figure 4.22a for the charge-per-pixel method and in Figure 4.22b for the charge-per-photopeak method. In both cases the observed gain curves are for all three devices compatible with the assumption of an exponential rise as presented by Equation 3.46.

Nearly identical slopes are obtained for the gain curves determined by charge-per-pixel method. Small deviations are observed at grid voltages of 350 V/cm and 360 V/cm for the device with chip ID F02-W0056. This is in agreement with the observations made in Section 4.15b for the charge spectrum of the device (cf. Figure 4.15). To further examine these deviations the charge-per-pixel spectra and fitted Polya functions are depicted for all three devices in Figure 4.23 for a grid voltage of 350 V. The spectra show a poor agreement with each other. For device H04-W0056 this is attributed to the very different calibration parameters which also causes the much higher threshold. For G02-W0056 and F02-W0056 the calibration curves are very similar, hence, the charge-per-pixel spectra should be similar too. This is indeed the case for the rising edge of the distribution. The falling edge in contrast, is for F02-W0056 shifted to higher values. This is reflected in the parameters of the fit functions. While the mean values (in electrons) of H04-W0056 and G02-W0056 differ by just 1.5 % the difference between F02-W0056 and G02-W0056 is approximately 15 %.

The gain curves obtained by the charge-per-photopeak method show larger differences between the three devices. Furthermore, a larger deviation of single data points to the fitted gain curve is observed for devices H04-W0056 and F02-W0056. This is in particular notable for small amplification voltages. The general trend already observed for the charge-per-pixel method can be confirmed. The gain is largest for F02-W0056 and smallest for H04-W0056.

Changes in the environmental conditions, in particular in the barometric pressure are only of small consequence to the observed gain, as elaborated in Appendix A.5.

Gain homogeneity

To further assess the homogeneity of the amplification process it is examined for one device (G02-W0056) in detail. To this end the amplification of a large data set (roughly 1 600 000 events) recorded at a grid voltage of 345 V is studied for each pixel. Only a cutout of the central 100×100 pixels is

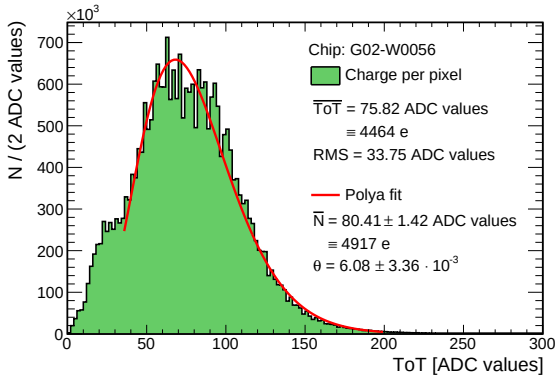

(a) Charge per pixel for the central chip area.

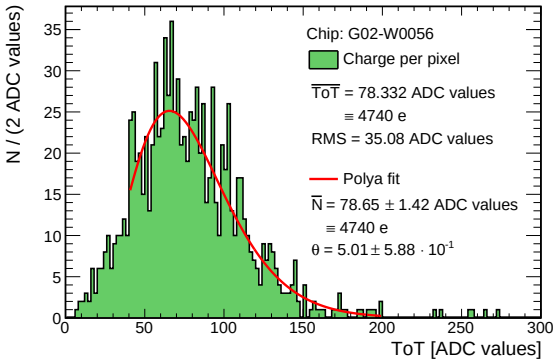

(b) Charge per pixel for a single pixel ($x = 79, y = 116$).

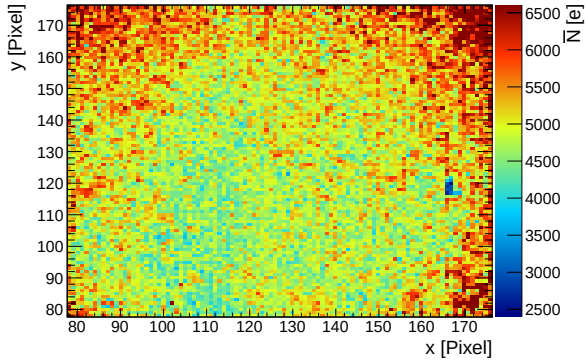

(c) Mean amplification for the central chip area.

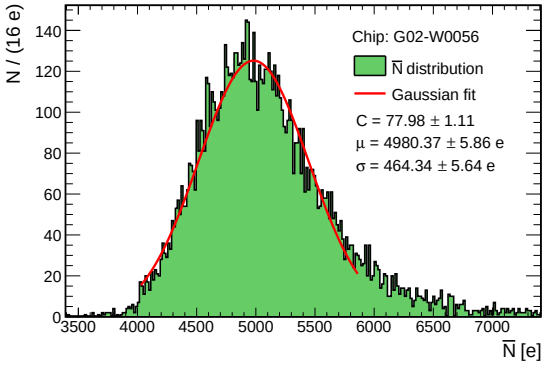

(d) Distribution of the Polya mean values.

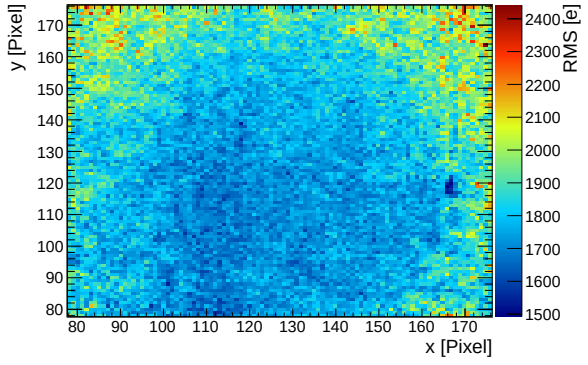

(e) RMS of the charge-per-pixel spectra for the pixels in the central chip area.

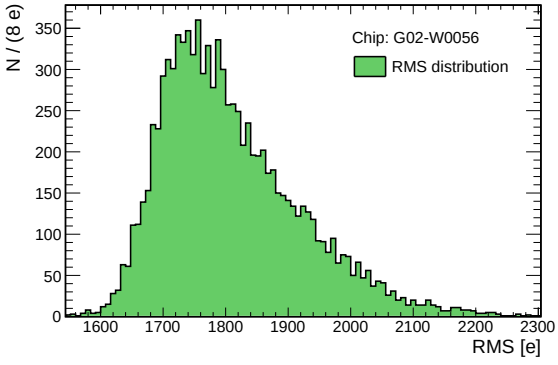

(f) RMS distribution.

Figure 4.24: Gain per pixel for a cutout of the central 100 × 100 pixels area of the chip.

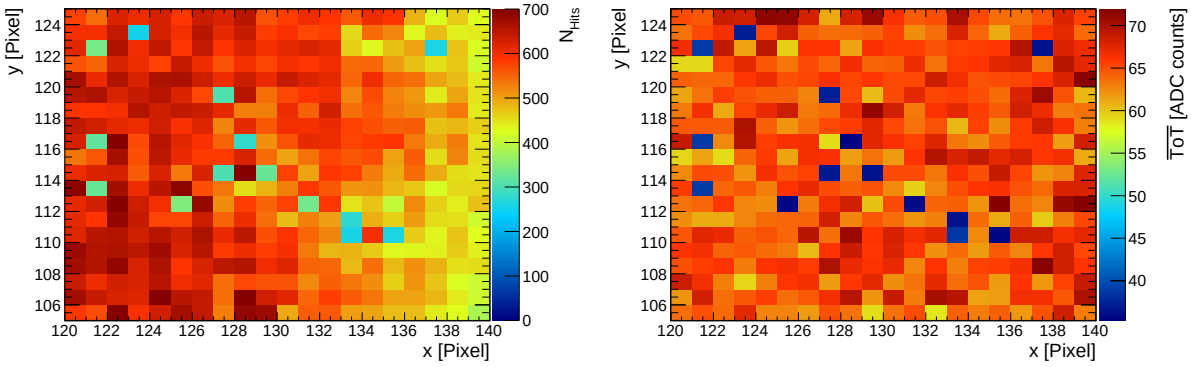

(a) Occupancy

(b) Mean amplification

Figure 4.25: Comparison of occupancy (a) and mean amplification (b) for the same 20×20 pixels cutout of the Timepix InGrid H04-W0056.

considered. This way, regions of low occupancy, and hence, low statistics are excluded. From the distribution shown in Figure 4.24a it is apparent, that the charge-per-pixel distribution in the selected area is very similar to those of the whole chip area and its mean amplification value of $\bar{N} \approx 4900$ matches the expectation obtained from the fitted gain in Figure 4.19b (which computes to 4887).

A charge-per-pixel spectrum is created for each individual pixel and a Polya is fitted to it. An exemplary result is depicted in Figure 4.24b. The mean values, $\bar{N}$, are depicted in Figure 4.24c according to their position on the chip. The resulting distribution is not very homogeneous. Especially in the upper corners a much higher amplification is observed than in the central region. The distribution of the mean values (Figure 4.24d) further supports this observation. The distribution can be approximated with a Gaussian which is in agreement with the central limit theorem. The center of the Gaussian is roughly at the position of the mean gas gain and it possesses a tail towards higher amplification values. The width of $\sigma = 464$ electrons is comparatively high, which means that the amplification shows significant fluctuations over the chip area. This is further backed up by the root mean square deviations. These are depicted for each pixel in Figure 4.24e and their distribution is given Figure 4.24f. The distribution of the RMS values per pixel follows basically that of the Polya mean values. However, the peak value of the RMS distribution is roughly located at 1750 electrons, which is considerable and implies large deviations of the gas gain.

As the occupancy is mainly determined by the position of the radioactive source (cf. Figure 4.12), there is no absolute measure for the occupancy of an arbitrary pixel. A relative measure can be obtained by comparing the occupancy of a pixel with the occupancy of its direct neighbors. This is done in Figure 4.25a for a 20×20 pixels cutout of the chip H04-W0056. The transition from reddish colors in the left and central part of the cutout to yellowish colors in the right part is caused by occupancy differences due to the position of the source. Besides this color gradient, there are individual blueish/greenish pixels which stick out. They are activated significantly less often than their neighbors. The same pattern is observed in Figure 4.25b which depicts the mean gain per pixel for the same cutout area. Most pixels show a mean gas gain roughly in the range of 55 to 72 ADC counts. Only the pixels for which a reduced occupancy is observed show considerably reduced gain. This confirms the assumption of a correlation between reduced gain and reduced occupancy for single pixels.

4.3.7 Spark protection

An important property of pixel chips with an integrated amplification stage is their ability to withstand discharges. As the amplification process fluctuates statistically, discharges may occur even at moderate voltages. Without a sufficient protection the charge induced by such sparks is likely to destroy the electronics of the pixel chip. This is in particular a problem if the chip is used in an environment where huge localized charge depositions are possible which make discharges even more likely to occur.

When a discharge occurs a substantial amount of charge can be deposited onto the pixel chip. The spark can cause a high temperature plasma and locally melt the area around the hit pixel [123]. In addition, the pixel electronics may cease to work because of getting overcharged. This can affect large areas of the chip, as a failing pixel can create a short circuit between electric lines and many pixels share the same electric interconnections. Consequently, even a single spark is capable of destroying a pixel chip.

To prevent InGrids from being destroyed by discharges they have to be safeguarded. One way to achieve this is to cover the sensitive area of the chip with a thin but highly resistive layer which added directly on top of the pixel matrix of the chip. This concept has been first described in [137] and is inspired by resistive plate chambers (RPCs) [138]. For charges originating in the amplification processes the protection layer acts like a resistor, creating potential difference across the layer which results in a locally decreased electric field. This means that charge accumulating on the resistive layer is drained much slower than it is deposited by the discharge. Therefore, a space charge builds up and the field in amplification gap is reduced, quenching the discharge.

The fabrication process of such a layer is described in Section 4.2. It can be characterized by its virtual capacitance[7], C_{Prot}, and its resistance, R_{Prot}, which are given by

$$C_{Prot} = \frac{A\epsilon_r\epsilon_0}{d} \qquad \text{and} \qquad R_{Prot} = \frac{\rho d}{A} \tag{4.12}$$

respectively. Thereby, denotes d the thickness of the Si_xN_y-layer, A the area it covers and ϵ_0 the vacuum permittivity. Typical values for the relative permittivity, ϵ_r, are in the range of 6.5 to 8.7 [124], while the specific resistance, ρ, is typically about $10^{13}\,\Omega\,\mathrm{cm}$ [123].

The protection layer has to be of high quality to quench sparks effectively. It has been observed [131] for InGrids from the second production cycle that chips covered by layers with imperfections and defects are not sufficiently protected. They are destroyed even at moderate voltages as soon as discharges occur. An explanation for this can be illustrated with the help of Figure 4.26. The figure shows the cross section of the protection layer taken with a focused ion beam (FIB). The left picture depicts a device from the second production run. While the layer is in general very homogeneous, thin cracks can be observed. They run from the top of the Si_xN_y-layer down to the pixel. It is possible for charge carriers to follow these cracks and thereby pass the protection layer unhindered. This effectively degrades the protection offered by the layer to a point where the chip is nearly as easily destroyed as without it. The cracks were caused by a malfunction of the deposition machine. The result of the deposition procedure with a functional machine can be seen in the right hand side FIB image of Figure 4.26, which shows an InGrid from the third production cycle. The protection layer is very uniform and shows no hint of any cracks. The inhomogeneities in the picture result from the polishing required for FIB imaging and are no reason of concern.

[7] The capacitance is considered virtual because of the missing electrode on top of the layer which allows the charge carriers to move freely.

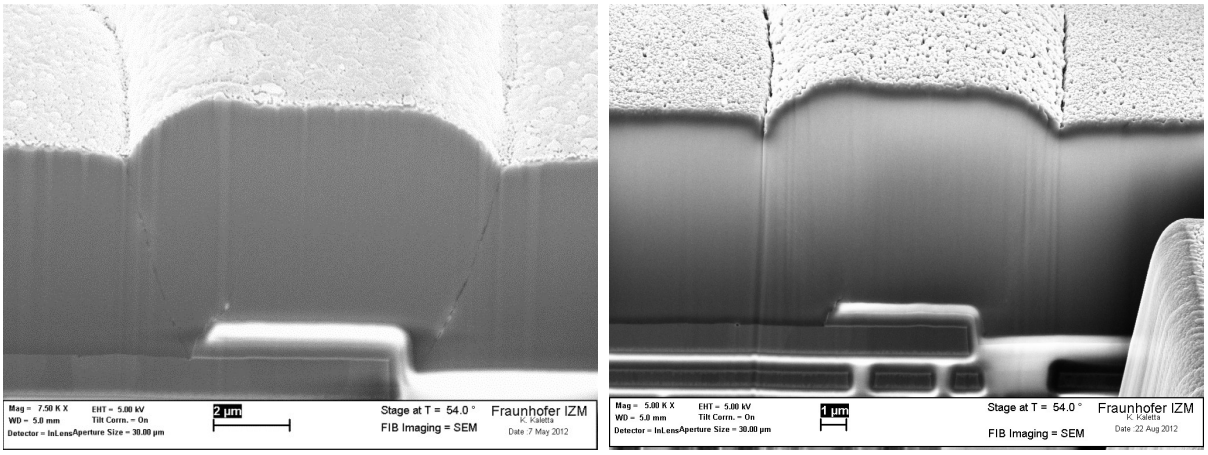

(a) Second production run [131].

(b) Third production run.

Figure 4.26: Focused ion beam pictures of the cross section of the Si_xN_y protection layer of InGrids produced on wafers. In (a) a device from the second production run is shown. Cracks run from the top of the layer down to the pixel. (b) shows a device from the third production run. The inhomogeneities result from the polishing for the picture creation. Otherwise, no cracks are visible.

Measurements

To verify the functioning of the protection layer dedicated tests have been performed. For this, the detector setup is used as described in Section 4.3.2. A ^{55}Fe source is employed to induce discharges by applying very high voltages to grid, i.e voltages in the range of 405 V to 450 V. Two event display of such a discharges are presented in Figure 4.27, for an event with one (a) and two (b) discharges respectively. The position of the discharge is clearly visible by the circular area of high charge deposition. The spark affects not only the pixels which are directly hit but causes also the columns containing these pixels to count large charge values. This can be explained by the fact that all pixels in one column are interconnected. Furthermore, the areas near to edges of the chip, parallel to the columns count large amounts of charges. The reason for this is, still under investigation. Another observation that can be made from Figure 4.27, is that in both events single hits are present, which seem not to be connected with the discharge. Indeed this behavior can be observed in many events at high grid voltages, even if no discharge occurs. These hits have already been observed in Reference [136] and a contribute to the phenomenon of hits exceeding the expected saturation limit at high charges (cf. Section 4.3.6). The origin of these additional hits is still unclear and needs further investigation.

Events like those depicted in Figure 4.27 indicate, that the InGrids from the third production cycle are capable of surviving single discharges. To further assess the quality of the protection layer of chips from the third production cycle, a more thorough testing is required. To this end, the experimental setup (cf. Section 4.3.2) is extended to measure signals on the amplification grid. This is possible, as electrons and ions created in the amplification process heed towards the pixel readout and grid respectively. The movement of the charges induces a current on the grid, which is compensated for by the high voltage supply. This manifests as a pulse on the high voltage line, which can be decoupled by a properly chosen capacitor. The detection of discharges follows the same measurement principle. The required circuitry is sketched in Figure 4.28a.

To decouple a signal from the grid two capacitors of 47 pF are connected to it. The two resistors R_{HV} and R_1 of 12 MΩ each prevent the signal from being drained by the high voltage supply and

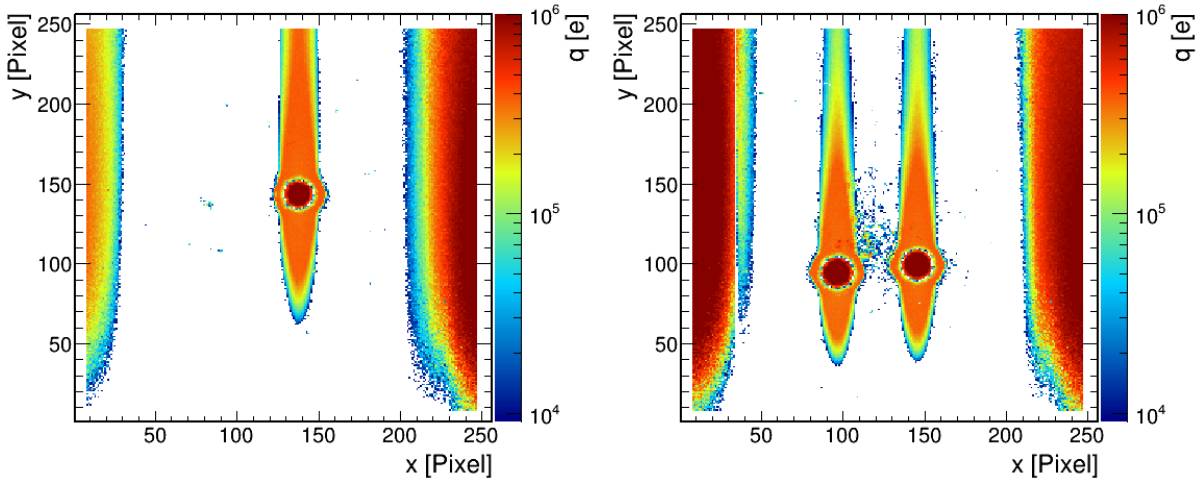

Figure 4.27: Discharges as recorded by a chip (G02-W0056) from the third production cycle. The position is of the discharges are marked by the circular areas of high charge values.

ground respectively. The test input V_{Test} and the connected capacitor $C_{Test} = 4.7\,pF$ allow for a charge calibration of the setup (cf. Appendix A.8).

The capacitors act as input for two channels of a charge sensitive amplifier (CSA), which amplifies the signals to an extent where they can be readout with a fast digital to analog converter (FADC) or further processed with a NEMbox[8] logic unit. The CSA has formerly been used in the TPC of the ALEPH experiment [140] and is well suited to the task. It comes with 16 channels and a linear range of about 1 V at an equivalent noise charge (ENC) of 600 [141]. The final shaping of the CSA output is done by a filter which shapes the signal into a bipolar pulse with a constant rise time, t_R, of about 200 ns. Signals recorded in the above way and digitized with a FADC at a sampling frequency of $f_S = 1\,GHz$ are depicted in Figure 4.28b. The green curve originates from a 5.9 keV X-ray photon, measured at a grid voltage of 410 V while the black curve represents a discharge, recorded at the same grid voltage. The different pulse heights of X-ray events and discharges makes it easy to distinguish the two cases. Thus, discharges can be detected by using a sufficient high trigger threshold, for which a value of 500 mV has been chosen. At higher grid voltages, starting at about 415 V, event displays suggest that no typical X-ray events can be recorded anymore, but each photon causes a discharge, so that the choice of the threshold becomes less important.

The counting of the discharges is performed by the NEMbox. The programmed counting logic does not only detect and count discharges, but makes also sure that the chip is still working. To this end the shutter signal (cf. Section 4.1) from the Timepix chip is also fed into the NEMbox and used for the creation of a gating signal. This means that the absence of the shutter is used to signal that the chip has stopped working. The shutter is not generated by the chip but by the readout. Thus it can be sent even if the chip is not working anymore. Additionally, if the chip is broken, the MUROS will not be able to communicate with it and abort data taking. Hence, no further shutter signals are sent. In this case the programmed logic takes care of a safe ramp down of the supply voltage of the grid and stops counting. The length of the gating signal has to be properly chosen to ensure continuous counting

[8] NEMbox - Nuclear Electronics Miniature Box, a standalone data acquisition module, which can be graphically programmed by the user to implement custom logic and data acquisition schemes [139].

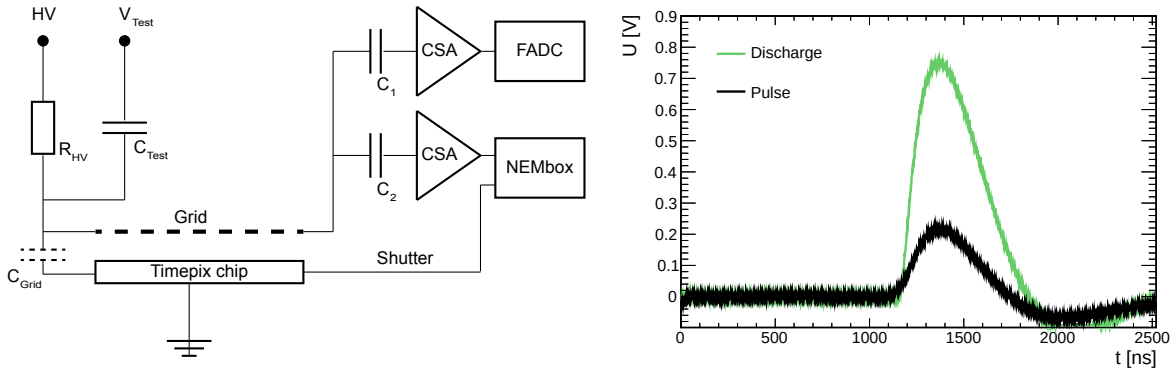

(a) Discharge counting logic.

(b) Signal pulses on the grid.

Figure 4.28: Spark counting. The circuitry for decoupling signals from the amplification grid (a) produces pulses (b), which greatly differ in size for discharges and regular signals.

without unnecessary ramp downs of the high voltage. The time required for the readout of the Timepix is not constant. Therefore, a gating signal with a length of 625 ms has been chosen, which is about five times the mean time required for the data acquisition and the subsequent readout of the chip. This way it is ensured that the setup stays active even if the time between two shutter signals takes much longer than usual. The gate is restarted each time a shutter is detected, yielding a gating scheme which is at most active for the fivefold time of an acquisition cycle after the chip is broken. Due to the long duration of the discharge measurements ($O(10^3$ s)) the maximum number of sparks counted after the breaking of a chip is negligible.

Four InGrids from the third production cycle have been tested for the ability to withstand discharges. Starting with 400 V, the grid voltage has been increased in steps of 5 V and the occurring discharges have been counted. The results of these measurements are summarized in Table 4.5. The functional range stated is the voltage range, for which the chip has been tested without any observed discharges, while the breaking voltage denotes the voltage applied when the chip died. Two chips from the second production cycle are listed for better comparison, even though no discharge counting has been performed on them. Each tested InGrids from the third run performed well for grid voltages in the range 300 V to 390 V while devices from the second run already ceased to work at voltage of 370 V to 380 V. For InGrids from the third run, discharges started to occur at about 400 V. Three of for tested chips were capable of withstanding $O(10^4)$ discharges. Up to a grid voltage of 445 V. Thus, it can be concluded, that InGrids from the third production cycles are much more resistant to occurring sparks than their predecessors from the second run. The refined procedure for the deposition of the Si_xN_y results in a protection layer of higher quality, which is in most cases capable of withstanding a large number of discharges. Moreover, the destruction of one chip, F02-W0056, at a moderate voltage of 400 V indicates, that individual devices still suffer from limited protection. For the readout of a TPC the protection seems to be already sufficient. For the used gas mixture of Ar:iC_4H_{10} (95:5), typical voltages for the operation of an InGrid are in the range of 340 V to 360 V, for which all tested devices showed a good and very stable performance.

Chip	Prod. cycle	Functional range	Recorded discharges	Breaking voltage
K07-W0057	2	300 V to 370 V	0	380 V
J07-W0057	2	300 V to 360 V	0	370 V
G02-W0056	3	280 V to 400 V	17 401	>450 V
F02-W0056	3	280 V to 390 V	14	400 V
H04-W0056	3	280 V to 400 V	10 854	450 V
L04-W0056	3	300 V to 390 V	12 987	>450 V

Table 4.5: Observed discharges for InGrids from the second and third production run. Dedicated measurements for the counting of discharges have only been performed for devices from the third run.

4.4 Summary

InGrids are a promising option for the readout of a TPC at the ILC, in particular due to their ability of detecting single primary electrons, their high spatial resolution and their integrated readout circuitry. To be applicable in such large experiments a large scale fabrication process is required. Such a process has been developed by transferring the original process to the production on 8″-wafers.

Devices from the first three production cycles of the new fabrication process have been tested. Energy resolutions of approximately 5 % and 7 % for pixel and charge spectrum respectively could be observed in measurements of the 5.9 keV line of a ^{55}Fe source which is comparable to values obtained with devices from the original production process. These values represent an upper limit for the performance of devices created by the new process so far. An analysis of the active region has shown that all devices suffer to some extent from contamination by residuals of the production process. These residuals cause local reductions of the gas amplification which results in a decrease of the detection efficiency. Due to these gain variations the distribution of the mean gas gain is additionally broadened which impacts charge based measurements. As a consequence, the production process has been extended. An additional step of oxygen-plasma cleaning is added to the development and cleaning procedure of the SU-8 to reduce the occurrence of residuals in future production cycles.

Chapter 5

Simulation of a pixelized TPC at the ILD

As presented in the previous chapter, it is possible to produce large amounts of InGrid detectors in one production cycle, making the technology available in large quantities. Thus, a central requirement for their application in large experiments like the ILD can be considered as fullfilled. Without building a large area prototype, the prospects of such an approach can only be assessed by detector simulations. Especially, when it comes to pixelized readouts the level of detail of the simulation has to be sufficiently high. As already mentioned in Section 3.5.1, a TPC readout consisting of InGrids is capable of resolving single electrons. This is one of the key features of a pixelized readout. To reflect this, the simulation of such a readout has to track individual primary electrons as well. This applies for all the major steps, starting with primary ionization over drift through to gas amplification and readout.

The level of detail is not the only matter to deal with when simulating a pixelized TPC for the ILD. As described in Chapter 3 the working principle of a TPC demands a homogeneous electric field to reach the highest possible resolution. Distortions of the drift field seem to be unavoidable. The problem of back-drifting ions has already been described in Section 3.6.1. But back drifting ions are not the only cause of field distortions. Ions originating from the primary ionization processes stay in the active TPC volume and distort the drift field in the same way as the ions originating from the amplification processes. The influence of field distortions is no problem specific to InGrid-based TPCs it has to be taken into account for a realistic description.

This chapter provides on overview on the tools and methods used to simulate an InGrid-based TPC as main tracking device of the ILD. In Section 5.1, the tools and methods are discussed, which are required, to simulate the backgrounds occurring in the TPC of the ILD. In Section 5.2 techniques for calculating the electric field caused by the background charges in the TPC are introduced. Putting these pieces together, Section 5.3 addresses the detailed simulation of muon tracks in the presence of backgrounds, as well as their reconstruction. Afterwards, in Section 5.4, the chapter is summarized and concluded.

5.1 Simulation of detector backgrounds at the ILD

Although, the ILC can be considered as a clean experimental environment, especially compared to hadronic colliders, backgrounds can not be avoided. The main origin of these backgrounds is beamstrahlung, as described in Section 2.1.3, which creates electron-positron pairs as well as hadronic showers (cf. Section 2.2.2). The impact of these backgrounds on the performance of a certain subsystem can not be assessed isolated from the other subsystem but has to be derived from the backgrounds' interaction with the full detector. This is due to the fact that background particles may cross a certain subsystem

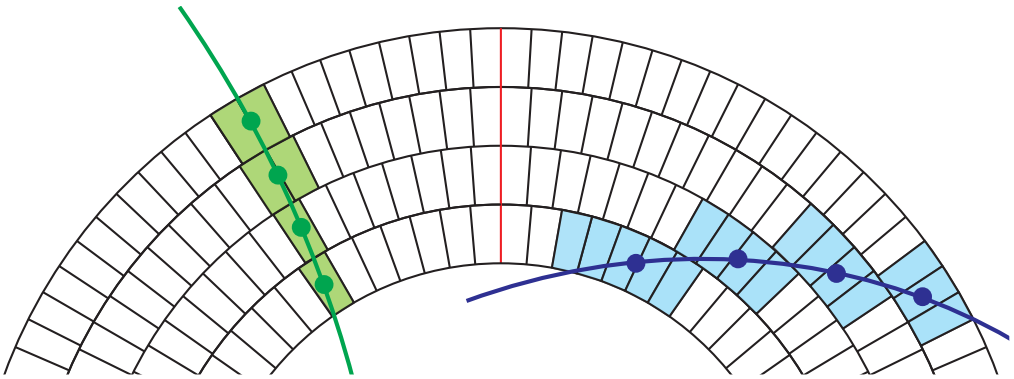

Figure 5.1: Row based hit placement in Mokka. The charge detected on the colored pads is summarized by a single hit per pad row.

unhindered, only to be scattered back from another detector component and eventually interact with the first subsystem. Another example are particle showers created by a background particle in one subdetector being detected in another detector system. Therefore, a full detector simulation is required to get a complete and realistic picture of the impact of background on individual detector systems.

The simulation program `Mokka`[142] has been developed to provide full detector simulations of the ILD. It is based on the `Geant4` framework[143] and capable of simulating several versions of the ILD as they have been defined so far as part of its optimization process. All models are accessible from a database, to which new versions can be easily added. This mechanism allows for fast and simple comparison of technology options and different version, thus, simplifying the optimization of the detector layout.

For the simulation of the e^+e^--pair background, `Mokka` takes its input from `Guinea-Pig`[144, 145], a simulation tool for beam-beam interactions at e^+e^--colliders. `Guinea-Pig` uses a so-called macroparticle approach in which the particles of a bunch are grouped together and filled into the bins of a spatial grid, from where they are tracked through the collision. Different models are used to describe the processes contributing to the incoherent pair production (cf. Section 2.2.2). The Breit-Wheeler process in which two real photons are involved is modeled from calculations of the leading order cross section. In contrast, the Bethe-Heitler process and the Landau-Lifshitz process, which involve virtual photons, are calculated by the means of the equivalent photon approximation (EPA) [146]. In the EPA virtual photons are replaced by an equivalent spectrum of real photons if their virtuality is not too large. `Guinea-Pig` generates output in its own ASCII[1] based format which can be read by `Mokka` without further conversions.

Furthermore, `Mokka` can take established generator file formats like StdHep[147] as input, allowing to use it in combination with typical physics event generators. This method is applied for the simulation of the backgrounds from $\gamma\gamma \rightarrow$hadrons, which are provided by event generator `Whizard`[148].

Designed as a full detector simulation, `Mokka` incorporates many different subdetectors. As for most full detector simulations, this means that a trade-off between the level of detail and the required computing time has to be made. Being the main simulation tool for any benchmarking studies performed for the ILD, it has to be applicable in the mass production of physics events. For the simulation of the TPC, some level of detail in the placing of the hits has been sacrificed in favor of computing time. In radial direction, the energy depositions from the primary ionization processes are placed in the middle of each pad row, at the same position the reconstruction algorithms for a real TPC would reconstruct

[1] ASCII - American Standard Code for Information Interchange.

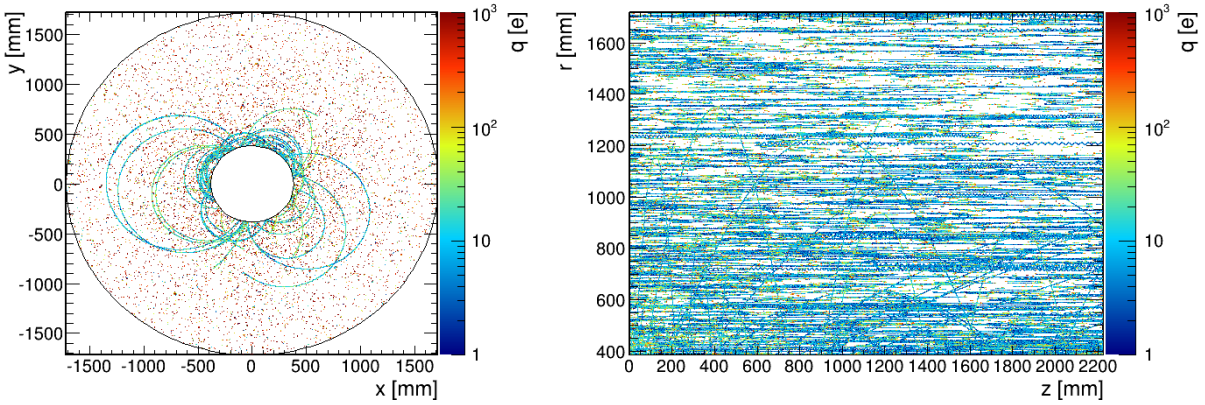

(a) *xy*-projection.

(b) *zr*-projection.

Figure 5.2: Overlay of 100 bunch crossings of the primary ionization of the e^+e^--pair background at a center-of-mass energy of 500 GeV. Depicted are projections into the *xy*-plane (a) and into the *zr*-plane (b).

them. In the following step, during the digitization of the hit with `MarlinReco`[149], a smearing of the size of the assumed detector resolution is applied. After this, any hits which are close to each other than the assumed double hit resolution are merged. This method is fast and simple, thus, it is well suited for producing a large number of events. It even yields the correct values for the covariance matrix when fitting tracks, since the errors applied to the hits are known.

For the simulation of a pixelized TPC, the above described method is not precise enough. Current detector models by default assume pads with a width of 1 mm in azimuthal direction and 6 mm in radial direction. Thus, each hit is separated by at least 6 mm, even if the track it belongs to runs radially from the beam pipe to the calorimeter. Pixels are much smaller. For this reason, not every row of pixels is hit and the simplified method of placing the energy depositions on the readout plane can not be applied. Another problem of the simplified method is that it is difficult to accurately determine the spread of the charge in the $r\varphi$-plane. This is in particular difficult for tracks with a low angle to the pad row, i.e. large angles to the pad axis, as indicated in Figure 5.1. However, a precise assessment of the number of activated readout channels is very important for any occupancy study.

The TPC simulation within `Mokka` can be put into a more detailed mode to avoid the above problems. In this mode the hit placement is not based on pad rows, but a fixed upper limit is applied to the simulation step length. This mode has originally been implemented for very low energetic particles. Particles with an extreme small transverse momentum curl with a small radius, not exceeding the height of a pad row. In the row based mode, it is possible that such particles never cross the center of a pad in radial direction. Thus, no charge deposition is created. Te detailed mode is applied to all particles of an energy below a user defined threshold. By setting this threshold to a value above the energy available for created particles, the step limit is applied to all particles in the TPC and not only to those with a very low transverse momentum. In Reference [150] it has been shown that the step limit is also working reliably when applied to particles with a high energy.

Figure 5.2 shows a practical example of background simulations performed with `Mokka` and a limited step length of 50 µm. Illustrated are 100 overlayed events of pair background projected into the *xy*-plane and *zr*-plane respectively. What appears in the *xy*-plane to be small and very localized charge depositions can be identified as microcurlers in the *zr*-plane. Moreover, individual tracks forming a helix around the inner beam pipe can be easily identified.

As part of the ILCSoft package `Mokka` stores its output in the linear collider I/O (`LCIO`) format, which represents a persistency framework and event data model [151]. This data model has in particular been developed to bridge the gap between simulation and reconstruction and represents the de-facto standard data format for software developments in the context of the ILC.

5.2 Calculation of field distortions

To evaluate the field distortions caused by space charges in a TPC it is necessary to determine potential and derived electric field at any point in the sensitive area of the TPC. As known from electrostatics the electric field $\vec{E}(\vec{x})$ originating from an arbitrary charge distribution can be calculated by solving Poisson's equation:

$$\Delta\phi(\vec{x}) = -\frac{\rho(\vec{x})}{\epsilon_r \epsilon_0}, \tag{5.1}$$

with electrostatic potential $\phi(\vec{x})$, vacuum permittivity ϵ_0, relative permittivity ϵ_r and the charge density function $\rho(\vec{x})$. The difficulty to find a solution strongly depends on the complexity of the charge density function and the presence of boundary conditions. Even if no analytical expression is available to describe the charge density function, the potential can be calculated by superimposing the potentials caused by individual charge depositions of the charge distribution, at least if their exact positions are known, which reduces the problem to finding an appropriate potential to satisfy any boundary conditions. In the case of a TPC the imposed boundary conditions are given by the surfaces, ∂V, surrounding the gas volume, V, which can be considered to be infinitely conductive. Therefore, a vanishing potential is enforced on these surfaces. Or in other terms: $\varphi(\vec{x}) = 0$ for all $\vec{x} \in \partial V$.

The geometry of a TPC in the environment of a collider, is described in Section 3.6.2. It can be approximately described by a coaxial cavity. A detailed modeling of the field cage is not necessary and surfaces surrounding the sensitive volume can be approximated by two concentric cylinders with radii $r = a$ and $r = b$ with $a < b$. The structure is closed by two areas which connect the inner and outer cylinder at $z = 0$ and $z = L$. A popular ansatz to satisfy boundary conditions like this is to construct an appropriate Green function, $G\left(\vec{x}, \vec{x'}\right)$.

The construction of such a Green function yields an infinite series of particular solutions of Equation (5.1), which can be found by the method of separation. However, there a several ways of finding the particular solutions, leading to different representations of the Green's function, each of them with different properties. This is a fortunate circumstance, as this can be exploited to avoid bad behavior of individual representations in certain cases. While one series may perform poorly under certain conditions another might work just fine, making adequate solutions available at any location by choosing the appropriate Green's function.

The following subsections illustrate three different representations of Green's functions solving Equation (5.1) for the boundary conditions imposed by the presence of a TPCs field cage. Whenever actual values for the dimensions of the TPC are required, they can be assumed to be $a = 0.354\,\mathrm{m}$ for the inner radius, $b = 1.748\,\mathrm{m}$ for the outer radius and $L = 2.225\,\mathrm{m}$ for the drift length. Each of the presented Green's functions is suitable to derive the electric field in a different spatial direction. The three representations are summarized from Ref. [152] and Ref. [153] which can be consulted for a detailed derivation and further reading.

5.2.1 Electric field in radial (r) direction

Since the present problem comes with a cylindrical symmetry, it is not surprising for solutions to rely on Bessel functions. For the calculation of the electric field in radial direction it is most convenient to choose a Green function represented by modified Bessel functions:

$$G(r,\varphi,z;r',\varphi',z') = \frac{1}{\pi L}\sum_{m=0}^{\infty}\sum_{n=1}^{\infty}(2-\delta_{m0})\cos(m(\varphi-\varphi'))\sin(\beta_n z)\sin(\beta_n z')\frac{R_{mn\,1}(r_<)R_{mn\,2}(r_>)}{I_m(\beta_n a)K_m(\beta_n b)-I_m(\beta_n b)K_m(\beta_n a)}, \tag{5.2}$$

with $\beta_n = n\pi/L$. The r-dependence in (5.2) is expressed by the product of

$$R_{mn\,1}(r) = K_m(\beta_n a)I_m(\beta_n r) - I_m(\beta_n a)K_m(\beta_n r)$$

and

$$R_{mn\,2}(r) = K_m(\beta_n b)I_m(\beta_n r) - I_m(\beta_n b)K_m(\beta_n r),$$

with $r_<$ and $r_>$ being a shorthand notation for

$$R_{mn\,1}(r_<)R_{mn\,2}(r_>) = \begin{cases} R_{mn\,1}(r)R_{mn\,2}(r'), & \text{for } a \le r < r' \le b, \\ R_{mn\,1}(r')R_{mn\,2}(r), & \text{for } a \le r' < r \le b. \end{cases} \tag{5.3}$$

The electric field in radial direction is obtained by differentiating (5.2) with respect to the radius. The derivatives in azimuthal and longitudinal direction yield divergent expressions, so that other representations have to be chosen to get the electric field in these directions. Differentiating (5.2) with respect to r yields the expression

$$\frac{\partial}{\partial r}G(r,\varphi,z;r',\varphi',z') = \frac{1}{\pi L}\sum_{m=0}^{\infty}\sum_{n=1}^{\infty}\cos(m(\varphi-\varphi'))\sin(\beta_n z)\sin(\beta_n z')\frac{\partial}{\partial r}\left(\frac{R_{mn\,1}(r_<)R_{mn\,2}(r_>)}{I_m(\beta_n a)K_m(\beta_n b)-I_m(\beta_n b)K_m(\beta_n a)}\right), \tag{5.4}$$

wherein only the r-dependent part, given by (5.3), has to be differentiated

$$\frac{\partial}{\partial r}\left(R_{mn\,1}(r_<)R_{mn\,2}(r_>)\right) = \begin{cases} R'_{mn}(a,r)R_{mn\,2}(r'), & \text{for } a \le r < r' \le b, \\ R_{mn\,1}(r')R'_{mn}(b,r), & \text{for } a \le r' < r \le b. \end{cases}$$

The term depends on the size of the radius with respect to the radial position of the charge deposition and on $R'_{mn}(s,t)$, which is given by

$$R'_{mn}(s,t) = \frac{\beta_n}{2}\left(K_m(\beta_n s)\left(I_{m-1}(\beta_n t)+I_{m+1}(\beta_n t)\right) + I_m(\beta_n s)\left(K_{m-1}(\beta_n t)+K_{m+1}(\beta_n t)\right)\right). \tag{5.5}$$

Charge distributions in TPCs at colliders can often be assumed to be symmetric in azimuthal direction. Here, any terms depending on φ or φ' have to disappear. This can be achieved by skipping the summation over m and setting m to $m = 0$ in (5.2) and (5.4) respectively. Thus, the cosine term vanishes and (5.5)

can be written as

$$R'_{0n}(s,t) = \beta_n \left(K_0(\beta_n s) I_1(\beta_n t) + I_0(\beta_n s) K_1(\beta_n t) \right), \tag{5.6}$$

which simpliefies any calculation of the electric field in radial direction significantly.

5.2.2 Electric field in azimuthal (φ) direction

This innovative representation of the Green's function has been introduced in Ref. [152] and makes use of modified Bessel functions with real arguments but imaginary order,

$$G(r,\pi,z;r',\varphi',z') = \frac{1}{L}\sum_{k=1}^{\infty}\sum_{n=1}^{\infty} \sin(\beta_n z)\sin(\beta_n z') \frac{\cosh\left(\mu_{nk}\left(\pi - |\varphi-\varphi'|\right)\right)}{\mu_{nk}\sinh(\pi\mu_{nk})} \frac{R_{nk}(r)R_{nk}(r')}{N_{nk}^2}, \tag{5.7}$$

wherein the function $R_{nk}(r)$, which is used to formulate the radial dependence, is given by

$$R_{nk}(r,\mu) = L_{i\mu}(\beta_n a) K_{i\mu}(\beta_n r) - K_{i\mu}(\beta_n a) L_{i\mu}(\beta_n r), \tag{5.8}$$

and makes use of the abbrevating term

$$L_{i\mu} = \frac{1}{2}\left(I_{-i\mu}(\beta_n r) + I_{i\mu}(\beta_n r) \right). \tag{5.9}$$

Of major importance in Equations (5.7) to (5.9) is the imaginary order μ_{nk} of the modified Bessel functions. These coefficients have to be chosen carefully to ensure the boundary conditions of a vanishing potential at the radii of the inner and outer field cages. While this is enforced by the construction of (5.8) for the inner radius a, only certain values of μ_{nk} guarantee the same for the outer radius b. These values of μ_{nk} can be calculated by finding the first zeros of function (5.8), where the k-th zero for a chosen order n corresponds to μ_{nk}. Function (5.8) for $r = b$ and continuous μ is shown in figure 5.3a, displaying its oscillatory behavior and the first 17 zeros. Figure 5.3b shows function (5.8) for order $n = 1$ and values of k from one to three, which is equivalent to the first three zeros depicted in Figure 5.3a. As depicted, the function satisfies the boundary condition at inner ($r = a$) and outer ($r = b$) radius for all three values of μ_{nk}. Calculating the correct values for the coefficients μ_{nk} is only part of the problem, as the even with this values the product $R_{nk}(r)$ and $R_{nk}(r')$ yields unscaled values which still have to be normalized. This can be done via the relation

$$\int_a^b R_{nk}(r) R_{ns}(r) \frac{\mathrm{d}r}{r} = \delta_{ks} N_{nk}^2, \tag{5.10}$$

which determines the normalization constant, N_{nk}. It is most convenient to calculate concrete values of N_{nk} by the means of numerical integration, even though an analytical expression for its calculation has been derived in Ref. [152]. It is not an option, due to the big computational demand of this approach.

At this point all the terms in (5.7) are known, hence, the azimuthal field component can be determined by taking the partial derivative with respect to φ, which can be formulated as

$$\begin{aligned} &\frac{\partial}{\partial\varphi} G(r,\varphi,z;r',\varphi',z') = \\ &\quad \frac{1}{L}\sum_{k=1}^{\infty}\sum_{n=1}^{\infty} \sin(\beta_n z)\sin(\beta_n z') \frac{R_{nk}(r)R_{nk}(r')}{N_{nk}^2} \frac{\partial}{\partial\varphi}\left(\frac{\cosh\left(\mu_{nk}\left(\pi - |\varphi-\varphi'|\right)\right)}{\mu_{nk}\sinh(\pi\mu_{nk})} \right). \end{aligned} \tag{5.11}$$

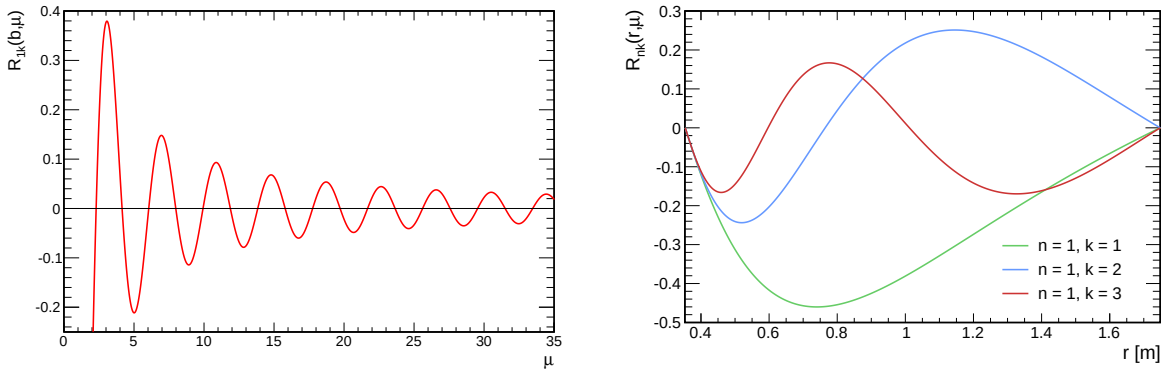

(a) $R_{nk}(r,\mu)$ for $r = b$ and continuous μ.

(b) $R_{nk}(r,\mu)$ for the first three zeros shown in (a).

Figure 5.3: Calculation of the coefficients μ_{nk} of the representation by Bessel functions of imaginary order and real argument.

Again, only the term actually depending on the φ-coordinate has to be differentiated, which resolves to the following solutions

$$\frac{\partial}{\partial\varphi}\left(\cosh\left(\mu_{nk}\left(\pi-\left|\varphi-\varphi'\right|\right)\right)\right)=\begin{cases}-\mu_{nk}\sinh\left(\mu_{nk}\left(\pi-\left(\varphi-\varphi'\right)\right)\right), & \text{for } 0\le\varphi'<\varphi\le 2\pi,\\ \mu_{nk}\sinh\left(\mu_{nk}\left(\pi-\left(\varphi'-\varphi\right)\right)\right), & \text{for } 0\le\varphi<\varphi'\le 2\pi.\end{cases}$$

5.2.3 Electric field in longitudinal (z) direction

Differentiating Green's functions (5.2) and (5.7) with respect to z leads to diverging expressions. Hence, another representation is necessary, one with a convergent derivative in longitudinal direction. Such a representation can be constructed with the help of ordinary Bessel function and is given by

$$G\left(r,\varphi,z;r',\varphi',z'\right)=\\ \frac{1}{2\pi}\sum_{m=0}^{\infty}\sum_{n=1}^{\infty}\left(2-\delta_{m0}\right)\cos\left(m\left(\varphi-\varphi'\right)\right)\frac{R_{mn}\left(r\right)R_{mn}\left(r'\right)}{\bar{N}_{mn}^{2}}\frac{\sinh\left(\beta_{mn}z_{<}\right)\sinh\left(\beta_{mn}\left(L-z_{>}\right)\right)}{\beta_{mn}\sinh\left(\beta_{mn}L\right)}. \tag{5.12}$$

In the above function the complete radial dependence is expressed with the help of the function $R_{mn}(s)$, similar to cases of Green's functions suitable for radial and azimuthal direction. In this case the function is given by

$$R_{mn}\left(r\right)=Y_m\left(\beta_{mn}a\right)J_m\left(\beta_{mn}r\right)-J_m\left(\beta_{mn}a\right)Y_m\left(\beta_{mn}r\right) \tag{5.13}$$

and has similar responsibilities as function (5.8) in the azimuthal case. While (5.13) guarantees a vanishing potential at the inner field cage, $\phi(r = a) = 0$, for arbitrarily chosen β_{mn} these coefficients have to be selected carefully to satisfy the boundary condition at the outer field cage simultaneously, i.e. $\Phi(r = b) = 0$. To determine appropriate coefficients an approach similar to the azimuthal case can be used and the coefficients are obtained by calculating the zeros of

$$J_m\left(x\right)Y_m\left(lx\right)-J_m\left(lx\right)Y_m\left(x\right), \qquad \text{with} \qquad l=\frac{a}{b}. \tag{5.14}$$

With x_{mn} denoting the n-th zero of (5.14), the coefficients β_{mn} are given by the relation $x_{mn} = \beta_{mn} b$. The normalization $\bar{N}^2_{mn}$ depends on these values and can be expressed as

$$\bar{N}^2_{mn} = \frac{2}{\pi^2 \beta^2_{mn}} \left(\frac{J^2_{mn}(\beta_{mn} a)}{J^2_{mn}(\beta_{mn} b)} - 1 \right). \tag{5.15}$$

The electric field in longitudinal direction results from the partial derivative of that variable. As for the representations given by (5.4) and (5.11) the derivative along the other two spatial directions results in a diverging expression. Only the hyperbolic functions in (5.12) depend on the z-coordinate, so that its derivative can be written as

$$\begin{aligned} &\frac{\partial}{\partial z} G(r, \varphi, r', \varphi', z') = \\ &\quad \frac{1}{2\pi} \sum_{m=0}^{\infty} \sum_{n=1}^{\infty} (2 - \delta_{m0}) \cos(m(\varphi - \varphi')) \frac{R_{mn}(r) R_{mn}(r')}{\bar{N}^2_{mn}} \frac{\partial}{\partial z} \left(\frac{\sinh(\beta_{mn} z_<) \sinh(\beta_{mn}(L - z_>))}{\beta_{mn} \sinh(\beta_{mn} L)} \right), \end{aligned} \tag{5.16}$$

with

$$\frac{\partial}{\partial z} \left(\sinh(\beta_{mn} z_<) \sinh(\beta_{mn}(L - z_>)) \right) = \begin{cases} \beta_{mn} \cosh(\beta_{mn} z) \sinh(\beta_{mn}(L - z')), & \text{for } 0 \le z < z' \le L, \\ -\beta_{mn} \cosh(\beta_{mn}(L - z)) \sinh(\beta_{mn} z'), & \text{for } 0 \le z' < z \le L. \end{cases}$$

5.2.4 Implementation

To make use of the calculation methods presented above, they have been implemented in a dedicated software tool. This tools allows to calculate the electric field resulting from arbitrary space charges at any given point in the volume of a TPC. The tool is not implemented into the `Marlin` framework [154] or based on it like most software packages for the ILC. The main reason for this is the required computing time. This applies in particular for the calculation of field values near to the source charge. To obtain these values with a high precision, the summations over the involved series has to be performed up to high orders. This makes these calculations very demanding in terms of computing time and therefore, they should be avoided in the per event simulation of the TPC.

The electric field is calculated in a more general way, to retain a decent computational effort when it is used in the simulation. Computing the field from the exact positions for all charge carriers in the TPC volume is not feasible. Therefore, the charge distribution in the active volume is discretized by dividing the TPC into small voxels. A field map is created for each of these voxels. Each field map consists of discrete set of field values. The steps between the individual values are of the same size as the voxels used for the binning of the charge. To this end, the charge of the voxel in question is set to unity and for all the remaining voxels to zero. This yields a generic set of field maps which can be used to model the electric fields caused by arbitrary charge distributions. This is done by scaling the individual field maps with the appropriate charge values and superimposing them.

In many cases, the distribution of the space charges in a TPC is symmetric in the azimuthal direction. The electric field caused by such distributions is also symmetric in this direction, i.e. its φ-component is zero. In this case, a two-dimensional field map is sufficient and volume of the TPC is only divided in radial and longitudinal direction. An example of the electric field caused by a positive sample charge symmetrically distributed in azimuthal direction is depicted Figure 5.4. The field in radial direction (a) is negative in the lower part of the chamber and positive in the upper part. Even though only the absolute values are shown, the transition from negative to positive field values is clearly visible. The difference in sign is caused by the mirror charges influenced on the inner field and outer field cages. The field lines

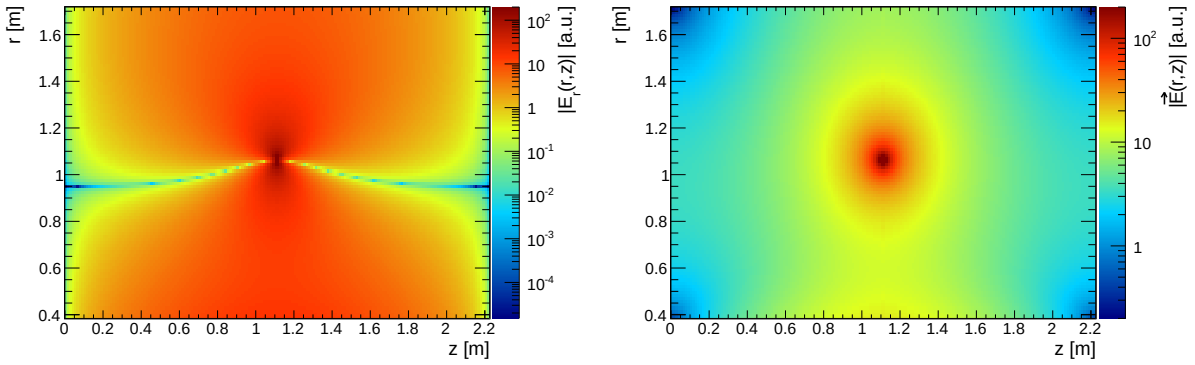

(a) $|E_r(r,z)|$ vs. z,r (b) $|\vec{E}(r,z)|$ vs. z,r

Figure 5.4: Electric field caused by sample charge symmetrically distributed in azimuthal direction. The absolute value of the electric field in radial direction, E_r (a) and the field magnitude $|\vec{E}|$ (b) as a function of the position z,r.

run from the charge deposition towards the field cages which act as drain of the potential. The field is largest close to the space charge and drops towards the boundaries. The decrease is larger towards the endplates where the radial component of the field has to vanish. The distribution of the absolute field values (b) resembles an ellipse. The absolute field values are higher in direction of the field cages, than in direction of the endplates. The field values are smallest where the field cages meet the endplates. This is according the expectations, since both field values have to be zero at the interconnection of both surfaces.

The calculated field maps are stored in generic data class of the `LCIO` data model. This way they are compatible with other software packages developed in the context of the ILC.

5.3 Simulation and reconstruction of tracks in an InGrid-based TPC

As discussed in Section 5.1, `Mokka` does not provide a very detailed simulation of the processes specific to TPCs. More specifically, it performs only the simulation, but not the digitization. The former refers to the interaction of primary particles with the detector, i.e. the generation of energy depositions in the detector. Digitization, in contrast, is refers to the simulation of the detector response to the primary interactions up to a ADC response, i.e. the resulting signal. `Mokka` is a tool for the simulation part only and the remaining steps have to be performed by other tools. For the mass production of events at the ILC this is done by `MarlinReco`, as already indicated in Section 5.1. To get a deeper understanding of the processes taking place in a TPC the digitization has to be performed with more detail. Even though there exists a difference between simulation and digitization in particle physics, both terms are summarized as simulation for the remainder of this work.

A very detailed simulation is available as part of the `MarlinTPC` framework [155]. `MarlinTPC` is developed as a collection of tools for the simulation, reconstruction, and analysis of TPC data in the context of detector developments for the ILC. It is a modular toolkit tailored to work with the event data model implemented by `LCIO`. The modular structure provides an uncomplicated mechanism for the comparison of different heuristics and algorithms, since modules, so-called processors, can be easily exchanged. Furthermore, the usage of `LCIO` as I/O model allows to import data from other ILC software packages, like `Mokka`, without conversion.

5.3.1 Detailed TPC simulation

To investigate the potential of a pixelized readout, which is capable of resolving single primary electrons, an equally detailed detector simulation is required. This means, the simulation has to capable of describing the processes taking place in TPC (see. Chapter 3) at the level of single electrons. `MarlinTPC` incorporates three different simulation chains, i.e. sequences of simulation modules, each with a different level of detail. For the simulation of a pixelized readout, the most detailed simulation chain is required. Its general setup is extensively described in Ref. [156] and Ref. [157], and, therefore only briefly summarized.

The primary ionization is simulated using a parametrization obtained from `HEED`[158]. Electron clusters are placed along an ionization track according to this parametrization. The processor allows for the simulation of curved tracks, due to the presence of a magnetic field. It furthermore includes the simulation of δ-electrons, if their range is larger than 100 µm.

The drift of primary electrons is simulated by a stepping algorithm based on a Runge-Kutta method of forth order. This allows to simulate the drift even in the presence of highly inhomogeneous electric and magnetic fields. No assumptions like constant drift velocity in longitudinal direction or constant $\omega\tau$ (cf. Section 3.2.3) are made, but the drift is determined by solving Equation (3.33) in each step. Since the stepping method also incorporates a self adjusting step size mechanism an optimal performance is obtained for arbitrary field configurations. Displacement from diffusion is applied in each step according to the size of the step to avoid any bias. Figure 5.5a depicts the total transverse diffusion values of drifted single electrons. The distribution is well described by a two-dimensional Gaussian whose width in both direction matches the expectation of $\sigma_{x,y} = 551\,\mu\text{m}^2$.

The simulation of the gas gain has to be done according to the technology used for the gas amplification. For the simulation of a triple GEM stack a parametrization obtained from dedicated measurements is available [68]. The gain is determined for each of the GEMs, taking collection and extraction efficiencies, as well as gain fluctuations into account. The resulting charges are distributed to the underlying pads according to a two dimensional Gaussian distribution as exemplary depicted in Figure 5.5b. For each pad an electronic response is simulated according to the amount of charge it received. Properties of the readout electronics, like sampling frequency, rise time, and dynamic range can be controlled by the user.

Simulation of a pixelized TPC readout

Pixelized TPC readouts are very different from pad based readouts. In case of InGrids, the charges created in the amplification stage are not distributed on multiple channels, but mostly collected on a single pixel. Thus, no detailed simulation of the charge distribution is required. The amount of charge is determined from random values of a Polya distribution (cf. Equation (3.47)). The mean amplification, $\bar{N}$, can be defined by the user, as well as the parameter controlling the width of the distribution, θ.

The electronic response of the charge collecting pixels is also different from pads. For pads, the pulses created by a CSA are measured with an ADC and sampled according to the readout frequency. This allows for a good multiple hit resolution, as hits can be separated by analyzing their pulse shapes. For the simulation of tracks in the TPC of the ILD, the same signal shaping is applied for pixels as pads. This can be considered an idealized pixel chip, since it has unlimited multi-hit capability and an extremely good signal separation due to the faster shaping. Even though an ASIC like this can not be built, it is sufficient for an general assessment of the tracking capabilities in a large TPC. As long as no signal splitting is required in longitudinal direction, i.e. only one track is simulated per event this

[2] Calculated via $\sigma_{x,y} = D_T\ [\mu\text{m}/\sqrt{\text{cm}}]\ \cdot\sqrt{\Delta z\ [\text{cm}]}$ with drift length Δz and transverse diffusion constant D_T.

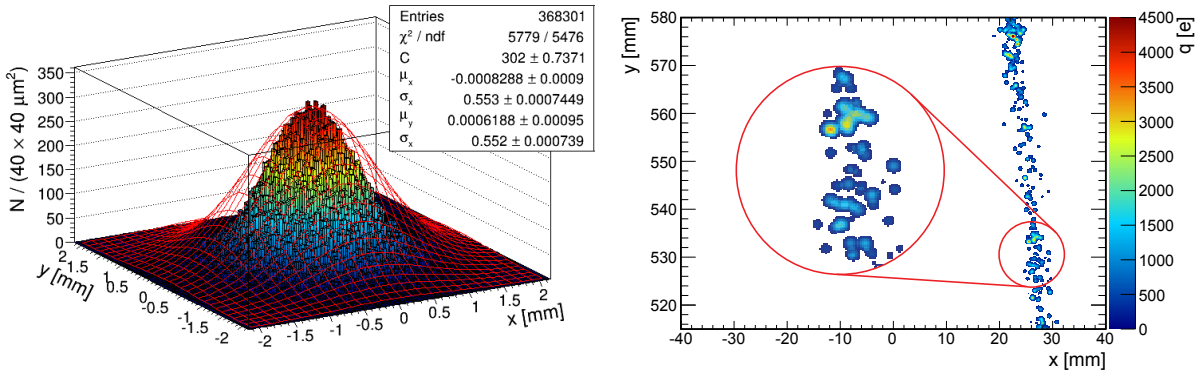

(a) Stepwise applied transverse diffusion.

(b) Charge depositions of a triple GEM stack.

Figure 5.5: Detailed TPC simulation muons emitted perpendicular to the beam pipe. The electrons have drifted an approximate distance of 2150 mm in T2K gas and a drift field of 280 V/cm. (a) Distribution of transverse diffusion values for single electrons and stepwise applied diffusion. (b) Charge depositions on a 100 µm × 100 µm pixel endplate with GEMs as amplification stage.

represents a valid approximation for the electronics of a pixel chip. Moreover, it allows for an easy comparison of different sizes of pads and pixels respectively.

If the length of the signal pulses is of importance the above signal shaping can not be applied anymore and has to be exchanged in favor of a more accurate method. Pixel chips, like the Timepix chip (cf. Section 4.1), measure charges usually by discharging a capacity fed by the CSA. The number of clock cycles required for this is proportional to the detected charge, as the discharging of the capacitor is mostly linear in time. The same scheme is also implemented in the readout chip of the next generation, the Timepix-3 [119]. Thus, pixel chips only return two values per detected signal, the total deposited charge, as measured in clock cycles, and the arrival time of the detected signal. To reproduce this values in a realistic way, a more detailed pulse shaping has been implemented, which determines the length of a signal pulse from a Timepix parametrization curve as described by Equation (4.3) and depicted in Figure 4.3b. This results in a gain dependent distribution of the pulse length. Such distributions are illustrated in Figure 5.6a for several mean values of the gas amplification. The distributions resemble Polya distributions. This is due to the fact, the relation between detected charge and counted clock cycles (cf. ToT-value in Section 4.1), is mostly linear. The non-linear part of the relation can be observed on the left edge of the distribution which does not drop as quickly as a real Polya distribution would. It can be observed that the distributions have an non zero intercept. This is caused by the charge threshold, that has to be exceeded to detect a signal.

The size of the pixels can be chosen by the user by setting their pitch. Thus, the pixels are always assumed to be quadratic in size. The active readout area of the TPC is represented by one large circular chip, with a circular cutout for the inner beam pipe. This is in analogy to the pad layout used in simulations, which is not divided into the actual readout modules too. The pixels are arranged in a square pattern with an edge length of two times the outer radius of the TPC. Afterwards, all pixels whose center is outside of the outer radius or inside the inner radius of the TPC are removed. This results in some pixels protruding into area defined as insensitive. The effect of these pixels is very small, as the pixel pitch, p, is typically well below 1 mm. The maximum distance a single pixel can protrude into the insensitive area is given by $d = \frac{p}{\sqrt{2}}$. Assuming nominal values for the inner and outer radius of $a = 384$ mm and $b = 1718$ mm respectively and a pixel pitch of $p = 1$ mm, the increase of

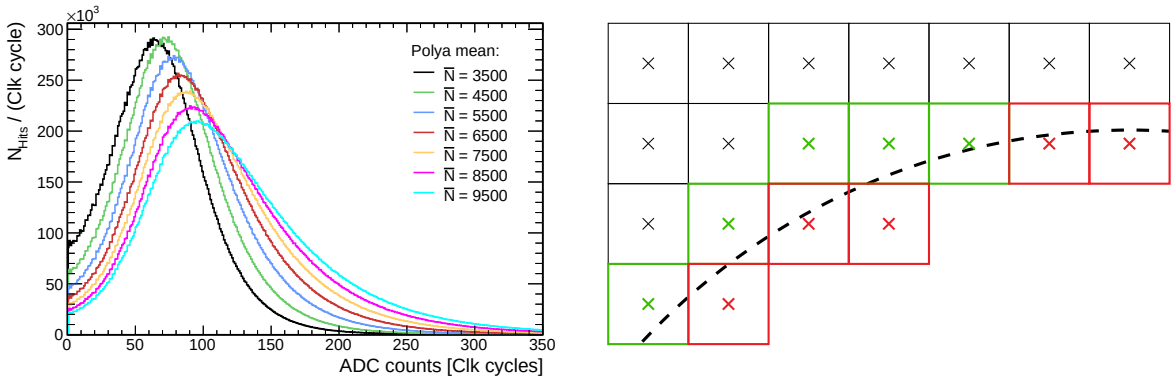

(a) Pulse length distributions for $\theta = 2.0$.

(b) Pixel layout at the inner field cage.

Figure 5.6: Pulse length distribution for different gas gains (a) and schematic of the pixel placing at the inner field cage of the TPC (b). The pixel layout is not to scale.

the sensitive area can be calculated to be well below 0.15 %. The placing of the pixels is sketched in Figure 5.6b. The broken line marks the inner radius of the sensitive volume. Pixels outlined in green are added to the readout, while red pixels are removed from the layout.

5.3.2 Track reconstruction

The reconstruction of the tracks is done just as the simulation with `MarlinTPC`. There exists a detailed reconstruction chain for the reconstruction of tracks in a GEM-based TPC with a pad readout. It covers the whole range from pulse and hit finding over the search for track candidates to the fitting of tracks. There exists flexibility in the choice of the heuristics, for instance, several methods for the finding of hits are available. The existing methods cover test beam data as well as the output of full detector simulations.

Compared to pad case, the existing reconstruction methods for tracks measured in an InGrid-based TPC are very limited. The existing reconstruction method has been developed for the use with prototype data. Therefore, it is only capable of dealing with a small amount of chips, i.e. a small sensitive readout area, and lacks some requirements for method applicable on large scales. For this reason a simplified method is employed. The hit finding is emulated by associating all activated pixels in an event to one track candidate. This can be done only in a background free environment, where each event contains only one single track. Thus, this fake hit finding is only applicable for simulated data, for which the occurrence of backgrounds and the number of tracks can be controlled. For the determination of the track parameters a helix is fitted to the track candidates. No charge information is used for the weighting of the hits. An iterative procedure of cutting and refitting is used for the reaction of outlying hits and δ-electrons. After the fitting, any hit with a residual larger than 2.5 times the root mean square of the tracks residual distribution is removed from the track. Afterwards, the track is refit. The procedure is repeated until the fit converges and shows no further improvement. This method provides a very basic kind of pattern recognition, which works well enough for the fitting of single tracks. The effect it has on the residuals of a track is illustrated by Figure 5.7, showing the residual distribution of a fitted track before (a) and after (b) the iterative refitting. δ-electrons cause long tails in the distributions, as they create a lot of charge when moving away from the track. The mechanism is illustrated in (c), where an example track is shown. The enhanced cutout depicts in blue the charge depositions included in the track fit, while the hits removed from the track are marked in orange. Excluding these hits improves the result of

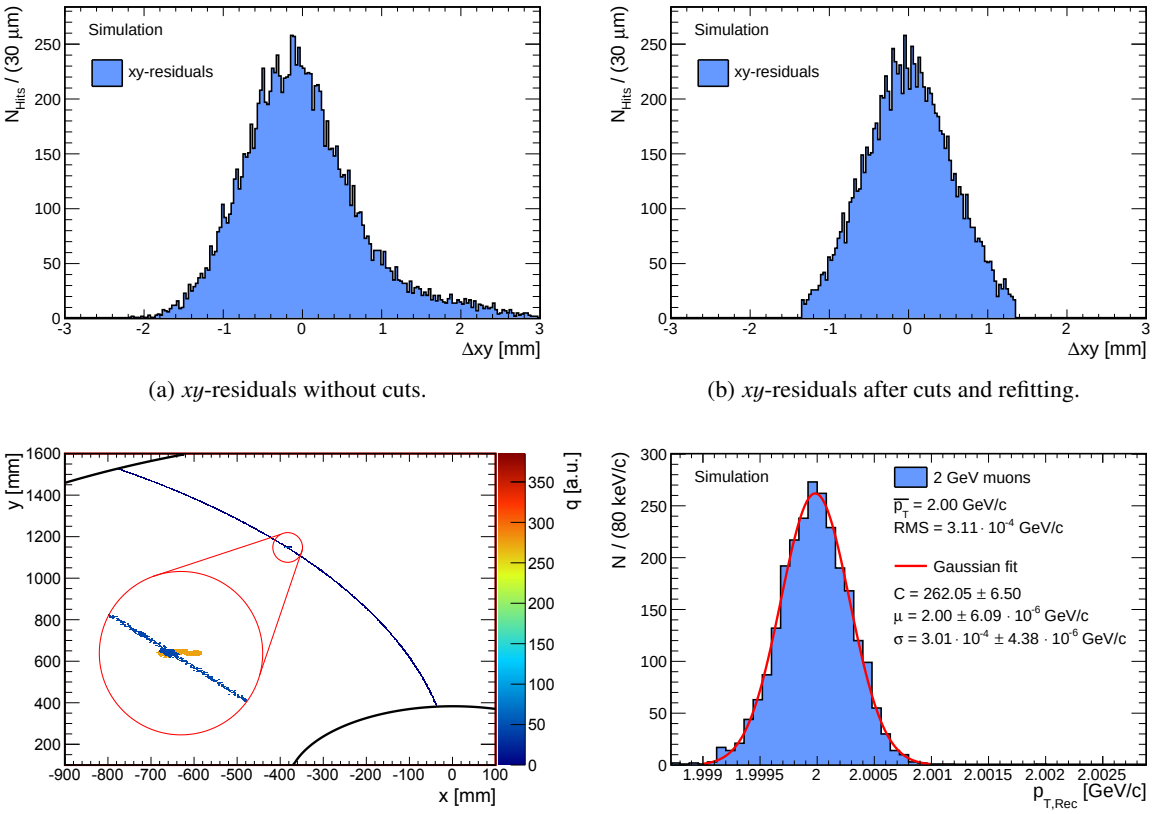

(a) *xy*-residuals without cuts.

(b) *xy*-residuals after cuts and refitting.

(c) Example track with outlier rejection.

(d) Reconstructed momenta of 2 GeV muons.

Figure 5.7: Track fitting by iterative outlier rejection and refitting. Residuals for a fitted track, before (a) and after (b) the iterative cutting of the tracker hits. The removed hits (in this case resulting from δ-electron) are shown in (c). The distribution of the reconstructed momenta of 2 GeV muons (d).

the final track fit significantly, allowing for a very precise reconstruction of the transverse momentum. The reconstructed momenta of 2500 muons emitted under an angle of $\theta = 90°$ to the beampipe are shown in (d). The reconstructed values agree very well with particle momementa of 2 GeV.

A large scale reconstruction scheme applicable to real data has yet to be developed. It requires a full-fledged pattern recognition, capable of identifying and removing δ-electrons as well as the identification of background. The track finding/fitting methods must be tailored to the use with pixel readouts as well. Due to the ability of resolving single primary electrons a very large number of track points is generated for each track. The track finding/fitting method has to work reliably even for such large numbers of hits. This is not the case for many methods developed for a pad based readout. For example, the Hough transformation as implemented in `MarlinTPC` performs well for pads and even for setups with a few pixel chips [110]. On larger scales it is not an option anymore, as the computational effort becomes too large. For this reason, dedicated reconstruction methods are currently under development [159].

5.3.3 Coordinate system

The coordinate system and the parameters used to describe tracks at the ILD is sketched in Figure 5.8. As elaborated in the Section 3.6.2, the TPC at the ILD consists of a large volume, bisected at height of

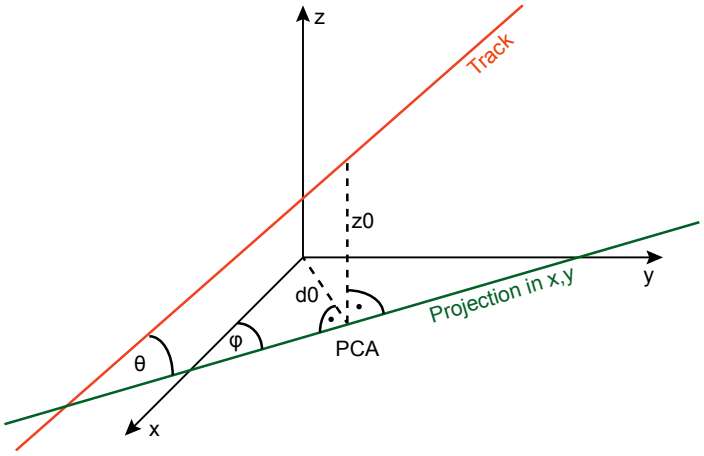

Figure 5.8: The coordinate system in the TPC of the ILD along with the parametrization of a track.

the interaction point (i.e. $z = 0\,\text{mm}$) by a common cathode. Both volumes can be distinguished from each other by the sign of the z-coordinate whereby by convention $z > 0$ denotes the side of the electron beam. Hence, the two readout areas are located at $z = \pm 2225\,\text{mm}$.

Two importan variables to parametrize tracks are $d0$ and $z0$ which denote the distance of the point of closest approach (PCA) of the track to the z-axis and readout plane, respectively.

5.4 Summary

The combination of several software tools allow for a detailed simulation of a pixelized TPC at the ILD, as illustrated in Figure 5.9, which shows whole simulation chain.

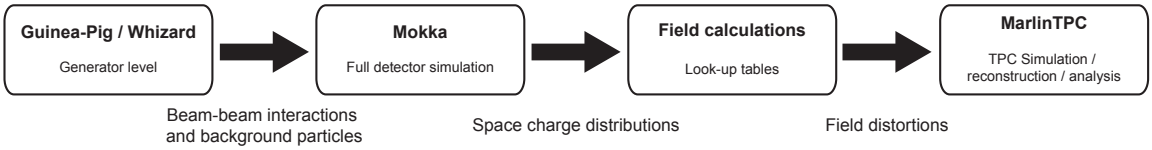

Figure 5.9: Simulation chain for the detailed simulation of the TPC at the ILD, including backgrounds and their impact on the electric drift field.

For the simulation of backgrounds, like $\gamma\gamma \rightarrow$ hadrons and e^+e^--pairs background, a full detector simulation is required. Only this way, all interactions and their influence on the TPC are taken into account. By employing a step size limit, `Mokka` can be tuned to simulate TPC backgrounds with a level of detail sufficiently high for a pixelized readout. Space charge distributions obtained from these simulations yield the input for the calculation of field distortions caused by them. Methods, like those summarized in Section 5.2 permit the exact calculation of electric fields resulting from arbitrary space charge distributions in a collider TPC. As the computational effort of these calculations is substantial, a fast method relying on look-up tables has been developed which allows for fast and easy incorporation of field maps caused by very complex space charge distributions. This way, they can be used in a sophisticated simulation which models all the processes in a TPC to a very high level, starting from primary ionization over electron drift through to a pixelized readout with integrated amplification stage.

Chapter 6

Prospects of a pixelized TPC in the presence of beam induced backgrounds

It has already been stressed in the previous chapters, that a very high momentum resolution is a key requirement for any ILC detector and in particular for its tracking systems. The TPC of the ILD has been designed to meet this requirement, but it has to be guaranteed, that it will do so even in the presence of backgrounds. This applies also to a pixelized TPC. Sources of background have been discussed in Section 2.2.2. They are basically beam induced and rather low compared to hadron colliders. They still affect the operation of a detector. Hence, they have to be included in performance studies.

For TPCs backgrounds typically manifest in the form of charge depositions, in the sensitive volume. More specifically, background processes produce electron-ion pairs in the same way as photons and charged particles (cf. Section 3.1). The resulting electrons may interfere with the reconstruction of physics events and are the major contribution to the occupancy of the readout channels. The ions, in contrast, need a long time to drift to the cathode where they are finally absorbed. Thus, a considerable amount of quasi-stationary ions can accumulate in the volume of the TPC and distort the drift field, as discussed in Section 3.6.1. These backgrounds have to be taken into account in a detailed simulation of a TPC for the ILD. The methods and tools introduced in Chapter 5, allow to simulate an InGrid-based ILD-TPC including backgrounds effects, such simulations have been performed for two center-of-mass energies of the ILC. The value of $\sqrt{s} = 500\,\text{GeV}$ represents the maximum energy foreseen by the baseline design, while the higher energy of $\sqrt{s} = 1\,\text{TeV}$ will be only accessible after an upgrade of the collider (cf. Chapter 2).

The simulation of space charges resulting from the two main backgrounds and their spatial distribution is discussed in Section 6.1 of this chapter. Next, the influence of the detector backgrounds on the occupancy of readout channels is addressed in Section 6.2. The field distortions in caused by charge depositions due to detector backgrounds and their influence on drifting electrons is discussed in Section 6.3. Subsequently, the pieces are put together and the impact of field distortions on the momentum resolution of a pixelized TPC is examined in detail (Section 6.4). Consequently, the chapter is briefly summarized in Section 6.5.

6.1 Space charges from beam induced backgrounds

To include charge depositions resulting from background processes in the simulation of a pixelized TPC for the ILD, the main background processes (cf. Section 2.2.2) are simulated with `Mokka` as described

e^-−beam	e^+−beam	σ [pb]	N/BX
B	B	230 318.0	0.63
B	W	152 207.0	0.42
W	B	152 174.0	0.42
W	W	98 525.1	0.27
Total		633 224.1	1.74

(a) $\sqrt{s}$ =500 GeV

e^-−beam	e^+−beam	σ [pb]	N/BX
B	B	273 742.0	1.37
B	W	210 364.0	1.05
W	B	210 415.0	1.05
W	W	124 809.0	0.62
Total		819 330.0	4.10

(b) $\sqrt{s}$ =1 TeV

Table 6.1: Cross sections for the $\gamma\gamma \rightarrow$ hadrons background processes and the corresponding occurrences per bunch crossing. B and W indicate beamstrahlung and Weizsäcker-Williams photons respectively [160].

in Section 5.1 of the previous chapter. A comprehensive list of the simulation parameters is given in Table B.3 which can be found in Appendix B.

The simulation of the e^+e^--pair backgrounds is straight forward. The output of `Guinea-Pig` yields one event of e^+e^--pairs induced from beamstrahlung per bunch crossing. Hence, the simulation of 1312 and 2625 events for center-of-mass energies of 500 GeV and 1 TeV respectively yields the total occurrence of e^+e^--pairs during a bunch train. The corresponding beam parameters are listed in Table 2.2 where the ILC and the structure of its beams are discussed.

In the case of $\gamma\gamma \rightarrow$ hadrons the situation is different. The occurrence of this background process is determined by its cross section, σ, and the luminosity per bunch crossing, $\mathcal{L}_{BX}$. The number of events per bunch crossing, N_{BX}, can by calculated from these parameters via

$$N_{BX} = \mathcal{L} \cdot \sigma \qquad \text{with} \qquad \mathcal{L}_{BX} = \frac{\mathcal{L}}{f_{rep} \cdot n_b} \tag{6.1}$$

where f_{rep} is the number bunch trains per second and n_b the number of bunches per train. The process $\gamma\gamma \rightarrow$ hadrons can be can be divided into four subprocesses depending on the contribution from beamstrahlung photons and Weizsäcker-Williams photons. The numbers calculated for the four subprocesses and both center-of-mass energies are listed in Table 6.1. The total number of $\gamma\gamma \rightarrow$ hadrons events per bunch crossing computes to 1.74 and 4.10 for $\sqrt{s}$ = 500 GeV and $\sqrt{s}$ = 1 TeV respectively.

The simulation of these backgrounds yields energy depositions in the TPC volume, which relate to the number of electron-ion pairs by the ratio of the deposited energy, E_D, and the average ionization potential, w_I = 26 eV [44], of the gas. The amount of charge deposited per bunch crossing in the sensitive volume of the TPC is depicted in Figure 6.1. The charge depositions from e^+e^--pairs follow Gaussian distributions with mean value, μ, and width, σ. At $\sqrt{s}$ = 500 GeV, as shown in (a), mean value and width are given by

$$\mu_{500\,\text{GeV}} = 2.19 \times 10^5\ e\ \pm 1.54 \times 10^3\ e \qquad \text{and} \qquad \sigma_{500\,\text{GeV}} = 4.40 \times 10^4\ e\ \pm 1.33 \times 10^3\ e,$$

respectively. For a center-of-mass energy of 1 TeV, as depicted in (c), these values come out as

$$\mu_{1\,\text{TeV}} = 6.83 \times 10^5\ e\ \pm 1.85 \times 10^3\ e \qquad \text{and} \qquad \sigma_{1\,\text{TeV}} = 7.84 \times 10^4\ e\ \pm 1.54 \times 10^3\ e.$$

From these numbers it can be concluded that the charge deposition per bunch crossing rises approximately by a factor of three when the center-of-mass energy is upgraded to 1 TeV. Thus, the total charge deposition due to e^+e^--pairs can be expected to be approximately six times higher than for

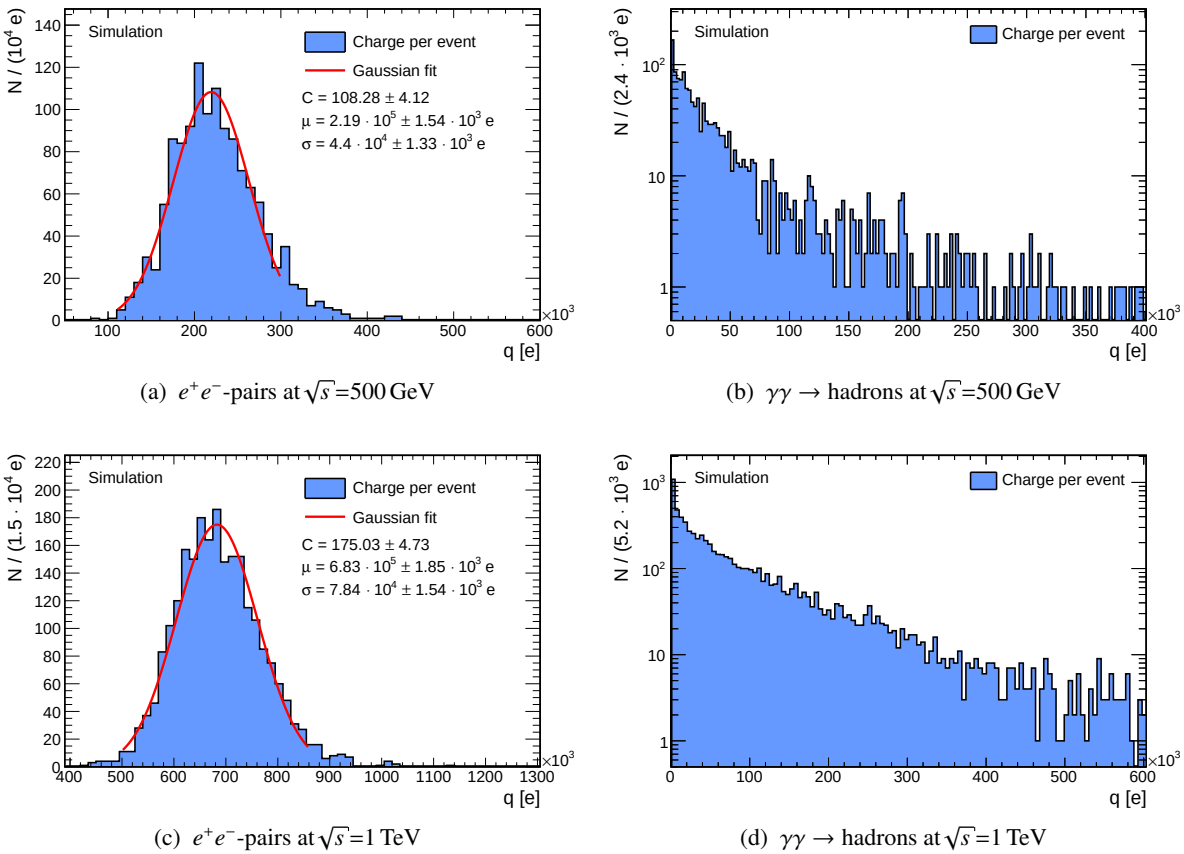

(a) e^+e^--pairs at $\sqrt{s}$=500 GeV

(b) $\gamma\gamma \rightarrow$ hadrons at $\sqrt{s}$=500 GeV

(c) e^+e^--pairs at $\sqrt{s}$=1 TeV

(d) $\gamma\gamma \rightarrow$ hadrons at $\sqrt{s}$=1 TeV

Figure 6.1: Charge deposition per bunch crossing due to background processes. In (a) and (b) the charge depositions from e^+e^--pairs and $\gamma\gamma \rightarrow$ hadrons respectively are shown for a center-of-mass energy of 500 GeV. In (c) and (d) the same distributions are shown for a center-of-mass energy of 1 TeV. The amount of charge for the hadronic backgrounds is shown in logarithmic scale.

$\sqrt{s}$ = 500 GeV, as the upgrade also includes an increase of the number of bunches per train by a factor of approximately two (cf. Table 2.2).

The case of $\gamma\gamma \rightarrow$ hadrons backgrounds behaves very differently from the case of e^+e^--pairs. As depicted in (b) and (d), the distributions do not resemble a Gaussian. The amount of charges deposited by hadrons roughly follows an exponential distribution. Only the largest charge depositions are compatible in size to the average amount deposited by e^+e^--pairs. Still the amount of charge is considerable and cannot be neglected when backgrounds are discussed.

6.1.1 Space charge distributions

Concerning charge depositions in a TPC, not only the amount of charge is of importance, but also its spatial distribution. The radial behavior of the charge depositions caused by e^+e^--pairs is shown in Figure 6.2a for $\sqrt{s}$ = 500 GeV and in Figure 6.2b for $\sqrt{s}$ = 1 TeV. Plotted is in each case the charge density, ρ, as a function of the radius, r. The charge density is given by the amount of charge in a unit volume. Thus, it takes into account that a step in the radial direction can represent different volumes, depending on the absolute value of the radius. The charge densities show a strong dependence on the radius which can be described by a quadratic decrease towards higher radii.

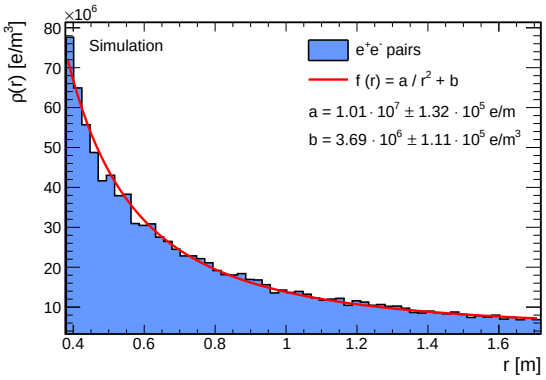

(a) Radial distribution at $\sqrt{s}$ =500 GeV

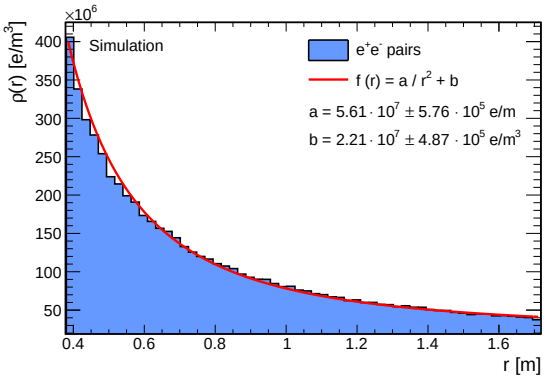

(b) Radial distribution at $\sqrt{s}$ =1 TeV

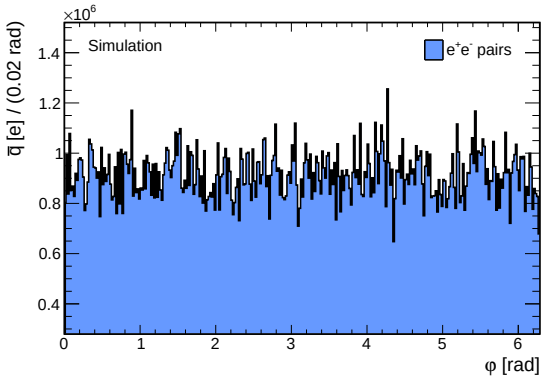

(c) Azimuthal distribution at $\sqrt{s}$ =500 GeV

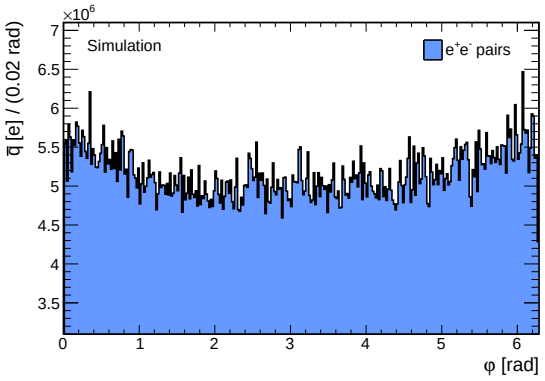

(d) Azimuthal distribution at $\sqrt{s}$=1 TeV

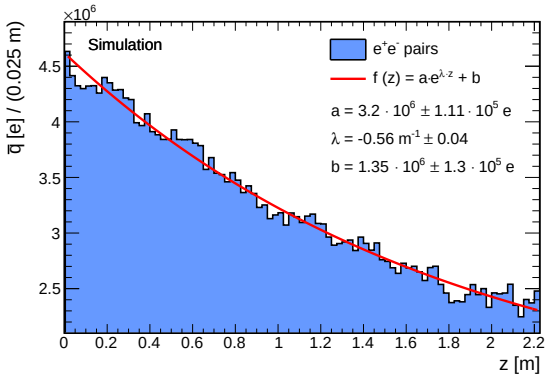

(e) Longitudinal distribution at $\sqrt{s}$ =500 GeV

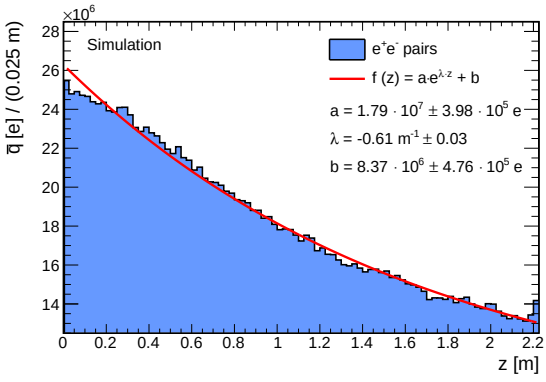

(f) Longitudinal distribution at $\sqrt{s}$ =1 TeV

Figure 6.2: Spatial distribution of space charges caused by e^+e^--pairs. The distributions as a function of the azimuthal angle (c,d) are averaged over r and z. The distributions as a function of the z-coordinate (e,f) are averaged over φ and z.

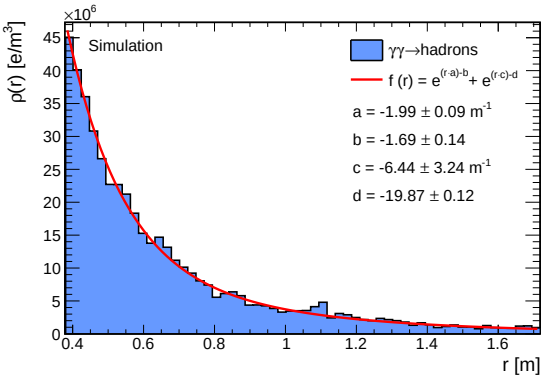

(a) Radial distribution at $\sqrt{s}$ =500 GeV

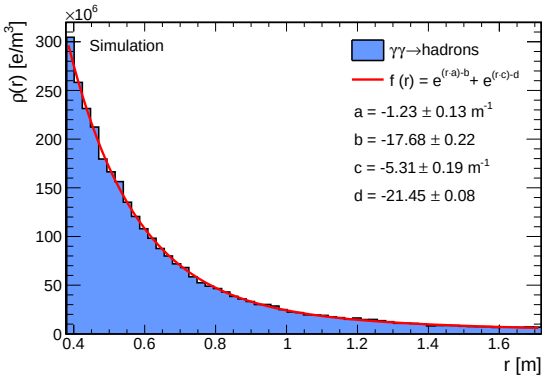

(b) Radial distribution at $\sqrt{s}$ =1 TeV

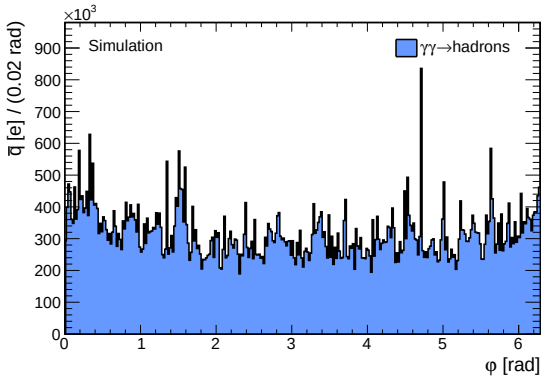

(c) Azimuthal distribution at $\sqrt{s}$ =500 GeV

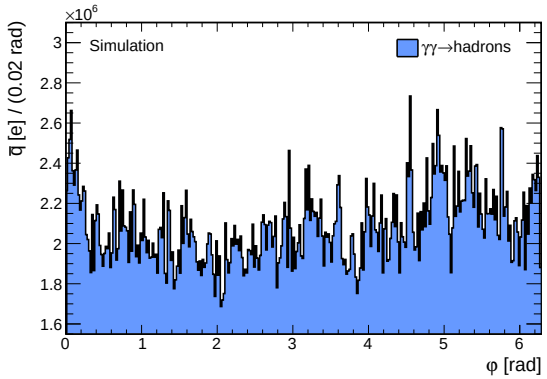

(d) Azimuthal distribution at $\sqrt{s}$ =1 TeV

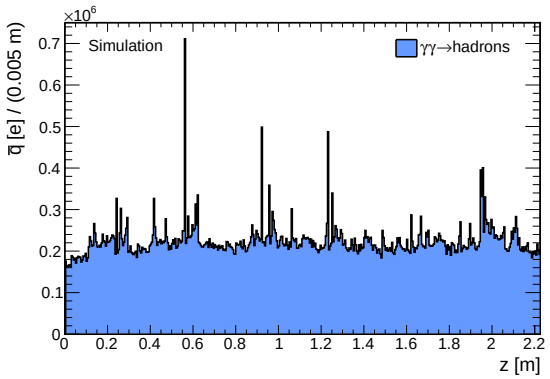

(e) Longitudinal distribution at $\sqrt{s}$ =500 GeV

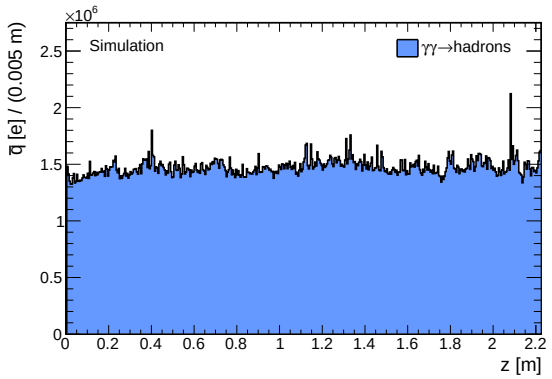

(f) Longitudinal distribution at $\sqrt{s}$ =1 TeV

Figure 6.3: Spatial distribution of space charges caused by $\gamma\gamma \rightarrow$ hadrons. The charge distributions as a function of the z-coordinate (a,b) are scaled to unit volume, while the distributions as function of the azimuthual angle, φ, (c,d) and z-coordinate (e,f) are averaged over r, z and r, φ, respectively.

The charge distributions for e^+e^--pairs in azimuthal direction are shown in Figure 6.2c and Figure 6.2d. The charge is plotted as a function of the azimuthal angle φ. In this case it is not necessary to use the charge densities, as equidistant steps in φ-direction represent volumes of the same size. The distributions show for both center-of-mass energies some fluctuations around their mean values, but no general dependency on the φ-coordinate is observed.

The charge distribution in longitudinal, z, direction is shown for e^+e^--pairs in Figure 6.2e and Figure 6.2f. The amount of charge deposited in TPC decreases rapidly with increasing distance to the interaction point, i.e. increasing values of the z-coordinate. The behavior can be described by an exponential function as indicated in the two figures.

The space charges resulting from $\gamma\gamma \rightarrow$ hadrons processes are plotted in the same way as function of the spatial coordinates as for the charges deposited by e^+e^--pairs. Figure 6.3a and Figure 6.3b depict the charge density, ρ, as function of the radius, r, for both center-of-mass energies. Similar to the e^+e^--pairs case, the charge density strongly depends on the radius. It highest close to the inner beam pipe and drops even more rapidly for increasing radii than for e^+e^--pairs. The decrease can be described by a combination of two exponential functions for both center-of-mass energies.

The dependency on the azimuthal angle φ, is depicted in Figure 6.3c for $\sqrt{s} = 500\,\text{GeV}$ and in Figure 6.3d for $\sqrt{s} = 1\,\text{TeV}$. The distributions show some statistical fluctuations around an average value of. In contrast to the case of e^+e^--pairs both distributions show a few spikes indicating large localized charge depositions. In general the distributions show no systematic dependency on the azimuthal angle.

The charge distribution in longitudinal direction from e^+e^--pairs and $\gamma\gamma \rightarrow$ hadrons are very different from each other. For the hadronic background the distributions are depicted in Figure 6.3e for a center-of-mass energy of 500 GeV and in Figure 6.3f for the 1 TeV case. In contrast to the distributions from e^+e^--pair backgrounds discussed above, no systematic dependency on the z-coordinate is observed. The amount of charge fluctuates around an average value, similar to the distributions for azimuthal angle. Moreover, isolated spikes, representing large localized charge depositions. Apart from these spikes, the charge depositions can be regarded as equally distributed along the z-coordinate.

Some general conclusions can be draw from the charge distributions, as they have been described above. The deposited charge strongly depends on the radius. This is the consistent with the expectation of both backgrounds being focused in the very forward direction (cf. Section 2.2.2). The same applies for the missing azimuthal dependency. For the $\gamma\gamma \rightarrow$ hadrons backgrounds, spikes indicating large localized charge depositions are observed. These result from single events creating large amounts of charge in the TPC. From Figure 6.1 it is evident that these events are rare. The spikes in the distributions are much more prominent for $\sqrt{s} = 500\,\text{GeV}$, than for $\sqrt{s} = 1\,\text{TeV}$. This indicates, that these events perish for $\sqrt{s} = 1\,\text{TeV}$ in the much higher statistics.

6.2 Occupancy

With the distribution of background charge depositions at hand, the occupancy can be determined. The occupancy in a TPC depends on several factors, like the granularity of the readout, electronics shaping of the detected signals. Pixelized readouts offer a much higher segmentation of the readouts area, hence, a much lower occupancy of the readout channels is expected.

The pixel/pad occupancy is a measure for the amount of pixels/pads detecting a signal during the course of a bunch train. To assess it, all electrons created by background processes are used as input for the detailed TPC simulation as described in Section 5.3.1. The electrons are drifted in T2K gas with a drift field of 280 V/cm (corresponding to a drift velocity of $v_{drift} = 78.87\,\text{mm}/\mu\text{s}$) to the anode. The simulation is performed with a readout frequency of $f = 40\,\text{MHz}$ for various segmentations of the

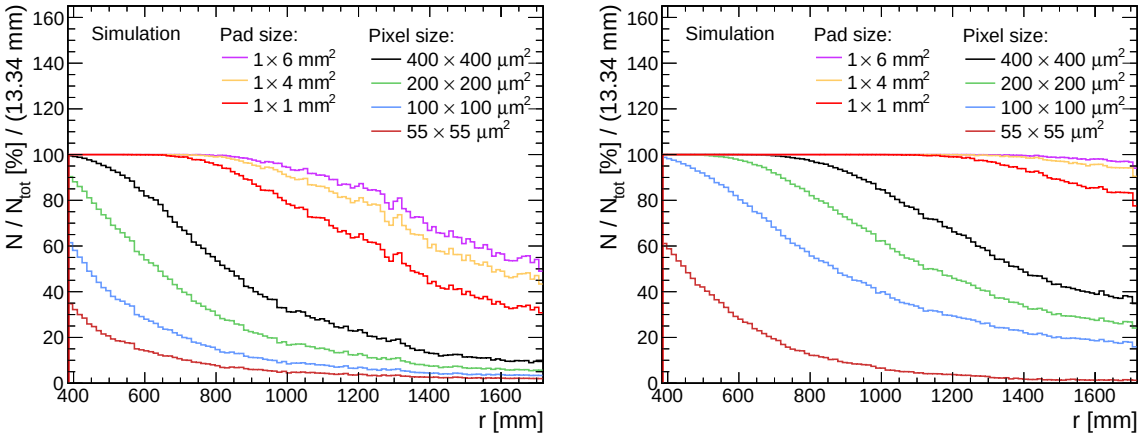

(a) $\sqrt{s}$ = 500 GeV (b) $\sqrt{s}$ = 1 TeV

Figure 6.4: Pixel/pad occupancy for various pixel/pad sizes at a center-of-mass energy of 500 GeV (a) and at a center-of-mass energy of 1 TeV (b).

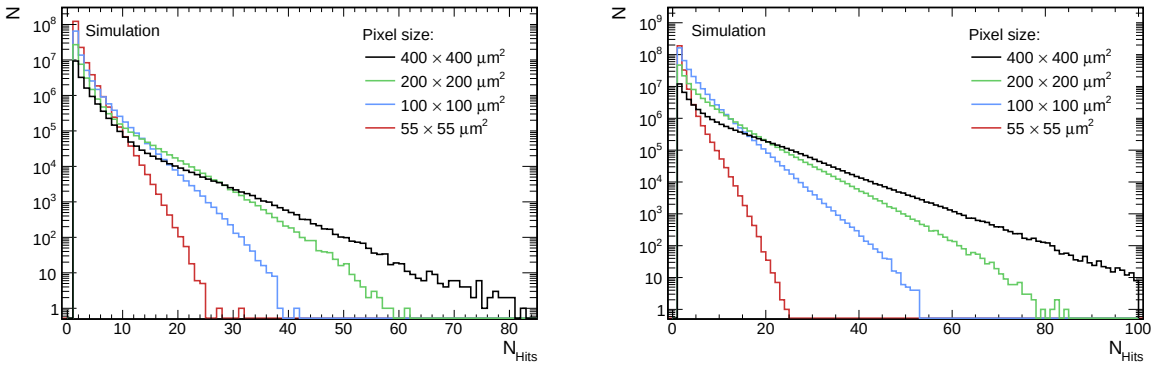

(a) $\sqrt{s}$ = 500 GeV (b) $\sqrt{s}$ = 1 TeV

Figure 6.5: Number of hits per pixel for four pixel sizes. Illustrated are values for a center-of-mass energy of 500 GeV (a) and 1 TeV (b).

readout area. While the gas gain is always fixed to 5000, GEMs are used for the amplification in case of a pad-based readout and InGrids in case of a pixelized readout.

Pad sizes of $1 \times 6\,\mathrm{mm}^2$, $1 \times 4\,\mathrm{mm}^2$ and $1 \times 1\,\mathrm{mm}^2$ have been examined. The results are depicted as a function of the radius in Figure 6.4 for backgrounds at $\sqrt{s}$ = 500 GeV in (a) and $\sqrt{s}$ = 1 TeV in (b) respectively. At a center-of-mass energy of 500 GeV basically all pads up to a radius of approximately 900 mm receive a charge signal at some point of the bunch train. This value decreases for higher radii, but is still in the range of 20 % to 50 %, depending on the pad size, at the outer radius of the TPC. For a center-of-mass energy of 1 TeV the amount of occupied pads is much higher. For pad sizes of $1 \times 4\,\mathrm{mm}^2$ and $1 \times 6\,\mathrm{mm}^2$ the fraction of pads detecting a signal barely decreases at all. For a pad size of $1 \times 1\,\mathrm{mm}^2$ the pad occupancy drops to about 80 %. Pads that small are already at the limit of the technically feasible, as the routing of their connections to the readout electronics is virtually impossible for so many pads.

Pixels with a pitch of 400 µm, 200 µm, 100 µm and 55 µm are simulated and compared with the pad occupancies. In this case, the amount of pixels receiving a charge signal during a bunch train is much smaller than for pads. The pixel occupancy for large pixels, i.e. pixels with a pitch of 200 µm and 400 µm, comes close to a value 100 % near to the inner beam pipe. For smaller pixels, i.e. pixels with a pitch of 100 µm and 55 µm, the occupancy is much lower. In any case, the pixel occupancy drops rapidly with a growing distance to the inner beam pipe. At a center-of-mass energy of 1 TeV, the pixel occupancy rises to 100 % for all but the smallest considered pixel size. Still, it decreases quickly towards larger radii and is much smaller than the observed pad occupancy. Given the high occupancy at small radii the readout ASIC should have the ability to detect multiple hits during a bunch train combined with a sufficiently short shaping time to resolve these hits in z-direction.

As the stated values for the pixel occupancy arise from background only, it can be concluded that any chip used for a pixelized readout requires the capability to detect multiple hits during a bunch train. The number of hits per pixel is illustrated in Figure 6.5, assuming a readout frequency of 40 MHz. The size of the pixels has a strong influence on the number of hits per pixel. At a center-of-mass energy of 500 GeV approximately 80 % of all activated pixels with a pitch of 55 µm detect only one signal during the course of a bunch train. For larger pixel sizes, the amount of pixels receiving a single hit lies between 71 % (100 µm pixel pitch) and 55 % (400 µm pixel pitch) for $\sqrt{s} = 500\,\text{GeV}$. At the higher center-of-mass energy of 1 TeV the situation is different. For the smallest pixel size of $55 \times 55\,\mu\text{m}^2$, nearly no change can be observed and the amount of pixels detecting one hit and less than five hits is 80 % and 99 %. Also the maximum number of signals per pixels remains at 25 hits, with just some few outliers at higher values. For larger pixel sizes, the number of pixels detecting one hit drops by approximately 20 %. A difference can be observed for the amount of pixels detecting less than five hits which is given by 92 %, 83 % and 74 % for pixels with a pitch of 100 µm, 200 µm and 400 µm respectively.

It is apparent from the above values that with a pixel size of $100 \times 100\,\mu\text{m}^2$ the ratio of pixels detecting less than five hits during the course of a bunch train is above 90 % for both center-of-mass energies. This indicates that it should be possible to detect more than 90 % of the electrons arriving at the readout individually if the readout ASIC features multi-hit capability of $N_{hits}^{max} \geq 5$, provided that the electrons are sufficiently separated in z-direction. This is of particular importance if the time required to measure a charge deposition on a pixel is high. The number of clock cycles (i.e. time bins) required for the readout of a complete bunch train is given by

$$t_{readout} = n_b \cdot \Delta t_b + \frac{l \cdot f}{v_{drift}} \tag{6.2}$$

where the first term with number of bunch crossings, n_b, and bunch separation, Δt_b, describes the length of a bunch train and the second term the time required for the readout of one TPC volume. For values of n_b and Δt_b as stated in Table 2.2, a chamber length of 2225 µm and frequency and drift velocity as stated above, $t_{readout}$ computes to 1855 µs and 2025 µs for center-of-mass energies of 500 GeV and 1 TeV respectively. Comparing these numbers with the mean pulse length of 72 clock cycles (cf. Figure B.2 in Appendix B.2) it can be concluded that the probability for pulses resulting from two electrons being merged together is rather low.

If each single electron is detected on a single pixel it can be argued whether it is necessary to measure the charge at all, as this only provides a measurement of the fluctuations of the gas gain. The simultaneous measurement of charge and time is for Timepix basically eligible for two reasons. First, charge measurements allow to correct time measurements for the timewalk effect (cf. Reference [114]). Second, the amount of charge detected on a pixel can indicate whether the charge deposition results from one or two primary electrons. If timewalk effects are of no concern, charge measurements could

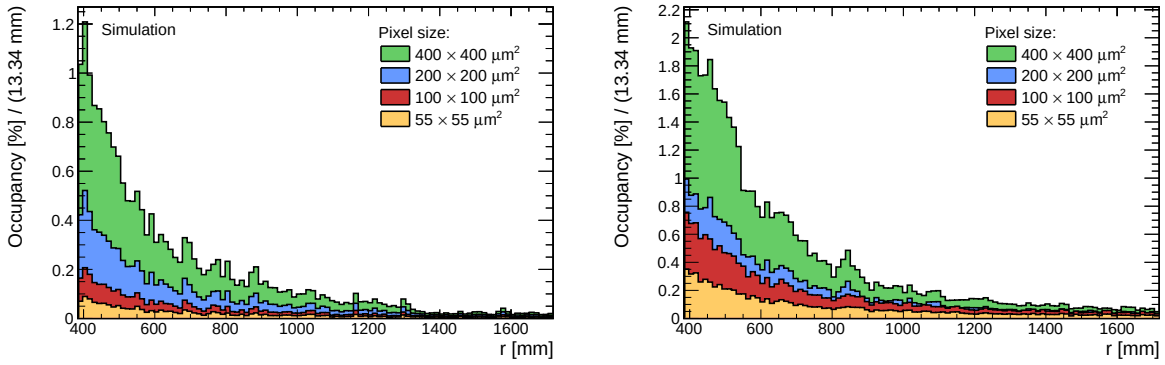

(a) $\sqrt{s} = 500\,\text{GeV}$ (b) $\sqrt{s} = 1\,\text{TeV}$

Figure 6.6: Voxel occupancy caused by backgrounds at a center-of-mass energy of 500 GeV (a) and 1 TeV (b) for for four different pixel sizes and readout frequency of 40 MHz.

be exchanged for threshold measurements. Multiple threshold levels, as implemented for example in the Medipix-3 [161] could be used to check for the number of electrons causing the deposition and thus, replace a detailed charge measurement. Such circuitry can be implemented to be much faster than the discharging of a capacitor and can reduce the deadtime significantly.

6.2.1 Voxel occupancy

The average[1] three-dimensional occupancy, or voxel occupancy, is the ratio of three-dimensional cells (voxels) receiving a signal and the total number of voxels. The size of a voxel is given in $r\varphi$-direction by the segmentation of the readout, which is the pixel size, and in z-direction by the length of a time sample multiplied with the drift velocity. For the above values of drift field and sampling frequency the length of a voxel computes to $\Delta z_{voxel} \approx 2\,\text{mm}$.

The voxel occupancy for four pixels sizes is depicted in Figure 6.6 as a function of the radius for both center-of-mass energies. It allows to check for the above conclusions on the single electron detection efficiency. In case of each single electron being individually detected by a single pixel in a single time bin a scaling effect should be visible. The that if full efficiency is reached at a given pixel size the three-dimensional occupancy should drop for smaller pixels according to the difference in size of the pixels. This means n times smaller pixels yield a n times smaller occupancy as the amount of activated pixels remains constant while their total number is increased. In Figure 6.6 this effect can be seen for both center-of-mass energies when comparing the occupancies for a pixels with a size of $100 \times 100\,\mu\text{m}^2$ and $50 \times 50\,\mu\text{m}^2$. The agreement is not perfect which indicates that full single electron efficiency is reached at a pixel size slightly smaller than $100 \times 100\,\mu\text{m}^2$.

Nevertheless, the largest amount of occupied voxels is roughly 1.2 % and 2.1 % for $\sqrt{s} = 500\,\text{GeV}$ and $\sqrt{s} = 1\,\text{TeV}$ respectively, which demonstrates the extremely low occupancy even for the largest pixel pitch of 400 µm and the comparatively long pulses.

[1] Averaged over φ and z.

6.3 Distortions of the electric field

Methods for calculating the electric field caused by a space charges in a collider TPC have been discussed in Section 5.2. These methods can be used to determine the total field distortions caused by the backgrounds from e^+e^--pairs and $\gamma\gamma \rightarrow$ hadrons. In general, the cause of the field distortions can be divided into primary and secondary ions as discussed in Section 3.6.1. They are treated differently at the calculation of the electric field as elaborated below.

6.3.1 Distortions caused by primary ionization

As previously discussed, the electric field is computed from precalculated field maps which have been scaled with the appropriate amount of charge. Each of these field maps results from the charge of a single voxel. The amount of charge in this voxel is determined by numerical integration of the space charge distributions discussed in Section 6.1.1 over the volume of the voxel. Since the charge distributions can be assumed to be symmetric in azimuthal direction, a two-dimensional field map is sufficient. The charge values are most easily obtained by integration of the charge density functions in radial direction. These functions are scaled to unit volume, thus, the integration in longitudinal direction has to take this into account. This is done by scaling the integral of the longitudinal distribution to unity.

The charge density functions presented in Figure 6.2 and Figure 6.3 are averaged over the whole length of the TPC volume. Using them to determine the amount of charge at any given z-position is only valid, if they are constant in longitudinal direction. This is examined with the help of Figure 6.7. It depicts two kinds of graphs for the considered background processes and center-of-mass energies. For the graphs on the left hand side, the TPC volume is divided into slices of 25 mm along the z-axis. For each of this slices, the charge distribution is obtained as function of the radius. These charge distributions are scaled to unity and plotted into a common graph. This way, the deviation from the mean value can be determined for each z-slice and for each bin in radial direction. The histogram of these deviations yields the distributions on the right hand side. The x-axis indicates the percentaged deviation and the y-axis the occurrences. The distributions can be described by Gaussian functions for all considered background processes and center-of-mass energies. The distributions of the e^+e^--pair backgrounds are more narrow than those of the $\gamma\gamma \rightarrow$ hadrons backgrounds. At a center-of-mass energy of 500 GeV it is approximately $\sigma = 0.10$ for the e^+e^--pairs and $\sigma = 0.17$ for the $\gamma\gamma \rightarrow$ hadrons background. For the higher center-of-mass energy of 1 TeV these values change to $\sigma = 0.06$ and $\sigma = 0.09$ respectively. Furthermore, it can be observed that the distributions for the $\gamma\gamma \rightarrow$ hadrons background have small tail towards higher values. The tails have the same origin as the spikes in the spatial charge distributions mentioned in Section 6.1.1. They are caused by individual $\gamma\gamma \rightarrow$ hadrons events depositing large amounts of charge in the sensitive volume.

The following conclusions can be drawn. The deviation of the radial charge distribution in dependence of the z-position deviates according to a Gaussian distribution around its mean value. Hence, the mean value plus a safity margin of 2.5σ provides an upper limit for the radial distribution which can be applied at all z-positions.

The primary ions present in the sensitive volume of a TPC are not only caused by backgrounds from one bunch train, but from three different bunch trains. They drift towards the cathode in the same way as explained for secondary ions in Section 3.6.2. The phenomenon is illustrated in Figure 6.8 for the $\gamma\gamma \rightarrow$ hadrons background at a center-of-mass energies of 500 GeV and 1 TeV in (a) and (b) respectively. The charge distribution in radial direction remains unchanged during the drift. Thus, the primary ionization can be determined by applying proper scalings and superposition.

The resulting field distortions for both backgrounds combined are depicted in Figure 6.9 for both

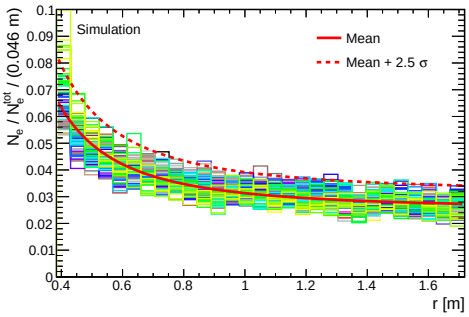

(a) e^+e^--pair background at $\sqrt{s}$ = 500 GeV

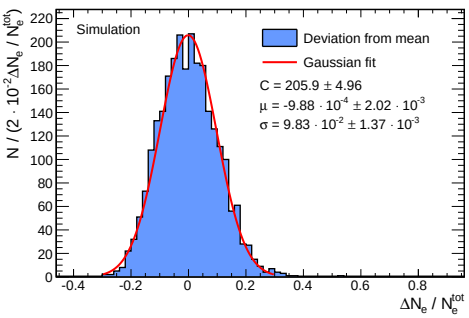

(b) e^+e^--pair background at $\sqrt{s}$ = 500 GeV

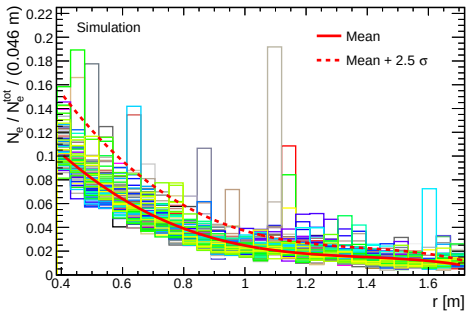

(c) $\gamma\gamma \rightarrow$ hadrons background at $\sqrt{s}$ = 500 GeV

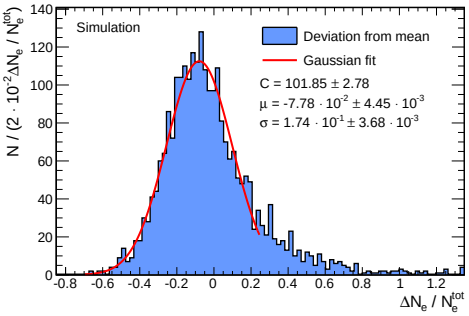

(d) $\gamma\gamma \rightarrow$ hadrons background at $\sqrt{s}$ = 500 GeV

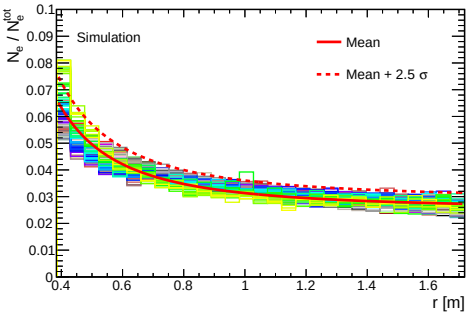

(e) e^+e^--pair background at $\sqrt{s}$ = 1 TeV

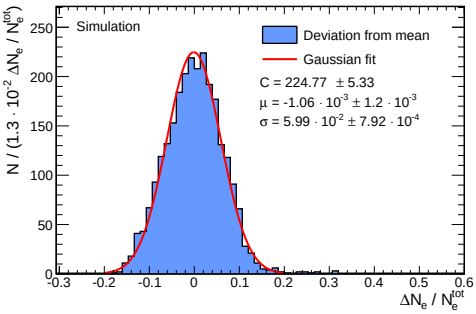

(f) e^+e^--pair background at $\sqrt{s}$ = 1 TeV

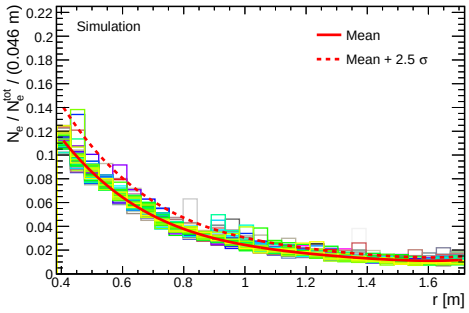

(g) $\gamma\gamma \rightarrow$ hadrons background at $\sqrt{s}$ = 1 TeV

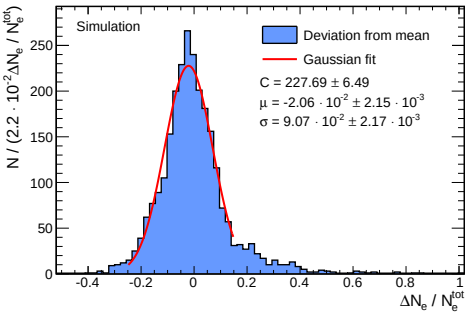

(h) $\gamma\gamma \rightarrow$ hadrons background at $\sqrt{s}$ = 1 TeV

Figure 6.7: Dependence of the radial charge distribution on the z-position.

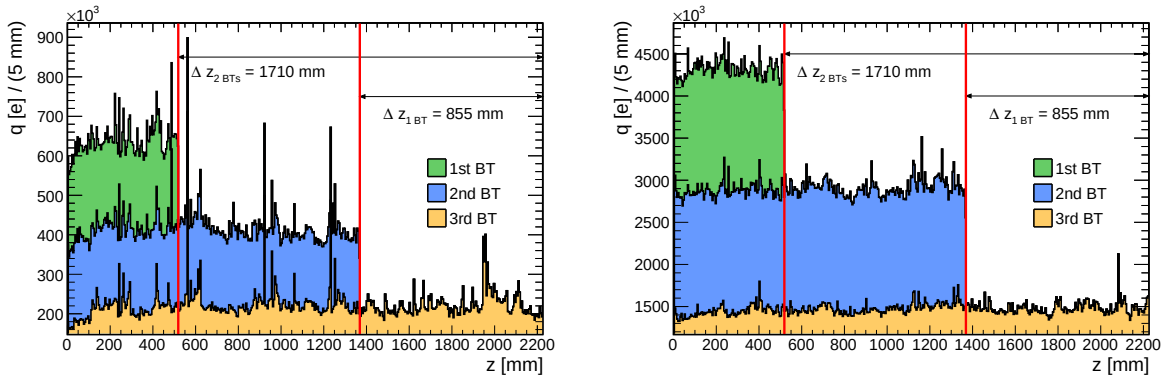

(a) $\sqrt{s} = 500\,\text{GeV}$ (b) $\sqrt{s} = 1\,\text{TeV}$

Figure 6.8: Overlay of primary ionization due to $\gamma\gamma \rightarrow$ hadrons background from three bunch trains. The indicated drift distances refer to the T2K gas mixture (cf. Section 3.6.2).

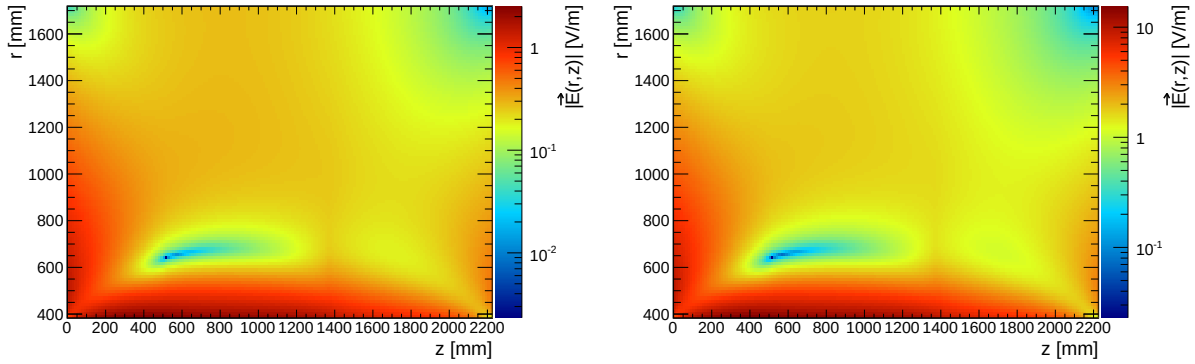

(a) $\sqrt{s} = 500\,\text{GeV}$ (b) $\sqrt{s} = 1\,\text{TeV}$

Figure 6.9: Field distortions caused by primary ions resulting from background processes (e^+e^--pairs and $\gamma\gamma \rightarrow$ hadrons combined) at $\sqrt{s} = 500\,\text{GeV}$ (a) and $\sqrt{s} = 1\,\text{TeV}$ (b).

.

center-of-mass energies. The general behavior is in both cases very similar and agree with the course of the primary ionization, i.e. the distortions are highest close to the inner field cage and to the cathode plane. The overall scale of the distortions is for $\sqrt{s} = 1\,\text{TeV}$ roughly six times higher than for $\sqrt{s} = 500\,\text{GeV}$ which is in good agreement to the amount of charge deposited in the chamber as discussed in Section 6.1.

6.3.2 Distortions caused by secondary ionization

No dependency on the z-position has to be taken into account for the calculation of the field distortions caused by secondary ionization, i.e. ion discs (cf. Section 3.6.2). The radial distribution of the ion discs results from the distribution of the primary electrons. In longitudinal direction the discs are very thin. Assuming a mobility of $1.535\,\text{cm}^2/\text{V s}$ [162] and an electric field strength of $280\,\text{V/cm}$, the maximum drift distance of an ion during the course of a bunch train computes to 3.1 mm. This also defines the maximum thickness of an ion disc, since it determines the distance between secondary ions created in

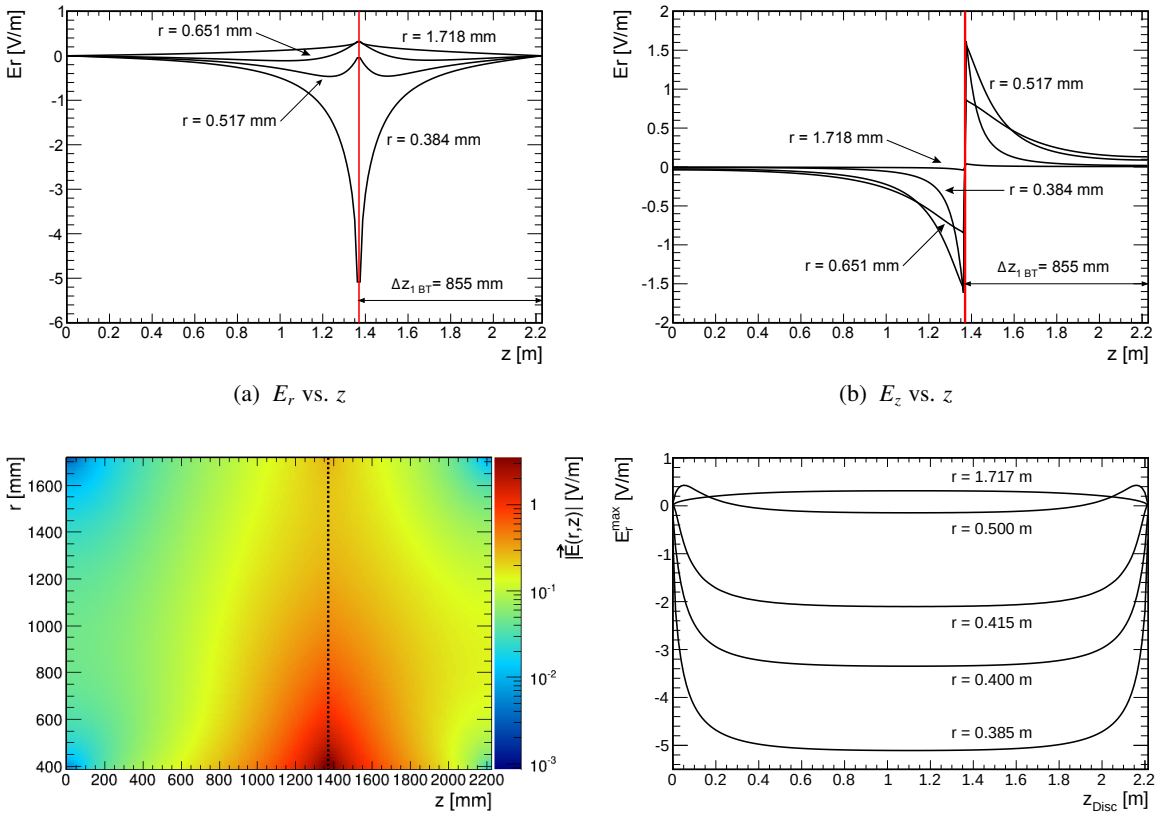

(a) E_r vs. z

(b) E_z vs. z

(c) $|\vec{E}(r,z)|$ vs. (r,z)

(d) E_r^{max} vs. z_{disc}

Figure 6.10: Electric field of an ion disc for $IBF = 1$ and a center-of-mass energy of $\sqrt{s} = 500\,\text{GeV}$. Field components in radial (a) and longitudinal (b) direction as a function of the z-position at several radii. The position of the disc is indicated by the red line. The magnitude of the field distortions in the zr-plane (c), position of the disc is indicated by the dotted line. Field values in radial direction as a function the z-position of the disc (d).

first and in last bunch crossings of a bunch train. The ions can be assumed to be equally distributed over this small range. Consequently, the radial distribution of the charge carriers in a disc is given by the charge density functions.

The charge density functions presented in Figure 6.2 and Figure 6.3 only include charge depositions from primary ionization processes. While the course of these functions describes the course of the charge distributions in the ion disc, the amount of charge is mainly determined by the gas amplification stage. The problem of ion back drift in a TPC has already been discussed in Section 3.6.1. It is the amount of back drifting ions, which provides the main contribution to the charge in an ion disc. It is determined by the product of the ion back drift as defined by Equation (3.56) and the gas gain, G,

$$IBF = I_B \cdot G. \tag{6.3}$$

This variable allows to study and compare different settings of any amplification stage without any further assumptions on the correlation of gain and ion back drift. Any combination of ion back drift and gas amplification can be modeled by applying an appropriate scaling factor to the ion disc.

Figure 6.10a and Figure 6.10b depict the field values in radial and longitudinal direction respectively.

The field values have been calculated from charge density functions for a center-of-mass energy of 500 GeV and $IBF = 1$. They are plotted for various radii as a function of the longitudinal position. The field values are largest close to the inner beam pipe. The magnitude of the field distortions drops rapidly with increasing radius. At a distance of 350 mm to the inner beam pipe, it is only one fifth of the size of the field close to the beam pipe. Furthermore, it can be observed, that the radial field distortions change their sign. For small radii the sign is negative.

This is caused by the center of gravity of the charge distribution in radial direction. As the background processes deposit much more charge (per unit volume) at small radii, the center of gravity is also located at small radii. Hence, the field lines run towards the inner field cage for small radii and start to bend outwards with increasing radius, until they point completely in positive direction for large radii. The field distortions in longitudinal direction are much smaller than in radial direction. They also show a dependency on the radius. The observed behavior is similar to that of the field in radial direction. The maximum distortions are largest close to the beam pipe and decrease towards larger radii. For small radii their course is very narrow and they drop rapidly with increasing distance to the disc. For larger radii the maximum values are smaller, but the distortions drop not as fast. The change of the sign is expected for the longitudinal field, as the distortions are caused by positive ions. The disc acts as source of the field which has to point away from it. The field is for both components sharply peaked around the position of the disc. It decreases rapidly with growing distance to the disc. This can also be observed in Figure 6.10c, which shows the magnitude of the electric field as a function of the two-dimensional position in the TPC volume. The field distortions exceed 1 V/m at very small radii and close to the disc.

The electric field caused by an ion disc shows a strong dependency on the position of the disc. This is illustrated in Figure 6.10d. It shows the maximum field distortions in radial direction as a function of the disc's position. The field distortions are largest if the disc is located in the central region of the detector. There they assume a nearly constant value. Towards the end plates, however, the distortions decrease. This is due to the boundary conditions the endplates impose on the electric field which suppress space charge effects in their vicinity.

6.3.3 Deviations of the electron drift paths

The maximum field distortions observed in Figure 6.10 are rather low compared to the nominal drift field of 280 V/cm. Nevertheless, they have an impact on the drift of electrons. This influence can be studied with the help of test charges at predefined positions. Starting from these positions, the electrons are drifted to the readout. No diffusion is applied during the drift. Thus, the deviation from the undisturbed drift path due to the field distortions can be determined by comparing the electron position in the $r\varphi$-plane before and after drift. In the absence of diffusion, field distortions are the sole reason for the displacement of the drifting electrons.

The displacement of electrons due to field distortions caused by secondary ionization is illustrated in Figure 6.11 for a center-of-mass energy of 500 GeV and $IBF = 1$. The influence of $\gamma\gamma \rightarrow$ hadrons and e^+e^--pairs is shown separately. The graphs show the deviation from the drift path as a function of the drift length for several initial radii. The deviations increase greatly if the drifting electrons have to pass through an ion disc. For these electrons, the deviations are smallest if their start point is close to the disc. The deviations increase with growing distance to the disc until they reach a level of saturation. For electrons starting behind the disc, i.e. between the disc and the readout, the behavior is different. In this case, the influence of the disc is strongest for electrons starting close to the disc. The closer the starting point of the electrons to the readout, the smaller the deviations. Furthermore, it can be observed that the deviations are strongest close to the beam pipe and decrease rapidly for increasing radii. In this they follow the charge distribution in the ion disc. The z-coordinate of the ion disc has also a large impact

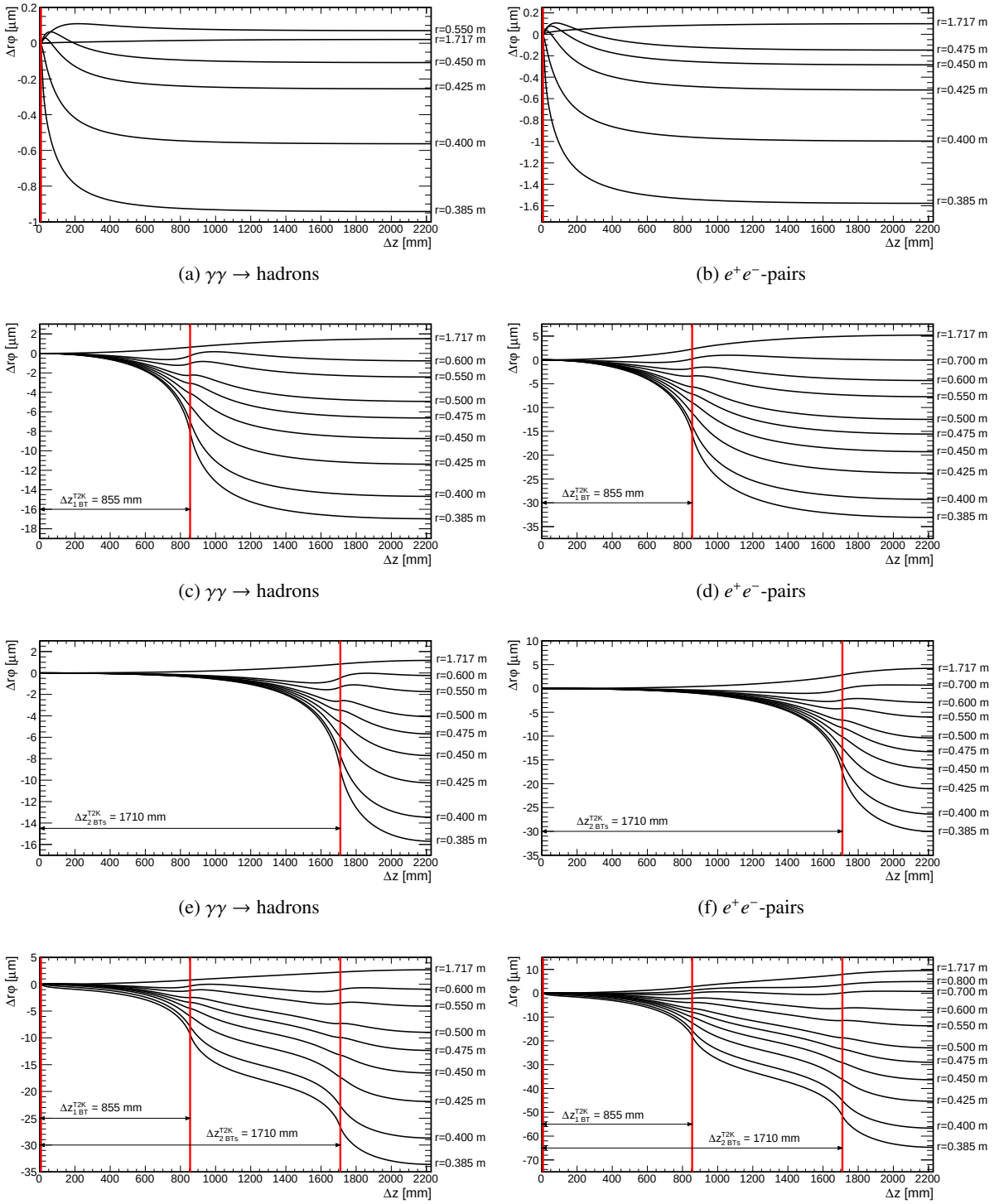

(a) $\gamma\gamma \rightarrow$ hadrons (b) e^+e^--pairs

(c) $\gamma\gamma \rightarrow$ hadrons (d) e^+e^--pairs

(e) $\gamma\gamma \rightarrow$ hadrons (f) e^+e^--pairs

(g) $\gamma\gamma \rightarrow$ hadrons (h) e^+e^--pairs

Figure 6.11: Displacement of electron end points caused by ion discs at different z-positions. The position of the discs has been calculated for the T2K gas mixture and a drift field of 280 V/cm. Shown are the effects of backgrounds from $\gamma\gamma \rightarrow$ hadrons (a,c,e,g) and e^+e^--pairs (b,d,f,h) for a center-of-mass energy of 500 GeV. The red lines indicate the position of the ion discs.

on the deviation of the drift paths. The displacement of the electrons is smaller for ion discs close to an endplate, than for discs near to the chamber. This is caused by the decrease in the field strength for ion discs close to an endplate, as discussed above.

The deviations caused by $\gamma\gamma \rightarrow$ hadrons are smaller than those caused by e^+e^--pairs. This is according to expectations, as the latter process deposits much more charge in the volume in the TPC. The maximum deviation from three ion discs of $\gamma\gamma \rightarrow$ hadrons background alone is approximately 34 µm. In the case of e^+e^--pairs, the maximum displacement of 65 µm is nearly twice as large. At this point it should be stressed, that the simulations presented in Figure 6.11 have been performed for an ion back drift ratio of $IBF = 1$. This represents a rather optimistic setting, since a gas gain of 3500 combined with an ion back drift of $I_B = 1$ ‰ already yields a value of $IBF = 3.5$. This is of particular importance for a center-of-mass energy of 1 TeV. While the general course of the displacement is the same as for $\sqrt{s} = 500$ GeV, the absolute values are much higher. This is according to the expectations because of the larger amount of charge deposited in the detector (cf. Figure B.1).

Estimation of the impact on the momentum resolution

It can be difficult to obtain the momentum resolution without already possessing a precise knowledge of the momentum of the measured particle. During the prototyping phase of a detector system, this knowledge is typically provided by dedicated external measurement systems. For the final detector system this measurements are usually not available. For this reason, approximation methods have been developed to circumvent this problem. A frequently encountered approach for estimating the momentum resolution is the Gluckstern formula [163]

$$\frac{\sigma_{p_\mathrm{T}}}{p_\mathrm{T}^2} = \sqrt{\frac{720}{N+4}} \cdot \frac{\sigma_{r\varphi}}{0.3 \cdot L^2 B}. \tag{6.4}$$

It allows to calculate the momentum resolution, $\sigma_{p_\mathrm{T}}/p_\mathrm{T}^2$, from the number of track points, N, which have been measured with precision $\sigma_{r\varphi}$ on a track of length L in a magnetic field of magnitude B. The formula assumes the precision of the single point measurements to be the same for all track points. It is in general only valid for a large number of track points, i.e. $N \geq 10$. In a pixelized TPC, this condition is easily fulfilled. Since single primary electrons can be resolved, the expected number of hits expected in a large ILD-TPC is $O(10^4)$. Formula (6.4) takes only measurement errors into account which are statistically distributed with a width of $\sigma_{r\varphi}$ around a mean value. For this reason it is in general not possible to apply Equation (6.4) to determine the impact of field distortions on the momentum resolution, as these distortion represent a systematic effect. Thus, it should be stressed that the following derivation can just serve as a very rough estimate.

To estimate the impact of field distortions values for the measurement precision, number of track points and the track length have to be obtained. The track length can be estimated by the distance between the inner and outer field cage of the TPC which computes to $L = r_{outer} - r_{inner} = 1334$ mm. The number of track points can be estimated from the number of electrons-ion pairs produced by a charged particle traversing the active volume from the inner to the outer field cage, i.e. on a distance of 1334 mm. `Heed` simulations yield a most probable value of approximately 11 000 electron-ion pairs for such track in the T2K gas mixture (see. Figure B.4). Assuming a detection efficiency of 90 % to 95 % [63] and approximately 10 % of losses of active area in radial direction (e.g. due to module borders and gaps between individual chips) this yields roughly 9000 measured track points. To determine the measurement precision a grid of equally spaced test charges is created in the (r, φ)-plane of the detector. The grid has a spacing of 5.75 mm and 5 mm in radial and longitudinal respectively. This results in 232×445 test

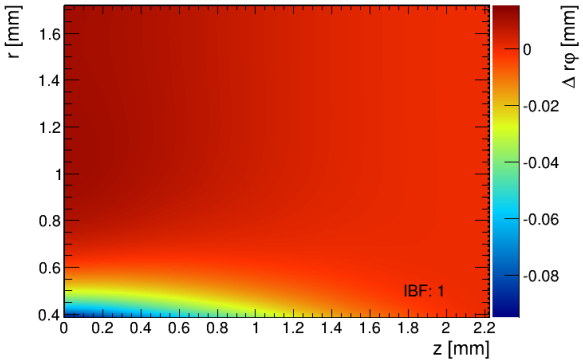

(a) Ion gate, $IBF = 1$

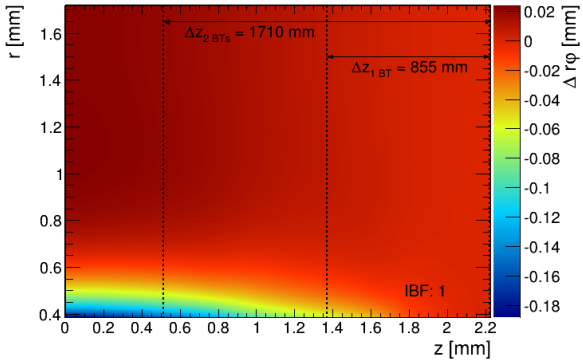

(b) No ion gate, $IBF = 1$

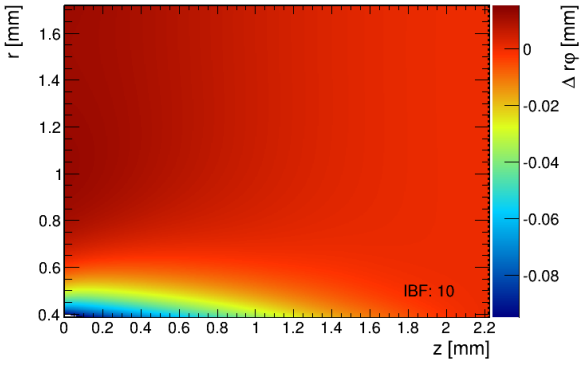

(c) Ion gate, $IBF = 10$

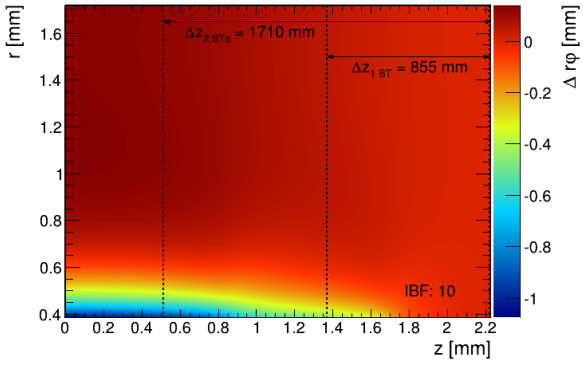

(d) No ion gate, $IBF = 10$

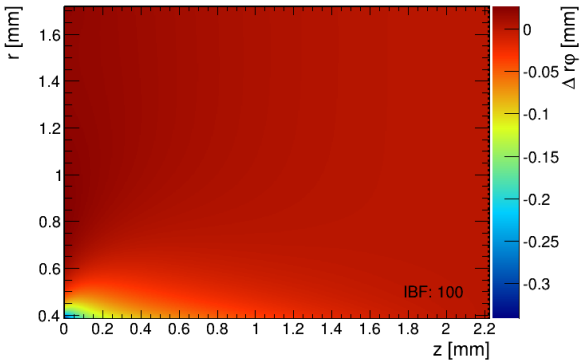

(e) Ion gate, $IBF = 100$

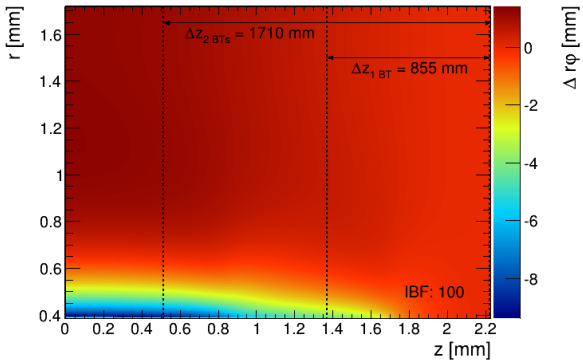

(f) No ion gate, $IBF = 100$

Figure 6.12: Drift deviations in a TPC with T2K gas w/o ion gate, for several ion back drift ratios. Both backgrounds are considered for a center-of-mass energy of 500 GeV. The deviations are plotted against the initial positions of the electrons, for the whole $r\varphi$-plane. In the ungated case (a,c,e) only one disc is present in the TPC in contrast to three discs for the gated (b,d,f) case. The dotted lines indicate the positions of the ion discs.

IBF	With ion gate		Without ion gate	
	Max. deviation	Momentum resolution	Max. deviation	Momentum resolution
1	66.0 µm	$8.55 \times 10^{-5}\, c/\mathrm{GeV}$	134.3 µm	$8.73 \times 10^{-5}\, c/\mathrm{GeV}$
5	73.1 µm	$8.56 \times 10^{-5}\, c/\mathrm{GeV}$	414.8 µm	$1.06 \times 10^{-4}\, c/\mathrm{GeV}$
10	82.1 µm	$8.58 \times 10^{-5}\, c/\mathrm{GeV}$	766.6 µm	$1.44 \times 10^{-4}\, c/\mathrm{GeV}$
50	153.5 µm	$8.80 \times 10^{-5}\, c/\mathrm{GeV}$	3490.0 µm	$5.35 \times 10^{-4}\, c/\mathrm{GeV}$
100	243.0 µm	$9.25 \times 10^{-5}\, c/\mathrm{GeV}$	6893.1 µm	$1.05 \times 10^{-3}\, c/\mathrm{GeV}$

(a) $\sqrt{s}$ = 500 GeV

IBF	With ion gate		Without ion gate	
	Max. deviation	Momentum resolution	Max. deviation	Momentum resolution
1	406.1 µm	$1.05 \times 10^{-4}\, c/\mathrm{GeV}$	827.4 µm	$1.51 \times 10^{-4}\, c/\mathrm{GeV}$
5	449.7 µm	$1.09 \times 10^{-4}\, c/\mathrm{GeV}$	2526.5 µm	$3.92 \times 10^{-4}\, c/\mathrm{GeV}$
10	504.4 µm	$1.14 \times 10^{-4}\, c/\mathrm{GeV}$	4620.4 µm	$7.05 \times 10^{-4}\, c/\mathrm{GeV}$
50	942.8 µm	$1.66 \times 10^{-4}\, c/\mathrm{GeV}$	19 911.6 µm	$3.02 \times 10^{-3}\, c/\mathrm{GeV}$
100	1428.1 µm	$2.32 \times 10^{-4}\, c/\mathrm{GeV}$	36 720.0 µm	$5.27 \times 10^{-3}\, c/\mathrm{GeV}$

(b) $\sqrt{s}$ = 1 TeV

Table 6.2: Momentum resolution as predicted by the Gluckstern formula based on the highest observed deviation for center-of-mass energies of 500 GeV (a) and 1 TeV (b).

charges. The displacement of the drift test charges due to space charge effects is determined in the same way as discussed in Section 6.3.3. The results of these simulations are depicted in Figure 6.12 for a TPC with and without ion gate and for five values of IBF. The field distortions result from primary as well as secondary ionization due to backgrounds at a center-of-mass energy of 500 GeV (the corresponding results for the case of $\sqrt{s}$ = 1 TeV is depicted in Figure B.2). The measurement error is computed for the maximal deviation, σ_{max}, observed for the different cases via

$$\sigma_{r,\varphi} = \sqrt{\sigma_{max}^2 + \sigma_{diff}^2} \qquad \text{with} \qquad \sigma_{diff} = D_T[\mu\mathrm{m}/\sqrt{\mathrm{cm}}] \cdot \sqrt{\Delta z\,[\mathrm{cm}]} \tag{6.5}$$

where $D_T = 37.59\,\mu\mathrm{m}/\sqrt{\mathrm{cm}}$ is the transverse diffusion constant for T2K (at $|\vec{B}| = 3.5$ T) and Δz = 222.5 cm the largest possible drift length.

The momentum resolutions obtained by the above procedure are summarized in Table 6.2a and Table 6.2b for center-of-mass energies of 500 GeV and 1 TeV respectively. The influence of the field distortions can be estimated by comparing these values with the undistorted case which can be computed by setting $\sigma_{r\varphi} = \sigma_{diff}$. This yields a value of $\sigma_{p_\mathrm{T}}/p_\mathrm{T}^2 = 8.05 \times 10^{-5}\, c/\mathrm{GeV}$for the obtainable momentum resolution. The results can be summarized as follows. Field distortions caused by backgrounds at $\sqrt{s}$ = 500 GeV are of no concern if an ion gate is operated. The required momentum resolution of $10^{-4}\, c/\mathrm{GeV}$ is obtained even for values of IBF as high as IBF = 100. Without gate it is very important to limit the amount of back drifting ions. For values of $IBF \leq 5$ the target value is still reached while the distortions become too large at higher values. For the $\sqrt{s}$ = 1 TeV case the situation changes because of the much larger distortions. Even with an ion gate it is important to control back drifting ions to values of $IBF \leq 5$ in order to retain the required resolution.

It has to be considered that the large flexibility in the choice of IBF is a result of the large segmentation provided by a pixelized readout. Due to this high granularity the amount of measured track points

Parameter	Value
Inner radius of the gas volume	354 mm
Outer radius of the gas volume	1748 mm
Maximum drift length	2225 mm
Gas	T2K
Nominal drift field	280 V/cm
Magnetic field	3.5 T

(a) TPC parameters

Parameter	Value
Inner radius of the active area	384 mm
Outer radius of the active area	1718 mm
Gain	5000
Pixel size	$100 \times 100\,\mu m^2$
Number of readout channels	880 839 520
Readout frequency	40 MHz

(b) Readout parameters

Table 6.3: Parameters used in the detailed TPC simulation.

is one to two orders of magnitude higher than for pad based readouts. The number of track points (in radial direction) is given for pad based readouts by the number of pad rows, since each row provides one measurement (cf. Figure 5.1 in Section 5.1). Pad readouts for an ILD-TPC currently foresee 220 pad rows. Comparing this value with $N \approx 9000$ for a pixelized readout yields that the required measurement precision can be $\sqrt{\frac{N_{pixel}+4}{N_{pads}+4}} \approx 6.3$ times lower for a pixelized readout than for a pad based readout. This applies as long, as $\sigma_{r\varphi}$ remains unchanged. However, for pads the fact has to be taken into account that each reconstructed hit is caused by multiple electrons, which alters the calculation of $\sigma_{r\varphi}$ significantly [164].

The considerations above are based on a simplified model in which the highest observed deviations are used as a constant measurement precision. In doing so the fact is ignored that field distortions are a vector quantity. Indeed, a change in sign is observed with increasing radii (cf. Figure 5.4 in Section 5.2.4). This may impact the momentum resolution in a way not accounted for. To examine such effects a full track simulation is required, which is discussed in the next section.

6.4 Tracking with a pixelized readout

The discussion of the field distortions in the previous section has been rather generic. The results can applied to all kinds of readouts and amplification stages, since only the deviations of the electron drift paths are studied. To assess the impact on a pixelized readout based on InGrids for gas amplification a full detector simulation is required. Thus, a series of simulations has been performed, using the simulation methods and tools discussed in Section 5.3.1.

The parameters used for the description of the TPC volume and its readout are listed in Table 6.3. The geometric parameters match those used in the simulation of the backgrounds (cf. Table B.2). The drift field of 280 V/cm corresponds to the maximum drift velocity for the T2K gas mixture of $v_D = 78.78\,mm/\mu s$ (cf. Figure 3.3) and diffusion values of $37.59\,\mu m/\sqrt{cm}$ and $205.34\,\mu m/\sqrt{cm}$ for transverse and longitudinal diffusion (with a 3.5 T magnetic field in transverse direction) respectively.

Taking the findings of Section 6.2 into account, a pixel size of $100 \times 100\,\mu m^2$ is chosen for the readout, as for this size nearly all primary electrons are detected on separate pixels. The gas gain of 5000 in combination with a readout frequency of 40 MHz results in a mean pulse length of 72 clock cycles (cf. Figure B.3). This corresponds to a pulse length of 1.8 µs which is rather long, especially given the fact that overlapping pulses can not be resolved. The large length is still of no concern as due to the lack of an advanced reconstruction scheme for large scale pixel readouts only events containing

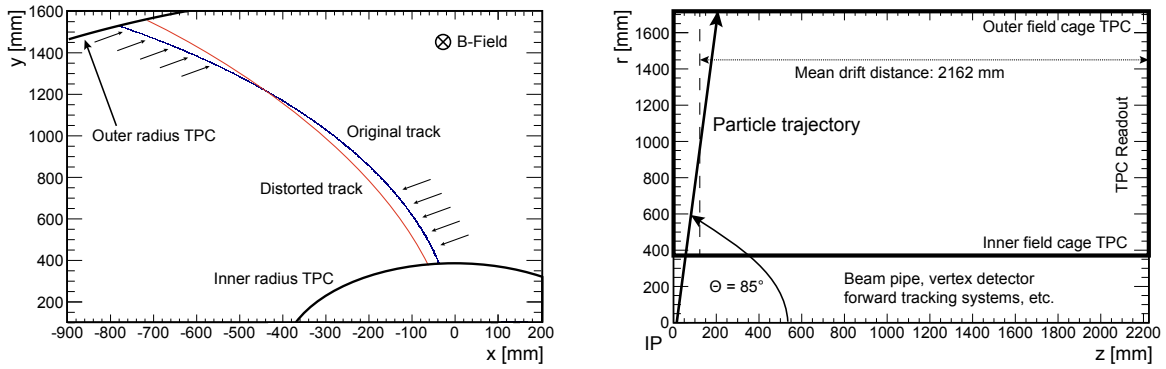

(a) $r\varphi$-plane (b) zr-plane

Figure 6.13: Sketch of a muon track in the TPC of the ILD, in the $r\varphi$-plane (a) and the zr-plane (b). The blue line in (a) indicates the primary ionization trail and the red line the expected track measurement.

single tracks are simulated.

Field distortions resulting from backgrounds for center-of-mass energies of 500 GeV and 1 TeV are used in the simulations and examined separately. Values of IBF in the range of 1 to 100 are applied to study the influence of ion-back-drift suppression on the momentum resolution. The dependence on the particle momentum and the impact impact of gating are only investigated for values of IBF of 10 and 100. With the chosen gas gain of $G = 5000$ this corresponds to an ion back drift of $I_B = 2\ ‰$ and $I_B = 2\%$ respectively. The lower value is an ambitious, yet achievable goal for the ion-back-drift suppression as discussed in Reference [63], while the larger value represents a less constrained setting. Since the TPC for the ILD foresees an ion gate, only one disc directly in front of the readout is used. Nevertheless, the impact of an ion gate is addressed in Section 6.4.4 where the effect of field distortions resulting from three discs in the active volume is investigated for the ion-back-drift values of $IBF = 10$ and $IBF = 100$.

Muons are used as test particles. Data samples of 1250 muons are used to study the effects caused by backgrounds in the volume of the TPC. The muons are created with an emission angle of $\theta = 85°$ to the beam pipe at a position of $\vec{x_0} = (0, 0, 5)$ mm which prevents primary electrons from being created beyond the cathode plane and results in an average drift distance of 2162 mm for the primary electrons. In most cases, muons with a momentum of 2 GeV are used, as the impact of field distortions is expected to be largest for tracks with a high curvature.

A sketch of the trajectory of a 2 GeV with respect to the detector geometry is depicted in Figure 6.13 for the $r\varphi$-plane (a) and the zr-plane (b), respectively. The effect of the field distortions on the measured particle track is sketched as well. For small radii, the field distortions point radially to the inner field cage, while they are directed to the outer field cage for larger radii. According to the second term in Equation (3.34), this results in a deviation of the electron drift paths in azimuthal direction. The sign of the deviations is determined by the direction of the magnetic field. The direction of the deviations are sketched in Figure 6.13a for the positive TPC volume (i.e. $z > 0$) along with the expectation for the measurement of the distorted track. The deviations of the electron drift paths result in straightening of the measured particle track and, hence, in a shift of the momentum resolution towards higher values. According to this, the momenta of muons with a positive charge are expected to be shifted towards lower values, since their curvature is reversed with respect to their negative counterparts. In addition to a shifted momentum, a difference for the reconstructed point of closest approach (cf. Section 5.3.3) is

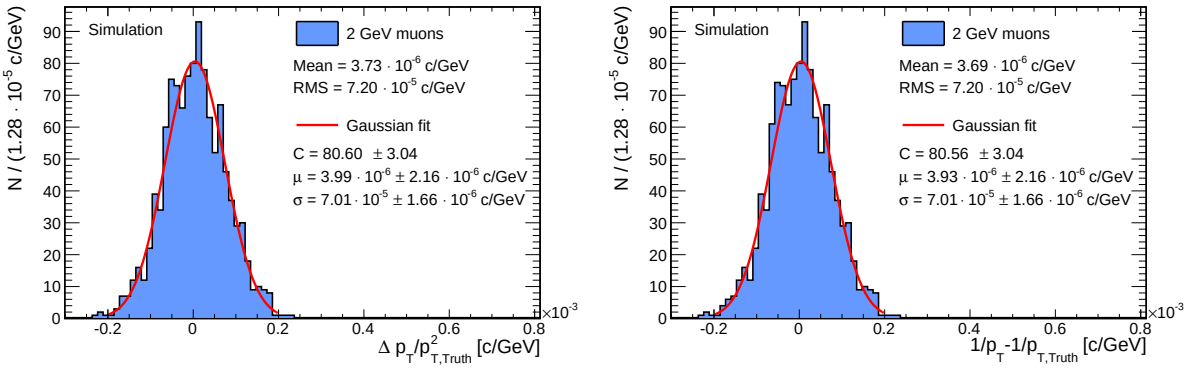

(a) $(\Delta p_\mathrm{T}/p^2_\mathrm{T,Truth})$-distribution (b) $(1/p_\mathrm{T} - 1/p_\mathrm{T,Truth})$-distribution

Figure 6.14: Comparison of two methods of obtaining the momentum resultion.

expected due to the shift in the reconstructed trajectory.

6.4.1 Momentum resolution

The momentum resolution is determined by the width of a Gaussian fitted either to the $(\Delta p_\mathrm{T}/p^2_\mathrm{T,Truth})$-distribution or the $(1/p_\mathrm{T} - 1/p_\mathrm{T,Truth})$-distribution of reconstructed particles. Muons with an energy of 2 GeV have been simulated in order to compare both methods. The resulting distributions are shown in Figure 6.14. In both cases momentum resolution of

$$\sigma = 7.01 \times 10^{-5} \pm 1.66 \times 10^{-6} c/\mathrm{GeV}$$

is obtained which is well below the resolution goal of $10^{-4}\, c/\mathrm{GeV}$ for the central tracking device. Both distributions are well centered around zero from which it can be concluded that there is no systematic error on the reconstructed momentum. Moreover, a good agreement between both distributions is observed which indicates that they are compatible. For this reason, it is not necessary to apply both methods in a study of the field distortions. Thus, in the following, momentum resolution refers to the width of the $(\Delta p_\mathrm{T}/p^2_\mathrm{T,Truth})$-distribution.

6.4.2 General influence of field distortions

The general influence of field distortions is depicted in Figure 6.15. Shown are the distributions obtained for muons (μ^-) and anti-muons (μ^+) in the presence of magnetic fields of $|\vec{B}| = 3.5\,\mathrm{T}$ and $|\vec{B}| = -3.5\,\mathrm{T}$, respectively. In this, positive field values denote a field parallel to the electric drift field and a negative value the anti-parallel case. In order to make the differences between the four combinations of magnetic field and (anti-) particle clearly apparent, a setup with a high ion-back-flow value, $IBF = 100$, is chosen for the1 TeV environment.

As shown in the figure, muons in a positive field follow the same distribution as anti muons in a negative field. The same is true for the opposite cases. All distributions are equidistant to zero. The mean values and widths of Gaussian functions fitted to the distributions are summarized in Table 6.4. They agree within their margin of error with each other. This further confirms the assumption that the four cases behave identical concerning the impact on the width of the distribution. There is only a difference in the sign for the shift of the distributions away from zero. For this reason, further on only

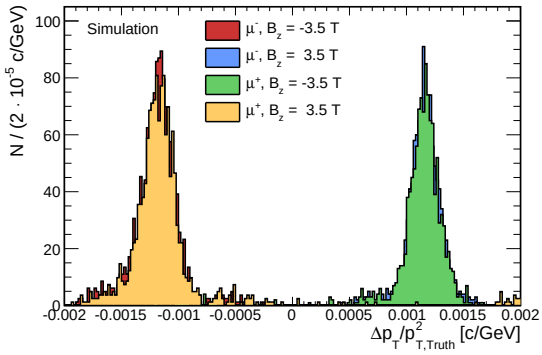

Particle	$\vec{B}$	μ 10^{-3} $[c/\text{GeV}]$	σ 10^{-4} $[c/\text{GeV}]$
μ^-	$-3.5\,\text{T}$	-1.18 ± 0.004	1.26 ± 0.04
μ^-	$3.5\,\text{T}$	1.17 ± 0.004	1.12 ± 0.03
μ^+	$-3.5\,\text{T}$	1.16 ± 0.004	1.17 ± 0.04
μ^+	$3.5\,\text{T}$	-1.17 ± 0.004	1.31 ± 0.03

Figure 6.15 & Table 6.4: General influence of field distortions for muons (μ^-) and anti-muons (μ^+) in the presence of magnetic fields of $|\vec{B}| = 3.5\,\text{T}$ and $|\vec{B}| = -3.5\,\text{T}$.

muons (μ^-) in the presence of a positive magnetic field are regarded.

6.4.3 Influence of primary ionization

As discussed in Section 3.6.2 and Section 6.3, there are three different cases for charge depositions resulting from primary ionization due to background processes. The first case considers only primary ions from the current bunch train. In the second case, ions from the current bunch train and the previous bunch train, which have partially left the chamber, are taken into account. The third case, finally, represents the typical situation in the ILD-TPC. Ions from the current bunch train are present in the chamber of the TPC together with remaining parts of the previous two bunch trains which have not yet left the chamber.

A data sample of muons with a momentum of 2 GeV is used to study the influence of field distortions caused by primary ionization. Ions resulting from e^+e^--pairs and $\gamma\gamma \rightarrow$ hadrons are taken into account. The momentum resolutions obtained for all three cases are depicted in Figure 6.16 for both center-of-mass energies. The obtained distributions are similar to the undisturbed case (see. Figure 6.14) and are well described by Gaussian functions. The distributions are broadened and their central values are shifted towards higher values, i.e. the reconstructed momenta are too large. The observed effect increases with the number of bunch trains taken into account, due to the stronger distortions at small z-positions.

In general, it can be summarized that for both center-of-mass energies the obtainable momentum resolution in the presence of primary ions alone is

$$\sigma_{500\,\text{GeV}} = 7.33 \times 10^{-5} \pm 1.63 \times 10^{-6} c/\text{GeV}$$

for $\sqrt{s} = 500\,\text{GeV}$ and

$$\sigma_{1\,\text{TeV}} = 8.36 \times 10^{-5} \pm 2.30 \times 10^{-6} c/\text{GeV}$$

for $\sqrt{s} = 1\,\text{TeV}$ respectively. Both values are well below the target value of $10^{-4}\,c/\text{GeV}$ for a TPC at the ILD. Stronger than the effect on the width of the distribution is the shift in the reconstructed momenta, which is given by the central value, μ. With charge depositions from three bunch trains in the active

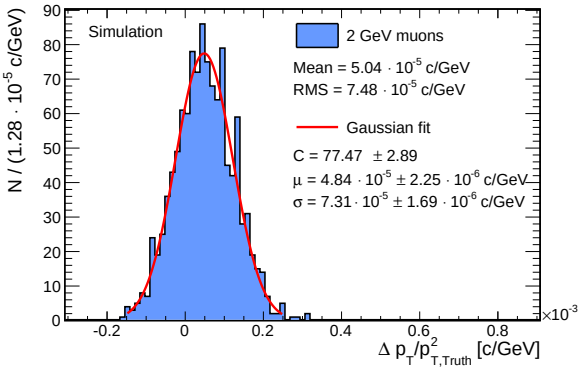

(a) Single BT, $\sqrt{s}$ = 500 GeV

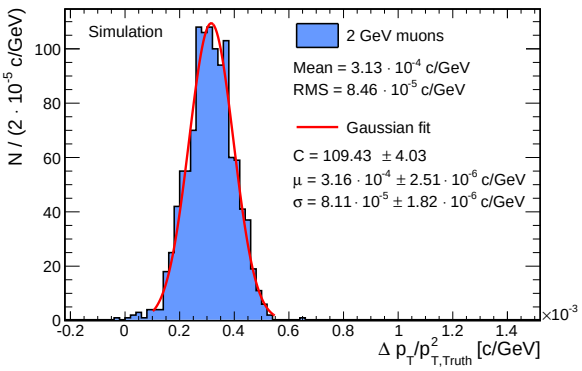

(b) Single BT, $\sqrt{s}$ = 1 TeV

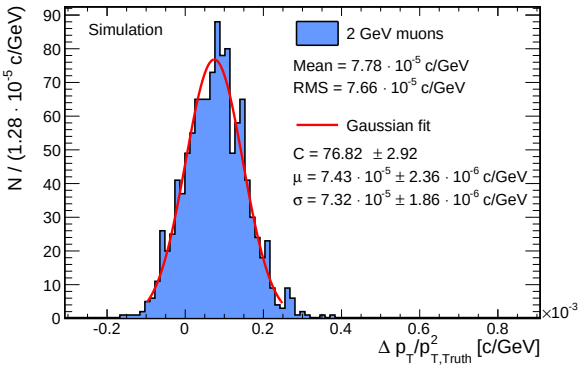

(c) Two BTs, $\sqrt{s}$ = 500 GeV

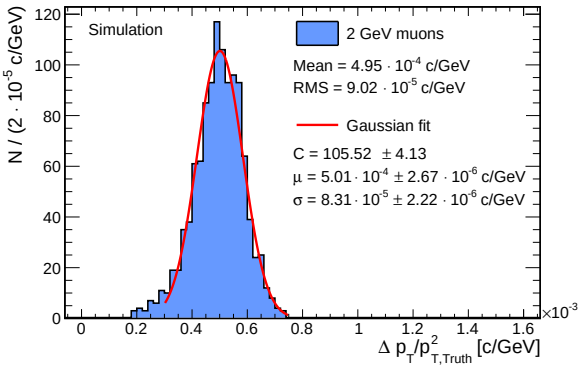

(d) Two BTs, $\sqrt{s}$ = 1 TeV

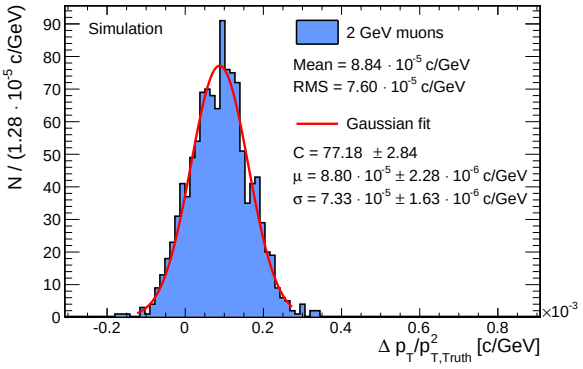

(e) Three BTs, $\sqrt{s}$ = 500 GeV

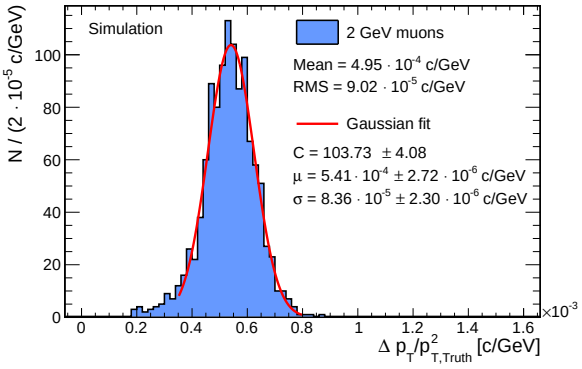

(f) Three BTs, $\sqrt{s}$ = 1 TeV

Figure 6.16: Influence of the primary ionization on the momentum resolution for both backgrounds combined.

volume of the TPC, the central values are given by

$$\mu_{500\,\mathrm{GeV}} = 8.80 \times 10^{-5} \pm 2.28 \times 10^{-6} c/\mathrm{GeV} \quad \text{and} \quad \mu_{1\,\mathrm{TeV}} = 5.41 \times 10^{-4} \pm 2.72 \times 10^{-6} c/\mathrm{GeV}$$

for the two center-of-mass energies of $\sqrt{s} = 500\,\mathrm{GeV}$ and $\sqrt{s} = 1\,\mathrm{TeV}$ respectively.

6.4.4 Influence of secondary ionization

The TPC of the ILD foresees an ion gate to prevent ions created in the gas amplification stage from entering the active volume (cf. Section 3.6.2). This means that only one disc of secondary ions is present in the TPC. This disc is located directly in front of the readout. Its influence on drifting electrons and, hence, on the obtainable momentum resolution strongly depends on IBF, as this value determines the amount of charge in the disc.

The momentum resolution obtained for several values of IBF are depicted in Figure 6.17 and Figure 6.18 for center-of-mass energies of $\sqrt{s} = 500\,\mathrm{GeV}$ and $\sqrt{s} = 1\,\mathrm{TeV}$ respectively. $\gamma\gamma \rightarrow$ hadrons and e^+e^--pair backgrounds are taken into account, as well as the contributions from primary ionization.

The following observations are made. The obtainable momentum resolution at a center-of-mass energy of 500 GeV and for small values of IBF, i.e. $IBF \leq 10$, is mainly determined by the effects of primary ionization. The width of the fitted distributions remains basically unchanged and not before values of $IBF \geq 50$ a significantly reduced resolution is observed which is still below the resolution goal of $10^{-4}\,c/\mathrm{GeV}$ for the central tracking device of the ILD . At a center-of-mass energy of 1 TeV the influence of the ion disc is stronger and the broadening of the distributions becomes already significant at small values of IBF. In all cases but for $IBF = 100$ at $\sqrt{s} = 1\,\mathrm{TeV}$ the obtained resolution is still well below the target value and even for this sole exception the value is missed by just 10 %. The shift of the central value of the distributions is a linear function of IBF with slope m and intercept b which computes to

$$\mu\,(IBF) = 1.05 \times 10^{-6} \pm 2.75 \times 10^{-8} c/\mathrm{GeV} \times IBF + 8.52 \times 10^{-4} \pm 1.34 \times 10^{-6} c/\mathrm{GeV}$$

for a center-of-mass energy of 500 GeV and

$$\mu\,(IBF) = 6.22 \times 10^{-6} \pm 2.84 \times 10^{-7} c/\mathrm{GeV} \cdot IBF + 5.48 \times 10^{-4} \pm 9.01 \times 10^{-6} c/\mathrm{GeV}$$

for a center-of-mass energy of 1 TeV respectively. The slope obtained for the higher center-of-mass energy of $\sqrt{s} = 1\,\mathrm{TeV}$ is roughly six times higher than that for a center-of-mass energy of $\sqrt{s} = 500\,\mathrm{GeV}$. The difference in the slopes is caused by the different amounts of charge deposited in the active volume during the course of a bunch train. It is the bigger amount of charge in the $\sqrt{s} = 1\,\mathrm{TeV}$ case, which make this setting more sensitive to the gain and ion-back-drift suppression of the amplification stage.

The dominance of effects resulting from primary ionization over those caused by secondary ionization can be further confirmed by studying the impact of field distortions which result only from secondary ionization. The momentum resolution obtained for a single ion disc with values of $IBF = 10$ and $IBF = 100$ without effects of primary ionization is depicted in Figure 6.19 for center-of-mass energies of 500 GeV (a,b) and 1 TeV (c,d) respectively. It is clearly apparent, that the influence of the ion disc is small compared to that of primary ions. The observed momentum resolution at $IBF = 10$ is for both center-of-mass energies better than for the case of primary ionization (from three bunch trains) as depicted in Figure 6.17f and Figure 6.18f. Furthermore, the shift of the distribution towards higher momenta is also smaller than the one observed for primary ions alone. In case of $IBF = 100$, the momentum resolution approximates for both center-of-mass energies the one obtained with primary

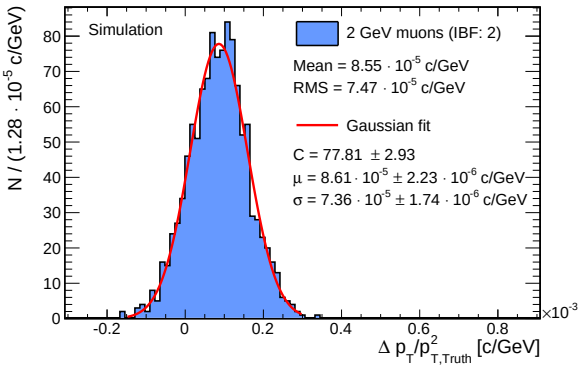

(a) $IBF = 2$

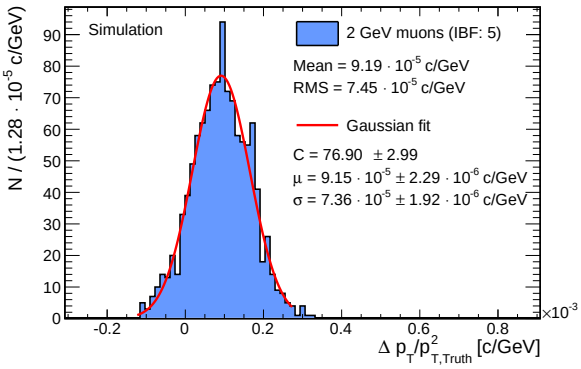

(b) $IBF = 5$

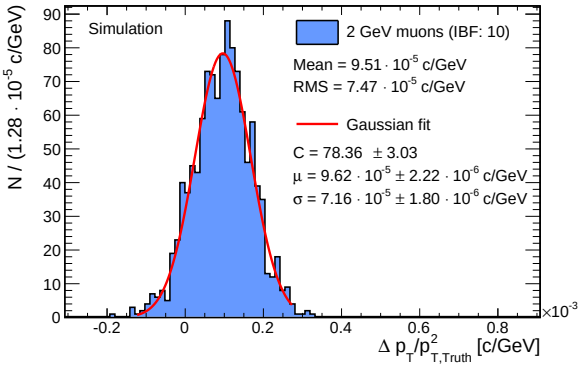

(c) $IBF = 10$

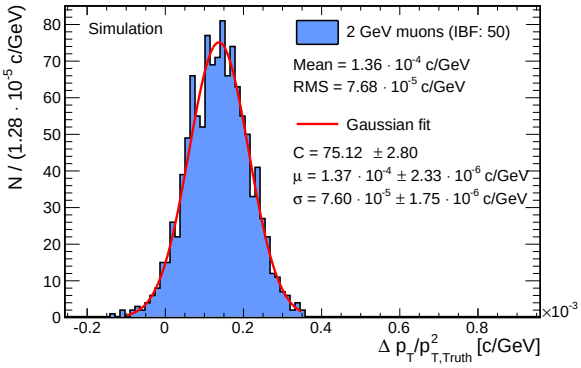

(d) $IBF = 50$

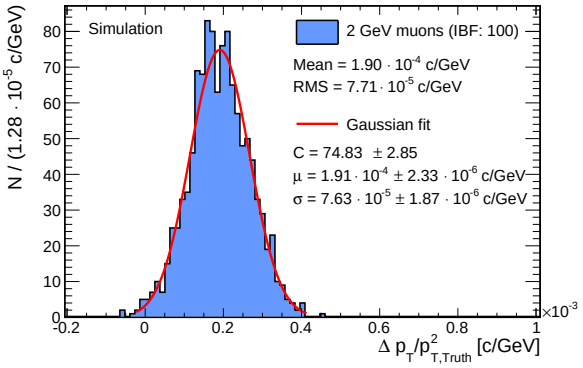

(e) $IBF = 100$

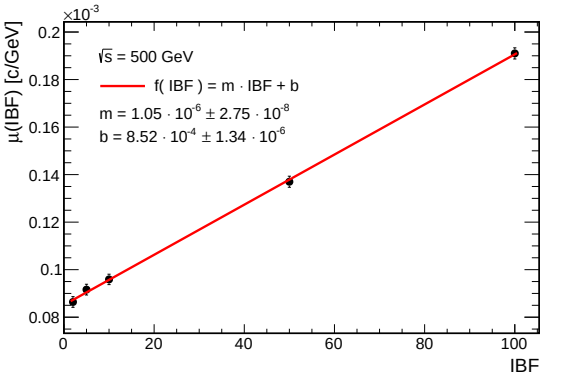

(f) μ as a function of IBF

Figure 6.17: Dependence of the momentum resolution on IBF for combined backgrounds at a center-of-mass energy of $\sqrt{s} = 500\,\text{GeV}$.

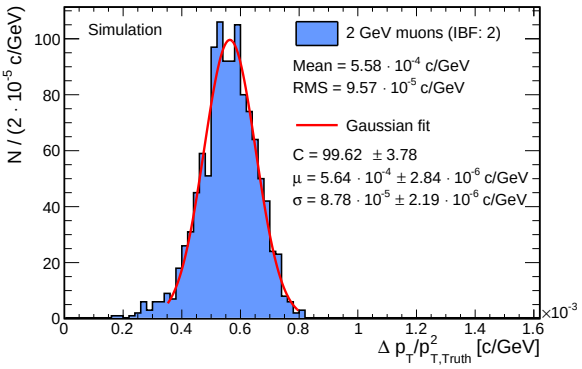

(a) $IBF = 2$

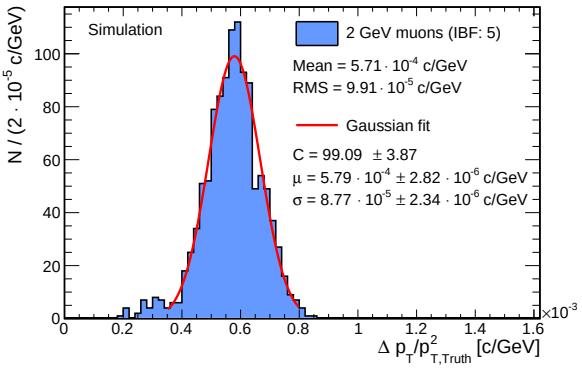

(b) $IBF = 5$

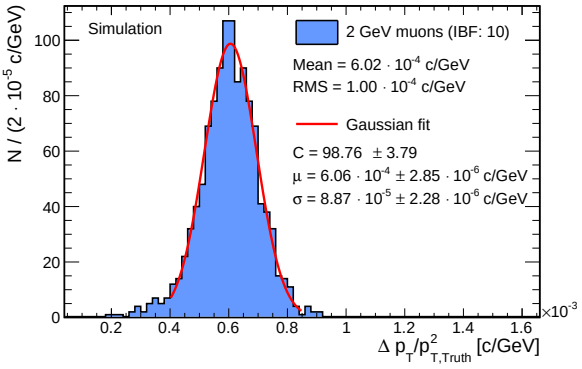

(c) $IBF = 10$

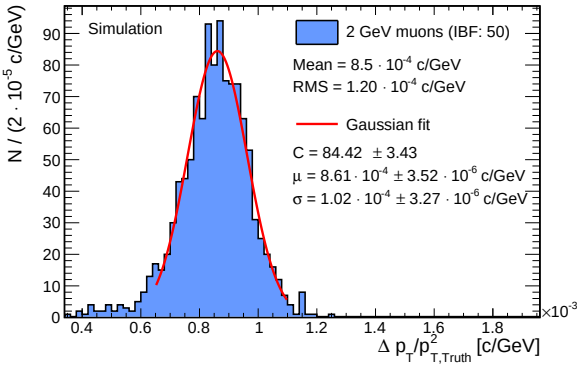

(d) $IBF = 50$

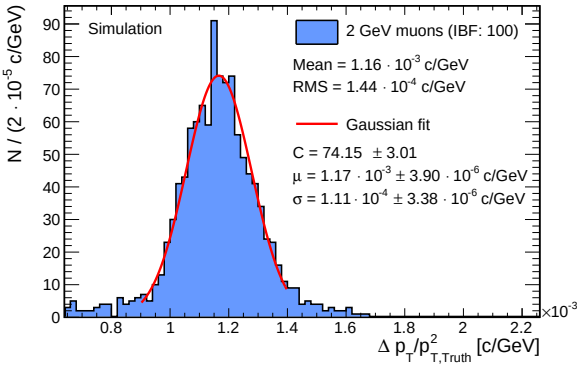

(e) $IBF = 100$

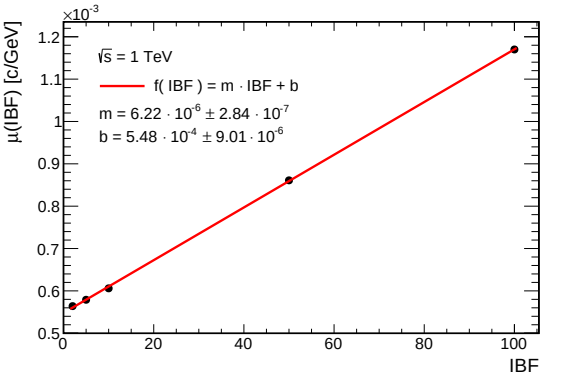

(f) μ as a function of IBF

Figure 6.18: Dependence of the momentum resolution on IBF for combined backgrounds at a center-of-mass energy of $\sqrt{s} = 1$ TeV.

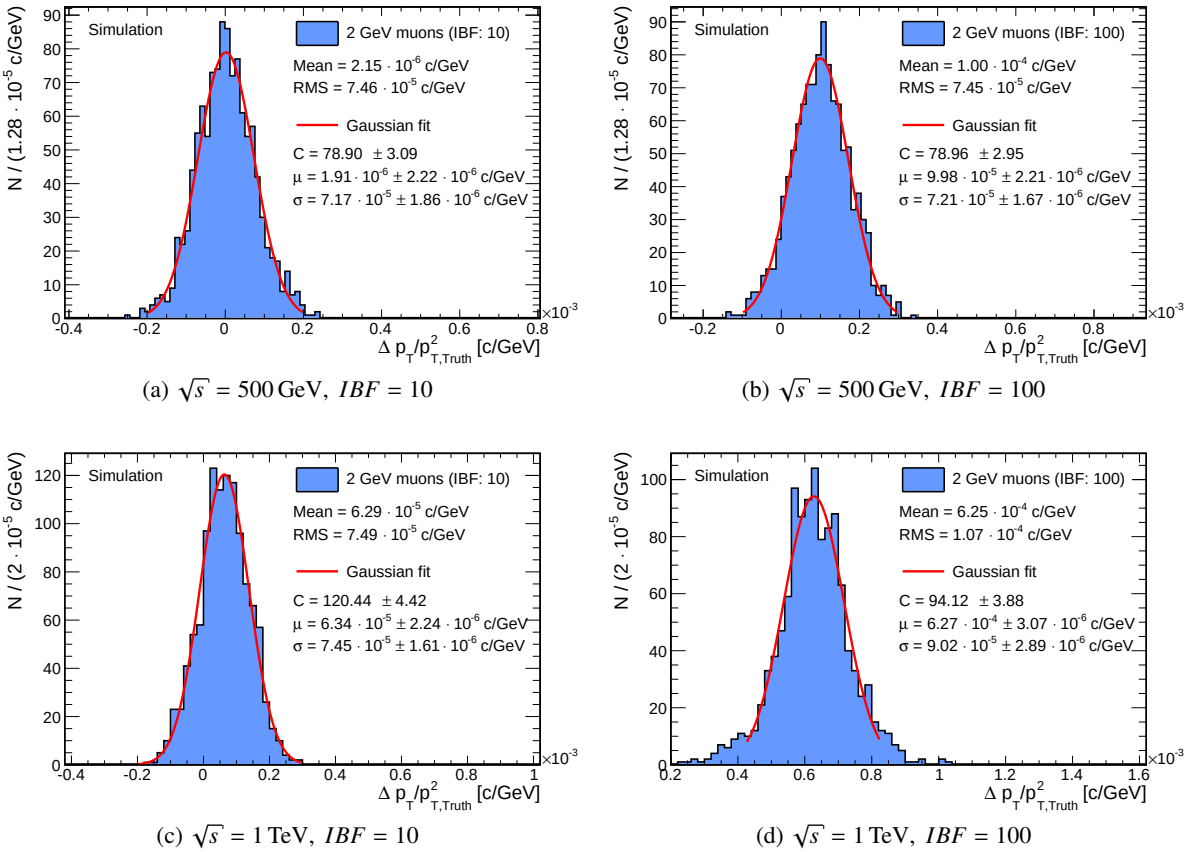

(a) $\sqrt{s}$ = 500 GeV, IBF = 10

(b) $\sqrt{s}$ = 500 GeV, IBF = 100

(c) $\sqrt{s}$ = 1 TeV, IBF = 10

(d) $\sqrt{s}$ = 1 TeV, IBF = 100

Figure 6.19: Momentum resolution influenced by field distortions resulting from secondary ionization (without primary ions) for center-of-mass energies of 500 GeV (a,b) and 1 TeV (c,d).

ions alone, while the shift of the central value of the distribution is already slightly larger than that observed for primary ions. Still, the measured resolution does not exceed the resolution goal. From these findings it can be concluded that values of IBF in the range of 10 to 100 the effect of a single ion disc on the obtainable momentum resolution is approximately of the same size as the effect of primary ions.

Influence of an ion gate

The presence of an ion gate has been assumed in the above discussion of the impact of secondary ions on the momentum resolution . Such a gate does not prevent the build-up of an ion disc during the course of a bunch train but prevents it from drifting further into the active volume of the detector in the time between two trains. The gating procedure for an ILD-TPC is described in Section 3.6.2, as is the phenomenon of multiple discs in the drift volume.

To study the effect of an ion gate, field distortions caused by three discs in the active volume (plus primary ionization) are applied in the simulation of muon tracks. Examined are values of IBF = 10 and IBF = 100. The results are depicted in Figure 6.20 for both center-of-mass energies. Compared to the gated case all distributions are considerably broadened. For IBF = 10 and a center-of-mass energy of 500 GeV the distribution has already a larger width than for the gated case at IBF = 100. The same is

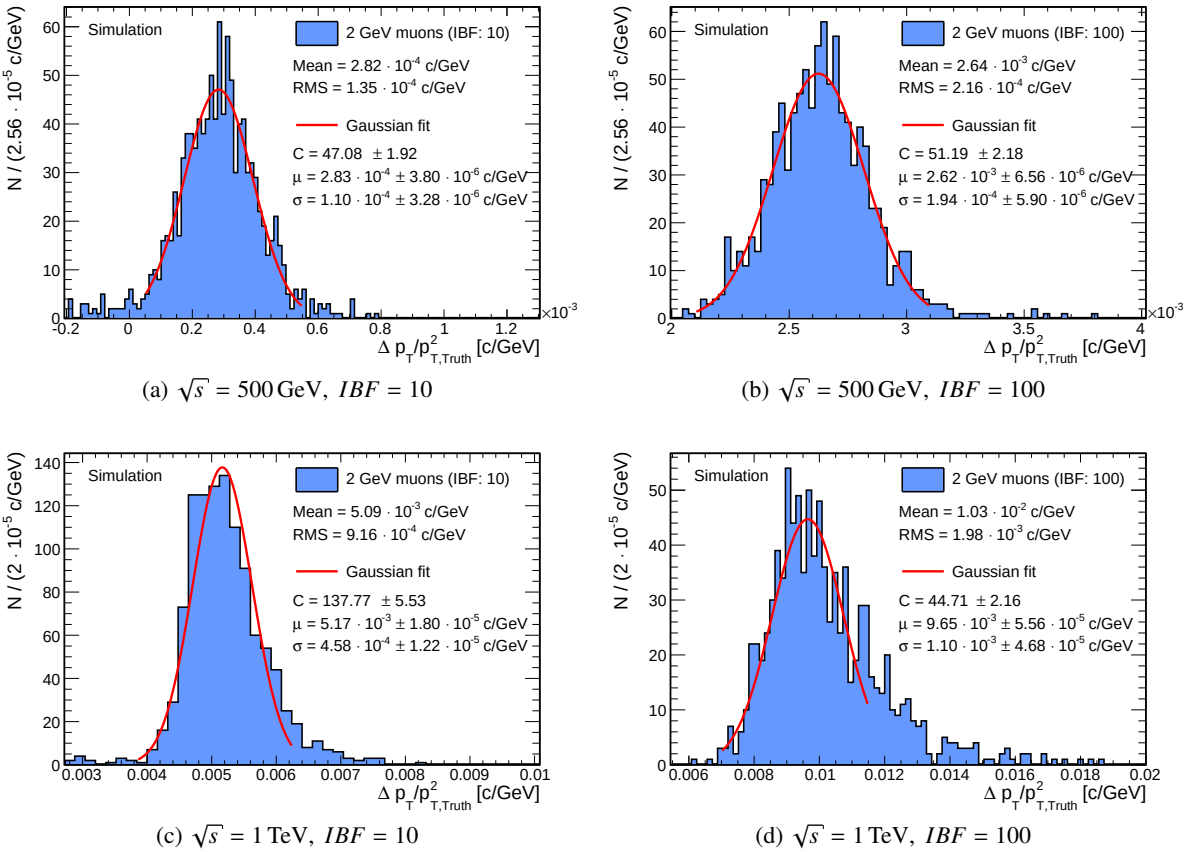

(a) $\sqrt{s} = 500\,\text{GeV}$, $IBF = 10$ (b) $\sqrt{s} = 500\,\text{GeV}$, $IBF = 100$

(c) $\sqrt{s} = 1\,\text{TeV}$, $IBF = 10$ (d) $\sqrt{s} = 1\,\text{TeV}$, $IBF = 100$

Figure 6.20: Momentum resolution without ion gate for center-of-mass energies of 500 GeV and 1 TeV and values of IBF of 10 and 100.

true for distortions caused by backgrounds at $\sqrt{s} = 1\,\text{TeV}$. The distributions show at $IBF = 100$ for both center-of-mass energies some deviations from the GAUSSIAN shape observed for the gated case, a phenomenon which is in particular distinct at a center-of-mass energy of 1 TeV. The obtained resolutions exceed in any case the target value for an ILD-TPC, even though the excess for $IBF = 10$ is $\sqrt{s} = 10$ is just 10 % and may be correctable as the shape of the distribution is preserved. For larger values of IBF and especially for backgrounds at $\sqrt{s} = 1\,\text{TeV}$ gating seems to be advisable as the target resolution is missed by at least a factor of two and the deviations from a GAUSSIAN shape become more severe.

The general finding of a significantly decreased momentum resolution is according to expectations, even though a very small impact of a single disc (without primary ionization) close to the readout has been observed in Figure 6.19. Three discs are present in the drift volume if no gate is operated. According to Figure 6.10d, the magnitude of the field distortions caused by an ion disc increases with growing distance to the endplates. Hence, discs which have drifted further into the TPC volume have a stronger influence on the drifting electrons than a disc positioned directly in front of the readout.

6.5 Summary

Backgrounds resulting from e^+e^--pairs as well as $\gamma\gamma \rightarrow$ hadrons have been simulated for center-of-mass energies of 500 GeV and 1 TeV with a sufficient level of detail required for a pixelized TPC readout.

The occupancy obtained for various pixel sizes has been investigated and a significant reduction of the occupied readout channels with respect to a pad based readouts has been observed, despite the long pulse lengths of pixel readouts. Moreover, nearly full single electron detection efficiency is observed for both center-of-mass energies at a pixel pitch of 100 µm.

Primary and secondary ionization have a significant impact on the homogeneity of the drift field. While the absolute distortions resulting from primary ions are small with respect to the magnitude of the drift field, i.e. 1 % and 5 % for $\sqrt{s}$ = 500 GeV and 1 TeV respectively, they have a considerable impact on the electron drift paths. This results in a lowered momentum resolution which is indicated by a increase of the root mean square deviation by roughly by a factor of 1.5 and 7.3 for center-of-mass energies of 500 GeV and 1 TeV respectively. The influence of field distortions caused by secondary ionization depends strongly on the size of IBF whereby the displacement of the momentum-resolution distribution is related to IBF. If an ion gate is operated and IBF is small, the influence of the distortions is small compared to the effect of primary ions. In any case, the field distortions and their impact the track reconstruction is largest close to the beam pipe. Even simple correction methods, as excluding the innermost hits from the track fit, already result in a significant improvement of the obtained momentum resolution.

Chapter 7

Summary

The International Large Detector as presented in the first chapter of this thesis is powerful general purpose detector well suited for measuring the interactions of the ILC with unprecedented precision and accuracy. In its current design it features multiple design and technology options for certain subsystems. The final decision on the single options and technology choices is yet to be made, whereat performance, costs, and applicability have to be weighed up carefully.

Integrated pixel readouts are a promising technology for the readout of Time Projection Chambers in general and for the central tracking TPC of the ILD in particular. Devices from a novel production process, which transfers the production of single (few) devices to the production on 8″-wafers have been examined and compared with each other. Single devices manufactured in the novel process reach an energy resolution of

$$\left(\frac{\sigma}{\mu}\right)_{\mathrm{PP}} = 4.93\,\% \pm 0.3\% \qquad \text{and} \qquad \left(\frac{\sigma}{\mu}\right)_{\mathrm{EP}} = 8.03\,\% \pm 0.12\%$$

for the peaks of a ^{55}Fe-spectrum, which is compatible with the values obtained with devices from the original process. This shows that the new process is approaching a level of maturity in which the application of GridPix detectors in large scale experiments is finally within reach. Even though, the devices from the investigated production runs still lack the high overall uniformity of the original production process.

The applicability of integrated pixel readouts in the presence of beam induced backgrounds has been examined by detailed simulations of the processes from $\gamma\gamma \rightarrow$ hadrons and e^+e^--pairs creation at center-of-mass energies of $\sqrt{s} = 500\,\mathrm{GeV}$ and $\sqrt{s} = 1\,\mathrm{TeV}$, respectively. It could be shown that a pixel size of $100 \times 100\,\mu\mathrm{m}^2$ is sufficient to reach full single electron detection efficiency at both investigated center-of-mass energies. The impact of the beam induced backgrounds on the electric drift field and electron drift have been simulated by employing numerical methods which allow for a precise calculation of the size of these distortions.

The magnitude of the field distortions and consequently the distortions of the electron drift paths are mainly determined by the amount secondary ions in the active region of the detector, wile the impact of primary ionization is rather low. Considering only field distortions resulting from primary ions, momentum resolutions of

$$\sigma_{500\,\mathrm{GeV}} = 7.33 \times 10^{-5} \pm 1.63 \times 10^{-6} c/\mathrm{GeV} \quad \text{and} \quad \sigma_{1\,\mathrm{TeV}} = 8.36 \times 10^{-5} \pm 2.30 \times 10^{-6} c/\mathrm{GeV}$$

are obtained for the two examined center-of-mass energies. Both values are still well below the target resolution of the ILD tracker.

If ions created in the amplification processes are taken into account as well, the momentum resolution depends on the value of IBF and the center-of-mass energy. The obtainable momentum resolution at a center-of-mass energy of $\sqrt{s} = 500\,\text{GeV}$ remains well below the resolution goal up to values of $IBF = 100$. For the higher center-of-mass energy of $\sqrt{s} = 1\,\text{TeV}$ this limit is roughly met up to $IBF = 50$. The situation changes quite dramatically if no ion gate is operated. The two additional ion discs in the active region cause huge distortions of the electron drift paths, in especially if the electrons have to pass through the discs. In this case the momentum resolution meets the ILD requirements not even for value of $IBF = 10$ at the lower center-of-mass energy of $\sqrt{s} = 500\,\text{GeV}$.

Appendix A

InGrids produced on 8″ wafers

A.1 ToT-Calibration

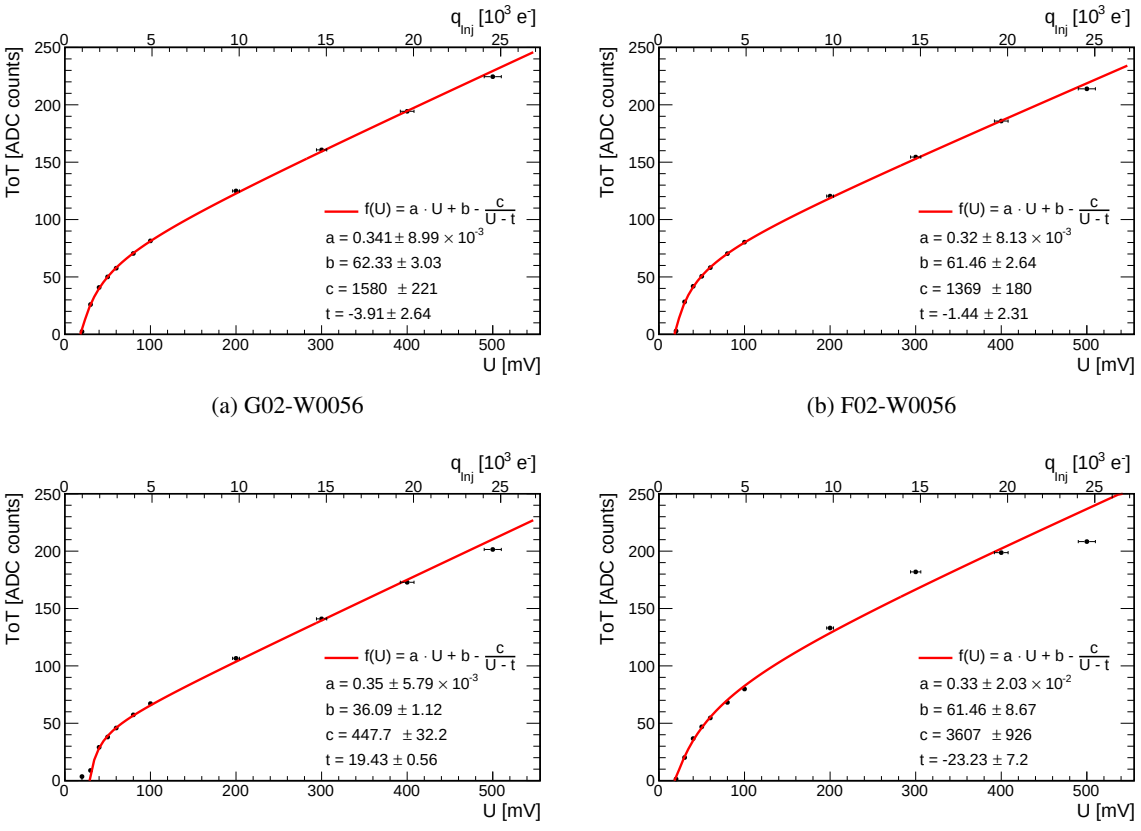

(a) G02-W0056

(b) F02-W0056

(c) H04-W0056

(d) L04-W0056

Figure A.1: Calibration curves for all tested chips of the third production cycle.

A.2 Active region

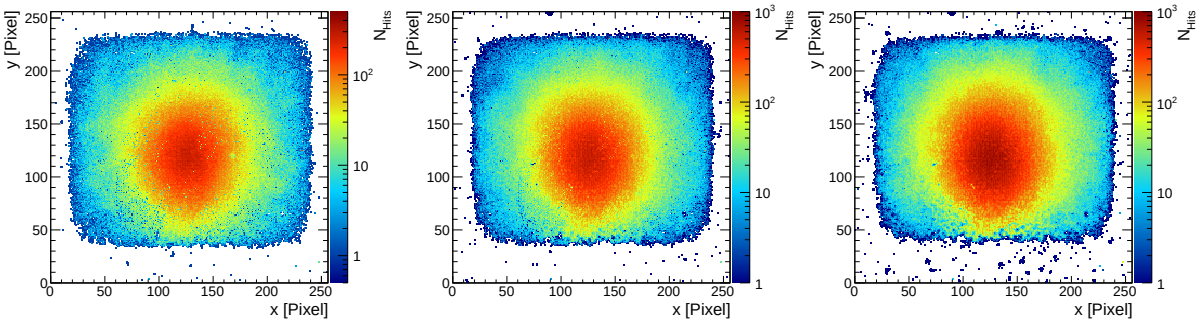

(a) $U_{Grid} = 310\,V$ (b) $U_{Grid} = 340\,V$ (c) $U_{Grid} = 370\,V$

Figure A.2: Occupancy of G02-W0056 at grid voltages of 310 V, 340 V and 370 V.

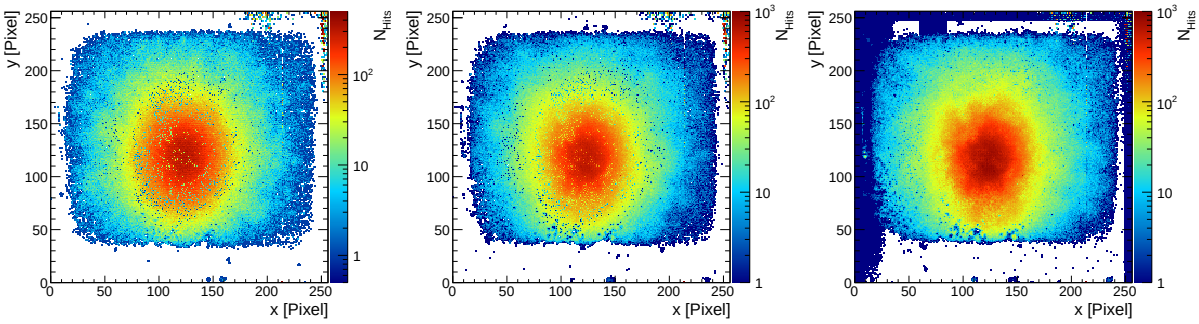

(a) $U_{Grid} = 310\,V$ (b) $U_{Grid} = 340\,V$ (c) $U_{Grid} = 370\,V$

Figure A.3: Occupancy of H04-W0056 at grid voltages of 310 V, 340 V and 370 V.

A.3 Energy resolution by pixel spectra

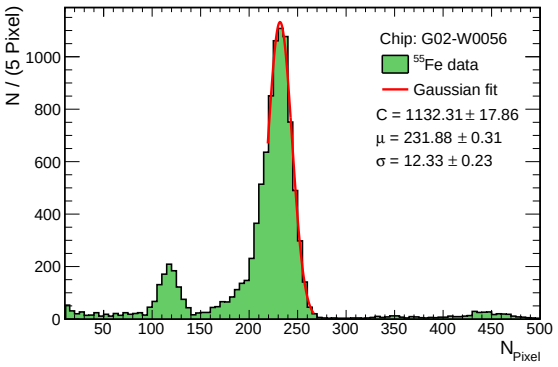

(a) G02-W0056

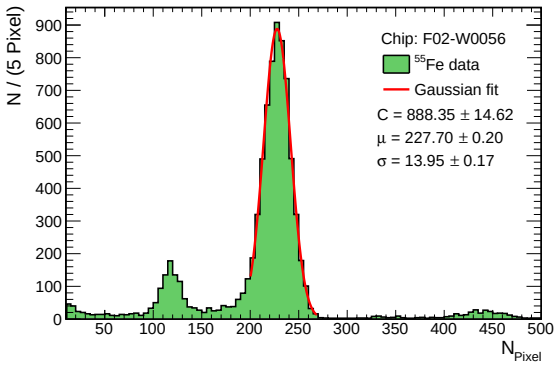

(b) F02-W0056

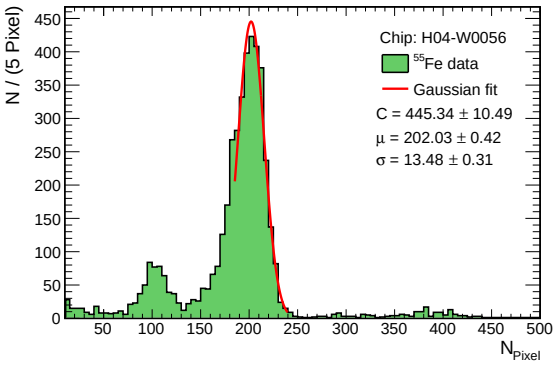

(c) H04-W0056

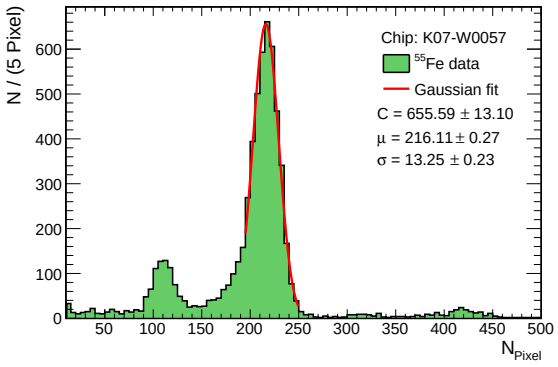

(d) K07-W0057

Figure A.4: Pixel spectra of various InGrids fabricated by the wafer scale production process. All measurements have been performed at a grid voltage of $U_{Grid} = 350\,V$. The stated values have been used to determine the energy resolution for the pixel method in Table 4.4.

A.4 Energy resolution by charge spectra

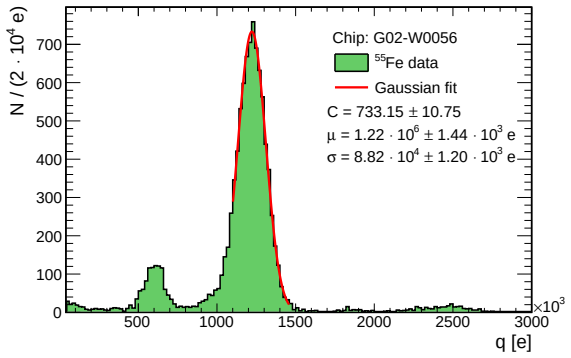

(a) G02-W0056

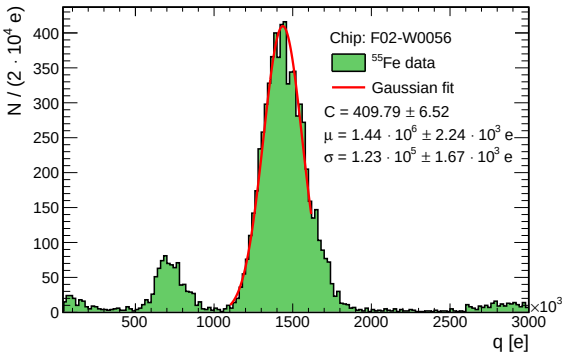

(b) F02-W0056

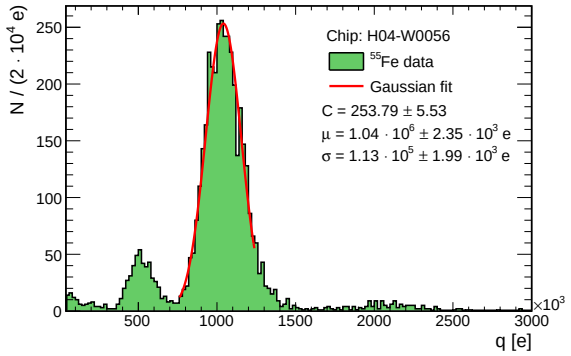

(c) H04-W0056

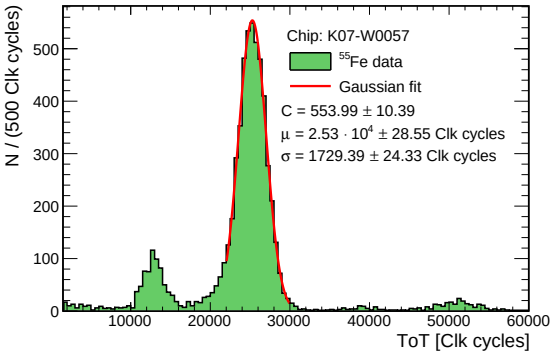

(d) K07-W0057

Figure A.5: Charge spectra of various InGrids fabricated by the wafer scale production process, (a) to (d). All measurements have been performed at a grid voltage of $U_{Grid} = 350\,V$. The stated values have been used to determine the energy resolution for the charge method in Table 4.4.

A.5 Dependence on the barometric pressure

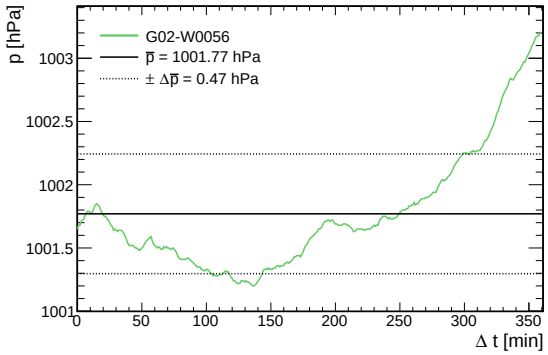

(a) G02-W0056

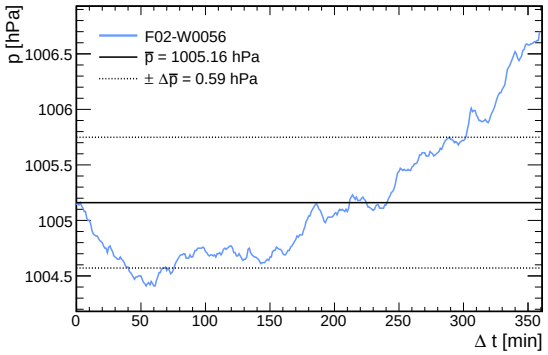

(b) F02-W0056

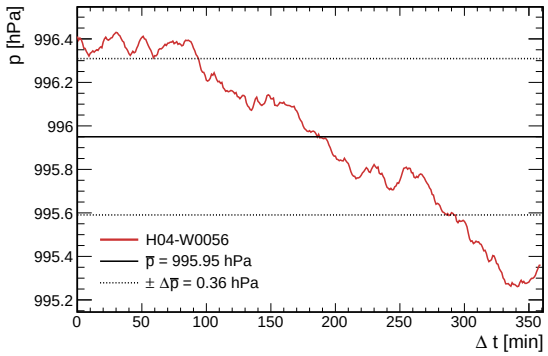

(c) H04-W0056

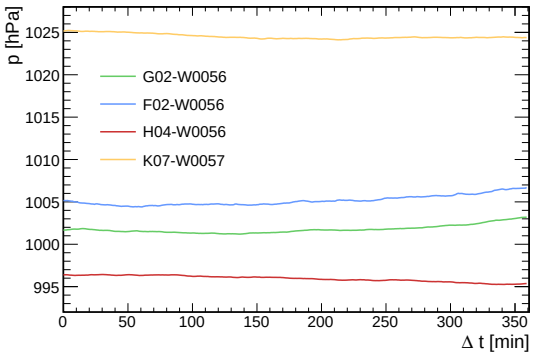

(d) Comparison for various devices.

Figure A.6: Progression of the barometric pressure during the measurements depicted in Figure A.5. (a) to (c) show the course of the pressure for measurements with InGrids from the third production cycle. A comparison of these curves, together with course for a device of the second run is depicted in (d).

The progression of the barometric pressure during the measurements presented in Figure A.5 is depicted in Figure A.6 for three devices from the third run (see (a) to (c)) and in comparison for all four tested devices in (d). The data have been taken from a webservice of the Meteorological Institute of the University of Bonn which provides a measuring point for every minute [165]. Each curve shows the barometric pressure for a period of six hours which is roughly the time required to gather the amount of presented data even though the exact durations may differ.

The individual curves for the three InGrids are subject to some fluctuations during the course of the measurements. By comparison with each other, as shown in (d), it becomes apparent that these fluctuations are small compared to the overall differences between the curves. For this reason, a simplified approach is chosen to compare the influence of the barometric pressure on the measurements. The mean pressure, $\bar{p}$, and its deviations, $\Delta\bar{p}$, are calculated via

$$\bar{p} = \frac{1}{N}\sum_{i=1}^{N} p_i \qquad \text{and} \qquad \Delta\bar{p} = \sqrt{\frac{1}{N}\sum_{i=1}^{N}(p_i - \bar{p})^2}\,. \tag{A.1}$$

Technically speaking, these formulas only apply for statistically accessible quantities. Even though this is not the case, they can be used for obtaining a measure of the size of the deviations around a common mean value. Applying Equation (A.1) to the measurements of the barometric pressure yields

$$p_{\text{H04-W0056}} = 995.95\,\text{hPa} \pm 0.36\,\text{hPa},$$

$$p_{\text{G02-W0056}} = 1001.77\,\text{hPa} \pm 0.47\,\text{hPa}$$

and

$$p_{\text{F02-W0056}} = 1005.16\,\text{hPa} \pm 0.59\,\text{hPa}$$

for the three tested devices of the third production cycle.

The dependence of the gas gain, G, on the gas density, ρ, is usually expressed by [60]:

$$\frac{\mathrm{d}G}{G} = -\frac{\lambda\,\ln 2}{\Delta V\,2\pi\epsilon_0}\frac{\mathrm{d}\rho}{\rho} \tag{A.2}$$

with voltage difference Δ V, charge per unit length λ and vacuum permittivity ϵ_0. With the relation $\rho \propto P/T$ between density on the one side and pressure, P, and temperature, T, on the other side the above equation can be used to deal with pressure and temperature fluctuations, respectively. The gain decreases with increasing density/pressure, as higher values result in a decreased mean free path between two collisions of electrons and gas molecules.

From the above considerations it becomes apparent, that the measured differences in the barometric pressure can not explain the gain differences observed for the three devices of the third production cycle. If pressure/density fluctuations were the cause the device with the highest mean pressure would show the lowest gain. But this device (F02-W0056) is indeed the one with the largest gain. Furthermore, the difference in pressure between G02-W0056 and H04-W0056 is nearly of the same size as the pressure difference between F02-W0056 and G02-W0056.

A.6 Peak performance

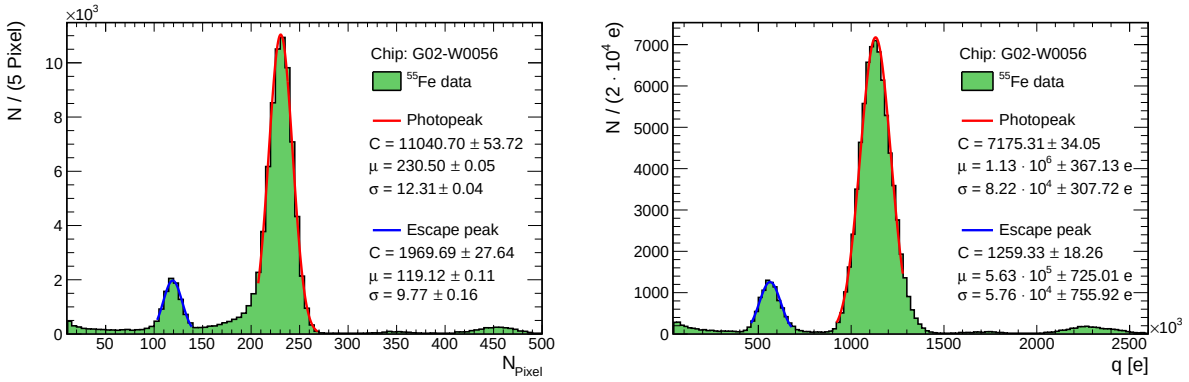

(a) Pixel spectrum.

(b) Charge spectrum.

Figure A.7: Uncut spectra for G02-W0056 and $U_{Grid} = 345\,V$.

Figure A.7 illustrates the spectra obtained with device G02-W0056 at a grid voltage of 345 V. The same binning is used as for the spectra in Figure A.4 and Figure A.5. If no cuts are applied except on the position of the reconstructed photon (cf. Section 4.3.2), the energy resolution computes to

$$\left(\frac{\sigma}{\mu}\right)_{PP} = 5.34\,\% \pm 0.02\,\% \qquad \text{and} \qquad \left(\frac{\sigma}{\mu}\right)_{EP} = 8.20\,\% \pm 0.13\,\%$$

for the pixel spectrum and to

$$\left(\frac{\sigma}{\mu}\right)_{PP} = 7.27\,\% \pm 0.03\,\% \qquad \text{and} \qquad \left(\frac{\sigma}{\mu}\right)_{EP} = 10.23\,\% \pm 0.13\,\%$$

for the charge spectrum. These values are compatible with those in Table 4.4 which have also been obtained without quality cuts.

A.7 Gas amplification

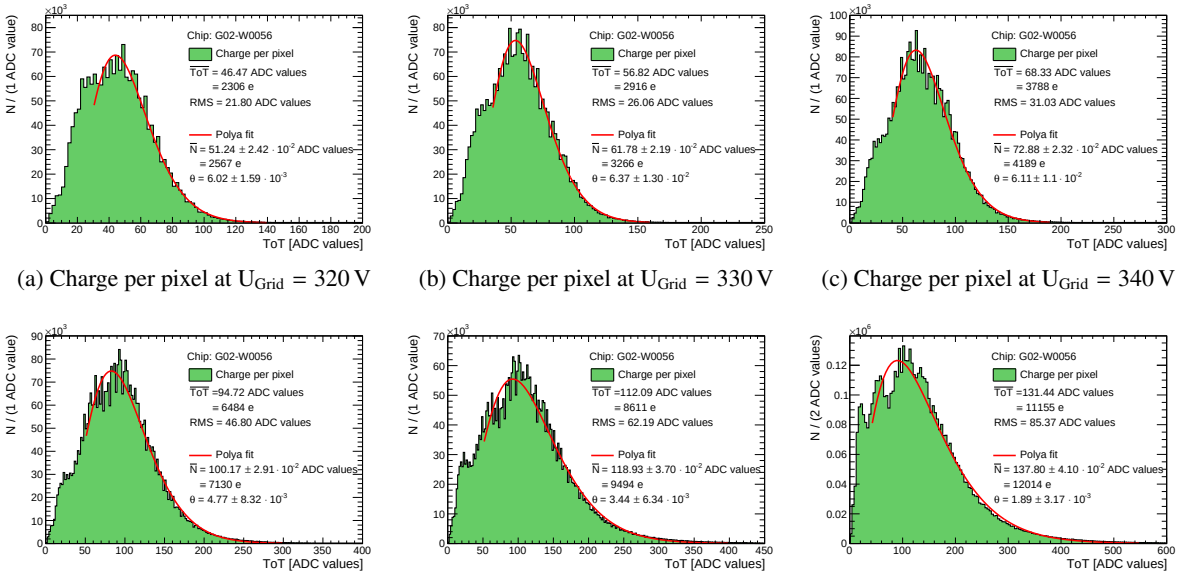

(a) Charge per pixel at $U_{Grid} = 320\,V$ (b) Charge per pixel at $U_{Grid} = 330\,V$ (c) Charge per pixel at $U_{Grid} = 340\,V$

(d) Charge per pixel at $U_{Grid} = 360\,V$ (e) Charge per pixel at $U_{Grid} = 370\,V$ (f) Charge per pixel at $U_{Grid} = 380\,V$

Figure A.8: Charge-per-pixel distributions of G02-W0056 with all pixels considered.

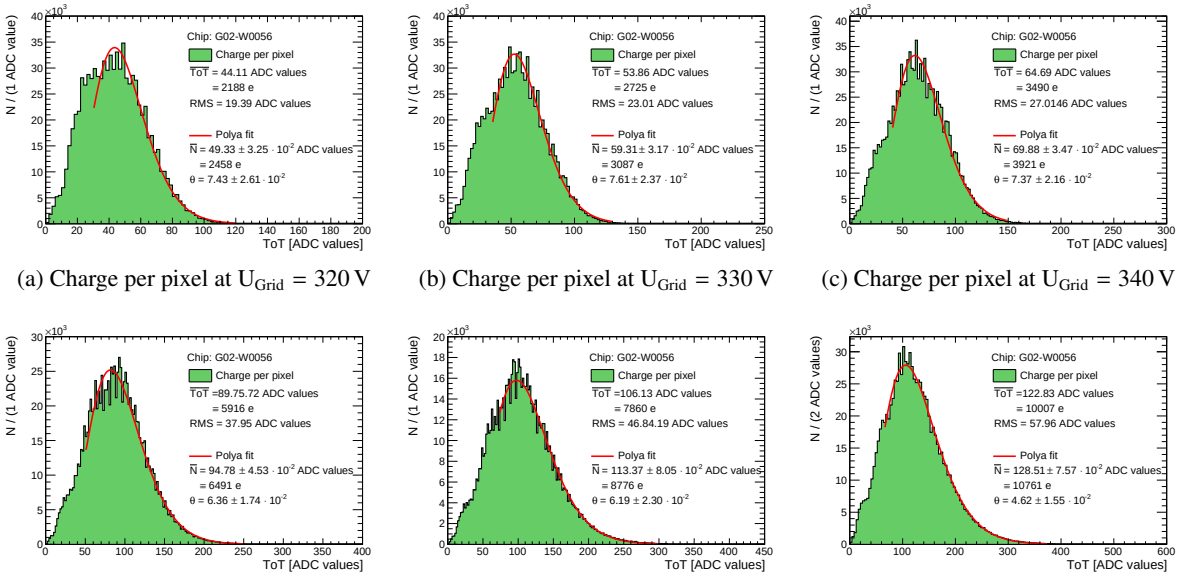

(a) Charge per pixel at $U_{Grid} = 320\,V$ (b) Charge per pixel at $U_{Grid} = 330\,V$ (c) Charge per pixel at $U_{Grid} = 340\,V$

(d) Charge per pixel at $U_{Grid} = 360\,V$ (e) Charge per pixel at $U_{Grid} = 370\,V$ (f) Charge per pixel at $U_{Grid} = 380\,V$

Figure A.9: Charge-per-pixel distributions of G02-W0056 with only isolated pixels considered.

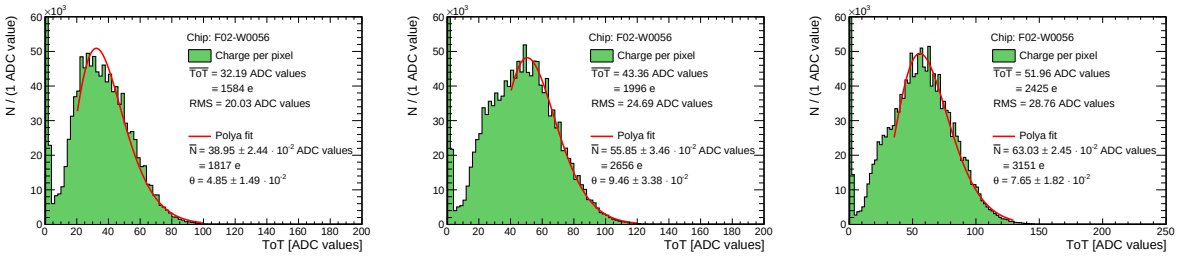

(a) Charge per pixel at $U_{Grid} = 310\,V$ (b) Charge per pixel at $U_{Grid} = 320\,V$ (c) Charge per pixel at $U_{Grid} = 330\,V$

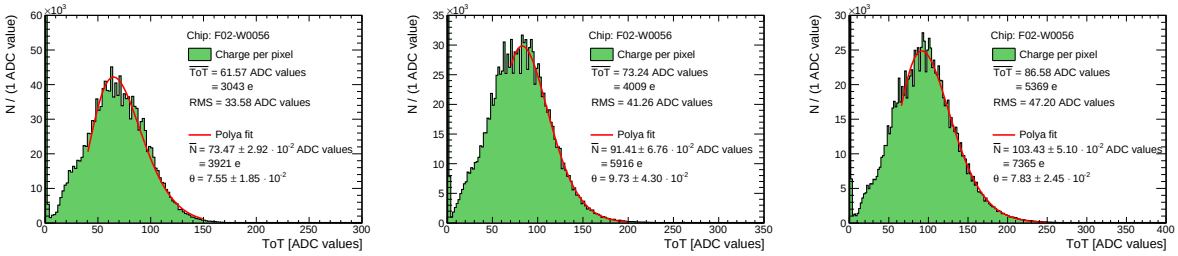

(d) Charge per pixel at $U_{Grid} = 340\,V$ (e) Charge per pixel at $U_{Grid} = 350\,V$ (f) Charge per pixel at $U_{Grid} = 360\,V$

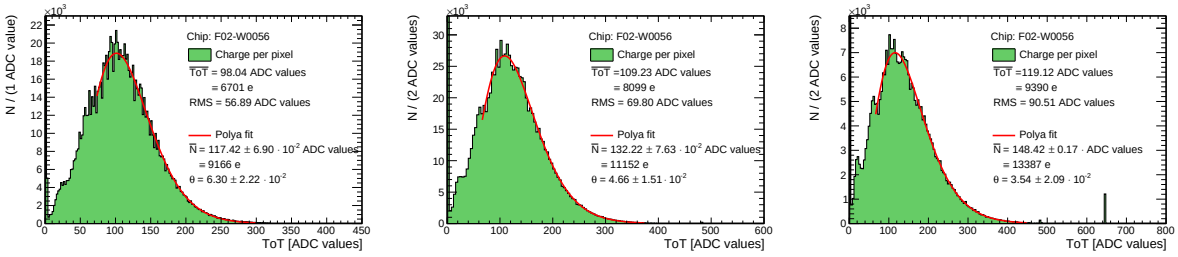

(g) Charge per pixel at $U_{Grid} = 370\,V$ (h) Charge per pixel at $U_{Grid} = 380\,V$ (i) Charge per pixel at $U_{Grid} = 390\,V$

Figure A.10: Charge-per-pixel distributions of F02-W0056 with only isolated pixels considered.

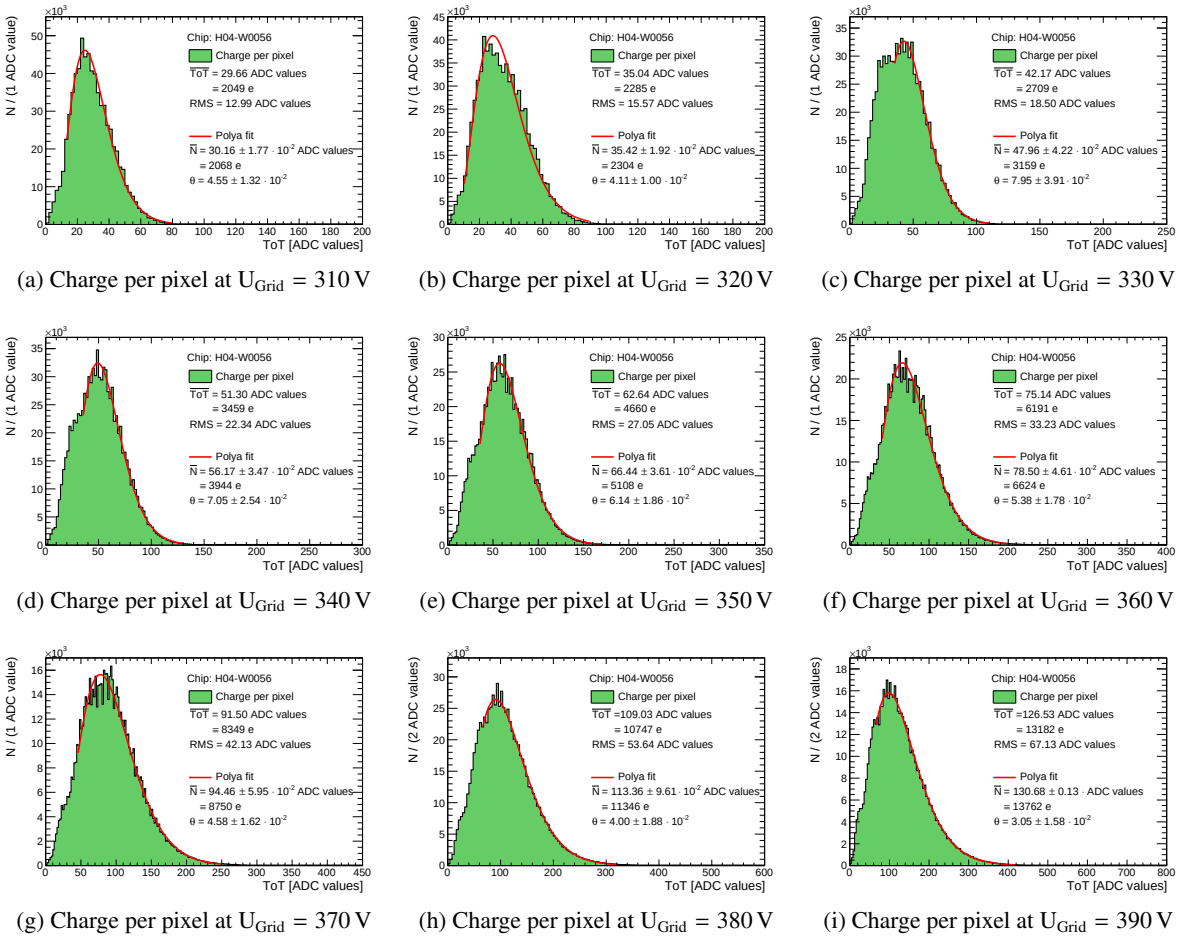

(a) Charge per pixel at $U_{Grid} = 310\,V$ (b) Charge per pixel at $U_{Grid} = 320\,V$ (c) Charge per pixel at $U_{Grid} = 330\,V$

(d) Charge per pixel at $U_{Grid} = 340\,V$ (e) Charge per pixel at $U_{Grid} = 350\,V$ (f) Charge per pixel at $U_{Grid} = 360\,V$

(g) Charge per pixel at $U_{Grid} = 370\,V$ (h) Charge per pixel at $U_{Grid} = 380\,V$ (i) Charge per pixel at $U_{Grid} = 390\,V$

Figure A.11: Charge-per-pixel distributions of H04-W0056 with only isolated pixels considered.

A.8 CSA calibration

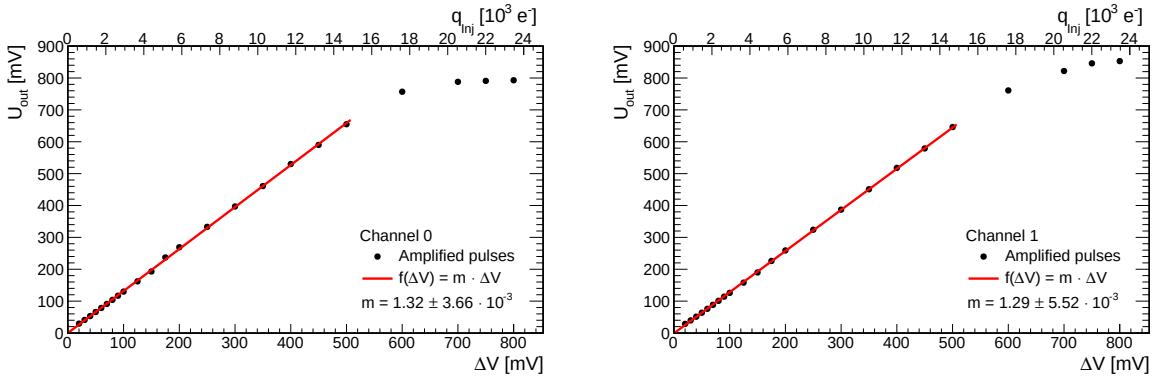

(a) FADC channel 0.

(b) FADC channel 1.

Figure A.12: Calibration curves of the two channels from the charge sensitive amplifier.

A charge calibration of the CSA output for the circuitry depicted in Figure 4.28a in Section 4.3.7 can be done by applying a voltage step ΔV at the input V_{Test}. This yields a defined charge quantity q_{Inj} via the relation

$$q_{Inj} = \Delta V \frac{C_{Test} C_{Grid}}{C_{Test} + C_{Grid}} \approx \Delta V C_{Test}, \tag{A.3}$$

where C_{Grid} is the capacity of the amplification grid. The approximation is only valid if the input capacity C_{Test} is small compared to the capacity of the grid, C_{Grid}. This requirement is well met for typical grid capacities in the range of 60 pF to 100 pF and an input capacity of $C_{Test} = 4.7$ pF.

Appendix B

Simulation of drift deviations in an ILD-TPC

Parameter	Value	Description
Detector model	ILD_o1_v05	Analog HCal
Lorentz transformation angle	7 mrad	Half beam crossing angle
Magnetic field map	fieldX03 1000	More detailed field map including the anti-DID.
TPCLowPtStepLimit	true	Use a step size limit.
TPCLowPtCut	3 TeV	Step size limit is applied for all particles with $p_T \leq 3$ TeV, i.e. for all particles.
TPCLowPtMaxStepLength	0.2 mm	Maximum step size.
TPCLowPtMaxHitSeparation	0.1 mm	
TPCCut	0 MeV	
rangeCut	0.005 mm	
Physics list	QGSP_BERT_HP	More detailed physics list.

Table B.1: Simulation parameters as used for the simulation of beam induced backgrounds with `Mokka` .

Parameter	Value	Remarks
Maximum drift length	2225 mm	
Inner radius TPC	329 mm	
Inner wall thickness	25 mm	
Inner radius gas volume	354 mm	Inner radius plus inner wall thickness.
Inner radius active area	384 mm	
Outer radius TPC	1808	
Outer wall thickness	60 mm	
Outer radius gas volume	1748 mm	Outer radius minus outer wall thickness.
Outer radius active area	1718 mm	

Table B.2: Geometric parameters of the TPC in the ILD_o1_v05 detector model of `Mokka`.

B.1 Deviations for backgrounds at $\sqrt{s}$ = 1 TeV

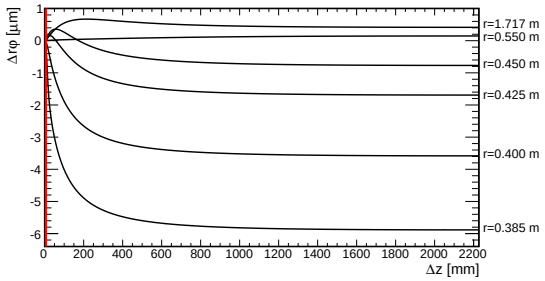

(a) $\gamma\gamma \rightarrow$ hadrons

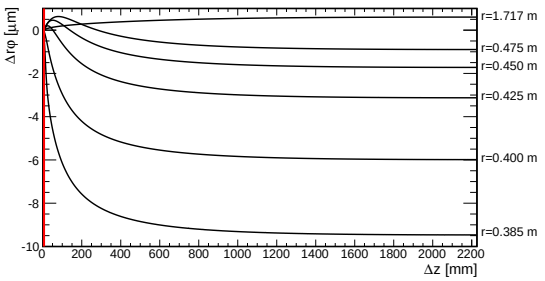

(b) e^+e^--pairs

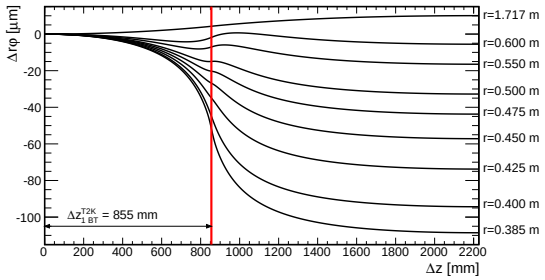

(c) $\gamma\gamma \rightarrow$ hadrons

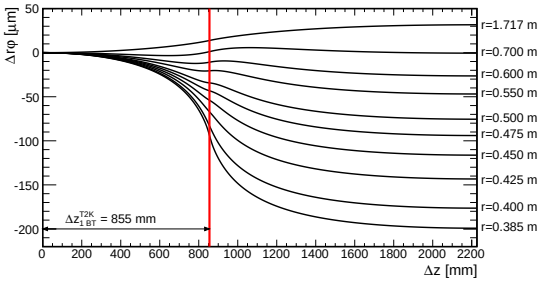

(d) e^+e^--pairs

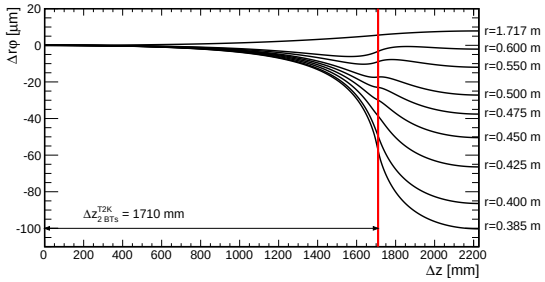

(e) $\gamma\gamma \rightarrow$ hadrons

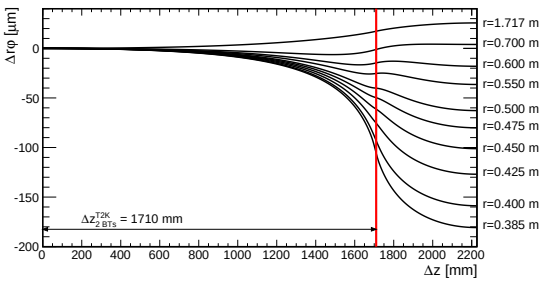

(f) e^+e^--pairs

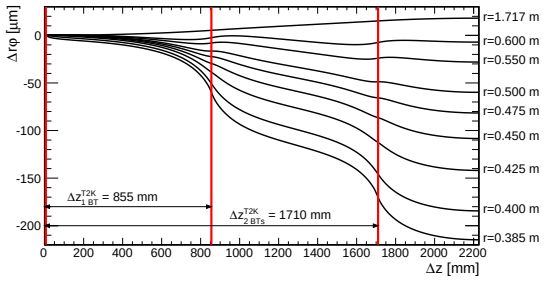

(g) $\gamma\gamma \rightarrow$ hadrons

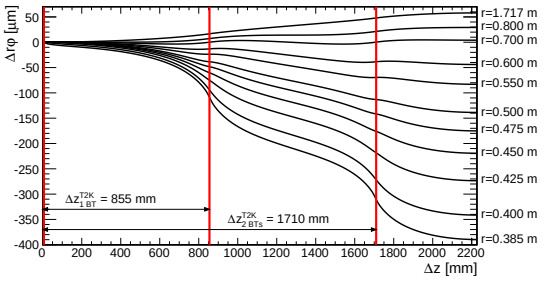

(h) e^+e^--pairs

Figure B.1: Displacement of electron end points caused by ion discs at different z-positions. The position of the discs has been calculated for the T2K gas mixture and a drift field 280 V/cm. Shown are the effects of backgrounds from $\gamma\gamma \rightarrow$ hadrons (a,c,e,g) and e^+e^--pairs (b,d,f,h) for a center-of-mass energy of 1 TeV. The red lines indicate the position of the ion discs.

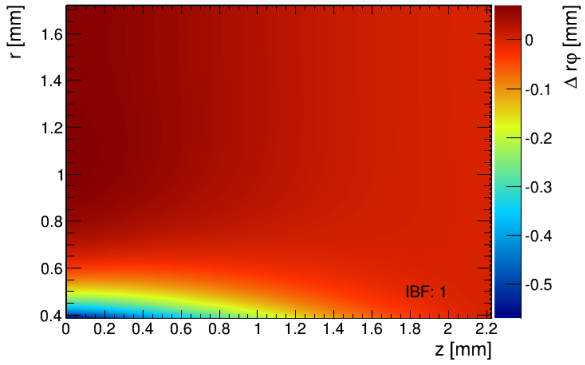

(a) Ion gate, $IBF = 1$

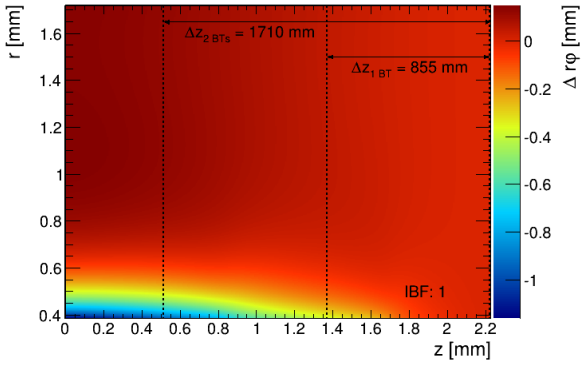

(b) No ion gate, $IBF = 1$

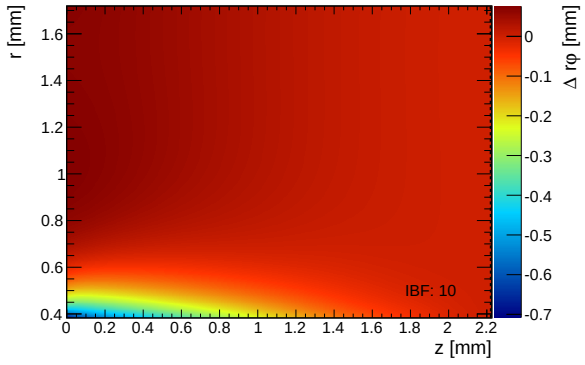

(c) Ion gate, $IBF = 10$

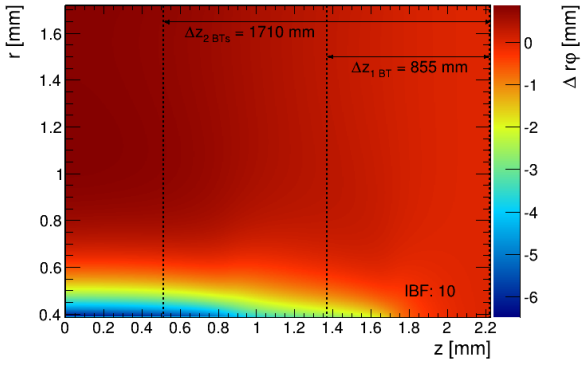

(d) No ion gate, $IBF = 10$

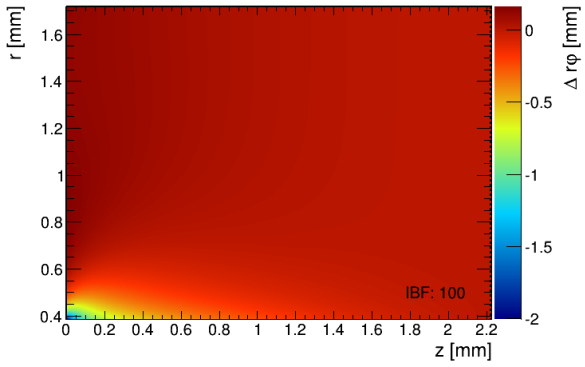

(e) Ion gate, $IBF = 100$

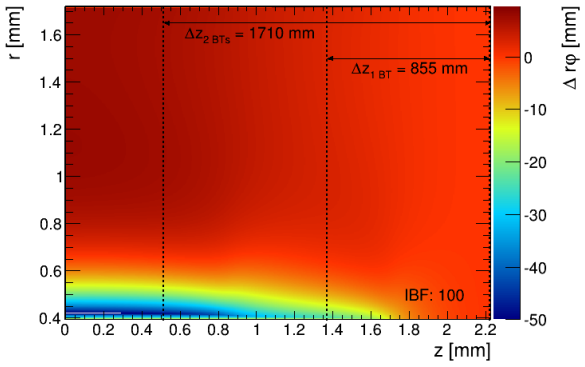

(f) No ion gate, $IBF = 100$

Figure B.2: Drift deviations in a TPC with T2K gas w/o ion gate, for several ion back drift ratios. Both backgrounds are considered for a center-of-mass energy of 1 GeV. The deviations are plotted against the initial positions of the electrons, for the whole $r\varphi$-plane. In the ungated case (a,c,e) only one disc is present in the TPC in contrast to three discs for the gated (b,d,f) case. The dotted lines indicate the positions of the ion discs.

B.2 Additions to the TPC simulation

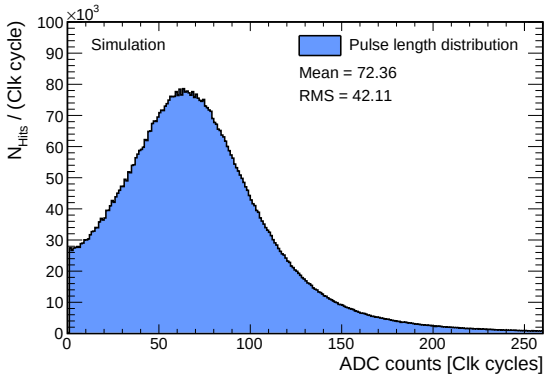

Figure B.3: Pulse length distribution for a mean gas gain of 5000.

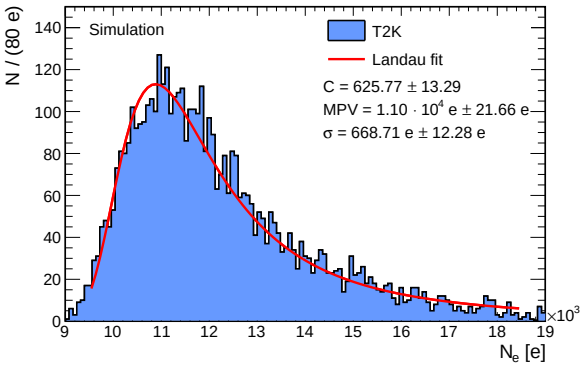

Figure B.4: Number of electron-ion pairs created by 2 GeV muons along a track of 1334 mm length in T2K gas.

Glossary

A

ADC Analog to Digital Converter.

ALICE A Large Ion Collider Experiment.

ASCII American Standard Code for Information Interchange.

ASIC Application-Specific Integrated Circuit.

ATLAS A Toroidal LHC Apparatus.

C

CALICE Calorimeter for Linear Collider Experiment.

CAST CERN Axion Solar Telescope.

CCD Charge-Coupled Device.

CERN European Organization for Nuclear Research.

CLIC Compact Linear Collider.

CMOS Complementary Metal-Oxide Semiconductor.

CMS Compact Muon Solonoid.

COMPASS Common Muon and Proton Apparatus for Structure and Spectroscopy.

CPS CMOS Pixel Sensor.

CSA Charge Sensitive Amplifier.

D

DAC Digital to Analog Converter.

DEPFET Depleted P-Channel Field-Effect Transistor.

E

ECAL Electromagnetic Calorimeter.

ENC Equivalent Noise Charge.

EP Escape Peak.

EPA Equivalent Photon Approximation.

ETD End-Cap Tracking Detector.

F

FADC Fast Analog to Digital Converter.

FIB Focused Ion Beam.

FPCCD Fine Pixel CCD.

FTD Forward Tracking Detector.

G

GEM Gas Electron Multiplier.

GLD Global Large Detector.

H

HCAL Hadronic Calorimeter.

I

ILC International Linear Collider.

ILD International Large Detector.

InGrid Integrated Grid.

L

LCIO Linear Collider I/O.

LDC Large Detector Concept.

LEP Large Electron-Positron Collider.

LHC Large Hadron Collider.

LPVD Low Pressure Vapor Deposition.

M

Marlin Modular Analysis and Reconstruction for the Linear Collider.

Micromegas Micro-Mesh Gaseous Detector.

MIP Mimimum Ionizing Particle.

MPGD Micro-pattern gaseous detector.

MUROS Medipix Universal Read-Out System.

P

PCB Printed Circuit Board.

PCR Pixel Configuration Register.

PECVD Plasma Enhanced Chemical Vapor Deposition.

PP Photo Peak.

R

RMS Root Mean Square.

RPC Resistive Plate Chamber.

S

SET Silicon External Tracker.

SIT Silicon Inner Tracker.

SLC Stanford Linear Collider.

SM Standard Model.

T

T2K Tokai to Kamioka.

TDR Technical Design Report.

ToA Time of Arrival.

ToT Time Over Threshold.

TOTEM Total Elastic and Diffractive Cross Section Measurement.

TPC Time Projection Chamber.

Bibliography

[1] O. S. Brüning et al., "LHC Design Report. 1. The LHC Main Ring," ed. by O. S. Brüning, Geneva: CERN, 2004, DOI: 10.5170/CERN-2004-003-V-1 (cit. on pp. 3, 4).

[2] O. S. Brüning, P. Collier, P. Lebrun, S. Myers, R. Ostojic, et al., "LHC Design Report. 2. The LHC infrastructure and general services," ed. by O. S. Brüning, Generva: CERN, 2004, DOI: 10.5170/CERN-2004-003-V-2 (cit. on pp. 3, 4).

[3] M. Benedikt, P. Collier, V. Mertens, J. Poole, and K. Schindl, "LHC Design Report. 3. The LHC injector chain" (2004), ed. by M. Benedikt, DOI: 10.5170/CERN-2004-003-V-3 (cit. on pp. 3, 4).

[4] G. Aad et al., "Observation of a new particle in the search for the Standard Model Higgs boson with the ATLAS detector at the LHC," *Phys. Lett.* B 716 (2012) 1–29, DOI: 10.1016/j.physletb.2012.08.020, arXiv: 1207.7214, URL: http://www.sciencedirect.com/science/article/pii/S037026931200857X (cit. on pp. 4, 5).

[5] S. Chatrchyan et al., "Observation of a new boson at a mass of 125 GeV with the CMS experiment at the LHC," *Phys. Lett.* B 716 (2012) 30–61, DOI: 10.1016/j.physletb.2012.08.021, arXiv: 1207.7235, URL: http://www.sciencedirect.com/science/article/pii/S0370269312008581 (cit. on pp. 4, 5).

[6] P. W. Higgs, "Broken symmetries, massless particles and gauge fields," *Phys. Lett.* 12 (1964) 132–133, DOI: 10.1016/0031-9163(64)91136-9, URL: http://www.sciencedirect.com/science/article/pii/0031916364911369 (cit. on p. 4).

[7] P. W. Higgs, "Broken Symmetries and the Masses of Gauge Bosons," *Phys. Rev. Lett.* 13 (16 Oct. 1964) 508–509, DOI: 10.1103/PhysRevLett.13.508, URL: http://link.aps.org/doi/10.1103/PhysRevLett.13.508 (cit. on p. 4).

[8] P. W. Higgs, "Spontaneous Symmetry Breakdown without Massless Bosons," 145 (4 May 1966) 1156–1163, DOI: 10.1103/PhysRev.145.1156, URL: http://link.aps.org/doi/10.1103/PhysRev.145.1156 (cit. on p. 4).

[9] M. Aicheler et al.,
"A Multi-TeV Linear Collider Based on CLIC Technology: CLIC Conceptual Design Report," tech. rep. CERN-2012-007. SLAC-R-985. KEK-Report-2012-1. PSI-12-01. JAI-2012-001, 2012 (cit. on p. 4).

[10] "SLAC Linear Collider Conceptual Design Report," Stanford: SLAC, 1980 (cit. on p. 4).

[11] "LEP design report," Copies shelved as reports in LEP, PS and SPS libraries, Geneva: CERN, 1984 (cit. on p. 4).

[12] V. Shiltsev, "Accelerator Science and Technology Breakthroughs, Achievements and Lessons from the Tevatron," Comments: Invited CERN 2010 John Adams Lecture - and to be published as such in CERN's Yellow Report; 17 pages, 18 Figures, Geneva: CERN, 2011 (cit. on p. 4).

[13] H. Baer, T. Barklow, K. Fujii, Y. Gao, A. Hoang, et al.,
"The International Linear Collider Technical Design Report - Volume 2: Physics" (Apr. 2013), ed. by H. Baer, arXiv: 1306.6352 [hep-ph], URL: http://edmsdirect.desy.de/edmsdirect/file.jsp?edmsid=D00000001021165&fileClass=native (cit. on pp. 4, 6).

[14] F. Abe et al., "Observation of Top Quark Production in $\overline{p}p$ Collisions with the Collider Detector at Fermilab," *Phys. Rev. Lett.* 74 (14 Apr. 1995) 2626–2631, DOI: 10.1103/PhysRevLett.74.2626 (cit. on p. 4).

[15] S. Abachi et al., "Observation of the Top Quark,"
Phys. Rev. Lett. 74 (14 Apr. 1995) 2632–2637, DOI: 10.1103/PhysRevLett.74.2632 (cit. on p. 4).

[16] T. Behnke, J. E. Brau, B. Foster, J. Fuster, M. Harrison, et al.,
"The International Linear Collider: Technical Design Report. Volume 1: Executive Summary," ILC-REPORT-2013-040 (Apr. 2013), ed. by T. Behnke,
arXiv: 1306.6327 [physics.acc-ph], URL: http://edmsdirect.desy.de/edmsdirect/file.jsp?edmsid=D00000001021135&fileClass=native (cit. on pp. 5–7, 9).

[17] H. Li, F. Richard, R. Poeschl, and Z. Zhang, "Precision Measurements of SM Higgs Recoil Mass and Cross Section for s**1/2 of 230-GeV and 250-GeV at ILC" (2009),
arXiv: 0901.4893 [hep-ex] (cit. on p. 5).

[18] H. Li et al., "HZ Recoil Mass and Cross Section Analysis in ILD" (2012),
arXiv: 1202.1439 [hep-ex] (cit. on p. 5).

[19] K. Hagiwara, H. Murayama, and I. Watanabe,
"Search for the Yukawa interaction in the process e+ e- —>; t anti-t Z at TeV linear colliders," *Nucl. Phys.* B 367 (1991) 257–286, DOI: 10.1016/0550-3213(91)90017-R,
URL: http://www.sciencedirect.com/science/article/pii/055032139190017R (cit. on p. 6).

[20] A. Djouadi, J. Kalinowski, and P. M. Zerwas,
"Higgs radiation off top quarks in high-energy e+ e- colliders," *Z. Phys.* C 54 (1992) 255–262, DOI: 10.1007/BF01566654 (cit. on p. 6).

[21] A. Juste, Y. Kiyo, F. Petriello, T. Teubner, K. Agashe, et al.,
"Report of the 2005 Snowmass top/QCD working group" (2006),
arXiv: hep-ph/0601112 [hep-ph] (cit. on p. 6).

[22] D. Schultz, J. Clendenin, J. Frisch, E. W. Hoyt, L. Klaisner, et al.,
"The Polarized electron gun for the SLC," *Conf.Proc.* C920324 (1992) 1029–1031
(cit. on p. 7).

[23] F. Furuta et al., "Experimental Comparison at KEK of High Gradient Performance of Different Single Cell Superconducting Cavity Designs" (2006) 3 p (cit. on p. 8).

[24] O. Napoly,
"The Luminosity for beam distributions with error and wake field effects in linear colliders,"
Part. Accel. 40 (1993) 181–203 (cit. on p. 8).

[25] C. Adolphsen, M. Barone, B. Barish, K. Buesser, P. Burrows, et al., "The International Linear Collider Technical Design Report - Volume 3.II: Accelerator Baseline Design"
(2013), ed. by C. Adolphsen, arXiv: 1306.6328 [physics.acc-ph],
URL: http://edmsdirect.desy.de/edmsdirect/file.jsp?edmsid=D00000001021265&fileClass=native (cit. on p. 10).

[26] J. E. Augustin, N. Dikansky, Y. Derbenev, J. Rees, B. Richter, et al., "Limitations on Performance of e+ e- Storage Rings and Linear Colliding Beam Systems at High Energy,"
eConf C781015 (1978) 009 (cit. on p. 9).

[27] K. Yokoya and P. Chen, "Beam-beam phenomena in linear colliders,"
Frontiers of Particle Beams: Intensity Limitations, ed. by M. Dienes, M. Month, and S. Turner, vol. 400, Lect. Notes. Phys. Springer Berlin Heidelberg, 1992 415–445,
DOI: 10.1007/3-540-55250-2_37 (cit. on pp. 10, 17).

[28] M. Venturini and W. Kozanecki, "The hourglass effect and the measurement of the transverse size of colliding beams by luminosity scans,"
Particle Accelerator Conference, 2001. PAC 2001. Proceedings of the 2001, vol. 5
3573–3575 vol.5, DOI: 10.1109/PAC.2001.988182 (cit. on p. 10).

[29] M. Horiuchi, *ILD illustrations*, 2011, URL: http://ilcild.org/documents/mdi/ild-illustrations/tentative-version-as-of-2011-aug.30/ (cit. on p. 11).

[30] T. Behnke, J. E. Brau, P. N. Burrows, J. Fuster, M. Peskin, et al.,
"The International Linear Collider Technical Design Report - Volume 4: Detectors"
(Apr. 2013), ed. by T. Behnke, arXiv: 1306.6329 [physics.ins-det]
(cit. on pp. 12, 36, 43, 44).

[31] Y. Fu, C. Hu-Guo, A. Dorokhov, O. Torheim, W. Zhao, et al., "Conceptual design of 3D integrated pixel sensors for the innermost layer of the ILC vertex detector,"
JINST 6 (2011) C12038, DOI: 10.1088/1748-0221/6/12/C12038,
URL: http://stacks.iop.org/1748-0221/6/i=12/a=C12038 (cit. on p. 12).

[32] O. Alonso et al., "DEPFET active pixel detectors for a future linear e^+e^- collider,"
Nuclear Science, IEEE Transactions on 60 (2013) 1457–1465,
DOI: 10.1109/TNS.2013.2245680, arXiv: 1212.2160 [physics.ins-det] (cit. on p. 12).

[33] I. Peric, P. Fischer, J. Knopf, and T. H. H. Nguyen,
"DCDB and SWITCHERB, the readout ASICS for belle II DEPFET pixel detector,"
Nuclear Science Symposium and Medical Imaging Conference (NSS/MIC), 2011 IEEE, 2011
1536–1539, DOI: 10.1109/NSSMIC.2011.6154365,
URL: http://ieeexplore.ieee.org/stamp/stamp.jsp?tp=&arnumber=6154365
(cit. on p. 12).

[34] Y. Sugimoto, H. Ikeda, D. Kamai, E. Kato, A. Miyamoto, et al.,
"R & D Status of FPCCD Vertex Detector for ILD" (2012),
arXiv: 1202.5832 [physics.ins-det] (cit. on p. 13).

[35] C. Adloff et al.,
"Construction and Commissioning of the CALICE Analog Hadron Calorimeter Prototype,"
JINST 5 (2010) P05004, DOI: 10.1088/1748-0221/5/05/P05004,
arXiv: 1003.2662 [physics.ins-det],
URL: http://stacks.iop.org/1748-0221/5/i=05/a=P05004 (cit. on p. 15).

[36] H. Abramowicz, A. Abusleme, K. Afanaciev, J. Aguilar, P. Ambalathankandy, et al.,
"Forward Instrumentation for ILC Detectors," *JINST* 5 (2010) P12002,
DOI: 10.1088/1748-0221/5/12/P12002, arXiv: 1009.2433 [physics.ins-det],
URL: http://stacks.iop.org/1748-0221/5/i=12/a=P12002 (cit. on p. 15).

[37] M. Czakon, J. Gluza, and T. Riemann,
"The Planar four-point master integrals for massive two-loop Bhabha scattering,"
Nucl. Phys. B 751 (2006) 1–17, DOI: 10.1016/j.nuclphysb.2006.05.033,
arXiv: hep-ph/0604101 [hep-ph],
URL: http://www.sciencedirect.com/science/article/pii/S0550321306004135
(cit. on p. 15).

[38] R. Settles, "LCTPC and the Magnetic Field for ILD: Update 2010,"
tech. rep. LC-DET-2011-002, Nov. 2011,
URL: http://www-flc.desy.de/lcnotes/notes/LC-DET-2011-002.pdf
(cit. on pp. 15, 44).

[39] F. Kircher et al., "CMS coil design and assembly,"
Applied Superconductivity, IEEE Transactions on 12 (2002) 395–398,
DOI: 10.1109/TASC.2002.1018427 (cit. on p. 15).

[40] F. Kircher et al., "Conceptual design of the ILD Detector Magnet System,"
tech. rep. LC-DET-2012-081, Oct. 2012,
URL: http://www-flc.desy.de/lcnotes/notes/LC-DET-2012-081.pdf (cit. on p. 15).

[41] C. F. von Weizsäcker, "Ausstrahlung bei Stössen sehr schneller Elektronen,"
Zeitschrift für Physik 88 (1934) 612–625, DOI: 10.1007/BF01333110 (cit. on p. 17).

[42] E. Williams, Correlation of Certain Collision Problems with Radiation Theory 4,
Levin & Munksgaard, 1935 (cit. on p. 17).

[43] C. Grupen, A. Boehrer, and L. Smolik, "Particle detectors,"
Camb.Monogr.Part.Phys.Nucl.Phys.Cosmol. 5 (1996) 1–455 (cit. on pp. 20, 21).

[44] J. Beringer et al., "Review of Particle Physics," *Phys. Rev.* D86 (1 July 2012) 010001,
DOI: 10.1103/PhysRevD.86.010001,
URL: http://link.aps.org/doi/10.1103/PhysRevD.86.010001
(cit. on pp. 21, 22, 71, 100).

[45] L. Landau, "On the energy loss of fast particles by ionization,"
J. Phys. (USSR) 8 (1944) 201–205 (cit. on p. 22).

[46] H. Bichsel, "Straggling in thin silicon detectors," *Rev. Mod. Phys.* 60 (3 July 1988) 663–699,
DOI: 10.1103/RevModPhys.60.663,
URL: http://link.aps.org/doi/10.1103/RevModPhys.60.663 (cit. on p. 22).

[47] H. Bichsel,
"A method to improve tracking and particle identification in TPCs and silicon detectors,"
Nucl. Instrum. Meth. A 562 (2006) 154–197, DOI: 10.1016/j.nima.2006.03.009,
URL: http://www.sciencedirect.com/science/article/pii/S0168900206005353
(cit. on p. 22).

[48] G. Musiol, J. Ranft, R. Reif, and D. Seeliger, "Kern- und Elementarteilchenphysik,"
VCH Weinheim, 1988 (cit. on p. 23).

[49] R. Bellazzini and F. Muleri, "X-ray Polarimetry: a new window on the high energy sky,"
Nucl. Instrum. Meth. A 623 (Nov. 2010) 766–770, DOI: 10.1016/j.nima.2010.04.006,
arXiv: 1004.4766,
URL: http://www.sciencedirect.com/science/article/pii/S0168900210007989
(cit. on p. 24).

[50] O. Klein and T. Nishina, "Über die Streuung von Strahlung durch freie Elektronen nach der neuen relativistischen Quantendynamik von Dirac," *Zeitschrift für Physik* 52 (1929) 853–868,
DOI: 10.1007/BF01366453 (cit. on p. 25).

[51] G. Audi, O. Bersillon, J. Blachot, and A. H. Wapstra,
"The Nubase evaluation of nuclear and decay properties," *Nucl. Phys.* A 729.1 (2003) 3–128,
DOI: http://dx.doi.org/10.1016/j.nuclphysa.2003.11.001,
URL: http://www.sciencedirect.com/science/article/pii/S0375947403018074
(cit. on p. 26).

[52] H. W. Schnopper, "Atomic Readjustment to an Inner-Shell Vacancy: Manganese K X-Ray Emission Spectra from an Fe^{55} K-Capture Source and from the Bulk Metal,"
Phys. Rev. 154 (1 Feb. 1967) 118–123, DOI: 10.1103/PhysRev.154.118,
URL: http://link.aps.org/doi/10.1103/PhysRev.154.118 (cit. on p. 26).

[53] M. Lupberger,
"Avalanche statistics and single electron counting with a Timepix-InGrid detector,"
Diploma thesis: Albert-Ludwigs Universität Freiburg, 2010 (cit. on pp. 26, 32).

[54] S. F. Biagi, "Monte Carlo simulation of electron drift and diffusion in counting gases under the influence of electric and magnetic fields," *Nucl. Instr. Meth.* A421.1-2 (1999) 234–240,
DOI: 10.1016/S0168-9002(98)01233-9,
URL: http://www.sciencedirect.com/science/article/pii/S0168900298012339
(cit. on pp. 27, 30).

[55] C. Ramsauer,
""Über den Wirkungsquerschnitt der GasmolekÃ¼le gegenüber langsamen Elektronen,"
Annalen der Physik 369 (1921) 513–540, DOI: 10.1002/andp.19213690603 (cit. on p. 27).

[56] N. Abgrall et al., "Time projection chambers for the T2K near detectors,"
Nucl. Instrum. Meth A637 (2011) 25–46, DOI: 10.1016/j.nima.2011.02.036,
URL: http://www.sciencedirect.com/science/article/pii/S0168900211003421
(cit. on pp. 27, 40).

[57] J. Aguilar-Saavedra et al.,
"TESLA: The Superconducting electron positron linear collider with an integrated x-ray laser laboratory. Technical design report. Part 3. Physics at an e+ e- linear collider" (2001),
arXiv: hep-ph/0106315 [hep-ph] (cit. on p. 27).

[58] L. G. H. (G. H. Huxley and (. a. Crompton R. W. (Robert Woodhouse), "The diffusion and drift of electrons in gases / [by] L. G. H. Huxley [and] R. W. Crompton," English, A Wiley-Interscience publication., New York : Wiley, 1974 (cit. on p. 30).

[59] E. B. Wagner, F. J. Davis, and G. S. Hurst, "Time-of-Flight Investigations of Electron Transport in Some Atomic and Molecular Gases," *J. Chem. Phys.* 47 (Nov. 1967) 3138–3147, DOI: 10.1063/1.1712365, URL: http://jcp.aip.org/resource/1/jcpsa6/v47/i9/p3138_s1 (cit. on p. 30).

[60] W. Blum, W. Riegler, and L. Rolandi, "Particle Detection with Drift Chambers," 2nd ed., Particle Acceleration and Detection, Springer-Verlag Berlin Heidelberg, 2008 (cit. on pp. 32, 33, 136).

[61] G. D. Alkhazov, "Statistics of electron avalanches and ultimate resolution of proportional counters," *Nucl. Instrum. Meth.* 89 (1970) 155–165, DOI: 10.1016/0029-554X(70)90818-9, URL: http://www.sciencedirect.com/science/article/pii/0029554X70908189 (cit. on p. 32).

[62] W. Legler, "The influence of the relaxation of the electron energy distribution on the statistics of electron avalanches," *British Journal of Applied Physics* 18.9 (1967) 1275, DOI: 10.1088/0508-3443/18/9/308, URL: http://stacks.iop.org/0508-3443/18/i=9/a=308 (cit. on p. 32).

[63] M. A. Chefdeville, "Development of micromegas-like gaseous detectors using a pixel readout chip as collecting anode," PhD thesis: University of Twente, Jan. 2009, URL: http://doc.utwente.nl/62815/ (cit. on pp. 32, 52, 53, 72, 75, 114, 118).

[64] S. G. Kappler, "Higgs Search Studies in the Channel *tartH* with the CMS Detector at the LHC and Development of a GEM-based TPC Readout for Future Collider Experiments," PhD thesis: Universität Karlsruhe (TH), 2004, URL: http://inspirehep.net/record/1088086/files/CERN-THESIS-2004-065.pdf (cit. on p. 34).

[65] J. Kaminski, "Developing studies for a time projection chamber at the International Linear Collider (ILC)," PhD thesis: Universität Karlsruhe (TH), 2005, URL: http://inspirehep.net/record/706650/files/iekp-ka2005-15.pdf (cit. on p. 34).

[66] F. Sauli, "GEM: A new concept for electron amplification in gas detectors," *Nucl. Instrum. Meth.* A386 (1997) 531–534, DOI: 10.1016/S0168-9002(96)01172-2 (cit. on p. 33).

[67] M. Killenberg et al., "Modelling and measurement of charge transfer in multiple GEM structures," *Nucl. Instrum. Meth.* A 498 (2003) 369–383, DOI: 10.1016/S0168-9002(02)02079-X, arXiv: physics/0212005, URL: http://www.sciencedirect.com/science/article/pii/S016890020202079X (cit. on p. 34).

[68] S. Lotze, "Ion Backdrift Minimisation in a GEM-Based TPC Readout," PhD thesis: RWTH Aachen, 2006, URL: http://darwin.bth.rwth-aachen.de/opus3/volltexte/2006/1499/ (cit. on pp. 34, 41, 94).

[69] M. Altunbas, M. Capeans, K. Dehmelt, J. Ehlers, J. Friedrich, et al., "Construction, test and commissioning of the triple-GEM tracking detector for COMPASS," *Nucl. Instrum. Meth.* A 490 (2002) 177–203, DOI: 10.1016/S0168-9002(02)00910-5, URL: http://www.sciencedirect.com/science/article/pii/S0168900202009105 (cit. on p. 34).

[70] P. R. Barbosa-Marinho et al., "LHCb muon system: Technical Design Report," ed. by P. R. Barbosa-Marinho, Technical Design Report LHCb, Geneva: CERN, 2001 (cit. on p. 34).

[71] M. G. Bagliesi et al., "The TOTEM T2 telescope based on triple-GEM chambers," *Nucl. Instrum. Meth.* A 617 (2010) 134–137, DOI: 10.1016/j.nima.2009.07.006, URL: http://www.sciencedirect.com/science/article/pii/S0168900209013850 (cit. on p. 34).

[72] Y. Giomataris, P. Rebourgeard, J. Robert, and G. Charpak, "MICROMEGAS: A High granularity position sensitive gaseous detector for high particle flux environments," *Nucl. Instrum. Meth.* A 376 (1996) 29–35, DOI: 10.1016/0168-9002(96)00175-1, URL: http://www.sciencedirect.com/science/article/pii/0168900296001751 (cit. on p. 35).

[73] P. Colas, I. Giomataris, and V. Lepeltier, "Ion backflow in the Micromegas TPC for the future linear collider," *Nucl. Instrum. Meth.* A 535 (2004) 226–230, DOI: 10.1016/j.nima.2004.07.274, URL: http://www.sciencedirect.com/science/article/pii/S0168900204016080 (cit. on pp. 35, 41).

[74] S. Yildiz, S. Aune, T. Dafni, M. Davenport, G. Fanourakis, et al., "Performance of micromegas detectors in the CAST experiment," *J. Phys. Conf. Ser.* 347 (2012) 012029, DOI: 10.1088/1742-6596/347/1/012029, URL: http://stacks.iop.org/1742-6596/347/i=1/a=012029 (cit. on p. 35).

[75] D. Franco, "R&D for high pressure gas TPC readout with segmented Micromegas," *J. Phys. Conf. Ser.* 309 (2011) 012004, DOI: 10.1088/1742-6596/309/1/012004 (cit. on p. 35).

[76] I. Giomataris, R. De Oliveira, S. Andriamonje, S. Aune, G. Charpak, et al., "Micromegas in a bulk," *Nucl. Instrum. Meth.* A 560 (2006) 405–408, DOI: 10.1016/j.nima.2005.12.222, arXiv: physics/0501003, URL: http://www.sciencedirect.com/science/article/pii/S0168900205026501 (cit. on p. 35).

[77] S. Aune, J. Ball, M. Combet, M. El-Yakoubi, P. Konczykowski, et al., "Micromegas tracker project for CLAS12," *Nucl. Instrum. Meth.* A 604 (2009) 53–55, DOI: 10.1016/j.nima.2009.01.047, URL: http://www.sciencedirect.com/science/article/pii/S0168900209001144 (cit. on p. 35).

[78] S. Andriamonje, D. Attie, E. Berthoumieux, M. Calviani, P. Colas, et al., "Development and performance of Microbulk Micromegas detectors," *JINST* 5 (2010) P02001, DOI: 10.1088/1748-0221/5/02/P02001, URL: http://stacks.iop.org/1748-0221/5/i=02/a=P02001 (cit. on p. 35).

[79] G. Vasseur, "Operation of the T2K time projection chambers," *JINST* 7 (2012) C02040, DOI: 10.1088/1748-0221/7/02/C02040, arXiv: 1111.4426 [physics.ins-det], URL: http://stacks.iop.org/1748-0221/7/i=02/a=C02040 (cit. on p. 36).

[80] J. Galan, S. Aune, J. Carmona, T. Dafni, G. Fanourakis, et al., "Micromegas detectors in the CAST experiment," *JINST* 5 (2010) P01009, DOI: 10.1088/1748-0221/5/01/P01009, URL: http://stacks.iop.org/1748-0221/5/i=01/a=P01009 (cit. on p. 36).

[81] J. Pancin, U. Abbondanno, G. Aerts, H. Alvarez, S. Andriamonje, et al., "Measurement of the n−TOF beam profile with a micromegas detector," *Nucl. Instrum. Meth.* A 524 (2004) 102–114, DOI: 10.1016/j.nima.2004.01.055, URL: http://www.sciencedirect.com/science/article/pii/S0168900204001512 (cit. on p. 36).

[82] W. Shockley, "Currents to Conductors Induced by a Moving Point Charge," *JAP* 9 (Oct. 1938) 635–636, DOI: 10.1063/1.1710367, URL: http://link.aip.org/link/?JAP/9/635/1 (cit. on p. 36).

[83] S. Ramo, "Currents induced by electron motion," *Proc. Ire.* 27 (1939) 584–585, DOI: 10.1109/JRPROC.1939.228757 (cit. on p. 36).

[84] Z. He, "Review of the Shockley-Ramo theorem and its application in semiconductor gamma-ray detectors," *Nucl. Instrum. Meth.* A 463 (May 2001) 250–267, DOI: 10.1016/S0168-9002(01)00223-6, URL: http://www.sciencedirect.com/science/article/pii/S0168900201002236 (cit. on p. 37).

[85] R. Bellazzini et al., "Reading a GEM with a VLSI pixel ASIC used as a direct charge collecting anode," *Nucl. Instrum. Meth.* A 535 (2004) 477–484, DOI: 10.1016/j.nima.2004.07.269, URL: http://www.sciencedirect.com/science/article/pii/S0168900204017103 (cit. on p. 38).

[86] M. Campbell et al., "Detection of single electrons by means of a Micromegas-covered MediPix2 pixel CMOS readout circuit," *Nucl. Instrum. Meth.* A 540 (2005) 295–304, DOI: 10.1016/j.nima.2004.11.036, arXiv: physics/0409048 [physics], URL: http://www.sciencedirect.com/science/article/pii/S0168900204024428 (cit. on pp. 38, 47).

[87] P. Colas, A. Colijn, A. Fornaini, Y. Giomataris, H. van der Graaf, et al., "The readout of a GEM- or micromegas-equipped TPC by means of the Medipix2 CMOS sensor as direct anode," *Nucl. Instrum. Meth.* A 535 (2004) 506–510, DOI: 10.1016/j.nima.2004.07.180, URL: http://www.sciencedirect.com/science/article/pii/S0168900204017176 (cit. on p. 38).

[88] V. M. B. Carballo et al.,
"A Radiation Imaging Detector Made by Postprocessing a Standard CMOS Chip,"
IEEE Elec. Dev. Lett. 29 (May 2008) 585–588, DOI: 10.1109/LED.2008.925649,
URL: http://doc.utwente.nl/62384/ (cit. on p. 38).

[89] M. Chefdeville et al., "An electron-multiplying "Micromegas" grid made in silicon wafer post-processing technology," *Nucl. Instrum. Meth.* A 556 (2006) 490–494,
DOI: http://dx.doi.org/10.1016/j.nima.2005.11.065,
URL: http://www.sciencedirect.com/science/article/pii/S0168900205021418
(cit. on pp. 38, 39).

[90] V. M. Blanco Carballo et al., "GEMGrid: a wafer post-processed GEM-like radiation detector," *Nucl. Instrum. Meth.* A 608 (2009) 86–91,
DOI: http://dx.doi.org/10.1016/j.nima.2009.06.023,
URL: http://www.sciencedirect.com/science/article/pii/S0168900209012194
(cit. on p. 39).

[91] D. R. Nygren, "The Time Projection Chamber: A New 4 pi Detector for Charged Particles," *eConf* C740805 (1974) 58 (cit. on p. 39).

[92] J. Alme et al., "The ALICE TPC, a large 3-dimensional tracking device with fast readout for ultra-high multiplicity events," *Nucl. Instrum. Meth.* A622 (Jan. 2010) 316–367,
DOI: 10.1016/j.nima.2010.04.042,
URL: http://www.sciencedirect.com/science/article/pii/S0168900210008910
(cit. on pp. 39, 40).

[93] M. J. Schultens, "Teststrahlmessungen mit hochgranularer Auslese einer Zeitprojektionskammer bei verschiedenen Pixelgrößen,"
Diploma thesis: Rheinische Friedrich-Wilhelms-Universität Bonn, Sept. 2010,
URL: http://pi.physik.uni-bonn.de/pi_plone/lhc-ilc/theses/diplomarbeitschultens.pdf (cit. on p. 40).

[94] M. Hauschild, "dE/dx and Particle ID Performance with Cluster Counting,"
ILC Workshop - ECFA and GDE Joint Meeting, Nov. 2006, URL:
http://ilcagenda.linearcollider.org/conferenceOtherViews.py?confId=1049&view=cdsagenda&showDate=all&showSession=all&detailLevel=contribution
(cit. on p. 40).

[95] J.-F. Caron, C. Hearty, P. Lu, R. So, R. Cheaib, et al., "Improved Particle Identification Using Cluster Counting in a Full-Length Drift Chamber Prototype" (2013),
arXiv: 1307.8101 [physics.ins-det] (cit. on p. 40).

[96] M. Killenberg, "Resolution Studies of a GEM-Based TPC," PhD thesis: RWTH Aachen, 2007,
URL: http://darwin.bth.rwth-aachen.de/opus3/volltexte/2007/1802/
(cit. on p. 42).

[97] A. Vogel, "Beam-induced backgrounds in detectors at the ILD,"
PhD thesis: Universität Hamburg, 2008, URL: http://www.physnet.uni-hamburg.de/services/fachinfo/___Volltexte/Adrian___Vogel/Adrian___Vogel.pdf
(cit. on p. 43).

[98] T. Behnke, K. Dehmelt, L. Diener Hallermann, T. Matsuda, V. Prahl, and P. Schade, "A Lightweight Field Cage for a Large TPC Prototype for the ILC," *JINST* 5.10 (2010) P10011, DOI: 10.1088/1748-0221/5/10/P10011, arXiv: 1006.3220 [physics.ins-det], URL: http://stacks.iop.org/1748-0221/5/i=10/a=P10011 (cit. on p. 43).

[99] LCTPC Collaboration, "Report to DESY PRC 2010" (2012), URL: http://www-flc.desy.de/lcnotes/notes/LC-DET-2012-067.pdf (cit. on pp. 43, 44).

[100] D. Peterson, "Development of a Low-Material TPC Endplate for ILD" (2012), URL: http://www-flc.desy.de/lcnotes/notes/LC-DET-2012-072.pdf (cit. on pp. 43, 44).

[101] M. Kobayashi, R. Yonamine, T. Tomioka, A. Aoza, H. Bito, et al., "Cosmic ray tests of a GEM-based TPC prototype operated in Ar-CF4-isobutane gas mixtures," *Nucl. Instrum. Meth.* A 641 (2011) 37–47, DOI: 10.1016/j.nima.2011.02.042,10.1016/j.nima.2012.09.016, arXiv: 1008.5068 [physics.ins-det], URL: http://www.sciencedirect.com/science/article/pii/S016890021100355X (cit. on p. 43).

[102] K. Ackermann et al., "Results from a TPC Prototype for the Linear Collider Tracker with the MWPC and GEM Endplate Technologies," tech. rep. LC-DET-2012-066, July 2012, URL: http://www-flc.desy.de/lcnotes/notes/LC-DET-2012-066.pdf (cit. on pp. 44, 47).

[103] R. Menzen, "InGrid based TPC readout," Master thesis: Rheinische Friedrich-Wilhelms-Universität Bonn, Sept. 2013 (cit. on p. 44).

[104] F. Klöckner, "Teststrahlmessungen einer GEM-basierten TPC mit simulatner Datenauslese von acht Timepix-Chips," Diploma thesis: Rheinische Friedrich-Wilhelms-Universität Bonn, May 2010, URL: http://pi.physik.uni-bonn.de/pi_plone/lhc-ilc/theses/DiplomarbeitKloeckner.pdf (cit. on p. 44).

[105] M. Lupberger, Personal communication, 2012 (cit. on p. 44).

[106] P. Gros and A. Sugiyama, "Considerations for an ion gate for LCTPC" (2012), URL: http://www-flc.desy.de/lcnotes/notes/LC-DET-2012-079.pdf (cit. on p. 45).

[107] F. Sauli, L. Ropelewski, and P. Everaerts, "Ion feedback suppression in time projection chambers," *Nucl. Instrum. Meth.* A 560 (2006) 269–277, DOI: http://dx.doi.org/10.1016/j.nima.2005.12.239, URL: http://www.sciencedirect.com/science/article/pii/S0168900205026781 (cit. on p. 45).

[108] A. Bamberger et al., "Readout of GEM detectors using the Medipix2 CMOS pixel chip," *Nucl. Instrum. Meth.* A 573 (2007) 361–370, DOI: 10.1016/j.nima.2006.12.049, URL: http://www.sciencedirect.com/science/article/pii/S0168900206024739 (cit. on p. 47).

[109] F. Müller, "Commissioning and Characterization of a TPC with an InGrid-Based Readout" (Nov. 2011), URL: http://pi.physik.uni-bonn.de/pi_plone/lhc-ilc/view.php?lang=de&c=t&id=38 (cit. on p. 47).

[110] S. Zimmermann, "Data Reconstruction and Analysis of GEM-Based Time Projection Chambers with Pixel Readout," Diploma thesis: Rheinische Friedrich-Wilhelms-Universität Bonn, Sept. 2008, URL: http://pi.physik.uni-bonn.de/pi_plone/lhc-ilc/view.php?lang=de&c=t&id=4 (cit. on pp. 47, 49, 64, 97).

[111] X. Llopart, M. Campbell, R. Dinapoli, D. San Segundo, and E. Pernigotti, "Medipix2: A 64-k pixel readout chip with 55- mu;m square elements working in single photon counting mode," *Nuclear Science, IEEE Transactions on* 49.5 (Oct. 2002) 2279–2283, DOI: 10.1109/TNS.2002.803788 (cit. on p. 48).

[112] X. Llopart, R. Ballabriga, M. Campbell, L. Tlustos, and W. Wong, "Timepix, a 65k programmable pixel readout chip for arrival time, energy and/or photon counting measurements," *Nucl. Instrum. Meth.* A 581 (2007), Proceedings of the 11th International Vienna Conference on Instrumentation 485–494, DOI: 10.1016/j.nima.2007.08.079, URL: http://www.sciencedirect.com/science/article/pii/S0168900207017020%22 (cit. on p. 48).

[113] X. Llopart Cudie, "Design and Characterization of 64K Pixels Chips Working in Single Photon Processing Mode," Presented on 25 May 2007, PhD thesis: Mid Sweden University, 2007, URL: http://cds.cern.ch/record/1056683/files/thesis-2007-062.pdf (cit. on p. 48).

[114] C. Brezina, "A GEM based Time Projection Chamber with pixel readout," PhD thesis: Rheinische Friedrich-Wilhelms-Universität Bonn, May 2013, URL: http://hss.ulb.uni-bonn.de/2013/3316/3316.pdf (cit. on pp. 50, 106).

[115] J. Jakubek, A. Cejnarova, T. Holy, S. Pospisil, J. Uher, and Z. Vykydal, "Pixel detectors for imaging with heavy charged particles," *Nucl. Instrum. Meth.* A 591 (2008) 155–158, DOI: http://dx.doi.org/10.1016/j.nima.2008.03.091, URL: http://www.sciencedirect.com/science/article/pii/S0168900208004245 (cit. on p. 50).

[116] J. Jakubek, "Precise energy calibration of pixel detector working in time-over-threshold mode," *Nucl. Instrum. Meth.* A 633, Supplement 1 (2011) S262–S266, DOI: http://dx.doi.org/10.1016/j.nima.2010.06.183, URL: http://www.sciencedirect.com/science/article/pii/S0168900210013732 (cit. on p. 50).

[117] V. Kroner, "Signal development and pad-size studies in a GEM TPC with pixel readout," Master thesis: Rheinische Friedrich-Wilhelms-Universität Bonn, Nov. 2012 (cit. on p. 51).

[118] T. Poikela, J. Plosila, T. Westerlund, J. Buytaert, M. Campbell, et al., "Architectural modeling of pixel readout chips Velopix and Timepix3," *JINST* 7 (2012) C01093, DOI: 10.1088/1748-0221/7/01/C01093, URL: http://stacks.iop.org/1748-0221/7/i=01/a=C01093 (cit. on p. 52).

[119] V. Gromov, M. van Beuzekom, R. Kluit, F. Zappon, V. Zivkovic, et al., "Development and applications of the Timepix3 readout chip," *PoS* VERTEX2011 (2011) 046 (cit. on pp. 52, 95).

[120] J. Schmitz, "Adding functionality to microchips by wafer post-processing," *Nucl. Instrum. Meth.* A 576 (2007) 142–149, DOI: 10.1016/j.nima.2007.01.142, URL: http://www.sciencedirect.com/science/article/pii/S0168900207002288 (cit. on p. 52).

[121] J. Schmitz, "The InGrid chip post-processing technology for radiation imaging," *PoS* VERTEX2009 (2009) 022 (cit. on p. 52).

[122] V. M. B. Carballo et al., "A Radiation Imaging Detector Made by Postprocessing a Standard CMOS Chip," *Electronic Device Letters, IEEE* 29 (June 2008) 585–587, DOI: 10.1109/LED.2008.925649 (cit. on p. 52).

[123] M. Fransen, "GridPix: TPC development on the right track. The development and characterisation of a TPC with a CMOS pixel chip readout.," PhD thesis: University of Twente, 2012, URL: http://www.nikhef.nl/pub/services/biblio/theses_pdf/thesis_M_Fransen.pdf (cit. on pp. 52, 71, 80).

[124] V. M. Blanco Carballo, "Radiation imaging detectors made by wafer post-processing of CMOS chips," PhD thesis: University of Twente, June 2009, URL: http://doc.utwente.nl/61528/ (cit. on pp. 53, 80).

[125] M. J. Madou, "Fundamentals of Microfabrication: The Science of Miniaturization," 3rd ed., CRC Press, 2002 (cit. on p. 53).

[126] S. A. Campbell, "The Science and Engineering of Microelectronic Fabrication," Oxford series in electrical and computer engineering, Oxford University Press, 2001 (cit. on p. 53).

[127] C. Krieger, "Construction and First Measurements of a GridPix based X-ray Detector," Master thesis: Rheinische Friedrich-Wilhelms-Universität Bonn, Feb. 2012, URL: http://pi.physik.uni-bonn.de/pi_plone/lhc-ilc/view.php?lang=de&c=t&id=24 (cit. on pp. 58, 61, 64).

[128] K. Zioutas, *CAST - CERN Axion Solar Telescope*, 2013, URL: http://cast.web.cern.ch/CAST/ (visited on 25/09/2013) (cit. on p. 58).

[129] Y. Bilevych, Personal communication, 2012 (cit. on pp. 59, 61, 64).

[130] R. Schön, Personal communication, 2012 (cit. on pp. 60, 64).

[131] T. Krautscheid et al., "Gridpix: Production and application of integrated pixel readouts," *Nucl. Instrum. Meth.* A 718 (2013) 391–394, DOI: 10.1016/j.nima.2012.10.055, URL: http://www.sciencedirect.com/science/article/pii/S0168900212011904 (cit. on pp. 61, 80, 81).

[132] D. S. S. Bello, M. van Beuzekom, P. Jansweijer, H. Verkooijen, and J. Visschers, "An interface board for the control and data acquisition of the Medipix2 chip," *Nucl. Instrum. Meth.* A 509 (2003) 164–170, DOI: http://dx.doi.org/10.1016/S0168-9002(03)01566-3, URL: http://www.sciencedirect.com/science/article/pii/S0168900203015663 (cit. on p. 63).

[133] T. Holy, J. Jakubek, S. Pospisil, J. Uher, D. Vavrik, and Z. Vykydal, "Data acquisition and processing software package for Medipix2," *Nucl. Instrum. Meth.* A 563 (2006) 254–258, DOI: http://dx.doi.org/10.1016/j.nima.2006.01.122, URL: http://www.sciencedirect.com/science/article/pii/S0168900206002075 (cit. on p. 63).

[134] D. Turecek, T. Holy, J. Jakubek, S. Pospisil, and Z. Vykydal, "Pixelman: a multi-platform data acquisition and processing software package for Medipix2, Timepix and Medipix3 detectors," *JINST* 6.01 (2011) C01046, DOI: 10.1088/1748-0221/6/01/C01046, URL: http://stacks.iop.org/1748-0221/6/i=01/a=C01046 (cit. on p. 63).

[135] S. S., "Vermessung der Untergrundunterdrückung eines neuen CAST-Detektors mittels multivariater Methoden aus TMVA," Bachelor thesis: Rheinische Friedrich-Wilhelms-Universität Bonn, Sept. 2013 (cit. on p. 64).

[136] C. Krieger, J. Kaminski, and K. Desch, "InGrid-based X-ray detector for low background searches," *Nucl. Instrum. Meth.* A 729 (2013) 905–909, DOI: http://dx.doi.org/10.1016/j.nima.2013.08.075, URL: http://www.sciencedirect.com/science/article/pii/S0168900213012163 (cit. on pp. 70, 72, 81).

[137] H. van der Graaf, "GridPix: An integrated readout system for gaseous detectors with a pixel chip as anode," *Nucl. Instrum. Meth.* A 580.2 (2007) 1023–1026, DOI: 10.1016/j.nima.2007.06.096, URL: http://www.sciencedirect.com/science/article/pii/S0168900207013162/ (cit. on p. 80).

[138] M. Adinolfi, G. Carboni, R. Messi, L. Pacciani, L. Paoluzi, and E. Santovetti, "Performance of low-resistivity single and dual-gap RPCs for LHCb," *Nucl. Instrum. Meth.* A 456 (2000), Proceedings of the 5th Int. Workshop on Resistive Plate Chambers and Related Detectors 95–98, DOI: 10.1016/S0168-9002(00)00970-0, URL: http://www.sciencedirect.com/science/article/pii/S0168900200009700 (cit. on p. 80).

[139] W-IE-NE-R Plein & Baus GmbH, *NEMbox / NIMbox Programmable NIM Module*, 2013, URL: http://www.wiener-d.com/sc/modules/nim--modules/nembox-nimbox.html (visited on 23/10/2013) (cit. on p. 82).

[140] D. Decamp et al., "ALEPH: A detector for electron-positron annnihilations at LEP," *Nucl. Instrum. Meth.* A 294 (1990) 121–178, DOI: 10.1016/0168-9002(90)91831-U, URL: http://www.sciencedirect.com/science/article/pii/016890029091831U (cit. on p. 82).

[141] W. Blum, "The ALEPH handbook: 1989," ed. by W. Blum, Geneva: CERN, 1989 (cit. on p. 82).

[142] P. Mora de Freitas, G. Musat, et al., *Mokka - A detailed Geant4 simulation for the International Linear Collider detectors*, 2013, URL: http://polzope.in2p3.fr:8081/MOKKA (visited on 29/09/2013) (cit. on p. 86).

[143] S. Agostinelli et al., "Geant4: A Simulation toolkit," *Nucl. Instrum. Meth.* A 506 (2003) 250–303, DOI: http://dx.doi.org/10.1016/S0168-9002(03)01368-8, URL: http://www.sciencedirect.com/science/article/pii/S0168900203013688 (cit. on p. 86).

[144] D. Schulte, "Study of Electromagnetic and Hadronic Background in the Interaction Region of the TESLA Collider," PhD thesis: Universität Hamburg, 1996, URL: http://flash.desy.de/sites2009/site_vuvfel/content/e403/e1644/e1314/e1316/infoboxContent1932/tesla1997-08.pdf (cit. on p. 86).

[145] D. Schulte, *Guinea Pig*, 2003, URL: http://www-project.slac.stanford.edu/lc/bdir/programs/guinea_pig/gp_index.html (visited on 29/10/2013) (cit. on p. 86).

[146] M. Chen and P. M. Zerwas, "Equivalent-Particle Approximations in electron and Photon Processes of Higher Order QED," *Phys. Rev.* D12 (1975) 187, DOI: 10.1103/PhysRevD.12.187 (cit. on p. 86).

[147] L. Garren and P. Lebrun, *StdHep*, 2013, URL: http://cepa.fnal.gov/psm/stdhep/ (visited on 21/10/2013) (cit. on p. 86).

[148] W. Kilian, T. Ohl, and J. Reuter, "WHIZARD: Simulating Multi-Particle Processes at LHC and ILC," *Eur. Phys. J.* C 71 (2011) 1742, DOI: 10.1140/epjc/s10052-011-1742-y, arXiv: 0708.4233 [hep-ph] (cit. on p. 86).

[149] T. Krämer et al., *MarlinReco, a Marlin based Reconstruction Package for the ILC*, 2006, URL: http://ilcsoft.desy.de/MarlinReco/v00-02/manual_html/manual.html (visited on 29/09/2013) (cit. on p. 87).

[150] M. Killenberg, "Software and Parameters for Detailed TPC Studies in th CLIC CDR" (Sept. 2011), URL: http://cds.cern.ch/record/1498742/files/software_detailed_TPC_studies_CDR.pdf (cit. on p. 87).

[151] S. Aplin, J. Engels, F. Gaede, N. Graf, T. Johnson, et al., "LCIO: A Persistency Framework and Event Data Model for HEP" (2012) 2075–2079 (cit. on p. 88).

[152] S. Rossegger, "Static Green's functions for a coaxial cavity including an innovative representation" (2009) (cit. on pp. 88, 90).

[153] S. Rossegger, "Simulation and Calibration of the ALICE TPC including innovative Space Charge Calculations," PhD thesis: TU Graz, 2009, URL: https://cds.cern.ch/record/1502388/files/CERN-THESIS-2012-214.pdf?version=1 (cit. on p. 88).

[154] F. Gaede, "Marlin and LCCD-Software tools for the ILC,"
Nucl. Instrum. Meth. A 559 (2006) 177–180, DOI: 10.1016/j.nima.2005.11.138,
URL: http://www.sciencedirect.com/science/article/pii/S0168900205022643
(cit. on p. 92).

[155] J. Abernathy et al., "MarlinTPC: A Marlin based common TPC software framework for the LC-TPC collaboration," *eConf* C0705302 (2007) TRK01,
arXiv: 0709.0790 [physics.ins-det] (cit. on p. 93).

[156] A. Münnich, "Simulation Studies for a High Resolution Time Projection Chamber at the International Linear Collider," PhD thesis: RWTH Aachen, 2007,
URL: http://darwin.bth.rwth-aachen.de/opus3/volltexte/2007/1893/
(cit. on p. 94).

[157] T. Krautscheid, "Simulationen zur Ionenrück in einer Zeit-Projektionskammer am ILC," Diploma thesis: Rheinische Friedrich-Wilhelms-Universität Bonn, Aug. 2008, URL:
http://pi.physik.uni-bonn.de/pi_plone/lhc-ilc/view.php?lang=de&c=t&id=5
(cit. on p. 94).

[158] I. B. Smirnov, "Modeling of ionization produced by fast charged particles in gases,"
Nucl. Instrum. Meth. 554 (2005) 474–493, DOI: 10.1016/j.nima.2005.08.064,
URL: http://www.sciencedirect.com/science/article/pii/S0168900205016724
(cit. on p. 94).

[159] M. Rogowski,
"Working title: Reconstruction of particle tracks in a large area TPC with a pixelized readout,"
forthcoming, Master thesis, 2014 (cit. on p. 97).

[160] J. Engels and F. Gaede, *ILC MC Database 2012*, 2012,
URL: https://ilcproddb.desy.de/admin/ild/gen/?process_type=aa_lowpt (visited on 17/11/2012) (cit. on p. 100).

[161] R. Ballabriga, M. Campbell, E. Heijne, X. Llopart, L. Tlustos, and W. Wong,
"Medipix3: A 64k pixel detector readout chip working in single photon counting mode with improved spectrometric performance,"
Nucl. Instrum. Meth. A 633, Supplement 1 (2011) 15–18,
DOI: 10.1016/j.nima.2010.06.108,
URL: http://www.sciencedirect.com/science/article/pii/S0168900210012982
(cit. on p. 107).

[162] B. Smirnov, "Diffusion and Mobility of Ions in a Gas,"
Soviet Physics Uspekhi 10.3 (1967) 313,
URL: http://stacks.iop.org/0038-5670/10/i=3/a=R04 (cit. on p. 110).

[163] R. Gluckstern, "Uncertainties in track momentum and direction, due to multiple scattering and measurement errors," *Nucl. Instrum. Meth.* 24 (1963) 381–389,
DOI: http://dx.doi.org/10.1016/0029-554X(63)90347-1,
URL: http://www.sciencedirect.com/science/article/pii/0029554X63903471
(cit. on p. 114).

[164] R. Yonamine,
"Measuring the top Yukawa coupling at the ILC at $\sqrt{s}$ = 500 GeV and R&D for the ILD-TPC,"
PhD thesis: School of High Energy Accelerator Science, 2012,
URL: http://www-hep.phys.saga-u.ac.jp/ILC-TPC/ (cit. on p. 117).

[165] A. Bott, *Meteorologisches Institut Universität Bonn*, 2013,
URL: `http://www.meteo.uni-bonn.de/` (visited on 31/10/2013) (cit. on p. 135).

List of Figures

List of Tables